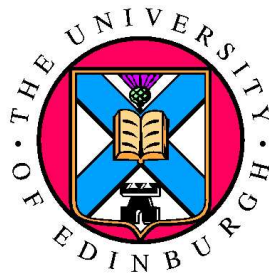


Reconstruction of the Past and Forecast of the
Future European and British Ice Sheets and
Associated Sea–Level Change

Magnus K. M. Hagdorn



Thesis submitted in fulfilment of
the requirements for the degree of
Doctor of Philosophy
to the
University of Edinburgh — 2003

This work is licensed under the Creative Commons Attribution-ShareAlike License. To view a copy of this license, visit <http://creativecommons.org/licenses/by-sa/1.0/> or send a letter to Creative Commons, 559 Nathan Abbott Way, Stanford, California 94305, USA.

Declaration

I declare that this thesis has been composed solely by myself and that it has not been submitted, either in whole or in part, in any previous application for a degree. Except where otherwise acknowledged, the work presented is entirely my own.

Magnus K. M. Hagdorn
September 2003

Foreword

This project is sponsored by United Kingdom Nirex Limited (Nirex) as part of the Nirex Research Programme. Nirex is responsible for carrying out research relating to the safe disposal of intermediate and low level radioactive waste in the UK. Nuclear waste poses a challenging problem: much radioactive waste remains toxic for tens of thousands of years and more, and therefore, needs to be safely stored for its toxic lifetime. Radionuclides will eventually migrate to the biosphere. ‘Safely stored’, therefore, means that the concentrations are below guidance levels over reasonable timescales. Radionuclides can reach the surroundings of the repository (other than by human intervention, both accidentally or purposefully), by groundwater transport. The patterns and rates of groundwater flow over timescales of tens of thousands of years or more are influenced by, amongst other factors, changes in sea-level and lithosphere loading by ice sheets. A post-closure safety assessment of a nuclear repository, therefore, has to consider the effects of large-scale climate change, including the possible advance and retreat of ice sheets, the associated sea-level changes and the crustal stress states influenced by such changes which determine hydromechanical and geotechnical properties of the rock a repository is emplaced in. Thus, this thesis has been stimulated by the need to develop realistic scenarios for future ice-sheet development and associated environmental effects over northern Europe, in general, and the British Isles, in particular.

Abstract

The aim of this project is to improve our understanding of the past European and British ice sheets as a basis for forecasting their future. The behaviour of these ice sheets is investigated by simulating them using a numerical model and comparing model results with geological data including relative sea-level change data. In order to achieve this aim, a coupled ice sheet/lithosphere model is developed.

Ice sheets form an integral part of the Earth system. They affect the planet's albedo, atmospheric and oceanic circulation patterns, topography, and global and local sea-level change. In order to understand how these systems work, it is necessary to understand how ice sheets interact with other parts of the climate system. This project does this by simulating ice behaviour as part of the climate system and evaluating model behaviour in relation to evidence of past ice sheets.

Ice sheet simulations can be treated with more confidence if they can be evaluated against independent data. A methodology is therefore developed that compares relative sea-level records with simulations of past sea-level which result from modelling past ice sheets with a dynamic, high-resolution thermo-mechanical ice sheet model coupled to an isostatic adjustment model. The Earth's response to changing surface loads is simulated using both a regional, flat Earth approximation and a global, spherical self-gravitating Earth model.

The coupled model is tested by initially simulating the past Fennoscandian ice sheet because of the simpler topographic framework and the quality of geological evidence of past fluctuations against which to evaluate model behaviour. The model is driven by a climatic forcing function determined so that the simulated ice sheet resembles the past Fennoscandian ice sheet as reconstructed from geomorphological evidence. The Fennoscandian climate driver is then transferred to the British Isles to simulate the past British ice sheet. Finally, a non-linear regression technique is used to construct future ice sheet drivers from future sea-level change scenarios to forecast sea-level change around the British Isles during the next glacial cycle.

The data used for the inversion procedure is limited to southern Scandinavia. Outside this area, the simulation compares poorly with reconstructions based on geological observations. However, model fit within this region is good and the simulation is also in good agreement with features not used during the inversion process. This approach illustrates the benefit of using a model coupling realistic ice physics to a realistic Earth model to help constrain simultaneously unknowns

of Earth rheology and ice thickness. Ultimately, relative sea-level data together with other strands of data, such as geomorphological evidence, and a coupled ice sheet/isostatic rebound model can be used to help infer past climates.

Acknowledgements

First of all, I would like to thank my supervisors Geoffrey Boulton and Nick Hulton for getting me started with this very interesting project and for supporting me with their advice and many stimulating discussions. Thank you very much, Nick, for helping me beat this thesis into shape. This project was funded by UK Nirex Ltd as part of the Nirex Research Programme. In particular, I would like to thank Paul Degnan and Mike Thorne for the many helpful comments throughout this project and the careful review of this thesis.

It is rare that computer modellers get to go to exotic places. It was, therefore, fantastic to be able to go to Australia where I spent six months at the RSES, the Australian National University in Canberra to work with Kurt Lambeck and Paul Johnston on coupling their spherical Earth model with the ice sheet model. I am very grateful for the warm welcome and the help I received from the people I met in Australia. In particular, I would like to thank Stuart who took me along to explore the Australian wildlife.

I want to take this opportunity to thank the many people writing free (as in *libre*) software without which much of this work could not have been realised. This document was typeset using L^AT_EX the only sane way of writing a large document.

Edinburgh would only be half as fantastic without all the new family, friends and flat mates who kept me sane during all this time. Special thanks go to Alex and Stu for the innumerable giggles and crazy discussions. Great thanks also go to Richard, the independent mind, who read this thesis and complained about my writing and gaps in logic.

Ich möchte mich nun auch bei meiner Familie, insbesondere bei meinen lieben Eltern und meiner lieben Schwester für ihre Unterstützung bedanken. Ihr seid einfach großartig!

Finally, I want to thank Rowan for her unyielding support and her great patience.

For Rowan and Felix.

Contents

Declaration	iii
Foreword	v
Abstract	vii
Acknowledgements	ix
Contents	xi
List of Tables	xv
List of Figures	xvii
List of Symbols	xxi
1 Introduction	1
1.1 Rationale	1
1.2 Modelling Ice Sheets and the Earth System	3
1.2.1 Feedback Mechanisms within the Ice—Climate System	4
1.2.2 Approaches to Ice Sheet Modelling	8
1.2.3 The Edinburgh Ice Sheet Model	9
1.3 Constraining Model Behaviour with Multi–Proxy Data	10
1.3.1 Evidence of Past Ice Sheets	11
1.3.2 Causes of Ice Ages	13
1.4 Relative Sea–Level Change	14
1.4.1 Causes of Sea–Level Change	15
1.4.2 SPECMAP and Equivalent Sea–Level Change	17
1.4.3 Relative Sea–Level Data Sets	19
1.5 Objectives and Thesis Plan	21

2	Theory	23
2.1	The Ice Sheet Model	24
2.1.1	Thermomechanical Equations Governing Ice Flow	24
2.1.2	Boundary Conditions	27
2.2	Earth Models	32
2.2.1	First Approximations to Isostatic Adjustment	33
2.2.2	The Full Spherical Earth Model	37
2.2.3	The Earth Model and Global Sea–Level Change	40
2.3	Model Implementation	42
2.3.1	Ice Sheet Model	42
2.3.2	Earth Models	47
2.3.3	Testing and Comparing the Isostasy Models	50
2.4	Summary	54
3	Fennoscandian Experiment	59
3.1	Model Setup	60
3.1.1	Topography	60
3.1.2	Temperature Forcing	61
3.2	ELA Forcing and Ice Sheet Evolution	65
3.3	Ice Sheet Parameters	74
3.3.1	Isostatic Response	76
3.3.2	Parameters Affecting Ice Flow	77
3.4	Ice Streams	80
3.4.1	Bedrock Topography Control	85
3.4.2	Streams of the S-10 Experiment	87
3.5	Relative Sea–Level Change	89
3.6	Conclusion	95
4	Reconstruction of the Past British Ice Sheet	99
4.1	British Ice Sheet Model Setup	100
4.1.1	Topography	100
4.1.2	ELA forcing	101
4.2	Ice Sheet Evolution	102
4.2.1	The Norwegian Channel Ice Stream	104
4.2.2	Relative Sea–Level Change	108
4.3	Conclusion	108

5	Projecting the Evolution of a Future British Ice Sheet	113
5.1	Climate Drivers for Simulating Future Ice Sheet Scenarios	114
5.1.1	Additivity and Variance Stabilising Transformations (AVAS)	115
5.1.2	Modelling the Past ELA Driver using AVAS	116
5.1.3	Modelling the Past Temperature Driver using AVAS	117
5.2	Simulating the Past Ice Sheets using the AVAS Drivers	117
5.2.1	The Past European Ice Sheet	117
5.2.2	The Past British Ice Sheet	124
5.3	Simulating the Future British Ice Sheet	128
5.3.1	LLN–2D Climate Model and Future Global Sea–Level Scen- arios	128
5.4	Conclusion	130
6	Conclusions	135
6.1	Summary	135
6.2	The Ice Sheet Model and Real Processes	136
6.3	Coupling the Ice Sheet and the Lithosphere	137
6.4	Model Simulations	138
6.4.1	Simulations of Past Ice Sheet Activity	138
6.4.2	The Future British Ice Sheet	139
6.4.3	Linking Ice Sheets to Climate	139
6.5	Using and Developing Models	140
6.6	Multi–Proxy Data and Inverse Approaches	141
6.6.1	Data Management	141
6.6.2	An Automatic Inversion Procedure	141
A	Mathematical Definitions	143
A.1	Kelvin Functions	143
A.2	AVAS transforms	146
A.2.1	ELA Model 1	146
A.2.2	ELA Model 2	148
A.2.3	ELA Model 3	150
A.2.4	ELA Model 4	152
A.2.5	ELA Model 5	154
A.2.6	Temperature Model 1	155
A.2.7	Temperature Model 2	157
B	Software	159
B.1	CD-ROM	159
B.2	File Description	160
	References	163

List of Tables

2.1	Parameters for a continental and maritime mass balance curves. . .	29
2.2	Earth Model parameters used.	52
2.3	Earth model parameter sets with the best fit and their corresponding errors for different disk loads.	54
2.4	Averaged best fitting parameters and their associated errors. . . .	56
3.1	Parameters for temperature Model 1 leading to the best fit with the observations.	64
3.2	Earth model parameters used in Section 3.3.1.	76
5.1	Statistical models using different combinations of regression variables for modelling the ELA forcing function.	119
5.2	Summary of the statistical models used for modelling the smoothed temperature forcing function.	121
5.3	Summary of climate simulations performed by Burgess (1998) using the LLN-2D model (adapted from Goodess <i>et al.</i> , 2000b).	129

List of Figures

1.1	Feedback mechanisms of the ice sheet — lithosphere system.	5
1.2	The Earth’s orbital parameters.	13
1.3	Temporal and spatial scales of processes causing sea-level change	15
1.4	Schematic diagram of the coupled ice sheet—Earth system.	18
1.5	Global sea-level curve used for forcing the ice sheet model.	18
1.6	World map showing locations of the relative sea-level observations used.	19
1.7	Schematic illustrations of different types of relative sea-level curves.	20
1.8	Example relative sea-level data and the equivalent sea-level curve based on SPECMAP.	21
2.1	Illustration of the coordinate system used for developing the equations governing ice dynamics.	24
2.2	Altitude—mass balance relationship for extreme maritime and continental climates.	30
2.3	Isostatic adjustment of the lithosphere due to an ice sheet.	32
2.4	Isostatic adjustment to a disk load.	35
2.5	Approximating a square ice load with a number of disk loads.	36
2.6	Far-field isostatic components of the relative sea-level equation	42
2.7	Vertical scaling of the ice sheet model.	44
2.8	Domain decomposition used for the parallelisation of the ice sheet model.	45
2.9	Speedup and efficiency of the MPI code.	48
2.10	Flow diagram illustrating how the spherical Earth model is coupled to the ice sheet model.	51
2.11	Test load configuration used for comparing Earth models.	52
2.12	Sea-level change as a function of time for different test locations and isostasy models.	53
2.13	Plots of the variation of the mean difference between the full Earth model and the ELRA approximation.	55
2.14	Differences between the spherical Earth model and the ELRA approximation.	57
3.1	Schematic plan illustrating the setup of the past European ice sheet experiment.	60

3.2	European bedrock topography.	61
3.3	Temperature reconstructions along a transect through Europe. . .	62
3.4	Input temperature data plotted as a function of latitude.	63
3.5	Spatially averaged input temperatures as a function of time. . . .	65
3.6	Parameters of Temperature Model 2.	66
3.7	Modelled temperatures plotted against palaeoclimatic reconstructions and histogram of residuals for Temperature Model 1.	67
3.8	Modelled temperatures plotted against palaeoclimatic reconstructions and histogram of residuals for Temperature Model 2.	67
3.9	Temperatures at 60°N using the standard model and models S-10 and S-15 derived from the GRIP core.	68
3.10	Flowline through Europe.	69
3.11	Flow diagram illustrating the fitting procedure adopted to determine the equilibrium line altitude forcing function.	70
3.12	Mass balance forcing and resulting ice area, ice volume and model fit with geological reconstruction.	71
3.13	Evolution of the S-10 ice sheet model. Snapshots are every 6ka, from -119ka to -35ka.	72
3.14	Evolution of the S-10 ice sheet model. Snapshots are every 2ka, from -28ka to 0ka.	73
3.15	Mass balance forcing and resulting ice area and ice volume for simulations with varying equilibrium line altitude forcing.	75
3.16	Average isostatic response as a function of time.	77
3.17	Plots of ice surface and bedrock elevation and isostatic adjustment.	78
3.18	Area covered by ice and the corresponding ice volume as a function of time for the standard, cold, no sliding and reduced speed-up experiments.	79
3.19	Ice sheet extent at -85ka for the standard, cold, no sliding and reduced speed-up models.	80
3.20	Ice bed and surface elevation and surface velocities along transects.	81
3.21	Surface velocities on a log scale for the S-10, cold, no sliding and reduced speed-up experiments.	82
3.22	Basal temperatures corrected for the pressure melting point of ice for the S-10, cold, no sliding and reduced speed-up experiments.	83
3.23	Smoothed European bedrock topography.	86
3.24	Surface velocity and temperature fields of the smoothed topography experiment.	86
3.25	Enlargement of the northern part of the smoothed topography ice sheet showing surface velocities and basal temperatures.	87
3.26	Ice surfaces and surface and basal velocities of the smoothed bedrock experiment along transects.	88
3.27	Enlargement of the S-10 model run at -85ka showing ice velocities and basal temperatures.	90

3.28	Velocities of the S-10 model run at -85ka and profile showing ice velocities and temperatures.	91
3.29	Relative sea-level residual histogram ($\Delta\zeta_{\text{model}} - \Delta\zeta_{\text{obs}}$) of the standard and S-10 experiments.	93
3.30	Distribution of average relative sea-level residuals.	94
3.31	Sea-level change at selected European sites.	95
3.32	Simulated present-day crustal uplift rates from the S-10 experiment.	96
4.1	Schematic plan illustrating the setup of the past British ice sheet experiment.	100
4.2	Expanded British/European bedrock topography.	101
4.3	Additional equilibrium line altitude dependence on longitude introduced for the simulations of the past British ice sheet.	102
4.4	Time-distance diagrams showing ice margin of the British ice sheet simulation along transects.	103
4.5	The simulated British ice sheet at the glacial maximum (European/British and B5 experiments), 17ka BP.	104
4.6	The combined Fennoscandian and British ice sheet model runs.	105
4.7	Snapshots of the combined European and British simulation showing the surface velocity field and ice flow direction.	106
4.8	Reconstruction of the Norwegian Channel ice stream showing directions of ice flow.	107
4.9	Relative Sea-Level Change at selected sites for the British ice sheet simulations.	109
4.10	Relative sea-level residual histograms ($\Delta\zeta_{\text{model}} - \Delta\zeta_{\text{obs}}$) of the British simulations and their geographic distribution.	110
5.1	Schematic plan illustrating the setup of the future British ice sheet experiment.	114
5.2	Plots of regression variables used for the AVAS procedure.	118
5.3	Comparisons of the original ELA forcing function (solid lines) and the modelled ELA forcing functions (dashed lines).	120
5.4	Modelled temperature (dashed lines) and the smoothed temperature time series (solid lines) for the two temperature AVAS models.	121
5.5	Plots of the ice sheet evolution of the two AVAS simulations.	123
5.6	Snapshots of the S-10, AVAS ELA and AVAS ELA/temperature ice sheet experiments at the simulated Last Glacial Maximum (17ka BP).	124
5.7	Relative sea-level change computed by the experiments with the AVAS forcing functions.	125
5.8	British ice sheet evolution using the B5 and AVAS climate drivers.	126
5.9	Time-distance diagrams showing the movement of the ice margin of the simulated ice sheets using the B5 and AVAS climate drivers.	127
5.10	Snapshots of the maximum British ice sheet configuration using the B5 and AVAS climate drivers.	127

5.11	Plots of future global eustatic sea-level change, temperature and equilibrium line altitude forcing functions and resulting ice volume and area covered by the simulated ice sheet.	131
5.12	Sea-level change at selected sites for future British ice sheet simulations.	132
5.13	Snapshots of the future British ice sheet model forced by the AN5 climate scenario.	133
A.1	Plots of the Kelvin functions on the interval $[0,10]$	144

List of Symbols

$\Delta\text{ELA}(t)$	ELA forcing function
$\Delta\zeta$	sea level change
$\Delta\zeta^{\text{esl}}$	equivalent sea level change
δ_{ij}	Kronecker delta
$\dot{\epsilon}_{ij}$	Strain rate of polycrystalline ice in 2D, $\dot{\epsilon}_{ij} = \frac{1}{2} \left(\frac{\partial v_i}{\partial x_j} + \frac{\partial v_j}{\partial x_i} \right)$
ϵ	strain tensor
ε	error
η	viscosity
λ	latitude
λ, μ	Lamé parameters
Λ	tridiagonal matrix
ν	dynamic viscosity of the diffusive asthenosphere
ν_{lm}	viscosity of the lower mantle
ν_{um}	viscosity of the upper mantle
φ	longitude
Φ	heat generated due to internal friction
ϕ	gravitational potential
$\phi_i(X_i)$	AVAS carrier transformation of regression variable X_i
Ψ	geothermal heat flux
ρ	density

ρ_{ast}	effective density of the asthenosphere
ρ_{water}	density of water
ρ_{ice}	density of ice
$\boldsymbol{\sigma}$	stress tensor
τ	characteristic time constant of relaxed asthenosphere approximation
τ_b	basal shear stress
τ_{xz}, τ_{yz}	components of the horizontal stress tensor
τ_*	effective shear stress defined by the second invariant of the stress tensor
$\Theta(Y)$	AVAS response transformation of dependent variable Y
ϑ	colatitude
ξ	vertical coordinate, $\xi \in [0, 1]$
A	temperature-dependent flow law coefficient
a	radius of the (spherical) Earth
A_o	ocean area
b	atmospheric lapse rate
c_p	specific heat capacity of ice
D	flexural rigidity of a thin elastic plate
D_a	diffusion coefficient of the diffusive asthenosphere, $D_a = \frac{g\rho_{\text{ast}}H_a^3}{3\nu}$
E	Young's modulus
f	speed-up factor for tuning the flow law
G	Newton's universal constant of gravity
g	acceleration due to gravity
H	ice thickness
h	elevation of bedrock topography
h_0	unloaded equilibrium bedrock topography
H_a	thickness of the diffusive asthenosphere

H_L	thickness of a thin elastic plate
$h_n, l_n, (1 + k_n)$	Love numbers of harmonic degree n
H_{um}	thickness of the upper mantle
k_{ice}	thermal conductivity of ice
k_{rock}	thermal conductivity of rock
L_n	surface load of spherical harmonic degree n
L_r	radius of relative stiffness, $L_r = (D/(\rho_{\text{ast}}g))^{1/4}$
M	mass balance (accumulation minus surface melt rate)
N	effective pressure at ice base
p	pressure
Q	activation energy for creep
R	universal gas constant
r	radial coordinate
S	melt rate at the base of the ice column
t	time coordinate
T	temperature field
T^*	absolute temperature corrected for the dependence of the melting point on pressure, $T^* = T + 8.7 \cdot 10^{-4}(H + h - z)$
$T_{60^\circ\text{N}}$	surface temperatures at 60°N
$\tilde{T}_{60^\circ\text{N}}$	smoothed surface temperatures at 60°N
\mathbf{u}	displacement field
$u_n(r), v_n(r)$	radial and tangential spherical harmonic coefficients of deformation
U, V, W	spheroidal, poloidal and toroidal modes of a displacement field in spherical coordinates
\mathbf{v}	3D velocity field, $\mathbf{v} = (v_x, v_y, v_z)$
V_{ice}	ice volume
$\bar{\mathbf{v}}$	vertically averaged velocity

- w difference between the loaded bedrock topography in equilibrium and the unloaded topography in equilibrium
- (x, y, z) coordinates of a right-handed, Cartesian coordinate system with z positive upwards
- z_{ELA} equilibrium line altitude
- ∇ the gradient operator
- ∇_{H} the two-dimensional horizontal gradient operator $\left(\frac{\partial}{\partial x}, \frac{\partial}{\partial y}\right)$

Chapter 1

Introduction

The primary aim of this project has been to improve our understanding of the past European and British ice sheets as a basis for forecasting their future. The behaviour of these ice sheets was investigated by simulating them using a numerical model and by evaluating the model results against geological data including relative sea-level change records. In order to achieve this aim, a coupled ice sheet/lithosphere model was developed.

Ice sheets form an integral part of the Earth system. They affect the planet's albedo, atmospheric and oceanic circulation patterns, topography, and global and local sea-level change over timescales of tens of thousands of years. In order to understand how these systems work overall on these timescales, it is necessary to understand the behaviour of ice sheets. Global climate during the Quaternary epoch was characterised by a succession of extremely cold periods when large parts of the Northern Hemisphere were covered by large continental ice sheets and shorter intervening warm periods during which the ice sheets decayed. Thus, a large part of the recent Earth history of the Northern Hemisphere needs to be understood in the light of the role that ice sheets have played.

1.1 Rationale

There are a number of approaches to understanding ice sheet behaviour within the climate system. A fundamental problem exists in that ice sheets evolve slowly and so contemporary monitoring can only provide limited insight into longer-term behaviour. One approach is to seek evidence from the geology of former ice sheets. A great wealth of geological evidence for past glaciations has been collected since Louis Agassiz proposed the glacial theory in the mid-19th century. Evidence includes records of past sea-level changes (e.g. Dawson *et al.*, 1998; Tushingham and Peltier, 1993; Pirazzoli, 1991), past ice sheet extent and ice dynamics (e.g. Mangerud *et al.*, 2002; Boulton *et al.*, 2001b; Sejrup *et al.*, 1994; Denton and Hughes, 1981) and past climates (e.g. Bradley, 1999; Crowley and North, 1991).

These observations can be synthesised to form a coherent picture of past ice sheet behaviour.

A second, more recent strand of investigating former ice sheet behaviour is the development of numerical ice sheet models (see [Hindmarsh, 1993](#), for a review of ice sheet models). An early example of a three-dimensional ice sheet model is described by [Mahaffy \(1976\)](#). These models simulate the physics describing ice sheets in four dimensions, three spatial and one temporal. Powerful computers are required to simulate ice sheets at high resolutions in four dimensions. The capability of these models, therefore, goes hand in hand with the availability of computing power which has improved dramatically in recent years, since the development of microprocessors has followed Moore's law ([Moore, 1965](#)). Constraining the high-resolution models with observational data allows us to investigate the behaviour of the climate — ice sheet — lithosphere system.

From the outset, it is worth considering some essential questions with regard to the way in which models might be used. These influence the ability of the models to provide useful understanding:

1. Can the model reproduce geological evidence of past ice sheets, and if not, which aspects of the system are missing or are only poorly represented?
2. Do the models suggest that the dynamics of present ice sheets differ from the dynamics of past ice sheets?
3. Can the geological data be inverted using models to infer past climates, and, if so, are reconstructions unique?

The first question relates to the quality and adequacy of the model. The model needs to be evaluated in order to gain confidence in the simulation as an approximation to reality. Shortcomings of the model which are not anticipated point to new insights into how the coupled system works. The main point here is that obtaining a well-fitting model should not be an end in itself. Models can always be tuned to fit better a given pattern. What is significant is what the model explains in terms of the behavioural characteristics of a real ice sheet. It is important that it contains an adequate physical representation to encapsulate the process sequence under investigation but it cannot itself be reality. Any lack of fit is thus merely a question of degree but can itself illuminate the unexpected or unexplained. Equally a good fit may be purely coincidental and relate poorly to real events. Thus model results need to be interpreted with care in terms of the major behaviours of real systems that might reasonably be inferred to be represented within them.

In reference to the second question, climate during glacial periods when ice sheets covered large parts of the Northern Hemisphere was very different from that at the present day (e.g. [CLIMAP Project Members, 1976](#)). It is, therefore, not obvious that present ice sheet behaviour is a good analogue for past ice sheet behaviour. If ice sheet models are tuned to simulate present ice sheet behaviour

and the ice sheet model has difficulty simulating the inferred behaviour of past ice sheets, it follows that i) ice sheets during the past behaved in a characteristically different way; or ii) our knowledge and representation of the climate — ice sheet — lithosphere system is incomplete. Most important is the possibility that whilst the underlying ice–climate physics might reasonably be assumed to be constant, the system might be configured in such a way as to produce typical behaviours and large–scale system properties that are not observed in present ice sheets.

The third question addresses the possibility of inverting geological and geomorphological evidence of past ice sheet activity to reconstruct past climates. Assuming that the ice sheet model works adequately and that present and past ice sheets can be represented in the same way, it can be used to infer past climates by parameterising climate such that ice sheet model output follows known geological evidence. However, one of the most fundamental problems of geophysical inversions is that they are usually non–unique. The non–uniqueness problem can be reduced by integrating as many different strands of evidence as possible.

In addition to understanding ice sheet behaviour in general and in interpreting past ice sheet activity models can be used as a predictive tool. Projections of the future behaviour of a system as complicated as climate are difficult to establish and justify. James Hutton’s concept of *Uniformitarianism*, which can be paraphrased as “the present is the key to the past” and extended as “the present is key to the future”, allows us to infer what might happen to a system in the future, based on an extrapolation of its past behaviour. Conversely, a methodology designed to characterise future behaviour must at least be able to simulate the past. This project has been sponsored by United Kingdom Nirex Limited (Nirex), who are responsible for carrying out research relating to the safe disposal of intermediate– and low–level radioactive waste in the UK. As part of the Nirex Research Programme, Nirex is interested in understanding and collecting data on processes in the geosphere and biosphere that are relevant for radionuclide migration. In addition to developing scenarios of future climate change and ice sheet development, Nirex also need to assess the potential impact of future sea–level change around the British Isles on radionuclide transport. This project, therefore, also aims to provide projections of sea–level change around the British Isles.

As a final rationale, there is scientific curiosity. Ice sheets are among the most impressive natural phenomena. Understanding their behaviour and how they influence the Earth system is exciting work.

1.2 Modelling Ice Sheets and the Earth System

If we are to understand ice sheet behaviour properly we need to appreciate how it is linked to other parts of the Earth’s natural systems.

The concept of an *Earth System* views the geosphere, hydrosphere, cryosphere, atmosphere and biosphere as an interlinked dynamic system. Interactions between

the subsystems occur at a large range of temporal and spatial scales. Ice sheets play an important role within the Earth system on a scale of thousands of years and hundreds of kilometres. The various subsystems are linked via feedback mechanisms. The feedback mechanisms of the cryosphere and geosphere are illustrated in Figure 1.1. These subsystems, together with the feedback mechanisms linking them, are of primary importance on the temporal and spatial scales of interest and have to be represented by any comprehensive model. One of the fundamental problems of Earth system simulations is the multitude of physical processes occurring on all scales and how they relate to each other. Many of the processes have to be ignored or simplified for practical reasons, e.g. a process might be outside the spatial or temporal resolution, or there are not enough observations available to set initial or boundary conditions. Furthermore, our understanding of how some processes operate may be inadequate.

In the case of ice sheet models within the Earth System, whilst the fundamentals of ice thermodynamics are relatively well understood, the processes that link the ice sheet to other parts of the ice system are much harder to characterise. A further consideration is that different parts of the climate system operate on different characteristic timescales which leads to particular problems in representing the dynamical coupling between them. For instance, atmospheric processes operate over periods of minutes to days but the ice sheet only ‘sees’ the integral of these processes over several seasons. Of significance is the fact that evidence for ice sheet behaviour largely stems from the nature of these external links with other parts of the system. These linkages may be hard to describe in a physically complete way and yet often form the basis on which we wish to evaluate the model in comparison with available past evidence. For instance, if we want to use past sea-level data as a means of describing lithospheric adjustment under and beyond the ice, not only do we need to describe the individual physics of the Earth and ice sheet well, but we have to describe how they interact in an adequate way.

In review of the approach taken here, the following Sections describe the feedback mechanisms illustrated in Figure 1.1, how they influence the ice sheet system and how they are incorporated into models.

1.2.1 Feedback Mechanisms within the Ice—Climate System

Feedback Mechanisms Internal to Ice Sheets

There are two components of ice movement: i) ice flow and ii) basal décollement. Ice sheet flow depends on the gravitational driving stresses, and thus ice surface slope. Thick ice sheets tend to have steeper surface slopes and, therefore, also tend to flow faster due to the increased gravitational driving stress. Thick ice also tends to be warmer at its base than thin ice sheets because of the increased insulation it provides. Ice flow is temperature dependent: warm ice is less stiff and, therefore, flows faster; the converse is also true. Furthermore, fast-flowing ice

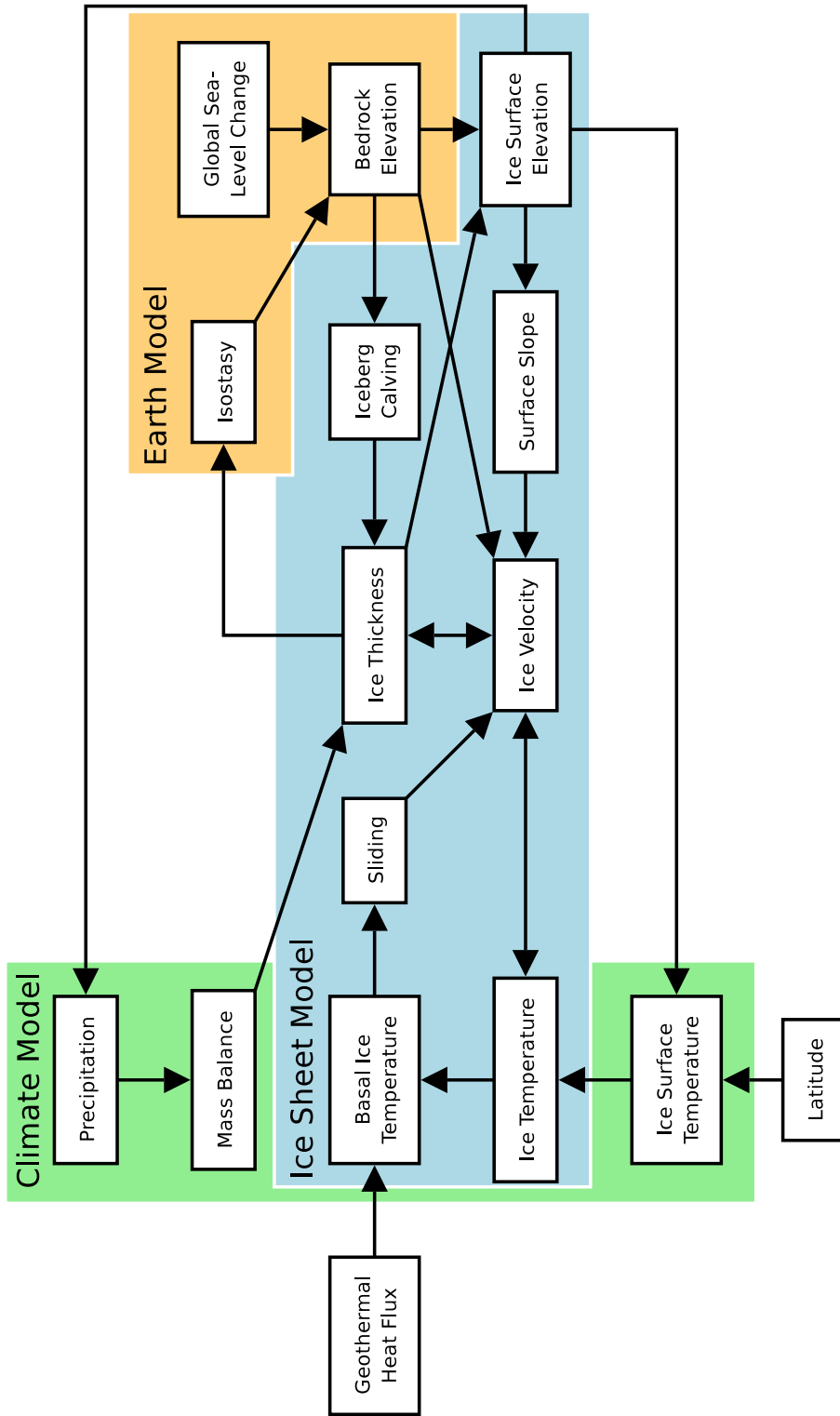


Figure 1.1: Flow diagram illustrating the ice sheet system composed of an isostatic rebound component (beige), a climate component (green) and processes within the ice sheet (blue) (adapted from Siegert, 2001)

generates heat due to internal friction, thus enhancing the temperature–velocity feedback. This feedback mechanism is known as *creep instability* (Clarke *et al.*, 1977).

The ice temperature depends on both the temperature at the ice surface and the ice base, where the ice is heated by the geothermal heat flux and friction. Heat is advected and conducted through the ice sheet. Conduction depends on the temperature gradient and, therefore, enters as a diffusive term in modelling. Basal melt water can form and basal décollement may occur when the temperature at the ice base reaches the pressure melting point of ice. Basal décollement is a complicated process, since it can occur within a layer of deforming till or directly at the ice–bedrock interface (Paterson, 1994). *Ice streams* are regions of relatively fast–flowing ice. They are self–regulating systems: increased ice flow tends to lower the surface slope, thus decreasing the ice flow due to reduced gravitational driving stress, and also decreasing the ice temperatures due to changes in insulation. The large flux within ice streams needs to be sustained which may deplete the ice supply of other streams (Payne, 1998).

A representation of these feedbacks is included within the ice sheet model by virtue of the simultaneous solution of the thermomechanical equations describing ice sheet behaviour.

Mass Balance

The *mass balance* of an ice sheet is the net amount of ice gained/lost due to ice accumulation and ice ablation. Variations of mass balance as an ice sheet’s surface evolves provide the main feedback between ice sheets and climate. Ice ablation is mainly determined by summer temperatures, whereas ice accumulation depends mainly on winter precipitation (e.g. Oerlemans and Reichert, 2000). At a certain altitude, the net ice accumulation will be equal to the net ice ablation, when averaged over a period of sufficient duration. This altitude is known as the *equilibrium line altitude* (ELA). Above the ELA, there is net ice accumulation and below the ELA net ablation. In general, temperature decreases with increasing elevation above sea–level according to the atmospheric lapse rate. Temperature also decreases with increasing latitude. As the ice sheet grows, an increasing surface area is located above the ELA, and thus more ice accumulates, enlarging the ice sheet even further. Precipitation patterns are also changed by the presence of an ice sheet. Moist air is transported to the edge of an ice sheet and is forced upwards by the topographical obstacle that it presents. Air precipitates moisture as it is forced upwards which adds to the positive mass balance. The air then becomes depleted of moisture. Therefore, the interior of an ice sheet, although very cold, has a very small positive mass balance (e.g. Hulton and Purves, 2000).

Surface relief is clearly important for initial ice sheet growth. In particular, inception of the European ice sheet is thought to have occurred in the Scandinavian Mountains, where small glaciers coalesced to form larger ice masses that eventually formed an ice sheet. Oerlemans (2002) investigated the topographic

control exerted on ice sheet inception and growth using a numerical ice sheet model run on a sinusoidally varying bedrock topography. He concluded that, in this simple case, there is an optimal topography where ice sheet inception is most efficient. This implies two competing effects: i) large amplitude orography initiates inception earlier and the height–mass balance feedback can be more efficient and ii) large slopes lead to large ice fluxes to regions where ice ablates.

Another hypothesis for ice sheet inception is known as *instantaneous glaciation* where large areas become permanently covered by snow so that large ice fields can form (Ehlers, 1996, and references therein). Under the influence of a positive mass balance, these ice fields are thought to be able to grow into a large ice sheet in a relatively short time. This mechanism is thought to have been responsible for the inception of the Laurentide ice sheet.

The overall approach in this research is to represent these feedbacks by an integrated description of mass balance relative to the ELA. This is adequate to simulate ice sheets on a large scale such as the Fennoscandian or British ice sheets.

The Lithosphere and Sea–Level Change

The lithosphere is not rigid but flexes under the mass of an ice sheet. Lowering the bedrock topography also tends to lower the ice surface elevation, which in turn reduces the mass balance (Oerlemans and van der Veen, 1984). The converse is also true. This adjustment is known as *glacio–isostatic adjustment* (GIA). Ice sheets store large amounts of water which is ultimately removed from the oceans. Sea–levels fall globally during episodes of major glaciation. This is known as *equivalent sea–level change*. Falling sea–levels have two effects:

1. The area above sea–level or covered by shallow seas is increased thus increasing the area available for the ice sheet to occupy.
2. Changing sea–levels affect the marine ice sheet margin (Boulton and Payne, 1992b). Grounded ice begins to float after it reaches a certain water depth due to Archimedes’ principle and forms an *ice shelf*. Ice is lost at the marine margin (from the ice shelf) due to ice berg calving. With falling sea–level the position of the marine ice–sheet margin and its characteristics change.

The parameterisation of the temperature field used implies a third possible effect of falling sea–levels: temperature decreases with elevation above sea–level (according to the atmospheric lapse rate) and, therefore, surface temperatures decrease with falling sea–levels alone. However, it is unclear if this effect occurs in reality.

In this project, global sea–level change is represented by a eustatic sea–level change curve whereas local lithospheric adjustment due to changing surface mass distribution is explicitly modelled.

Other External Feedback Mechanisms

Figure 1.1 only illustrates feedback mechanisms within the ice sheet — lithosphere system. Further feedback mechanisms exist, e.g. ice sheet — albedo and ice sheet — ocean circulation feedback mechanisms.

Atmospheric temperatures ultimately depend on the amount of incoming solar radiation and on how much of that radiation is reflected away from the Earth's surface. The albedo (the ratio between reflected and absorbed solar radiation) of ice and snow is very high, although it tends to decrease somewhat with the age of the snow layer. Therefore, air temperatures during episodes of major glaciations are further reduced by the presence of large areas covered by ice and snow reflecting solar radiation away from the Earth's surface. Dropping temperatures decrease ice ablation further, completing this feedback loop.

Ice sheets also interact with the oceans and ocean currents. The currents in the Atlantic transport heat from the equator northwards, delivering heat to Western Europe. This circulation system depends on the salinity of the sea water. Dense, salty water sinks in the North Atlantic and is transported southwards. Warm surface water flows in the opposite direction from the Mid Atlantic. Warm surface water is preferentially evaporated thus becoming more salty and dense. A sudden influx of fresh water (e.g. from a surging ice sheet) could halt this conveyor belt and hence air temperatures in Western Europe could drop sharply (e.g. Siebert, 2001).

These feedback mechanisms are not explicitly represented by the model used here. However, they are implicitly integrated into the mass balance parameterisation.

1.2.2 Approaches to Ice Sheet Modelling

Forward models seek unknown results to a prescribed set of assumed variables and parameters whereas inverse approaches assume the end result is fixed and seek a parameter/variable space that will permit that result to occur. Thus, there are two fundamentally different approaches to modelling ice sheets:

Deduction/Forward Model: The first class of model implements a physical description of ice sheet dynamics and is the approach most commonly applied to ice sheet modelling. The mechanical part of the model, describing how ice flows due to the gravitational driving stress, is coupled to the ice sheet's thermal evolution via a non-linear flow law. This type of model is forced by surface temperature and mass balance boundary conditions and may include parameterisation of basal décollement and the marine margin. Glacio-isostatic adjustment can also be included. Models of this class are employed, for example, by Huybrechts (1986), Boulton and Payne (1992b), Fastook and Holmlund (1994) and Mayer (1996). More recent examples of forward ice sheet models include work by Charbit *et al.* (2002), Takeda *et al.* (2002), Hulton *et al.* (2002) and Greve and Calov (2002). The adequacy of

forward models can be assessed by evaluating the model fit with observations of the real system.

Inversion: There are fewer examples of inverse approaches. One of the major problems is deciding which model behaviour the model is fixed upon. For instance, relative sea-level data can be inverted to produce a distribution of ice thicknesses assuming required parameters for the Earth model used are known. This approach is taken, for example, by [Lambeck *et al.* \(1998\)](#), [Tushingham and Peltier \(1992\)](#) and [Peltier \(1993\)](#). The argument is somewhat circular, since relative sea-level data are also used to constrain the Earth model parameters. However, this can be overcome by using far-field sites (i.e. sites that are little affected by glacio-isostatic adjustment) to constrain Earth parameters. As with all geophysical inversions, the solutions thus obtained are not unique. There is a trade-off between Earth parameters and ice thicknesses. Furthermore, the resulting ice sheet model might not be realistic, since it does not contain any ice physics and only consists of a distribution of ice thicknesses. [Johnston and Lambeck \(2000\)](#) improved this type of model by requiring the ice surface to be smooth. This highlights the problem of constraining model behaviour solely with a particular strand of evidence. The assumption is that the Earth physics are necessarily ‘right’ even if the ice formation required is not explained by a model based on plausible ice physics.

The fundamental difference between the two types is that the second class is used for inversion and does not include ice physics, whereas the first class is used for forward modelling and includes ice physics. Forward models can be used to forecast the future under specific scenarios of climatic change. The reliability of these forecasts is questionable, since geophysical systems are open and models describing them are not verifiable ([Oreskes *et al.*, 1994](#)). However, confidence in a model can be enhanced by comparing model predictions against independent observations ([van der Veen, 2002](#)) and by explicitly assessing the uncertainties involved in parameterisations and assumptions. Confidence in the model is increased by its ability to reproduce many independent observations. Simulations of future behaviour of the climate system cannot be compared against observations for obvious reasons. Confidence of the reliability of future simulations is, therefore, based on the assumption that the Earth system will behave in a similar manner as it did during the past, e.g. the next glacial/interglacial cycle will last about 100ka like the previous eight cycles. This assumption might not be true, since, for example, causes for the beginning of an ice age or its end are only poorly understood.

1.2.3 The Edinburgh Ice Sheet Model

In order to model ice sheets within the global system this research made use of an existing ice sheet model that was then adapted and coupled to models representing

other parts of the Earth system. The ice sheet model used is a three-dimensional, coupled thermomechanical ice sheet model. It was developed by [Boulton and Payne \(1992a\)](#) and is based on code originally written by [Huybrechts \(1986\)](#). The model was tested favourably against EISMINT¹ results. It was later rewritten to utilise a supercomputer with many processors ([Mineter and Hulton, 2001](#)) and has also been used to simulate the mountain ice cap of Patagonia during the last glacial cycle ([Hulton *et al.*, 1994](#); [Hulton and Sugden, 1995, 1997](#)).

The ice sheet model can resolve internal feedback mechanisms linking temperature to ice flow and thus also allows for the development, persistence and cessation of ice streams due to creep instability. A simple sliding mechanism dependent on basal temperatures and the gravitational driving stress is included. The parameterisations of the mass balance and surface temperature fields are altitude dependent, and thus feedbacks with the ice surface elevation can be included. The ice sheet model is coupled to Earth models of varying complexity that are used to calculate isostatic adjustment. Changes of global ice volume and thus global sea-level are assumed to be known and take the form of a forcing parameter. The marine limit of the ice sheet is also dependent on sea-level change. However, the ice sheet model does not include a representation of ice shelves: at the marine margin, ice is discharged as icebergs and, thus, lost to the system once the ice reaches a specified water depth. The model also does not include any of the feedback mechanisms described as “external”, above. The lack of these feedback mechanisms and processes will affect the behaviour of the model. However, these feedback mechanisms are outside the scope of this project and their omission has to be acknowledged and recognised as a potential matter for future research.

The software was originally written in Fortran77 and used the Cray `shmem` library for parallelisation. During this project, I updated the Fortran77 code to Fortran95 and reimplemented the parallelisation using the Message Passing Interface (MPI). In order to study the effects of isostatic adjustment, the model was coupled to an elastic lithosphere/relaxed asthenosphere model and the spherical, self-gravitating Earth model developed by [Johnston \(1993a\)](#) (see Chapter [2.3.2](#)).

1.3 Constraining Model Behaviour with Multi-Proxy Data

Ice sheet activity provides a wealth of evidence for past behaviour and this can be used to constrain models. Amongst a number of things this encompasses the geomorphological processes of erosion and deposition on and within the near-surface, the wholesale warping of the lithosphere and its subsequent recovery when ice disappears, changes in sea-level associated with lithospheric adjustment

¹European Ice Sheet Modelling INiTiative ([Huybrechts *et al.*, 1996](#))

and ice volume change and changes in the isotopic concentrations of oceanic and ice reservoirs. In turn, evidence for such ‘outputs’ to the ice—climate system can be linked to evidence for primary climatic drives such as insolation variations associated with the Earth’s orbital oscillations around the Sun. Earth System models can be considered as a mechanism for explaining ‘outputs’ produced as a function of the Earth processes modelled in terms of the input signal producing them. In general, many ice sheet models that aim to simulate past behaviour have seldom aimed to consider the full range of proxy data against which simulations might be compared.

Palaeo ice models are typically compared either with an inferred set of past ice margin positions (e.g. Boulton *et al.*, 1995; Hubbard, 1999) or rebound or sea level data (e.g. Lambeck, 1993c; Peltier, 1993). Seldom are ice simulations produced using a model that is internally physically consistent whose inputs are based around known climatic patterns and whose outputs are evaluated against a range of real evidence. The potential exists to produce models that are optimised around unknown or ‘free’ parameters such that they approximate well a number of aspects of system behaviour. For instance, in the case of a ‘real’ Fennoscandian simulation, the ideal would be to produce a physically reasonable model that, when driven with a consistent external climate signal could reproduce both ice extent and a lithological rebound history consistent with known patterns. Ideally too, such a model might predict major areas of erosion and deposition and the isotopic properties of groundwaters under the former ice mass. Evaluating the model against these multiple strands of evidence would help further constrain certain aspects of ice sheet behaviour, in particular its thermal characteristics.

Thus it is informative to review some of the major evidence strands that exist for the Fennoscandian ice sheet and how these can be used to constrain model behaviour. It is also worth considering how astronomical theory can be used as a basis to constrain climatic signals underpinning model inputs.

1.3.1 Evidence of Past Ice Sheets

We live in an ice age: an episode of Earth’s history when large parts of the Earth are covered by ice sheets. The polar regions have been ice free and climate in mid-latitudes has been milder during most of Earth’s history. The Quaternary ice age has intensified during the late Cenozoic, reaching its most intense phase after about 800ka Before Present (BP), since when it has been characterised by a succession of long *cold stages* or *glacials*, during which ice sheets expanded, and intervening *warm stages* or *interglacials*, when the mid-latitudes have been ice free. Further subdivisions of glacial periods are referred to as *stadials* (cold) and *interstadials* (temperate) (Ehlers, 1996). From about 2.5Ma BP (the onset of the Quaternary), until about 800ka BP, a glacial/interglacial cycle lasted for about 40ka. Since then, glacial/interglacial cycles have had a period of about 100ka (Duff, 1993).

Ice sheets are among the largest features on the Earth’s surface. It is, therefore,

not surprising that they leave evidence of their past activities in both the terrestrial and marine geological records. These features range from centimetre scale scratch marks to sedimentary fans that extend over an area of several million square kilometres. This wealth of geological and geomorphological evidence can be used to reconstruct the history of past ice sheet fluctuations.

The terrestrial record becomes increasingly sparse with increasing age because of the erosive nature of ice sheets and the fact that successive events overprint the evidence from previous ice sheets. However, marine and lacustrine sediment sequences can provide a more continuous temporal record of past climatic changes.

This section provides a brief overview of Quaternary environments reconstructed from geological and geomorphological evidence. Data records used for this project are described in detail later. The following discussion is based mainly on [Siegert \(2001\)](#), [Benn and Evans \(1998\)](#) and [Ehlers \(1996\)](#).

Terrestrial Record

Many of the surface features produced by ice sheets are related to the direction of ice flow. *Striae*, *drumlins* and *eskers*, for example, form parallel to flow, whereas *end moraines* form at the ice margin and are perpendicular to ice flow directions. The maximum ice extent and successive stages of retreat can be reconstructed by mapping end moraines. However, as end moraines are relatively rare, longitudinal features can be used to infer the trend lines of the retreating ice margin where end moraines are absent.

Ice sheets also modify landforms and deposit sediments at the ice base. These features give valuable information about ice dynamics and general flow direction. For example, [Boulton *et al.* \(2001b\)](#) used satellite images to map the pattern of eskers, moraines and drumlins together with the European varve radiocarbon chronologies to reconstruct the time-dependent, dynamic behaviour of the Fennoscandian ice sheet.

The geomorphological evidence is a three-dimensional record (the Earth's surface and a partial time-transgressive record of change on its surface) and can be used as a guide to a four-dimensional process (ice sheets span three spatial dimensions and change through time). Because of the erosive nature of ice sheets, the terrestrial record tends to relate only to the most recent ice sheet activity at a location.

This kind of evidence can potentially be compared with the changing pattern of simulated ice flow directions.

Marine and Lacustrine Records

Sediments in a marine or lacustrine environment are usually deposited sequentially. A time of sedimentation can be related to depth within the sequence of sediments, assuming the sedimentation rate is known and the sediments have not been disturbed or eroded. These records can, therefore, provide a continuous

record of events and processes during the Quaternary. Marine sediments include records of increased debris rafting attributed to major ice sheet surges, also known as Heinrich events (e.g. Broecker, 1994). Temperatures and global ice volume affect the chemistry and isotopic composition of sea water which in turn is reflected in the sediment record.

1.3.2 Causes of Ice Ages

The Earth's orbit is primarily determined by the gravitational field of the Sun. However, the gravitational influence of the other planets continuously modify the Earth's orbit. During the second half of the 19th century, Croll (1867) assumed that these periodical changes influence the terrestrial climate. This theory was later elaborated by Milankovitch (1941). The distribution of incoming solar radiation is influenced by the three orbital parameters (e.g. Ehlers, 1996; Siebert, 2001), eccentricity, obliquity and precession, shown in Figure 1.2.

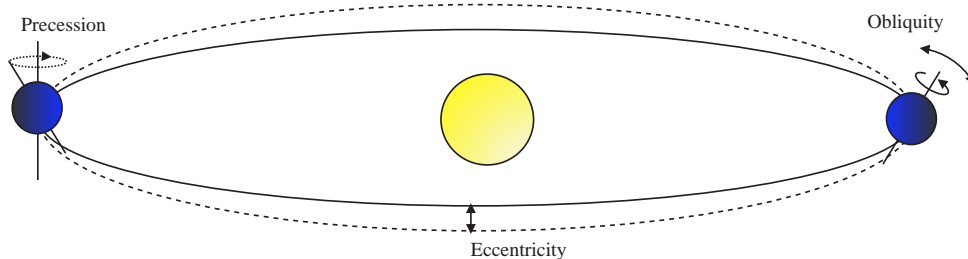


Figure 1.2: The Earth's orbital parameters: i) eccentricity — the Earth's orbit deviates from a circle by between 0.5 and 6.0% with periods of 100ka and 400ka; ii) obliquity — the angle between the Earth's rotation axis and the plane of the ecliptic varies by between 21.39° and 24.36° with a period of 41ka; and iii) precession — the Earth's axis rotates about the poles in a 19-23ka cycle. (adapted from Ehlers, 1996)

The variation of orbital parameters hardly influences the Earth's global radiation budget nor the hemispheric heat budgets. It does, however, affect the seasonal distribution of radiation. Decreasing the summer temperature in the high-latitudes lessens the potential to melt ice on the continental landmasses. Except for Antarctica, there are no major high-latitude landmasses in the Southern Hemisphere, whereas the major landmasses of the Northern Hemisphere, Eurasia and North America, occupy the 45° - 65° latitude band. Changing the summer radiation budget will, therefore, have the most significant effects in the Northern Hemisphere.

The time spectrum of glacials and interglacials inferred from the geological record correlates very well with Milankovitch cycles (Imbrie *et al.*, 1984), suggesting a relationship between the two. However, the direct effects of changes in insolation are not sufficient to explain the magnitude of the observed climatic

changes. Several feedback and amplification mechanisms are also involved. Thus, variations in the distribution of solar radiation affects atmospheric CO₂ content, oceanic and atmospheric circulation patterns and the formation of ocean deep water, all of which can influence the growth and decay of ice sheets (e.g. Bradley, 1999; Duff, 1993).

Since ice ages have occurred repeatedly during geological time, the question has been raised as to whether they are due to terrestrial or extra-terrestrial causes. As our solar system orbits around the galactic centre, it periodically passes through one of the galactic spiral arms which might affect solar radiation and thus trigger the onset of an ice age (McCrea, 1975). Possible terrestrial causes are (e.g. Ehlers, 1996) either related to i) tectonic and topographic changes, such as the distribution of continents, opening and closing of straits and changes in the Earth's relief and ii) direct influences on global climate, such as a long episode of large volcanic eruptions. It is not clear whether there is a single cause for the onset of ice ages. However, some of the above mentioned possible causes may act together to trigger an ice age.

This project has been concerned with a single glacial cycle. It could, therefore, be argued that the actual causes that trigger an ice age, comprising multiple glacial — interglacial cycles, are not relevant. However, since this project also attempts to forecast the development of an ice sheet and sea-level changes around the UK during the next glacial cycle, it is important to consider the mechanisms mentioned above. The distribution of continents and opening and closing of straits occur over longer timescales than one or two glacial cycles and can, therefore, be neglected in this study. The influence of volcanic episodes on climatic conditions and hence on ice sheet development would be a major study in its own right. It has not been addressed herein. However, the ice sheet modelling approach described here could be an important tool in investigating this issue. Also, ice sheets modify the surface relief by erosion and potentially affect large-scale atmospheric circulation patterns by their presence. These effects are not resolved by the model, although they potentially affect ice sheet dynamics on the timescale under consideration (see also Section 1.2.1).

1.4 Relative Sea-Level Change

Relative sea-level (RSL) observations provide an excellent data set that can be used to constrain the size of past ice sheets. In particular, RSL data allows us to constrain past ice thickness for which otherwise there is little direct evidence.

Past sea-levels can be inferred from a number of indicators. Some of these indicators are confined to the past tidal zone or occur at a specific water depth. These indicators include, for example, corals (e.g. Bard *et al.*, 1990) and mollusks (e.g. Bice *et al.*, 1996). They provide a *fixed* or *indicative* estimate for past sea-level change. Other indicators only provide *relational* or *directive* information,

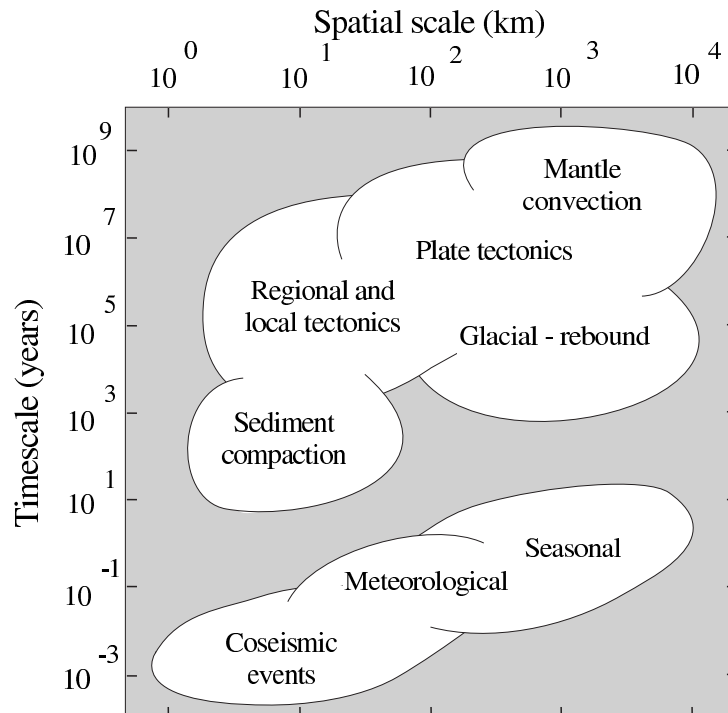


Figure 1.3: Temporal and spatial scales of processes causing sea-level change (from Fleming, 2000).

i.e. they simply indicate whether past sea-levels were above or below a certain point, e.g. the marine limit (Andrews, 1970).

Observations of past sea-level change have to be carefully analysed, since both the date and the inferred relative sea-level have associated errors. The error in the date arises from the dating technique used, e.g. a radio-isotopic method (Bradley, 1999). The error associated with the relative sea-level observation is due to the fact that the relation between the indicator and sea-level is often only poorly known. The data used here has been collected in other studies and is used as provided without further analysis.

1.4.1 Causes of Sea-Level Change

Processes leading to sea-level change act over a large range of temporal and spatial scales (see Fig. 1.3) and exhibit a large range of amplitudes. The net effect of these different processes are combined in the single sea-level record. Separating and measuring individual components is, therefore, problematic.

Causes for sea-level change can be classified by either the time scales over which they occur (Fairbridge, 1983) or whether they have local or global effects (Pirazzoli, 1991). The following causes can be identified:

1. *Changes of water mass:* The oceans exchange water mass with the other

parts of the hydrological system, i.e. the atmosphere, grounded ice (ice sheets and glaciers), lakes and rivers, and groundwater. This mass exchange occurs over a large range of time scales and involves widely varying amounts of water. During the Quaternary, exchange of water mass has been dominated by fluctuations of global ice volume (e.g. [Lambeck and Chappell, 2001](#)).

For example, if the present ice sheets of Antarctica and Greenland were to melt, global sea-levels would potentially rise by up to 70m ([van der Veen, 1987](#)). At the last glacial maximum, global sea-levels were about 120m lower than they are today ([Fairbanks, 1989](#)).

2. *Variation of ocean-basin geometry:* Keeping the water mass contained within the oceans fixed, but varying the shape of the ocean-basin, changes sea-level. Ocean basin geometry is affected by plate tectonics, sedimentation and isostatic adjustment due to changing surface loads. The dominant process over large time scales (10^6 to 10^7 years) is global tectonics ([Kennett, 1982](#)).
3. *Changes of water density:* Water volume and thus sea-level depend on the density of water. Warm water expands, thus raising sea-levels. 50% of the present rate of sea-level rise is thought to be due to the thermal expansion of the oceans (e.g. [Gehrels et al., 2002](#)). The density of water also depends on its salinity, although the thermal signal is more important ([Chen et al., 1998](#)). Global mean sea-level change shows a seasonal signal with an amplitude of a few millimetres. This signal is mainly due to seasonal variations of water density and mass exchange with the atmosphere and the continents ([Chen et al., 2001](#)).
4. *Vertical movement of the Earth's crust:* In general, vertical movement of the crust is a local process. It includes sediment compaction, tectonic uplift/subsidence and isostatic adjustment.

Recent sea-level change, as recorded by tide gauges, potentially contains a large anthropogenic signal arising from local land subsidence due to ground water extraction and land reclaiming ([Harvey et al., 2001](#)).

The Earth's crust is not brittle but flexes under loading. Emerging volcanoes, marine sediment deposition and erosion, changes in water mass (*hydro-isostasy*) and ice sheet mass (*glacio-isostasy*) impose a load on the lithosphere. As the lithosphere flexes downward, material within the underlying asthenosphere flows outwards pushing the surroundings upwards. When the load is removed, mantle material flows back to the formerly lowered area and pushes the lithosphere up again, whereas the surrounding area subsides. Processes governing vertical movement of the crust also influence ocean-basin geometry and vice-versa.

5. *Changes of water distribution:* The global distribution of water is influenced by changes of the Earth’s rotation tensor, e.g. due to polar wander, (Mound and Mitrovica, 1998), tides (e.g. Hinton, 2000), atmospheric forcing (e.g. Fukumori *et al.*, 1998; Plag and Tsimplis, 1999), ocean currents and variations of the geoid (Mörner, 1987).

The sea surface forms an equipotential surface. The development of large, localised ice masses increases the gravitational potential and raises sea-levels in the vicinity of an ice sheet. Variations of the gravitational potential due to ice sheet growth and decay during the Quaternary was the most significant contributor to changes of water distribution over that period (e.g. Tooley, 1993).

The shape of the geoid is influenced by density variations in the crust and processes of mantle convection (Kennett, 1982). These changes occur on long timescales and are of limited relevance to this project.

6. *Short-term variations arising from extreme events:* Extreme events such as tsunamis, catastrophic rock-slides and storms affect sea-levels over minutes to hours. They are, however, important since their deposits can be hard to distinguish from deposits resulting from more long-term processes (e.g. Long *et al.*, 1998).

Only some of the processes described above are resolved by the models used for this project: glacio- and hydro-isostatic processes are simulated using a regional, flat Earth approximation (elastic lithosphere-relaxed asthenosphere model, described in Chapter 2.2.1). The global sea-level curve is derived from the SPECMAP data as described in Section 1.4.2. Figure 1.4 illustrates the components influencing relative sea-level change. The full spherical Earth model used in this project additionally includes sea-level change due to changes of the geoid and the rotation tensor. Provided all major ice sheets are included in the simulation, the spherical Earth model also produces an *equivalent sea-level* curve.

1.4.2 SPECMAP and Equivalent Sea-Level Change

Sea-level change due to changing surface loads is calculated by the isostatic rebound model. However, the global equivalent sea-level² component due to changes of global ice volume cannot be calculated by the model, since only the past European and British ice sheets are simulated. A record of equivalent sea-level change is, therefore, needed as an external forcing function.

The global sea-level data set used here is based on a linear regression using the SPECMAP oxygen isotope record (Imbrie *et al.*, 1984) as independent variable to predict observed sea-level data from the Huon Peninsula (Chappell and Shackleton, 1986) and Barbados (Bard *et al.*, 1990). The underlying assumptions

²see Chapter 2.2.3 for definitions of equivalent and eustatic sea-level change

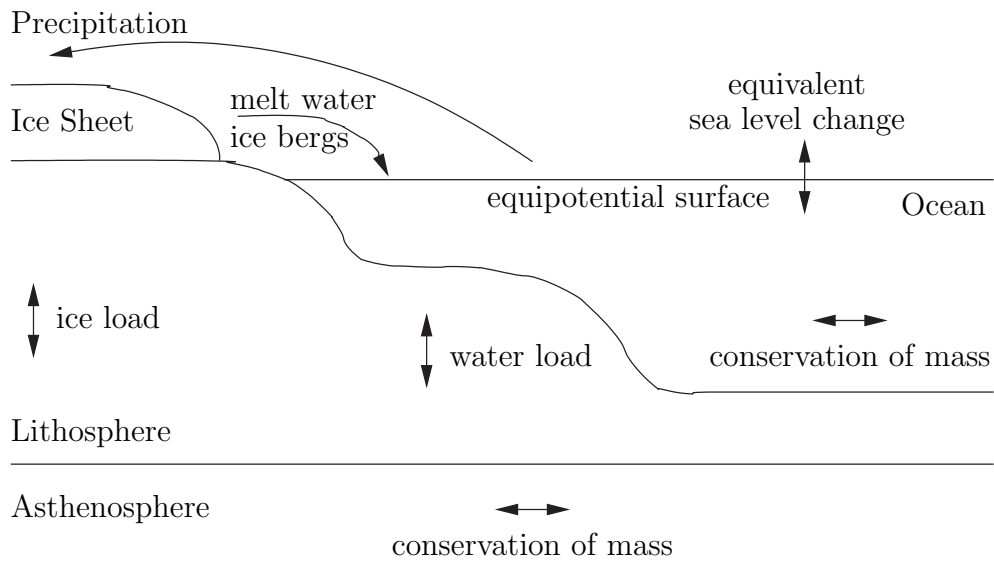


Figure 1.4: Schematic diagram of the coupled ice sheet—Earth system. The plane Earth approximation can only resolve glacio- and hydro-isostatic processes (vertical arrows). In addition to the isostatic effects, the spherical Earth model ensures conservation of mass (horizontal arrows and mass exchange between oceans and ice sheets) and enforces that the the sea surface is an equipotential surface.

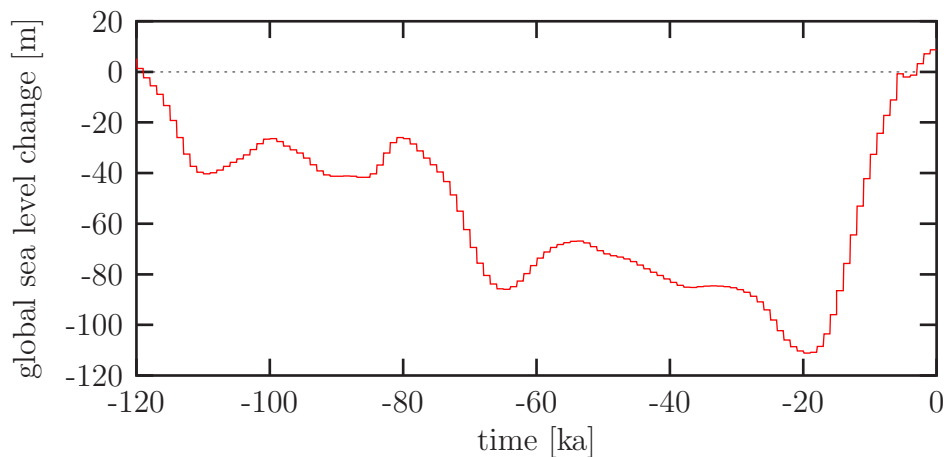


Figure 1.5: Global sea-level change as derived from the SPECMAP oxygen isotope record. Data set provided by [Goodess et al. \(2000b\)](#).

are that i) the oxygen isotope record contains a signal relating to the global ice volume and that ii) relative sea-level change recorded by the coral reef data is due to changes in water volume only. Both the Huon Peninsula and Barbados are far away from past mid-latitude ice sheets, so that glacio-isostatic effects are negligible. However, the relative sea-level data from Barbados had to be adjusted to account for tectonic uplift. The calculations were performed by Goodess *et al.* (2000b), who also provided the dataset used for the simulations (see Fig. 1.5).

1.4.3 Relative Sea-Level Data Sets

For this project, three different relative sea-level data sets were used. The first data set covers the entire globe and was compiled by Tushingham and Peltier (1993). The second data set covers Northern Europe (Broadgate, 1997) and the third one covers the British Isles (pers. com. I. Shennan and Shennan *et al.*, 2000). Figure 1.6 shows the coverage of the three data sets.

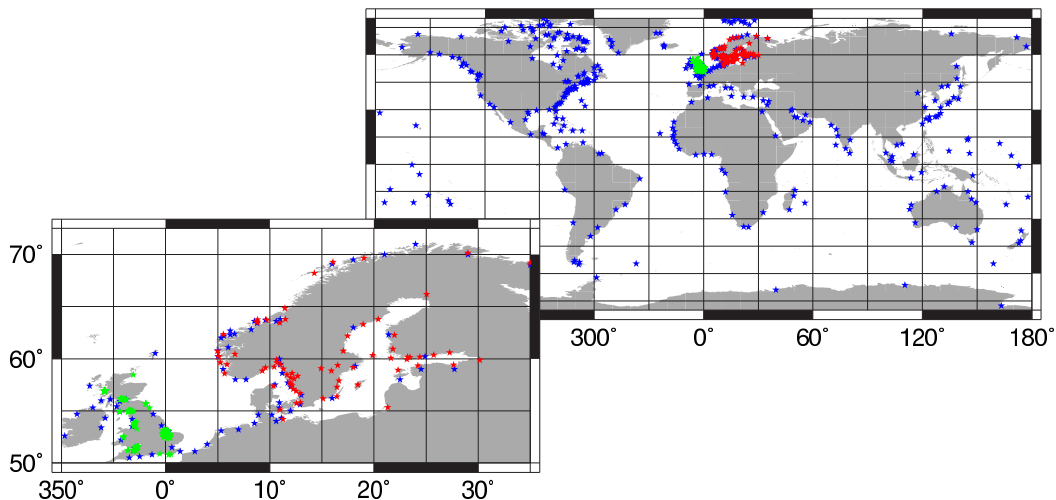


Figure 1.6: Map of the World showing the location of the relative sea-level sites. Sites marked red are from Broadgate (1997), the blue ones are from Tushingham and Peltier (1993) and green ones are from I. Shennan (pers. com.) and Shennan *et al.* (2000).

Relative sea-level sites can be divided into four groups depending on their geographic location relative to past ice sheets (Lambeck, 1993a):

1. *near-field sites*: sites within the past ice sheet. The major component contributing to relative sea-level change is the glacio-isostatic term. A characteristic sea-level curve shows a quasi-exponential fall towards the present (see Fig. 1.7A).
2. *ice marginal sites*: sites at the ice margin but within the ice sheet. The glacio-isostatic term and the equivalent sea-level term are of similar size

but opposite sign. Complicated temporal patterns of sea-level change can, therefore, arise (see Fig. 1.7B).

3. *intermediate-field sites*: the amplitude of the glacio-isostatic term rapidly diminishes away from the ice sheet. Relative sea-level at sites near past ice sheets (e.g. in the Netherlands) essentially follows the equivalent sea-level term with the important distinction that relative sea-levels continue to rise after deglaciation is completed (see Fig. 1.7C).
4. *far-field sites*: sites far away from past ice sheets. This type of RSL curve is dominated by changes in water volume. (see Fig. 1.7D). The mid-Holocene sea-level highstand at about 6.5ka BP is a consequence of ocean floor loading by the meltwater influx during deglaciation. This hydro-isostatic effect strongly depends on the coastline geometry (Johnston, 1995).

Figure 1.8 shows example relative sea-level observations covering the four geographic groups.

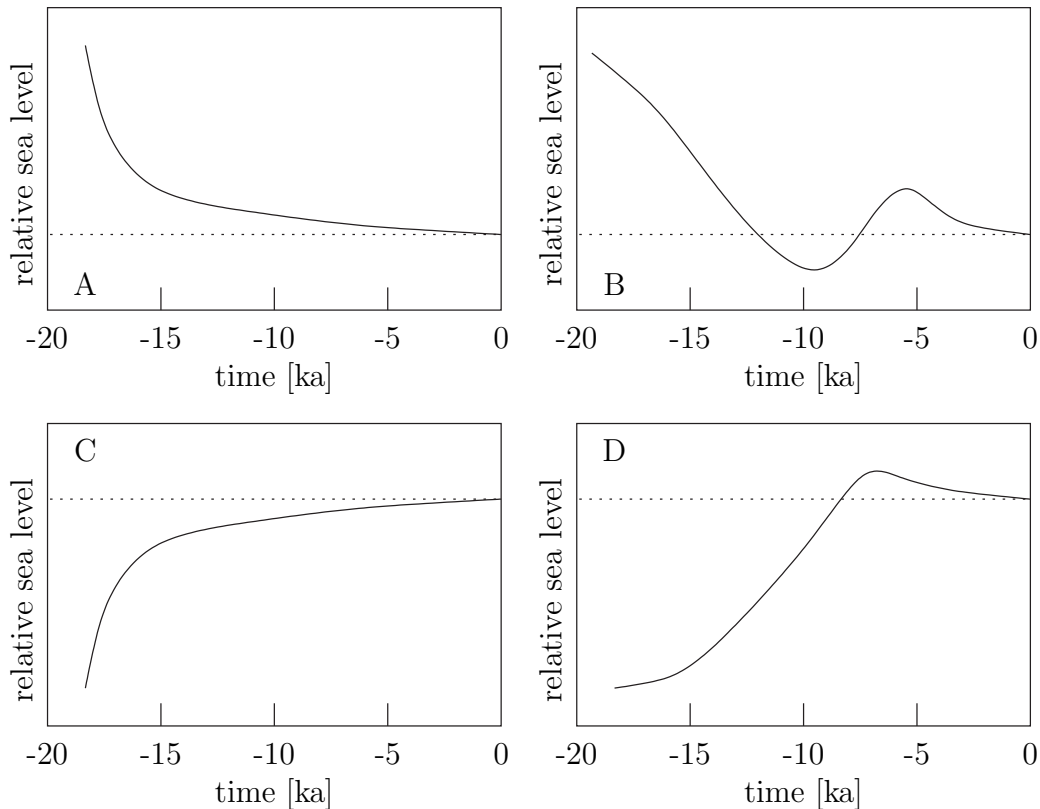


Figure 1.7: Relative sea-level change at (A) a site near the ice centre; (B) at a site near the ice margin but within the ice sheet; (C) a site in the intermediate field; and (D) a site in the far field (after Lambeck, 1993a).

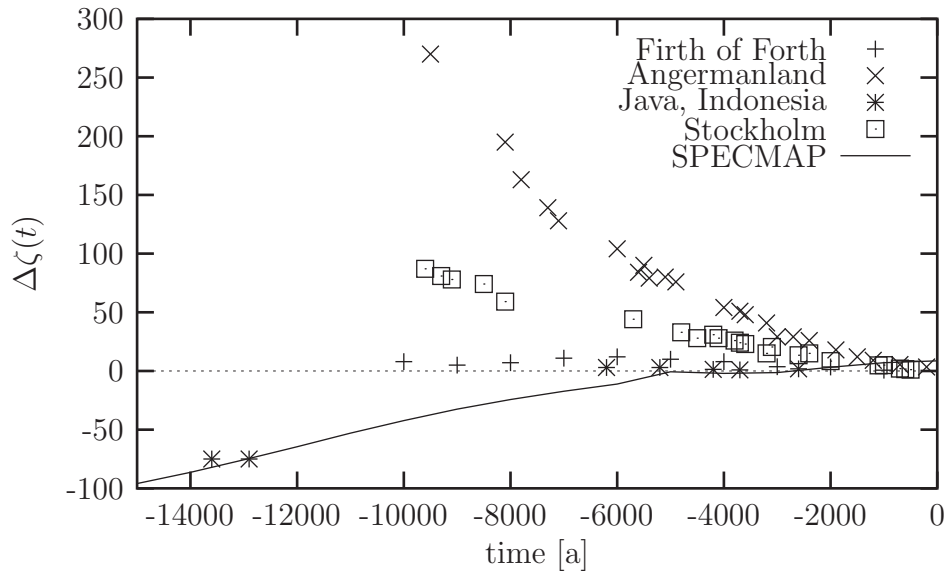


Figure 1.8: Example relative sea-level data and the equivalent sea-level curve based on SPECMAP.

1.5 Objectives and Thesis Plan

The aims of this project were to simulate the past British ice sheet using a high resolution coupled ice sheet — lithosphere model and to run this model into the future to forecast sea-level change around the British Isles for specific climate scenarios. However, the British ice sheet poses particular problems: the geometry of the past British ice sheet is complicated because the topography gave rise to several independent glaciation centres and the geological evidence of its pattern of fluctuations is poor. It was, therefore, best to test the capacity of the model to simulate past fluctuations by using it on an area that is topographically and climatologically simpler, and where the geological evidence is better. I have, therefore, chosen to initially simulate the Fennoscandian ice sheet because of the simpler topographic framework and the quality of geological evidence of past fluctuations. I then apply modified forcing functions of the Fennoscandian model to the British ice sheet, using the reasonable assumption that they were similar in the past and will, again, be similar in the future.

The approach to modelling the Fennoscandian and British ice sheet can thus be outlined as follows:

1. Develop a coupled ice sheet/lithosphere model. The coupled model is needed to simulate both ice dynamics and the Earth's response. Also, investigate the level of complexity required to simulate the ice sheet/lithosphere system. (Using the full spherical Earth model is computationally expensive, so a simple approximation, which is less computationally expensive, was also

studied to determine whether it would meet the requirements of this project.)

2. Test the coupled model to see whether the past Fennoscandian ice sheet can be simulated. Construct an ELA forcing function that produces an ice sheet that fits geological reconstructions.
3. Investigate how the model depends on the assumed known parameters: topography, surface temperature and ice rheology.
4. Simulate the past British ice sheet using the same ELA forcing function. Determine how the forcing function needs to be adjusted in order to simulate the past British ice sheet.
5. Expand the modelled area so that it encompasses both the Fennoscandian and the British ice sheet to investigate the interactive effects.
6. Construct a future ELA forcing function and run the British ice sheet model into the future.

The remaining chapters of this thesis are organised as follows: The mathematical background for modelling the coupled ice sheet — lithosphere system and the software implementation are described in Chapter 2. Temperature and mass balance forcing of the model and its application to the past Fennoscandian ice sheet are described in Chapter 3. Application of the model with a modified ELA forcing to the past British ice sheet is then described in Chapter 4. Finally, a future ELA forcing function is constructed using a statistical method to simulate sea-level change around the British Isles during the next glacial cycle. Results of this experiment are described in Chapter 5. Conclusions from the study are provided in Chapter 6.

Chapter 2

Theory

The mathematical approach adopted to modelling the coupled ice sheet–lithosphere system and its numerical implementation is introduced in this chapter. Ice sheet physics is described by a set of coupled partial differential equations for the mechanical and thermal evolution of an ice sheet. The complete set of equations cannot be solved analytically. Therefore, it is necessary to solve these equations numerically. The mathematical framework can be simplified by assuming that topography and ice surface slopes are sufficiently small so that normal stress components can be neglected (Hutter, 1983). This approximation is used in most ice sheet models (e.g. Huybrechts, 1986; Payne, 1999). The validity of the approximation has been tested by Cliffe and Morland (2000). The ice sheet interacts with the environment via boundary conditions prescribed at the ice base, ice surface and ice margins.

As ice sheets grow and decay, the ice mass distributed over the Earth’s surface changes. This affects the bedrock topography, since the Earth behaves like a fluid on large time scales. Simple approximations to isostatic adjustment on a plane Earth are discussed in the first part of Section 2.2. The second part of Section 2.2 outlines the full spherical Earth model developed by Paul Johnston. The full mathematical argument can be found in Johnston (1993a). The full spherical Earth model is preferred to the plane Earth approximations, but it is computationally more expensive. Plane Earth approximations are investigated to see if they provide an adequate alternative to the spherical Earth model.

Software implementation of the core components, the ice sheet model and the spherical Earth model, are described in Huybrechts (1986) and Johnston (1993a), respectively. Additions made to the model during this study, the Earth approximations used and the reimplementations of the parallelised ice sheet model using MPI, are described in Section 2.3.

Throughout the text, standard mathematical notation is used. Vectors are printed in bold. For some of the tensor equations, the Einstein summation convention¹ is also used, where a repeated index implies summation.

¹Short-hand notion for vector and tensor equations, where the repetition of an index implies

2.1 The Ice Sheet Model

2.1.1 Thermomechanical Equations Governing Ice Flow

A right-handed Cartesian coordinate system with the x, y -plane parallel to the geoid and positive z pointing upwards is defined. The sea surface is at $z = 0$ and the bedrock-ice interface is at $z = h$ (see Fig. 2.1).

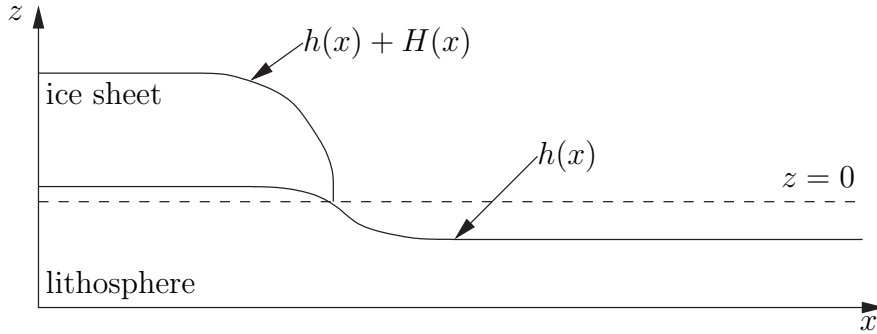


Figure 2.1: Illustration of the coordinate system used for developing the equations governing ice dynamics. The sea surface is at $z = 0$, the bedrock-ice interface is at $z = h$ and the ice surface is at $z = h + H$.

The evolution of the ice thickness H stems from the continuity equation:

$$\frac{\partial H}{\partial t} = -\nabla_{\mathbf{H}} \cdot (\bar{\mathbf{v}}H) + M - S, \quad (2.1)$$

where $\nabla_{\mathbf{H}}$ is the two-dimensional horizontal gradient, $\bar{\mathbf{v}}$ the vertically averaged velocity, M the mass balance (accumulation minus surface melt rate) and S the melt rate at the ice base.

For large-scale ice sheet models, the *shallow ice* approximation is generally used. This approximation states that bedrock and surface slopes are assumed to be sufficiently small so that the normal stress components can be neglected (Hutter, 1983). The horizontal shear stresses (τ_{xz} and τ_{yz}) can thus be approximated by

$$\begin{aligned} \tau_{xz}(z) &= -\rho_{\text{ice}}g(H + h - z)\frac{\partial(H + h)}{\partial x}, \\ \tau_{yz}(z) &= -\rho_{\text{ice}}g(H + h - z)\frac{\partial(H + h)}{\partial y}, \end{aligned} \quad (2.2)$$

where ρ_{ice} is the density of ice and g the gravitational acceleration. The validity of results obtained using this approximation has to be questioned. Mayer (1996)

summation. For example, the dot product of two vectors \mathbf{a} and \mathbf{b} expressed in this notation is $\mathbf{a} \cdot \mathbf{b} = a_i b_i = \sum_{i=1}^3 a_i b_i$.

numerically evaluated the full stress tensor in order to be able to assess the relative importance of the stress components. Cliffe and Morland (2000, 2001, 2002) investigated the effect of relatively large bedrock slopes on the two-dimensional ice surface slope and velocity distribution by comparing results from models using the full and reduced solution for a prescribed temperature field. Ice surfaces obtained from the shallow ice approximation are similar to the ice surfaces of the full solution. However, they find that the velocity profiles differ significantly. Ice flow and temperatures are strongly coupled via the flow law, Equation 2.3, and advection and strain heating, Equation 2.7. It can, therefore, be expected that ice surfaces will also differ when ice flow is fully coupled to the thermal evolution. However, the model used for simulating the European and British ice sheets does not resolve rapidly varying topography and the use of the shallow ice approximation is both plausible and practical in this context.

Another approach to moving away from the shallow ice approximation is to include average longitudinal deviatoric stresses. Hubbard (1999) used an ice sheet model of this type to simulate the Younger Dryas in Britain at a very high resolution.

Strain rates $\dot{\epsilon}_{ij}$ of polycrystalline ice are related to the stress tensor by the non-linear flow law:

$$\dot{\epsilon}_{ij} = A(T^*)\tau_*^{(n-1)}\tau_{ij} \quad i, j = x, y, z, \quad (2.3)$$

where τ_* is the effective shear stress defined by the second invariant of the stress tensor, n the flow law exponent and A the temperature-dependent flow law coefficient (Paterson, 1994). T^* is the absolute temperature corrected for the dependence of the melting point on pressure ($T^* = T + 8.7 \cdot 10^{-4}(H + h - z)$, T in Kelvin, Huybrechts, 1986). The parameters A and n have to be found by experiment. n is usually taken to be 3 (Paterson, 1994). A depends on factors such as temperature, crystal size and orientation, and ice impurities. Experiments suggest that A follows the Arrhenius relationship:

$$A(T^*) = fae^{-Q/RT^*}, \quad (2.4)$$

where a is a temperature-independent material constant, Q is the activation energy for creep and R is the universal gas constant. f is a tuning parameter used to ‘speed-up’ ice flow and accounts for ice impurities and the development of anisotropic ice fabrics (Payne, 1999; Tarasov and Peltier, 1999, 2000; Peltier *et al.*, 2000). It is used to lower the ice sheet profile to produce a better fit with relative sea-level data. The parameter a depends on hydrostatic pressure. However, this dependence is negligible if the temperature is taken relative to the pressure melting point (Paterson, 1994). There are two sets of flow parameters depending on whether the ice is cold or warm (e.g. Tarasov and Peltier, 1999; Payne, 1999). These are

$$a = 1.14 \cdot 10^{-5} \text{Pa}^{-3} \text{a}^{-1} \quad \text{and} \quad Q = 60 \text{kJmol}^{-1} \quad \text{for } T^* < 263.15 \text{K}, \quad (2.5a)$$

$$a = 5.47 \cdot 10^{10} \text{Pa}^{-3} \text{a}^{-1} \quad \text{and} \quad Q = 139 \text{kJmol}^{-1} \quad \text{for } T^* \geq 263.15 \text{K}. \quad (2.5b)$$

The horizontal velocity vector can be found by vertically integrating the flow law Eq. (2.3):

$$\mathbf{v}(z) - \mathbf{v}(h) = -2(\rho_{\text{ice}}g)^n (\nabla(H+h) \cdot \nabla(H+h))^{\frac{n-1}{2}} \nabla(H+h) \int_h^z A(T^*)(H+h-z)^n dz. \quad (2.6)$$

Integrating Equation (2.6) from the ice base to the surface gives the vertically averaged velocity $\bar{\mathbf{v}}$.

The flow law, Equation (2.3), depends on the temperature of ice. It is, therefore, necessary to determine how the distribution of ice temperatures changes with a changing ice sheet configuration. The thermal evolution of the ice sheet is described by

$$\frac{\partial T}{\partial t} = \frac{k_{\text{ice}}}{\rho_{\text{ice}}c_p} \nabla^2 T - \mathbf{v} \cdot \nabla T + \frac{\Phi}{\rho_{\text{ice}}c_p}, \quad (2.7)$$

where T is the absolute temperature, k_{ice} is the thermal conductivity of ice, c_p is the specific heat capacity and Φ is the heat generated due to internal friction. Thus, heat is transferred by both conduction (treated as a diffusive process) and advection (first and second terms of the RHS of Eq. (2.7), respectively) and generated within the ice body due to deformational friction (third term of the RHS of Eq. (2.7)).

Equation (2.7) is simplified by assuming that horizontal conduction is negligible relative to vertical conduction since horizontal temperature gradients are small. $\nabla^2 T$ can, therefore, be replaced with $\partial T / \partial z$. In general, the thermal conductivity, k_{ice} , depends on density and temperature (Paterson, 1994) which make Equation (2.7) non-linear. However, Equation (2.7) is further simplified by assuming constant density and thermal conductivity. Keeping the thermal conductivity constant tends to increase basal temperature, since $\partial k_{\text{ice}} / \partial z$, if included, reinforces vertical advection of heat (Paterson, 1994).

Heat is produced internally by the work done in straining. The internal heating rate per unit volume is

$$\Phi = \sum_{i,j} \dot{\epsilon}_{ij} \tau_{ij}. \quad (2.8)$$

Assuming that heating due to longitudinal strain-rates is small compared with that due to horizontal shear strain-rates, Equation (2.8) can be simplified to (Huybrechts, 1986):

$$\Phi = 2\dot{\epsilon}_{xz} \tau_{xz} + 2\dot{\epsilon}_{yz} \tau_{yz} = -\rho_{\text{ice}}g(H+h-z) \frac{\partial \mathbf{v}}{\partial z} \cdot \nabla(H+h). \quad (2.9)$$

2.1.2 Boundary Conditions

The ice sheet is linked to the outside world via conditions at the ice boundaries. Three distinct boundaries have to be considered: the ice base, the ice surface and lateral boundaries.

Ice Base

The basal boundary conditions strongly depend on the ice temperature; the ice sheet can be frozen to the bedrock, in which case ice movement is solely due to internal deformation within the ice column above and $\mathbf{v}(h) = 0$. The ice becomes free to move over its bed when the basal temperature has reached the pressure–corrected melting point of ice.

Basal décollement is a complicated process and can occur within a layer of till situated between the ice base and the bedrock or at the ice–bedrock interface itself. Sliding and bed deformation can also occur simultaneously. Finding a “sliding law”, i.e. a relation between basal velocity, shear stress and water pressure, is one of the major problems of glacier physics (Paterson, 1994). Large parts of the past European ice sheet were underlain by deformable sediments, suggesting that basal décollement could have occurred extensively. The main problem with developing a sliding law is the difficulty of observing processes at the base of an ice sheet. Empirical sliding laws usually take the form

$$\mathbf{v}(h) = a\tau_b^p N^{-q}, \quad (2.10)$$

where τ_b is the basal shear stress, N is the effective pressure and p , q and a are parameters (Paterson, 1994).

Currently, the ice sheet model employs a very simple binary sliding law of the form of Equation (2.10). Basal décollement is switched on when basal temperatures have reached the pressure corrected melting point of ice. Since the effective pressure, N , is not known, Equation (2.10) becomes

$$\mathbf{v}(h) \propto (H\nabla_H(H+h))^p, \quad (2.11)$$

where N^{-q} is absorbed into the constant of proportionality and $p = 3$ as suggested by Paterson (1994). The constant of proportionality is a run–time parameter and is used during model calibration. Sliding laws that take into account water pressure explicitly exist (e.g. Arnold and Sharp, 2002; Fowler and Schiavi, 1998; Pattyn, 1996). However, basal décollement introduces large velocity gradients which leads to the violation of the shallow ice approximation and it is not clear that these more complex sliding laws are any better as physical representations of the real world. The sliding law (2.11) is considered to be a good first approximation that can be tuned during calibration.

The temperature at the ice base depends both on the geothermal heat flux Ψ and frictional heating. The basal ice temperature is held constant if it reaches

the pressure-corrected melting point of ice:

$$\begin{aligned} T(h) &= T^* && \text{if } T(h) \geq T^*, \\ \left. \frac{\partial T}{\partial z} \right|_{z=h} &= \frac{\Psi}{k_{\text{rock}}} && \text{if } T(h) < T^*. \end{aligned} \quad (2.12)$$

where k_{rock} is the thermal conductivity of rock. Excess heat available when the temperature is held fixed at the pressure melting point is used to formulate melt rates at the lower boundary. The temperature perturbations penetrate into the bedrock and change the temperature gradient within the rock, i.e. the heat flux across the ice–bedrock interface depends on temperature variations. This feedback tends to reduce the amplitude of the temperature variation at the ice–bedrock interface (Ritz, 1987). The model used here does not include a bedrock layer necessary for computing this dependence. This will result in enlargement of the areas of basal melting and thus influence sliding and ice thicknesses.

The presence of melt water and the water drainage pattern below the ice sheet will affect basal décollement. Basal shear stresses are reduced if drainage is poor and, thus, water pressure is high (Boulton and Payne, 1992b). Reduced basal shear stresses lower the ice sheet profile and reduce surface slopes. However, these effects are not directly resolved by the model.

The underlying topography adjusts isostatically to the changing weight of the ice sheet above. Lithospheric adjustment is described in Section 2.2.

Ice Surface

The ice surface defines the boundary between atmospheric processes (e.g. air temperatures, precipitation, wind patterns) and the ice sheet. These processes are parameterised with two sets of boundary conditions: surface temperatures and mass balance.

Surface Temperatures The temperature of the ice surface is set to the annual mean air temperature. This is only a good approximation if the surface air temperatures are below freezing throughout the year. If this is not the case, during the summer, melt water percolates the topmost firn layer and freezes at depth, where it releases latent heat thus raising the temperature (Paterson, 1994). A firn model is not included and this process is, therefore, not represented.

The temperature field as a function of latitude λ , elevation above sea-level z and time t , is approximated by

$$T(\lambda, z, t) = \sum_{i=1}^N a_i \lambda^i + bz + \Delta T(t), \quad (2.13)$$

where a_i are (possibly time-dependent) parameters defining the temperature at sea-level, b is the lapse rate and $\Delta T(t)$ is the time-dependent, linear

modifier of the temperature field. The parameterisation of the temperature field used does not depend on longitude, φ . The parameters of (2.13) can be fixed by fitting the temperature model to palaeoclimatic reconstructions (see Chapter 3.1.2).

Mass Balance The mass balance at any modelled point (x, y, z) above sea-level is defined as the sum of ice accumulation and ice ablation. A previously unglaciated grid point with a positive mass balance will accumulate ice, allowing ice sheet inception. The *equilibrium line altitude* (ELA) is the altitude at which the mass balance is zero. The mass balance of the ice sheet model is parameterised using the ELA field and a function describing how the mass balance varies with elevation relative to the ELA. The model is then forced by raising/lowering the ELA.

The parameterisation used follows the approach of Boulton and Payne (1992a) and is used in many other studies, e.g. Hulton *et al.* (1994); Boulton *et al.* (1995) and Hulton and Sugden (1997). The mass balance field is assumed to vary parabolically around the ELA. Two parameters control the shape of the mass balance M : M_{\max} is the maximum mass balance value that can be reached and z_{\max} is the vertical distance above the ELA at which the maximum mass balance is reached. The mass balance in terms of M_{\max} and z_{\max} is then:

$$M(z^*) = \begin{cases} 2M_{\max} \left(\frac{z^*}{z_{\max}} \right) - M_{\max} \left(\frac{z^*}{z_{\max}} \right)^2 & \text{for } z^* \leq z_{\max} \\ M_{\max} & \text{for } z^* > z_{\max} \end{cases}, \quad (2.14)$$

where z^* is the vertical distance above the ELA.

Values for M_{\max} and z_{\max} are found by fitting Equation (2.14) to modern mass balance data published by Kuhn (1984). Figure 2.2 shows mass balance data from modern glaciers in a dry and cold climatic setting (Devon Ice Cap and White Glacier) and a maritime climate (Nigardsbreen) together with mass balance curves generated using Equation (2.14) together with the parameters shown in Table 2.1.

	M_{\max}	z_{\max}
Continental Mass Balance	0.3ma^{-1}	500m
Maritime Mass Balance 1	4ma^{-1}	1200m
Maritime Mass Balance 2	1.5ma^{-1}	1200m

Table 2.1: Parameters for a continental and maritime mass balance curves.

Maritime Climate 1 with a maximum mass balance of 4ma^{-1} is more realistic than Maritime Climate 2 which is similar to the continental climate parameterisation. However, it was necessary to use a mass balance—altitude relationship with a shallower gradient because the steep gradient

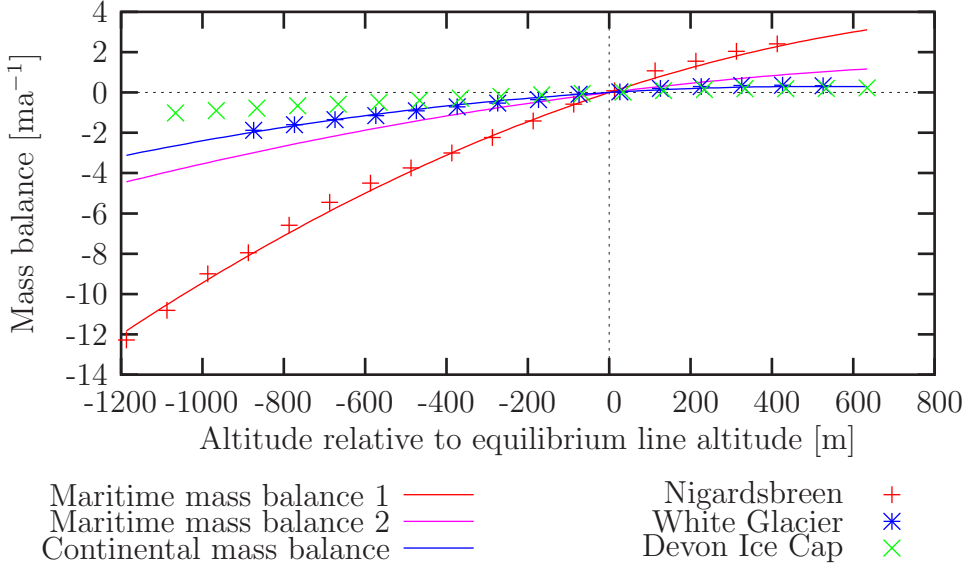


Figure 2.2: Mass balance for the extreme maritime and continental climates used throughout this project. This plot also shows the altitude—mass balance relationship of modern glaciers (data from [Kuhn, 1984](#)).

of Maritime Climate 1 introduces model instabilities. Maritime Climate 2 is therefore used here.

A continentality value, c , is defined for every grid point and can range between 0, for extreme maritime, to 1, for extreme continental climates. The values are found by considering a circle with a given radius, centred on each grid point. c is then the ratio of the area of land above sea-level to the total area within the circle.

Mass balance values for intermediate climates are found by scaling and adding the maritime and continental mass balances using the continentality value. The mass balance is thus

$$M = cM_{\text{cont}} + (1 - c)M_{\text{mar}}. \quad (2.15)$$

Finally, the latitudinal ELA gradient is assumed to be proportional to the temperature gradient. Fitting a quadratic function to present temperature data gives the following first approximation to the ELA field:

$$z_{\text{ELA}} = 10821.0 - 238.0\lambda + 1.312\lambda^2 \quad [\text{m}], \quad (2.16)$$

where λ is measured in degrees.

The parameterisation described above served as an initial, best guess and produces reasonable results for the European ice sheet, except for the eastern

margin, where the ice sheet continues to grow (see Chapter 3.2). However, an additional longitudinal ELA gradient was required to grow a British ice sheet (see Chapter 4.1).

Other mass balance treatments with varying complexity exist. The degree-day method (Braithwaite, 1984; Braithwaite and Olesen, 1989; Braithwaite, 1995) uses a statistical description of how temperatures vary throughout the year and allows a more detailed treatment of ice ablation. Huybrechts (2002) and Charbit *et al.* (2002) used this method, together with today's precipitation patterns perturbed by different climates derived from ice cores, to calculate ice accumulation rates. Hulton *et al.* (2002); Hulton and Purves (2000); Purves and Hulton (2000) used a regional precipitation model to calculate ice accumulation. Finally, Charbit *et al.* (2002) used snapshots from an atmospheric general circulation model (AGCM) to simulate precipitation and temperatures. The climate state between snapshots had to be interpolated, because running an AGCM is computationally expensive.

Lateral Boundary Conditions

The model simulates the evolution of an ice sheet occupying a specific region. The simulated ice sheet might reach the edge of the modelled area. Horizontal gradients of the ice surface elevation and temperature field are set to zero at the model boundaries.

At the marine margin, ice dynamics change drastically when the ice starts floating and forms an ice shelf where flow is dominated by longitudinal stretching. Ice shelves may help to keep the ice sheet in place by exerting backstresses on the inland ice (van der Veen, 1987). The ice sheet model used here does not include ice shelf physics. Instead, the simple assumption is made that a fraction of ice is lost due to iceberg calving when the ice sheet started to float. The ice lost due to iceberg calving enters the model as an additional mass balance term. The calving rate is set to 10% of the ice thickness at the marine margin per year.

Northern Hemisphere ice sheet models have not yet been coupled to an ice shelf model. Huybrechts (2002) coupled an ice shelf model to an ice sheet model for a simulation of the Antarctic ice sheet. However, the ice shelf model did not include a calving law. Both Huybrechts (2002) and Charbit *et al.* (2002) set the ice thickness of Northern Hemisphere ice sheets to zero once the ice starts to float. Only few studies on calving dynamics have been conducted, because of the inherent difficulties in observing these unpredictable, massive events (Paterson, 1994; Hughes, 2002).

Ice lost due to iceberg calving is completely removed from the modelled system. This assumption is only valid if ice is calved into the open oceans (e.g. the Atlantic). Ice calved into a lake will eventually fill up that lake and thus contribute to the advance of the ice sheet (Hughes, 2002).

2.2 Earth Models

The Earth's lithosphere is not infinitely stiff, but adjusts isostatically to changing surface loads. Ice sheets store large volumes of water, thus lowering global sea-levels. It is generally recognised that the Earth's adjustment to changing ice volumes affects ice sheet dynamics (e.g. Charbit *et al.*, 2002; Lambeck and Chappell, 2001; Benn and Evans, 1998; Le Meur and Huybrechts, 1996; Blanchon and Shaw, 1995; Peltier, 1994; Nakada and Lambeck, 1987). In isostatic equilibrium under loading conditions, bedrock depression will be about one third of the ice thickness (Le Meur and Huybrechts, 1996). Lowering the bedrock topography also tends to lower the ice surface elevation, which in turn reduces the mass balance. On the other hand, growing ice sheets remove water from the oceans, thus lowering global sea-levels. At the last glacial maximum, global sea-levels were about 120m lower than they are today (Fairbanks, 1989). Falling sea-levels have two effects: i) The area above sea-level or covered by shallow seas is increased, thus increasing the area available for the ice sheet to occupy and ii) changing sea-levels affect the stability of marine ice sheets through grounding line migration (Le Meur and Huybrechts, 1996; Mayer, 1996).

Isostatic adjustment of the lithosphere causes flow within the mantle. When an ice load is placed on the lithosphere it flexes downwards. Within the asthenosphere, material flows outwards causing the surrounding area to rise. When the ice sheet melts, lithosphere once covered by ice rises, since mantle material flows back to the formerly depressed area and the surrounding area subsides (see Fig. 2.3).

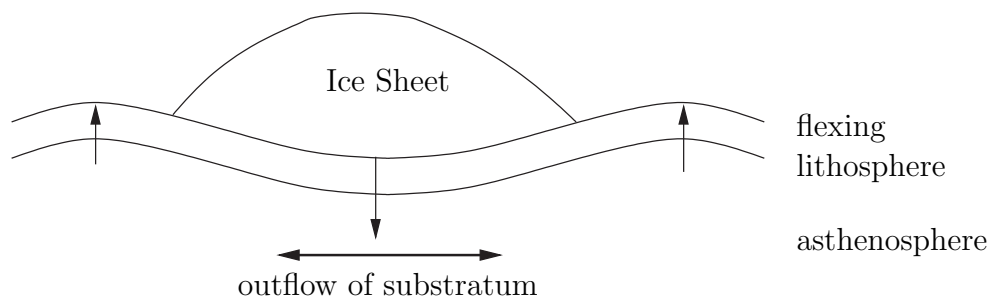


Figure 2.3: Isostatic adjustment of the lithosphere due to an ice sheet (after Oerlemans and van der Veen, 1984).

This simple model is only a qualitative description. The amount of flexure depends on the effective elastic thickness of the lithosphere, and the rate of isostatic adjustment on the viscosity structure of the Earth's mantle (Le Meur and Huybrechts, 1996).

Sea-level is an equipotential surface of the Earth's gravitational field, termed the geoid. Redistribution of mass, both on the Earth's surface (growth and decay of ice sheets and the associated change in water volume) and within the Earth,

changes the Earth's gravitational field (Lambeck *et al.*, 1998). However, sea-level adjusts itself so that the sea surface remains an equipotential surface.

Treatment of the lithosphere's isostatic adjustment in ice sheet models ranges from simple plane Earth approximations (e.g. Boulton *et al.*, 1995; Charbit *et al.*, 2002) to full spherical self-gravitating Earth models (e.g. Lambeck *et al.*, 1998; Le Meur and Huybrechts, 1998; Peltier, 1994). Le Meur and Huybrechts (1996) compared different ways of dealing with the Earth's isostatic adjustment, as discussed in the following subsections.

2.2.1 First Approximations to Isostatic Adjustment

The Earth can be treated to a first approximation as a thin elastic layer floating on top of a highly viscous asthenosphere. Earth models can be differentiated by how the two layers are treated (Le Meur and Huybrechts, 1996). The lithosphere can be described as a:

Local Lithosphere: the flexural rigidity of the lithosphere is ignored, i.e. this is equivalent to ice floating directly on the asthenosphere;

Elastic Lithosphere: the flexural rigidity is taken into account;

while the asthenosphere can be treated as a:

Fluid Asthenosphere: the mantle behaves like a non-viscous fluid, isostatic equilibrium is reached instantaneously;

Relaxing Asthenosphere: the flow within the mantle is approximated by an exponentially decaying hydrostatic response function, i.e. the mantle is treated as a viscous half-space;

Diffusive Asthenosphere: the flow within the mantle is approximated by a diffusion equation. This approximation corresponds to a viscous layer overlying a solid half-space.

Earth models are then formulated by combining one of the lithosphere with one of the mantle approximations. There are therefore six different simple Earth models referred to as local lithosphere/fluid asthenosphere (LLFA), local lithosphere/relaxing asthenosphere (LLRA), local lithosphere/diffusive asthenosphere (LLDA), elastic lithosphere/fluid asthenosphere (ELFA), elastic lithosphere/relaxing asthenosphere (ELRA) and elastic lithosphere/diffusive asthenosphere (ELDA).

Local Lithosphere

Since there are no lithospheric effects, the equilibrium bedrock depression w can be found from the ice thickness H according to Archimedes principle

$$w = \frac{\rho_{\text{ice}}}{\rho_{\text{ast}}} H, \quad (2.17)$$

where ρ_{ice} is the density of ice (910kgm^{-3}) and ρ_{ast} is the effective density of the asthenosphere (3000kgm^{-3}).

Elastic Lithosphere

The local lithosphere approximation can be improved by introducing a thin elastic plate resting on the asthenosphere. The additional elastic layer only affects the geometry of the deformation.

The downward deflection $w(r)$, due to a load q , of a thin elastic plate with thickness H_L and flexural rigidity D floating on a non-viscous medium with density ρ_{ast} can be written as (Lambeck and Nakiboglu, 1980; Le Meur and Huybrechts, 1996)

$$D\nabla_{\text{H}}^4 w + \rho_{\text{ast}}gw = q, \quad (2.18)$$

where ∇_{H} is the horizontal gradient operator and g is the gravitational acceleration. The flexural rigidity in terms of the Lamé parameters, λ and μ , and the plate thickness is (Lambeck and Nakiboglu, 1980)

$$D = \frac{\mu(\lambda + \mu)H_L^3}{3(\lambda + 2\mu)}. \quad (2.19)$$

The Lamé parameters can be inferred from the velocities of seismic waves travelling through the Earth (Stacey, 1992).

For a radially symmetric load of finite dimension with boundary at $r = B$, the boundary conditions to the 4th-order differential equation (2.18) are (Lambeck and Nakiboglu, 1980):

1. w and dw/dr are finite at $r = 0$
2. w and dw/dr are continuous at $r = B$
3. moments and shears are continuous at $r = B$
4. moments vanish at infinity: w and $r^{-1}/(dw/dr)$ vanish at infinity

Solutions of (2.18) for a uniform disk load of density ρ_{ice} , height H and radius A are, for $r \leq A$:

$$w(r) = \frac{\rho_{\text{ice}}H}{\rho_{\text{ast}}} \left[1 + C_1 \text{Ber} \left(\frac{r}{L_r} \right) + C_2 \text{Bei} \left(\frac{r}{L_r} \right) \right], \quad (2.20a)$$

and for $r \geq A$:

$$w(r) = \frac{\rho_{\text{ice}}H}{\rho_{\text{ast}}} \left[D_1 \text{Ber} \left(\frac{r}{L_r} \right) + D_2 \text{Bei} \left(\frac{r}{L_r} \right) + D_3 \text{Ker} \left(\frac{r}{L_r} \right) + D_4 \text{Kei} \left(\frac{r}{L_r} \right) \right], \quad (2.20b)$$

where the functions $\text{Ber}(x)$, $\text{Bei}(x)$, $\text{Ker}(x)$ and $\text{Kei}(x)$ are zeroth order Kelvin functions (see Appendix A.1). $L_r = (D/(\rho_{\text{ast}}g))^{1/4}$ is the *radius of relative stiffness*. The constants C_i and D_i arise from the boundary conditions and can be written as

$$\begin{aligned} C_1 &= a \text{Ker}'(a) \\ C_2 &= -a \text{Kei}'(a) \\ D_1 &= 0 \\ D_2 &= 0 \\ D_3 &= a \text{Ber}'(a) \\ D_4 &= -a \text{Bei}'(a), \end{aligned} \tag{2.20c}$$

where $a = A/L_r$ (Lambeck and Nakiboglu, 1980). The apostrophe denotes first derivatives, i.e. $f'(a) = \left. \frac{df(x)}{dx} \right|_{x=a}$. Figure 2.4 shows a plot of $w(r)$.

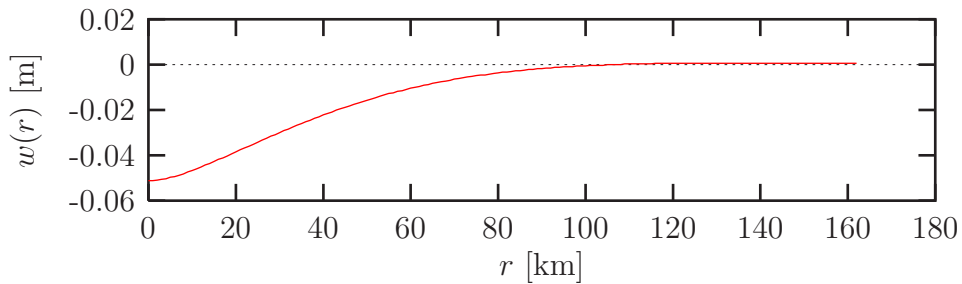


Figure 2.4: Plot of the isostatic adjustment of a disk load of radius 2.5km and a height of 1km. The radius of relative stiffness is found to be $L_r = 135.769\text{km}$.

The load imposed on the lithosphere by a square column with sides Δx can be approximated by a number of disk loads, provided the volume and thus the mass is conserved. Figure 2.5 shows the differences in lithospheric deflection when approximating a square load with one and four disks, four and 16 disks and 16 and 64 disks. The load is centred at the origin and is equivalent to an ice volume of $3\text{km} \times 400\text{km}^2$.

As expected differences are largest close to the load's centre and decrease with increasing distance from the centre. Also, the differences decrease with increasing number of disks. The largest difference at the origin between approximating the square load with a single disk and 64 disks is about 5cm for the load under consideration which corresponds to 0.017%. This does not justify using the extra computing time required.

Relaxing Asthenosphere

The simplest way to account for the time-dependence of the isostatic response is to estimate its characteristic time constant τ and assume that the rate of response is proportional to the difference between the loaded equilibrium, $h_0 - w$ and the current profile, h , and inversely proportional to the time constant (Le Meur and

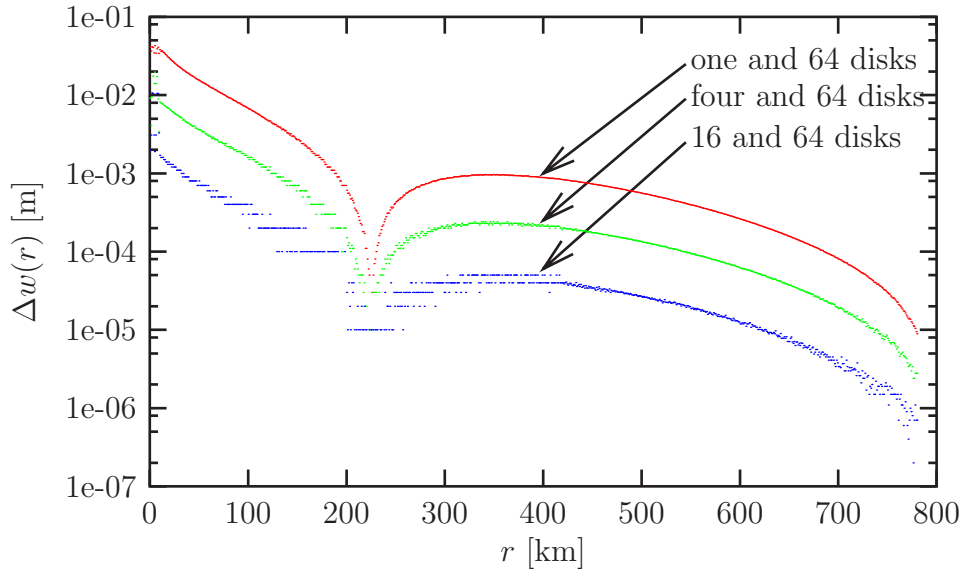


Figure 2.5: Differences in deflection of the lithosphere as a function of distance along a coordinate axis for approximating the square load with i) one and 64 disks, ii) four and 64 disks and iii) 16 and 64 disks. The load is centred at the origin and is equivalent to an ice volume of $3\text{km} \times 400\text{km}^2$.

Huybrechts, 1996). The rate of isostatic adjustment is then

$$\frac{dh}{dt} = -\frac{1}{\tau}(h - h_0 + w). \quad (2.21)$$

The present bedrock topography is assumed to be the unloaded equilibrium topography h_0 . This assumption is a crude estimate since the initial topography is unknown. Furthermore, glacial rebound is still ongoing in regions that were previously glaciated, e.g. present uplift rates over the Gulf of Bothnia are about 12mma^{-1} (Milne *et al.*, 2001).

Diffusive Asthenosphere

The time-dependent flow of mantle material can be found by considering the equation of motion, where horizontal flow is assumed to be inversely proportional to the dynamic viscosity ν of the asthenosphere (Oerlemans and van der Veen, 1984). The flow is driven by the horizontal pressure gradient, with the pressure taken to be proportional to the difference between the present topography, h , and the equilibrium bedrock topography under loading $h_0 - w$. The horizontal velocity, \mathbf{v} , as a function of depth z (positive downwards) can then be expressed as

$$\mathbf{v}(z) = \frac{g\rho_{\text{ast}}}{2\nu}(z^2 - 2H_a z)\nabla_{\text{H}}(h - h_0 + w), \quad (2.22)$$

where H_a is the depth below which the surface loading is not felt (Le Meur and Huybrechts, 1996). Using the principle of conservation of mass, we can relate the rate of isostatic adjustment to the flow of mantle material. This relation takes the form of a diffusion equation with a diffusion coefficient D_a :

$$\frac{dh}{dt} = D_a \nabla_H^2 (h - h_0 + w) \quad \text{with} \quad D_a = \frac{g \rho_{\text{ast}} H_a^3}{3\nu}. \quad (2.23)$$

Usually, the parameters H_a and ν are not used directly, instead the diffusion coefficient D_a is inferred from rebound measurements of the areas under consideration (Le Meur and Huybrechts, 1996).

2.2.2 The Full Spherical Earth Model

This Section gives a brief mathematical outline of the spherical, self-gravitating Earth model developed by Johnston (1993a). The spherical Earth model calculates both glacio- and hydro-isostatic adjustment of the lithosphere due to changing surface loads and sea-level change due to changes of the gravitational potential and changes of the Earth's rotation tensor (see also Chapter 1.4.1).

It is known that the Earth behaves elastically on short time scales from seismic studies (e.g. Stacey, 1992). From the Earth's shape and glacial rebound, it is also known that on large time scales the Earth behaves like a fluid (England, 1992). Laboratory experiments with minerals that occur in the mantle suggest a non-linear rheology (Karato and Wu, 1993). Undoubtedly, using a linear rheology to simplify the mathematics will introduce some errors. However, the use of a linear rheology can be justified by arguing that the mantle already experiences large stresses due to mantle convection. The stresses due to glacial loading and unloading of the Earth's surface can then be viewed as linear perturbations of the larger-scale convection. Earth rheology parameters such as mantle viscosity and lithospheric thickness inferred from glacial studies are thus effective parameters and do not necessarily match with those inferred from mantle convection studies.

The simplest linear, viscoelastic body behaving initially as an elastic solid and then as a viscous fluid under continued loading is a Maxwell body. This is the type of body used in the model. The model is further simplified by assuming that Earth parameters vary only radially. From seismic tomography it is known that lateral heterogeneities exist (Stacey, 1992). Also, the continental lithosphere is much thicker than the oceanic lithosphere (O'Nions, 1992). Using a spherically symmetric model implies that Earth parameters are averaged over spherical shells and parameters, such as lithospheric thickness and mantle viscosity should be viewed as effective parameters (Kaufmann and Wu, 2002).

Deformation of a spherical, elastic body

The central equation of this Earth model is the constitutive equation, relating the stress tensor $\boldsymbol{\sigma}$ to the strain tensor $\boldsymbol{\epsilon}$. The constitutive equation governs

how material within the Earth flows due to changing boundary conditions at the Earth's surface. The constitutive equation for an elastic body is, using the Einstein summation convention,

$$\sigma_{ij} = \lambda \epsilon_{kk} \delta_{ij} + 2\mu \epsilon_{ij}. \quad (2.24)$$

The strain tensor in terms of the displacement field, \mathbf{u} , is

$$\epsilon_{ij} = \frac{1}{2} \left(\frac{\partial u_i}{\partial x_j} + \frac{\partial u_j}{\partial x_i} \right). \quad (2.25)$$

External forces can either be applied directly on the Earth's surface by normal or shear stresses, or from a distance by gravitational attraction. Initially, the Earth is assumed to be in hydrostatic equilibrium, i.e. the following initial conditions must be satisfied

$$\sigma_{ij}^{(0)} = -p^{(0)} \delta_{ij} \quad (2.26a)$$

$$\nabla p^{(0)} = \rho^{(0)} \nabla \phi^{(0)} \quad (2.26b)$$

$$\nabla^2 \phi^{(0)} = -4\pi G \rho^{(0)}, \quad (2.26c)$$

where p is the pressure, ϕ the gravitational potential and G Newton's universal constant of gravity. The superscript (0) indicates the initial value of the variable under consideration. Furthermore, boundary conditions at the Earth's centre, the core–mantle boundary, the Earth's surface and any non–adiabatic boundary must be fulfilled.

Any displacement field in spherical coordinates can be expressed in terms of three scalar fields

$$\mathbf{u} = \hat{\mathbf{r}}U + \nabla V + \hat{\mathbf{r}} \times \nabla W, \quad (2.27)$$

where U , V and W are known as spheroidal, poloidal and toroidal modes, respectively. Since we are considering a spherically symmetric model, there is no net torque and thus no toroidal displacement field. The Earth's response to an arbitrary gravitational field can be most easily calculated when both Equation (2.27) and the external forcing field are expressed in spherical harmonics.

Solving the constitutive equation (2.24) together with the initial and boundary conditions, the Earth's response to a spherical harmonic surface load can be expressed in terms of Love numbers. Love numbers are dimensionless and are defined in terms of the gravitational potential $\psi_n(r)(r/a)^n Y_n(\vartheta, \varphi)$ of the spherical harmonic surface forcing of mass $Y_n(\vartheta, \varphi)$, where ϑ and φ are co–latitude and longitude, respectively. a is the radius of the Earth. The Love numbers for a load in terms of spherical harmonic coefficients are

$$\begin{pmatrix} h_n(r) \\ l_n(r) \\ 1 + k_n(r) \end{pmatrix} = \frac{2n+1}{4\pi a G} \begin{pmatrix} g^{(0)}(r) u_n(r) \\ g^{(0)}(r) v_n(r) \\ \phi_n(r) \end{pmatrix}, \quad (2.28)$$

where $u_n(r)$ and $v_n(r)$ are the radial and tangential spherical harmonic coefficients of deformation and $g^{(0)}(r)$ is the initial acceleration due to gravity before deformation occurs. The response of a particular Earth model to an arbitrary load is fully defined by a set of Love numbers that only need to be calculated once for each Earth model.

Response of a Maxwell Body and the Correspondence Principle

The constitutive equation of a Maxwell body is

$$\frac{\dot{\sigma}}{E} + \frac{\sigma}{\eta} = \dot{\epsilon}, \quad (2.29)$$

where E is the Young's modulus and η is the viscosity. The constitutive equation of a general linear, viscoelastic body is then

$$\sum_{k=0}^n p_k \frac{d^k \sigma}{dt^k} = \sum_{k=0}^n q_k \frac{d^k \epsilon}{dt^k}. \quad (2.30)$$

The solutions of the constitutive equation for linear, viscoelastic bodies consist of decaying exponentials. The problem at hand can therefore be simplified by taking the Laplace transform, defined as

$$\mathcal{L}[f(t)] = \tilde{f}(s) = \int_0^{\infty} f(t) e^{-st} dt, \quad (2.31)$$

of the constitutive equation. The Laplace transform of a differential equation converts derivatives to polynomials, similarly to the Fourier transform. The Laplace transform of Equation (2.30) is thus

$$\mathcal{P}(s)\tilde{\sigma} = \mathcal{Q}(s)\tilde{\epsilon}, \quad (2.32)$$

where the polynomials $\mathcal{P}(s)$ and $\mathcal{Q}(s)$ are

$$\mathcal{P}(s) = \sum_{k=0}^n p_k s^k \quad \text{and} \quad \mathcal{Q}(s) = \sum_{k=0}^n q_k s^k. \quad (2.33)$$

The constitutive equation in the Laplace domain (2.32) now looks like the constitutive equation for an elastic body, with s -dependent Young's modulus $\mathcal{Q}(s)/\mathcal{P}(s)$. This is the *correspondence principle*, which allows us to use the previously obtained solutions of the elastic problem together with the Laplace transformed shear modulus to obtain the Love numbers for a Maxwell body.

However, taking the inverse Laplace transform, back to the time domain, can be problematic. The general inverse Laplace transform arises from complex analysis and is in many situations unstable. In the case of glacial loading problems, we can assume that the poles lie on the negative real axis, since otherwise we would get an infinite response in the time domain. Using this assumption, it is possible to construct a stable inverse Laplace transform.

The Earth's Response to a Particular Load

We are concerned to find how the Earth responds to a particular loading history $L(\mathbf{r}, t)$. The spatial variation of the model is described in spherical harmonics, so it is necessary to express $L(\mathbf{r}, t)$ in spherical surface harmonics to get $L_n(t)$. The temporal variation of the model is described in the Laplace domain. The loading history $L_n(t)$ needs to be continuous in order to be able to also transform it to the Laplace domain. Assuming that the ice load is only known at discrete times t_i , $i = 0, 1, \dots, k$, a continuous loading history can be found by linearly interpolating between consecutive times using a modified Heaviside function:

$$L_n(t) = \sum_{i=1}^k \Delta L_n^i G\left(\frac{t - t_{i-1}}{\Delta t_i}\right), \quad (2.34)$$

where $\Delta L_n^i = L_n^i - L_n^{i-1}$ is the change of ice load between times t_{i-1} and $t_i = t_{i-1} + \Delta t_i$. The modified Heaviside function is defined as

$$G(\alpha) = \begin{cases} 0 & \text{for } \alpha < 0 \\ \alpha & \text{for } 0 \leq \alpha \leq 1. \\ 1 & \text{for } \alpha > 1 \end{cases} \quad (2.35)$$

The response to a loading history of spherical harmonic degree n in the Laplace domain is then given by multiplying the Laplace transform of Equation (2.34) with the Earth's response.

2.2.3 The Earth Model and Global Sea-Level Change

The concept of eustatic sea-level change was first introduced by Suess in 1885 and refers to a uniform and simultaneous global change of sea-levels (Pirazzoli, 1991). This implies that sea-level change is the same at stable localities. However, there are no truly stable localities, since changing water and ice loads deform the Earth's crust. Using a self-consistent model, an operational definition of eustatic sea-level change is the global average sea-level change. Nakada and Lambeck (1987) call this non-physical concept *equivalent sea-level change* to avoid confusion. Throughout this text, I mostly use the term equivalent sea-level change. However, sometimes I also use the widely adopted term eustatic sea-level change, by which I also mean the concept of equivalent sea-level change described here.

The equivalent sea-level change, $\Delta\zeta^{\text{esl}}(t)$, is a measure of the water mass exchanged between oceans and land-based ice sheets and is defined as

$$\Delta\zeta^{\text{esl}}(t) = -\frac{\rho_{\text{ice}}}{\rho_{\text{water}}} \int_{t_0}^t \frac{\dot{V}_{\text{ice}}(\tau)}{A_o(\tau)} d\tau. \quad (2.36)$$

$\dot{V}_{\text{ice}}(t)$ is the rate of change of global grounded ice volume and $A_o(t)$ the area covered by ocean at time t (Lambeck and Chappell, 2001). The ocean area does not include grounded ice below sea-level, but it does include floating ice shelves since they are in hydrostatic equilibrium with the ocean and, therefore, do not contribute to sea-level change. $A_o(t)$ does depend on sea-level change and, therefore, Equation (2.36) is an integral equation. If the ocean area is assumed to be invariant and equal to that of the present oceans, Equation (2.36) becomes

$$\Delta\zeta^{\text{esl}}(t) = -\frac{\rho_{\text{ice}}}{\rho_{\text{water}}} \frac{\Delta V_{\text{ice}}(t)}{A_o}, \quad (2.37)$$

where the change in equivalent sea-level and ice volume are relative to their values at $t = 0$.

The problem under consideration here is sea-level change around the British Isles. Sea-level change, $\Delta\zeta$ is a function of geographic position (φ, λ) and time t , and is dependent on changes of ice distribution and the Earth's response function. Sea-level change can be expressed as the sum of each ice sheet's contribution:

$$\begin{aligned} \Delta\zeta(\varphi, \lambda, t) &= \sum_{i \in \{\text{ice sheets}\}} \Delta\zeta_i(\varphi, \lambda, t) \\ &= \Delta\zeta_a(\varphi, \lambda, t) + \Delta\zeta_{\text{Fenn}}(\varphi, \lambda, t) + \Delta\zeta_{\text{Brit}}(\varphi, \lambda, t), \end{aligned} \quad (2.38)$$

where $\Delta\zeta_{\text{Fenn}}$ and $\Delta\zeta_{\text{Brit}}$ are contributions due to the Fennoscandian and British ice sheets and $\Delta\zeta_a$ is the sum of contributions due to all the other ice sheets. Sea-level change can be split up further into isostatic and equivalent components:

$$= \Delta\zeta_a^{\text{esl}}(t) + \Delta\zeta_a^{\text{iso}}(\varphi, \lambda, t) + \Delta\zeta_{\text{Fenn+Brit}}^{\text{esl}}(t) + \Delta\zeta_{\text{Fenn+Brit}}^{\text{iso}}(\varphi, \lambda, t), \quad (2.39)$$

where $\Delta\zeta^{\text{esl}}$ and $\Delta\zeta^{\text{iso}}$ are the equivalent and the isostatic components, respectively.

The Fennoscandian and British ice sheets which influence the near and intermediate fields are modelled directly, resulting in solutions for the terms $\Delta\zeta_{\text{Fenn+Brit}}^{\text{esl}}(t)$ and $\Delta\zeta_{\text{Fenn+Brit}}^{\text{iso}}(\varphi, \lambda, t)$.

The first term of Equation (2.39) can be calculated from the global sea-level curve determined from climate simulations performed by Goodess *et al.* (2000a) using the LLN-2D northern hemisphere climate model.

The only unknown term of Equation (2.39) is the far-field isostatic component $\Delta\zeta_a^{\text{iso}}(\varphi, \lambda, t)$. Figure 2.6 shows plots of the far-field isostatic component at 18ka BP. Unfortunately, this term is non-zero and is of the order of tens of meters at the last glacial maximum (Lambeck *et al.*, 1998).

The ice load contribution from the far-field isostatic component could be approximated by fitting the data to a plane. The water load contribution is far more complex since it follows the coast lines. However, these adjustments were not made. The error introduced by this omission is relatively small in comparison with the overall misfit between simulated sea-level change and sea-level change observations.

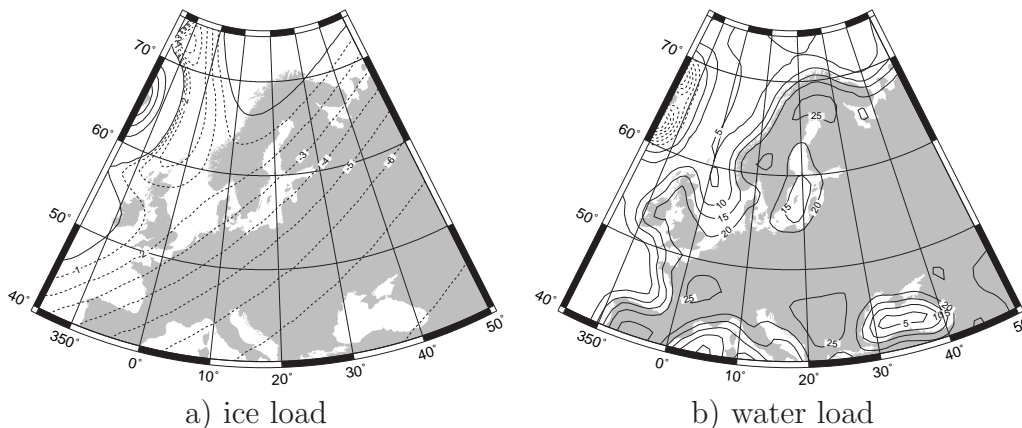


Figure 2.6: Far-field isostatic components for northern Europe, 18ka BP. Data provided by A. Purcell, RSES, ANU, Canberra.

2.3 Model Implementation

Computers can only deal with a finite amount of data, determined by the amount of memory available to the system. In order to solve continuous partial differential equations such as (2.1) and (2.7), the modelled region of interest has to be discretised. Broadly speaking, there are two spatial discretisation schemes: *finite differences* where the derivatives are approximated at grid points, and *finite elements* where the functions and their derivatives are approximated by polynomials. A finite difference scheme is employed in this study for solving the equations governing ice sheet physics. The ice sheet model is based on code originally developed by Huybrechts (1986). The spherical Earth model is based on a spectral scheme (Johnston, 1993b).

At the beginning of this project, the model code consisted of about 20000 lines of FORTRAN77 code spread over numerous files. Since then, the code has been reformatted and extended to use FORTRAN95 features; and a new build system has been implemented. The code compiles with the INTEL f95, NAG f95, DEC f90 and SUN f95 compilers and has been tested on SUN/SPARC, DEC/alpha and LINUX/Intel platforms. The I/O system utilises the netCDF² library for scientific data storage.

2.3.1 Ice Sheet Model

The discretisation of Equations (2.1, 2.6, 2.7) is described in detail by Huybrechts (1986). It should be noted, however, that the vertical coordinate, z , is scaled by the ice thickness analogous to the s -coordinate in numerical weather simulations (e.g. Holton, 1992). A new vertical coordinate, ξ , is introduced so that the ice

²<http://unidata.ucar.edu/packages/netcdf/index.html>

surface is at $\xi = 0$ and the ice base at $\xi = 1$, i.e.

$$\xi = \frac{H + h - z}{H}. \quad (2.40)$$

Figure 2.7 illustrates the new geometry. The derivatives of a function f in (x, y, z, t) become in the new $(\tilde{x}, \tilde{y}, \xi, \tilde{t})$ system (e.g. Bronstein and Semendjajew, 1991):

$$\frac{\partial f}{\partial x} = \frac{\partial f}{\partial \tilde{x}} + \frac{1}{H} \Delta_{\tilde{x}} \frac{\partial f}{\partial \xi}, \quad (2.41a)$$

$$\frac{\partial f}{\partial y} = \frac{\partial f}{\partial \tilde{y}} + \frac{1}{H} \Delta_{\tilde{y}} \frac{\partial f}{\partial \xi}, \quad (2.41b)$$

$$\frac{\partial f}{\partial t} = \frac{\partial f}{\partial \tilde{t}} + \frac{1}{H} \Delta_{\tilde{t}} \frac{\partial f}{\partial \xi}, \quad (2.41c)$$

$$\frac{\partial f}{\partial z} = \frac{1}{H} \frac{\partial f}{\partial \xi}, \quad (2.41d)$$

where the geometric factors, $\Delta_{\tilde{x}}$, $\Delta_{\tilde{y}}$ and $\Delta_{\tilde{t}}$, are defined by

$$\Delta_{\tilde{x}} = \left(\frac{\partial(H + h)}{\partial \tilde{x}} - \xi \frac{\partial H}{\partial \tilde{x}} \right), \quad (2.42a)$$

$$\Delta_{\tilde{y}} = \left(\frac{\partial(H + h)}{\partial \tilde{y}} - \xi \frac{\partial H}{\partial \tilde{y}} \right), \quad (2.42b)$$

$$\Delta_{\tilde{t}} = \left(\frac{\partial(H + h)}{\partial \tilde{t}} - \xi \frac{\partial H}{\partial \tilde{t}} \right). \quad (2.42c)$$

Transforming the vertical coordinate has the following implications (van der Veen and Whillans, 1989):

1. horizontal gradients of the ice surface and ice bed are contained in the geometry factors $\Delta_{\tilde{x}}$, $\Delta_{\tilde{y}}$ and $\Delta_{\tilde{t}}$;
2. the velocities are still parallel to the coordinate axes (x, y, z) . Vertical scaling does not affect the direction of the velocities. However, they are calculated at different levels depending on the ice thickness. This is important for visualisation of the three-dimensional temperature and velocity fields.

The ice thickness evolution (2.1) is solved using an alternating-direction-implicit (ADI) scheme (e.g. Press *et al.*, 1992). Each time step is split up into two half time steps. The equation is first solved along the x -axis, and then, during the second half step, it is solved along the y -axis. The resulting tridiagonal systems of linear equations are solved using LU decomposition (e.g. Press *et al.*, 1992), where the tridiagonal matrix is decomposed into a lower, L and an upper, U , triangular matrix. The new system of equations is then solved using a Gaussian

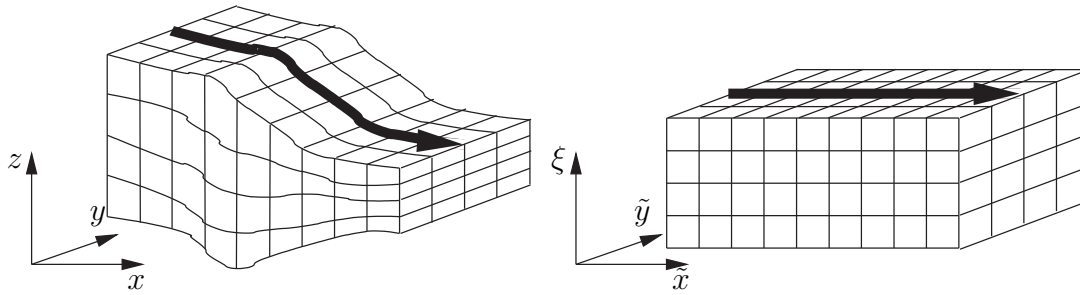


Figure 2.7: Vertical scaling of the ice sheet model. The vertical axis is scaled to unity. The horizontal coordinates are not changed (after Mayer, 1996).

elimination scheme. The equation could also be solved without splitting the time step. However, the resulting system is not tridiagonal, and a different sparse matrix technique would have to be used: More recently, iterative solvers, such as the conjugate gradient algorithm (Barrett *et al.*, 1994), have been employed to solve Equation (2.1). These methods can be faster and also more stable.

Parallelisation of the Ice Sheet Model

Computer models can be written so that the program utilises more than one processor. Parallelisation might be important in two cases:

1. The model under consideration requires large amounts of memory so that the program can not fit into the memory of a single processor computer; and
2. calculations which have to be performed on each grid point are very resource intensive resulting in prohibitively long total run times.

The ice sheet model is of the second type where the memory requirements are relatively modest and computations of the full three-dimensional grid very resource intensive.

The original parallel version of the ice sheet model used the Cray `shmem` library for message passing between processors (PEs) (Mineter and Hulton, 2001). However, the `shmem` library, although performing well, is not portable, since the library is only available on Cray supercomputers. During this project, the parallel version of the model was ported to the Message Passing Interface (MPI³, e.g. Gropp *et al.*, 1994). MPI implementations are freely available for clusters of workstations or are supplied with the development environment of dedicated supercomputers. The ice sheet model can now be run on a single workstation, a cluster of workstations and shared and distributed memory supercomputers.

³<http://www.mpi-forum.org>

Parallelisation is achieved by splitting up the modelled region into a two-dimensional grid of subregions. Each processor solves equations (2.6) and (2.7) on the assigned subgrid. After each update, values have to be exchanged at the inter-processor boundaries, i.e. each PE sends the rightmost column inside its grid to the left halo column of the PE processing the adjoining subgrid on the right, and vice-versa. The same process is repeated for the horizontal boundaries (see the left panel of Fig. 2.8 for an illustration of the subdomain decomposition). Each subgrid is surrounded by a halo of ghostpoints which are updated with corresponding data from neighbouring subgrids.

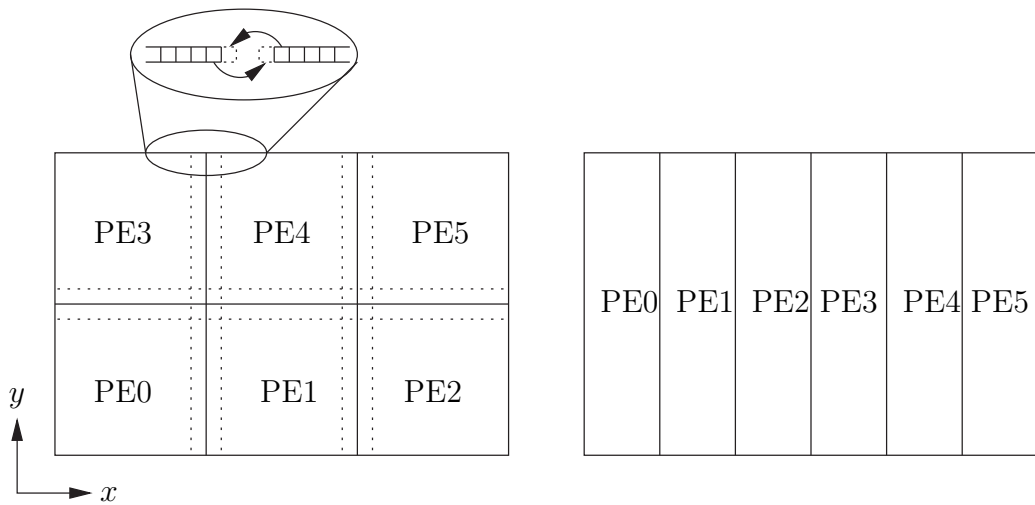


Figure 2.8: Domain decomposition for a 6 PE run. The left panel shows the regular 2D domain decomposition, halos are indicated by dotted lines. The right panel shows the original domain decomposition for the ADI step parallel to the y -axis. The domain decomposition for the ADI step along the x -axis is similar but rotated by 90° .

The ADI scheme, used to solve Equation (2.1), requires the solution of one tridiagonal system for each row (first ADI step, parallel to the x -axis) and one for each column (second ADI step, parallel to the y -axis). In the `shmem` version of the ice sheet model, entire rows/columns were gathered on each processor (see right panel of Fig. 2.8 for an illustration of the resulting domain decomposition of the second ADI step). This approach is very communication intensive, since a lot of data has to be exchanged between the processors. A slightly different tridiagonal matrix solver with a better communication pattern is used instead. The new algorithm is still based on LU decomposition and was developed by [Mattor *et al.* \(1995\)](#).

The tridiagonal systems of linear equations arising during the ADI steps are of the following form:

$$\mathbf{A}\mathbf{X} = \mathbf{R}, \quad (2.43a)$$

where

$$\mathbf{\Lambda} = \begin{pmatrix} B_1 & C_1 & & & & \\ A_2 & B_2 & C_2 & & & \\ & \ddots & \ddots & \ddots & & \\ & & A_{N-1} & B_{N-1} & C_{N-1} & \\ & & & A_N & B_N & \end{pmatrix}, \quad (2.43b)$$

$$\mathbf{X} = (X_1, X_2, \dots, X_N)^T, \quad (2.43c)$$

$$\mathbf{R} = (R_1, R_2, \dots, R_N)^T. \quad (2.43d)$$

The superscript T denotes the transpose of a matrix/vector. The linear system of N equations with N unknowns, Equation 2.43a, is to be solved using P processors. For simplicity, $N = PM$ with M an integer is assumed. The tridiagonal matrix, Equation (2.43b), can be divided into P submatrices \mathbf{L}_p , each of dimension $M \times M$:

$$\mathbf{L}_p = \begin{pmatrix} B_{M(p-1)+1} & C_{M(p-1)+1} & & & & \\ A_{M(p-1)+2} & B_{M(p-1)+2} & C_{M(p-1)+2} & & & \\ & \ddots & \ddots & \ddots & & \\ & & & A_{Mp-1} & B_{Mp-1} & C_{Mp-1} \\ & & & & A_{Mp} & B_{Mp} \end{pmatrix}. \quad (2.44)$$

\mathbf{X} and \mathbf{R} are similarly split up into P subvectors of length M . [Mattor et al. \(1995\)](#) define the following vectors for each subsystem:

$$\mathbf{L}_p \mathbf{x}_p^R \equiv \mathbf{r}_p, \quad (2.45a)$$

$$\mathbf{L}_p \mathbf{x}_p^{UH} \equiv (-A_{M(p-1)+1} \ 0 \ 0 \ \dots \ 0)^T, \quad (2.45b)$$

$$\mathbf{L}_p \mathbf{x}_p^{LH} \equiv (0 \ 0 \ 0 \ \dots \ -C_{Mp})^T. \quad (2.45c)$$

The superscripts of the \mathbf{x} denote ‘‘particular’’, ‘‘upper homogeneous’’ and ‘‘lower homogeneous’’ solution. In analogy to solving inhomogeneous linear differential equations, the general solution of each subsystem, \mathbf{x}_p consists of the particular solution added to a linear combination of the homogeneous solutions:

$$\mathbf{x}_p = \mathbf{x}_p^R + \xi_p^{UH} \mathbf{x}_p^{UH} + \xi_p^{LH} \mathbf{x}_p^{LH}, \quad (2.46)$$

where the coefficients ξ_p^{UH} and ξ_p^{LH} depend on the coupling to the neighbouring solutions. The coefficients are found by substituting (2.46) into (2.43a). This substitution leads to a reduced tridiagonal system of equations of size $(2P - 2) \times (2P - 2)$.

The algorithm used for solving Equation (2.43a) on P processors works as follows:

1. Each processor solves the subsystem, Equation (2.45a-c). No data needs to be moved between processors since they already store the data.

2. The reduced system is assembled on each processor. This step involves interprocess communication.
3. Each processor solves the reduced problem.
4. The general solution of the full problem, Equation (2.43a), is found on each processor by computing Equation (2.46) using the coefficients ξ_p^{UH} and ξ_p^{LH} obtained during the previous step.

A tridiagonal system of equations has to be solved for each column (row). These systems are independent from each other. Therefore, a further communication optimisation suggested itself: Each PE, first, solves all subsystems associated with its subgrid. Data required for assembling each reduced system is packed into an array which is then distributed among the other PEs. This approach does not reduce the total amount of data being exchanged. It does, however, decrease the number of messages sent. Message set up is computationally expensive. Reducing the number of messages sent, therefore, improves performance.

Performance of the MPI ice sheet model was measured using a simple EISMINT test case with all options switched on. Performance of a parallelised computer model is measured by *speedup* and *efficiency*. Speedup is defined as the ratio between the time taken for the most efficient sequential algorithm and the time take for the parallel algorithm on a machine with n processors. Efficiency is a measure of how well utilised the processors are and is defined as the ratio between speedup and the number of processors. Figure 2.9 shows speed-up and efficiency measurements of the model run on the SUN Enterprise HPC 6500 at the Edinburgh Parallel Computing Centre (EPCC). Performance seems to be reasonable. Superlinear speed-up is probably due to the fact that the MPI model was run on one PE instead of using the best-known sequential algorithm.

2.3.2 Earth Models

A major task of this project was concerned with the development and implementation of Earth approximations and coupling the spherical Earth model to the ice sheet model. The following sections describe these aspects.

Elastic Lithosphere

The equations describing the lithospheric deflection (2.20a) and (2.20b) are scaled by the load $(\rho_{\text{ice}}H)/\rho_{\text{ast}}$ imposed on the lithosphere. An operator \mathcal{W} can be defined which depends only on the distance scaled by the radius of relative stiffness $x = r/L_r$:

$$\mathcal{W}(x) = \frac{\rho_{\text{ast}}}{\rho_{\text{ice}}H} w(x) = \begin{cases} 1 + C_1 \text{Ber}(x) + C_2 \text{Bei}(x) & \text{if } r \leq A \\ D_3 \text{Ker}(x) + D_4 \text{Kei}(x) & \text{if } r > A \end{cases}. \quad (2.47)$$

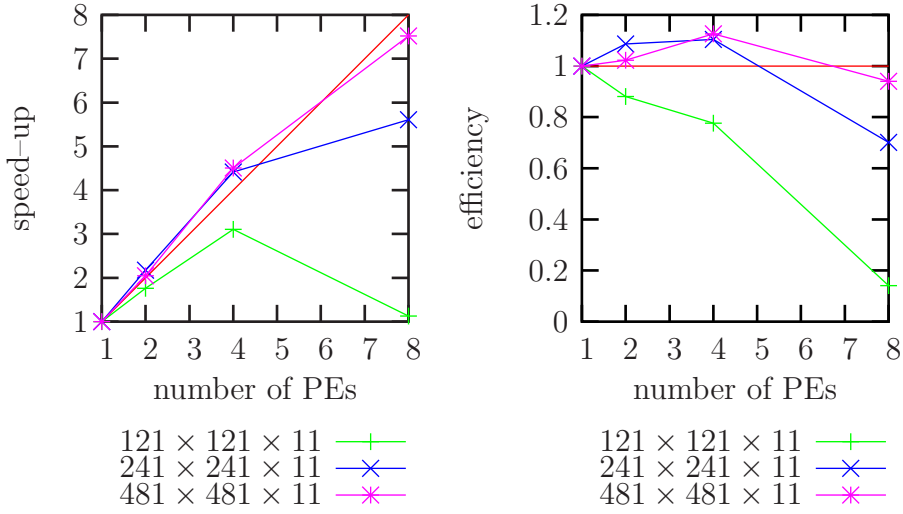


Figure 2.9: Speedup and efficiency of the MPI code for simulations with different grid dimensions. The runtime measurements were obtained by timing runs of a simple EISMINT test case with all options switched on.

\mathcal{W} is calculated and stored only once, when the model is initialised. Since \mathcal{W} is symmetric, it only needs to be evaluated for one quadrant. The discrete operator is then

$$\mathcal{W}_{m,n} = \mathcal{W} \left(\frac{\Delta x \sqrt{m^2 + n^2}}{L_r} \right) \quad m, n \in [0, w_{\text{size}}], \quad (2.48)$$

where $w_{\text{size}} = \text{int}(6L_r/\Delta x)$.

The lithospheric deflection w at node (i, j) due to the ice load H is then

$$w_{i,j} = \sum_{n=\max(1, j-w_{\text{size}})}^{\min(j_{\text{size}}, j+w_{\text{size}})} \sum_{m=\max(1, i-w_{\text{size}})}^{\min(i_{\text{size}}, i+w_{\text{size}})} \frac{\rho_{\text{ice}} H_{m,n}}{\rho_{\text{ast}}} \mathcal{W}_{|m-i|, |n-j|}, \quad (2.49)$$

where i_{size} and j_{size} denote the number of nodes in the x - and y -direction, respectively.

Pseudo-code for updating the entire deflection field is shown in Algorithm 2.1. Note, that the calculation of the ice load is taken outside the inner loops to optimise memory access patterns: The contributions of each cell, containing ice, to a single point are calculated in Equation (2.49). The inner loops of Algorithm 2.1 calculates the loading effects of a single cell on the entire grid.

Note, that the ice sheet model also takes into account isostatic effects due to changing water loads.

```

1: for all  $i \in [1, i_{\text{size}}]$  and  $j \in [1, j_{\text{size}}]$  do
2:    $w_{i,j} = 0.0$ 
3: end for
4: for  $j = 1$  to  $j_{\text{size}}$  do
5:   for  $i = 1$  to  $i_{\text{size}}$  do
6:      $f = (\rho_{\text{ice}} H_{i,j}) / \rho_{\text{ast}}$ 
7:     for  $n = \max(1, j - w_{\text{size}})$  to  $\min(j_{\text{size}}, j + w_{\text{size}})$  do
8:       for  $m = \max(1, i - w_{\text{size}})$  to  $\min(i_{\text{size}}, i + w_{\text{size}})$  do
9:          $w_{m,n} = w_{m,n} + f \mathcal{W}_{|m-i|, |n-j|}$ 
10:       end for
11:     end for
12:   end for
13: end for

```

Algorithm 2.1: Update lithospheric deflection field

Relaxing Asthenosphere

Solving the 1st-order ordinary differential equation (2.21) is simple since h_0 is independent of time and the deflection w is constant over the interval $[t_1, t_1 + \Delta t]$. The solution of (2.21) is then

$$h(t_1 + \Delta t) = (h_0 - w)(1 - e^{-\Delta t/\tau}) + h(t_1)e^{-\Delta t/\tau}. \quad (2.50)$$

Denoting the bedrock topography at times t_1 and $t_1 + \Delta t$ as h_n and h_{n+1} respectively, Equation (2.50) becomes

$$h_{n+1} = (h_0 - w)(1 - e^{-\Delta t/\tau}) + h_n e^{-\Delta t/\tau}, \quad (2.51)$$

which is straightforward to evaluate numerically.

Diffusive Asthenosphere

The equation governing the bedrock response to loading under the diffusive asthenosphere approximation, Equation (2.23), is solved in a similar manner to the ice thickness evolution equation (2.1). Initial testing using this approximation showed that there was a problem with the code. However, [Le Meur and Huybrechts \(1996\)](#) concluded that the relaxing asthenosphere should be preferred over the diffusive asthenosphere approximation. Hence, support for the diffusive asthenosphere approximation was dropped during the port to MPI.

Coupling the Earth Model to the Ice Sheet Model

Paul Johnston's sea-level program `calsea` requires as inputs an ice load history, the Earth model in the form of previously calculated Love numbers and the locations and times at which to calculate sea-level change.

The ice sheet model and the sea-level program cannot be run concurrently, since the entire ice loading history is required. Instead, the ice sheet model is run with one of the simple isostatic approximations to obtain an initial loading history. The sea-level program is then used to acquire the Earth's response to the previously calculated ice load. In principle, the ice sheet should be recomputed with the new topography as input to get full interaction with the spherical Earth model. This is not done because of the long run-times of `calsea`. Results from the spherical Earth model and the ELRA model are compared in Chapter 3.3.1.

The ice sheet model (`ism`) calculates the ice sheet evolution given forcing functions and a bedrock topography. The ice loading has to be projected onto a latitude-longitude grid. This coordinate transform has to conserve ice volume. The program `sl_files` transforms the ice thickness distribution and produces all the input files required by the spherical Earth model (`calsea`). The sea-level program then calculates the new bedrock topography adjusted to the ice load. The influence of far-field ice sheets can be included by specifying further ice sheets. The final program in the tool chain, `read_sl`, reads in the new topography and projects it onto a Cartesian grid so that it can be read in by the ice sheet model. Figure 2.10 shows a flow diagram of one iteration of the ice sheet model coupled to the full spherical Earth model. Originally, I envisaged that the procedure, outlined above, could be repeated until both the ice sheet and topography evolution converge. However, runtimes of all three programs, `sl_files`, `read_sl` and `calsea`, are very long because of the data format required by `calsea`. All three programs spend most of their run time doing disk I/O. Because of the excessive run time, only a single iteration was calculated. Ideally, the sea level program, `calsea`, would be rewritten to support netCDF I/O in order to optimise I/O operations.

2.3.3 Testing and Comparing the Isostasy Models

The default Earth model parameters used in the intercomparison experiments are summarised in Table 2.2. The parameters used for the simple approximations should be viewed as effective parameters that produce results similar to those from the spherical Earth model. However, these parameters do not necessarily reflect the actual characteristics of the Earth. Elastic parameters and the density of the Earth used for the spherical Earth model are based on the Preliminary Reference Earth Model (PREM) of [Dziewonski and Anderson \(1981\)](#). Furthermore, the spherical Earth is decomposed into one shell for the lithosphere and two shells for the mantle. Thicknesses, H_L and H_{um} , and viscosities, ν_{um} and ν_{lm} , of these shells are based on best-fitting parameters determined by [Lambeck \(1993c\)](#). The subscripts L, um and lm denote Lithosphere, upper mantle and lower mantle, respectively.

The effects of the different isostasy models can be most easily seen by loading the Earth models with a very simple test load. The test configuration used here consists of a square model region with a size of 2400km×2400km and surface

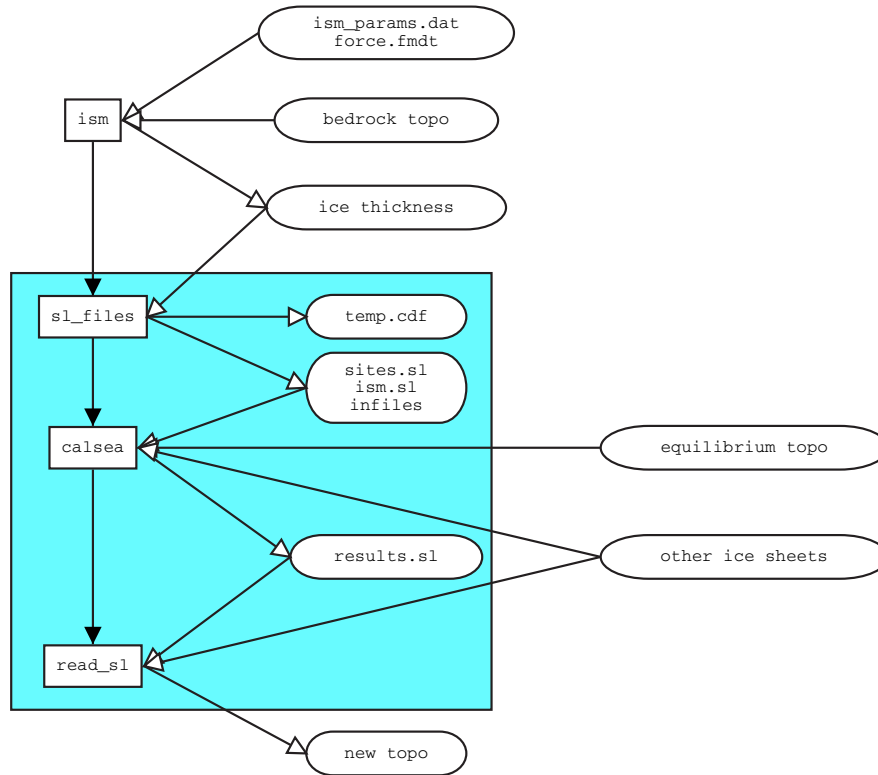


Figure 2.10: Programs (square boxes) and files (rounded boxes) needed to run the ice sheet model (`ism`) coupled to the sea-level program (`calsea`). The programs and files inside the box could be combined into a single program optimising I/O usage and thus run-time.

elevation $h = 1000\text{m}$. A disk load with radius 300km and a thickness of 1000m was placed at the centre of the modelled region and instantaneously removed after 25ka . Sea-level change (i.e. $\Delta\zeta(t, \mathbf{r}) = h(t, \mathbf{r}) - h(0, \mathbf{r})$) was calculated (i) at the centre of the load (Location 1), (ii) close to the edge of and inside the load (Location 2), (iii) close to the edge of and outside the load (Location 3) and (iv) well outside the test load (Location 4) (see Fig. 2.11). Additionally, the same loading configuration was used with the spherical Earth model. Results from experiments with the different isostasy models are shown in Figure 2.12.

As expected, the temporal behaviour of the isostatic adjustment is controlled by how the mantle is treated, whereas the geometry is controlled by the lithosphere. In the case of a fluid mantle, the system reaches isostatic equilibrium instantaneously. The discontinuities in results from the spherical Earth model reflect the initial elastic and gravitational response of the Earth to a changing load.

Model	Lithosphere	Mantle	Densities
Rigid Earth	—	—	—
LLFA	local	fluid	$\rho_{\text{ice}} = 910\text{kgm}^{-3}$ $\rho_{\text{ast}} = 3000\text{kgm}^{-3}$
ELFA	$D = 10^{25}, L_r = 173\text{km}$	fluid	
LLDA	local	$D_a = 10^8$	
ELDA	$D = 10^{25}, L_r = 173\text{km}$	$D_a = 10^8$	
LLRA	local	$\tau = 3000\text{a}$	
ELRA	$D = 10^{25}, L_r = 173\text{km}$	$\tau = 3000\text{a}$	
Spherical Earth	$H_L = 65\text{km}$	$H_{\text{um}} = 670\text{km}$ $\nu_{\text{um}} = 4 \cdot 10^{20}\text{Pas}$ $\nu_{\text{lm}} = 1 \cdot 10^{22}\text{Pas}$	PREM

Table 2.2: Earth Model parameters used.

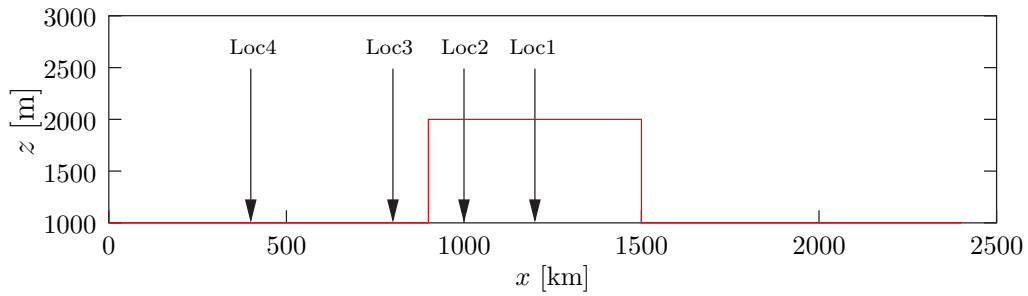


Figure 2.11: Disk load with a radius of 300km and thickness 1000m is centred on a square model region. The four locations where sea-level change is recorded are also indicated.

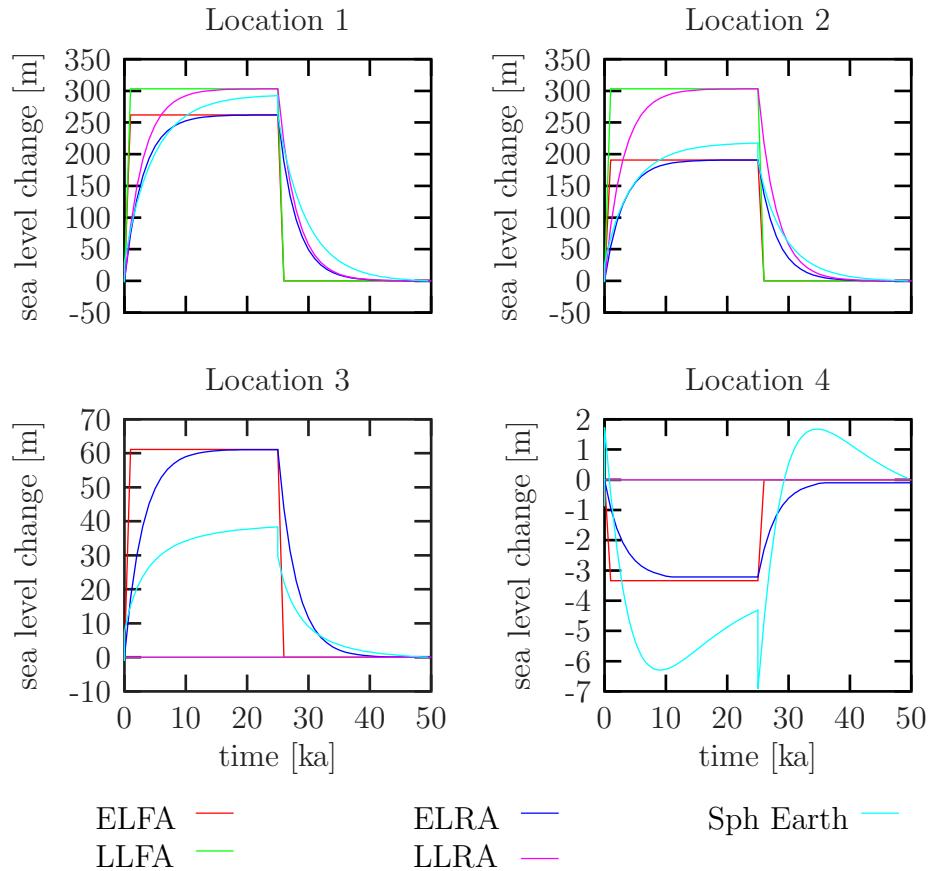


Figure 2.12: Sea-level change as a function of time for different test locations and isostasy models.

Parameters for the ELRA model

Following [Le Meur and Huybrechts \(1996\)](#), the parameters for the elastic lithosphere/relaxed asthenosphere model were examined in more detail. ELRA parameters D , ρ_{ast} and τ were selected from a range of values. The ELRA output was then compared with the output of the spherical Earth model by calculating the root mean sum of squared residuals, Δ :

$$\Delta(D, \rho_{\text{ast}}, \tau) = \frac{1}{N} \left(\sum_{i=1}^N (h_{\text{Earth}_i} - h_{\text{ELRA}_i}(D, \rho_{\text{ast}}, \tau))^2 \right)^{\frac{1}{2}}, \quad (2.52)$$

where N is the number of data points.

The loading interval was chosen so that both Earth models had time to reach equilibrium. After equilibrium had been reached the load was removed instantaneously. The models were then run until they return to the initial bedrock configuration. The geometry of the deflection is entirely controlled by the elastic

lithosphere parameters D and ρ_{ast} . The first experiment calculated the differences when both models are in equilibrium, Δ_{equil} , for $N = 361$ points along a line between the origin of the disk load and a point outside the load.

The second experiment calculated the differences between models, Δ_{hist} at time steps throughout the loading history and at the four locations described above.

These two experiments were repeated for disk loads with different radii. Table 2.3 shows the parameter sets for which the differences are smallest for load disks of radius $r = 200\text{km}$, 300km , 400km , 500km . Figure 2.13 shows how the differences vary on orthogonal slices through the parameter space containing the minima.

disk radius	D	ρ_{ast}	Δ_{equil}	D	ρ_{ast}	τ	Δ_{hist}
200km	0.23E+25	3460.	0.0750	0.25E+25	3360.	4100.	0.1128
300km	0.22E+25	3400.	0.1035	0.22E+25	3400.	4150.	0.1782
400km	0.25E+25	3340.	0.1817	0.25E+25	3340.	3950.	0.2339
500km	0.27E+25	3360.	0.2077	0.26E+25	3380.	3750.	0.2859

Table 2.3: Earth model parameter sets with the best fit and their corresponding errors for different disk loads.

The reason for the dependence of the best-fitting parameters on load size is not obvious. I would expect that larger loads sample the Earth’s mantle at a greater depth than smaller loads. The effective density should, therefore, increase with radius. However, the Earth model incorporates a two layer mantle. So the time constant τ should also be dependent on load size. The combination of effects of changing load size on responses of the two layers of the mantle might produce a more complicated pattern, such as the one in Figure 2.13. Certainly, the parameters resulting in the best-fitting solution are not very realistic and should be viewed as effective parameters.

The experiment was repeated with the averaged best-fitting Earth parameters (see Table 2.4). Experiments using this parameter set are referred to as ELRA2. Figure 2.14 shows the differences $H_{\text{Earth}}(t) - H_{\text{ELRA}}(t)$ for the four locations mentioned above. The most prominent features are the large spikes when the load is placed on and removed from the Earth’s surface. These errors are due to the fact that the simple ELRA model contains neither an instantaneous elastic response, nor does it calculate the gravitational effects of the load.

2.4 Summary

Glacier physics and approximations used in order to be able to solve the equations numerically have been discussed. The use of the shallow ice approximation, although standard practise, might lead to problems at boundaries with large horizontal gradients, for example where the flow regime changes between sheet

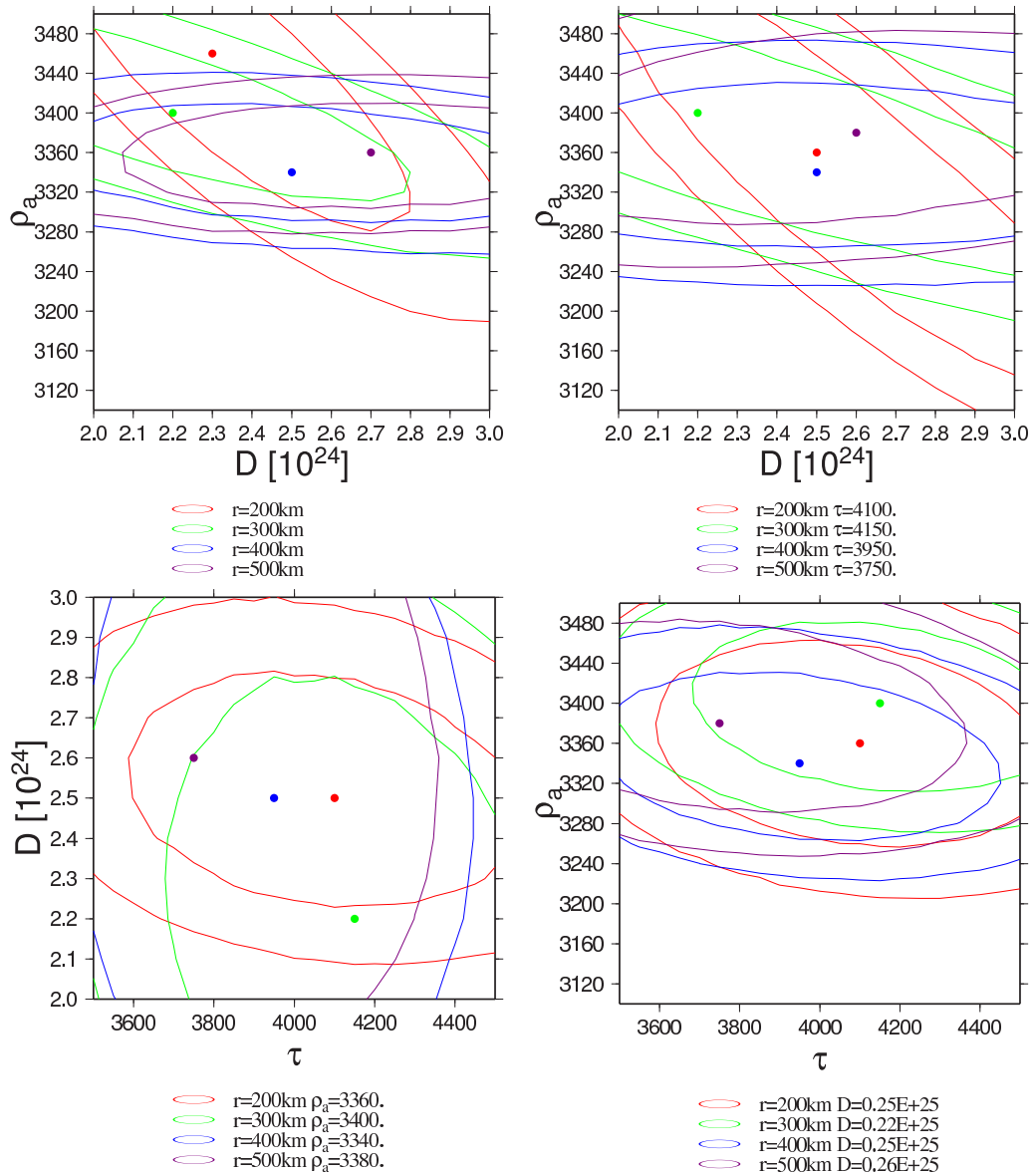


Figure 2.13: Plots of the variation of the mean difference between the full Earth model and the ELRA approximation as a function of the parameters D , ρ_{ast} and τ for test loads with differing radii. The upper left panel shows the relative error for one particular time, when the bedrock adjustment is in equilibrium. The other 3 panels show the differences with time. The dots indicate where the minimum errors are and contours are at 5cm and 10cm.

parameters	disk radius	Δ_{equil}	Δ_{hist}
$D = 0.24\text{E}+25$	200km	0.09	0.12
$\rho_{\text{ast}} = 3380.0$	300km	0.11	0.19
$\tau = 4000.0$	400km	0.20	0.25
	500km	0.23	0.30

Table 2.4: Averaged best fitting parameters and their associated errors.

flow and ice streams or at the ice margin. The resolution of the model of 10km takes the shallow ice approximation to its limits. The formulation of the model could be improved, at the cost of additional complexity, by including longitudinal stresses.

The plane Earth, elastic lithosphere/relaxed asthenosphere approximation is preferred for practical reasons. Run times of the coupled ice sheet/spherical Earth models are prohibitively long. However, considering the approximations taken regarding the equivalent sea-level curve (considered an input) and neglecting the influence of far-field ice sheets, the ELRA approximation is considered to be fit for the purpose of simulating the development of the Fennoscandian and British ice sheets in this project. On the other hand, file I/O of the spherical Earth model could be substantially improved, thus improving run times and possibly allowing the use of the more complex model.

Throughout this project, I was able to access ever faster computer systems allowing me to perform ever more detailed simulations and to increase the total number of experiments. The simulations presented in the following three chapters always reflect the then available processing power and insights gained from previous simulations. In consequence, some simulations could be improved substantially given faster computers and more experience.

This project also required the development of numerous data analysis, processing and visualisation tools. These tools are not described in this thesis, which focuses on the scientific advances achieved. However, the resulting images can be seen throughout the following chapters and permit an evaluation of the adequacy of these tools.

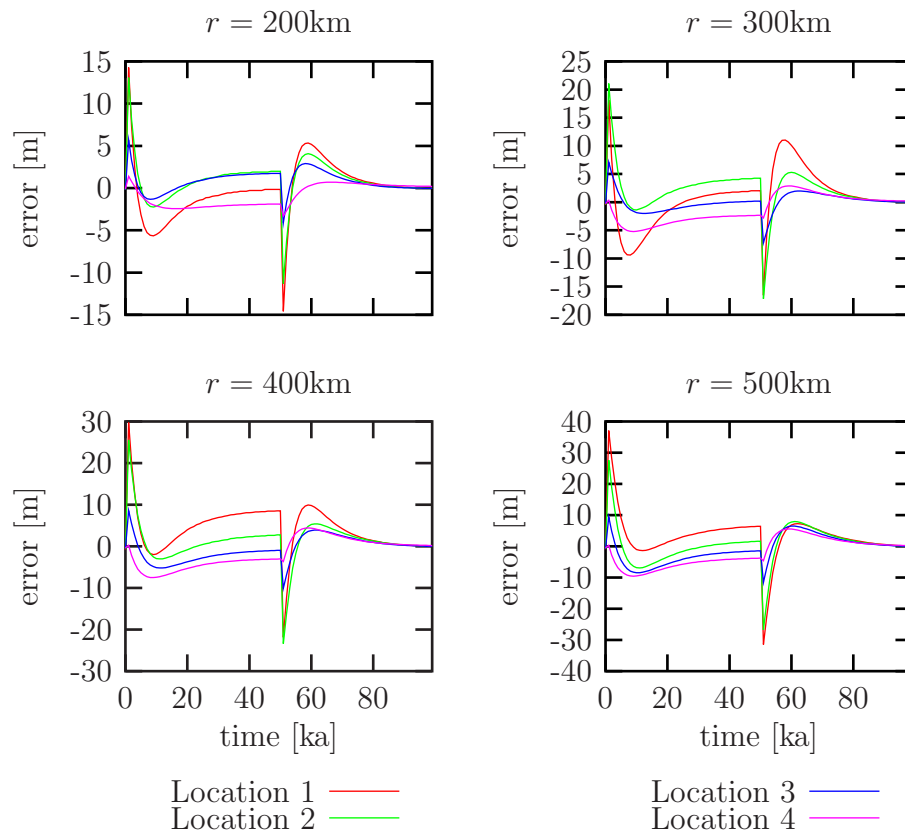


Figure 2.14: Differences between the spherical Earth model and the ELRA approximation as a function of time for four different locations.

Chapter 3

Fennoscandian Experiment

The ultimate purpose of this project was to simulate the past British ice sheet and to characterise the development of a possible future British ice sheet under specific climatic assumptions. However, as noted previously, the British ice sheet poses particular problems. The geometry of the past British ice sheet is complicated because the topography gave rise to independent glaciation centres and the geological evidence for its pattern of fluctuations is poor. This relative complexity and limitations of field data makes it less suitable when developing model features and assessing the ability of the model to represent real ice sheets. It is hard to know if any complex modelled ice behaviour is reflective of an unstable simulation, or whether it is reflective of the complexity of the real world. It is far better to develop and evaluate the model for a better known and simpler context. I have, therefore, chosen to simulate the Fennoscandian ice sheet because of the simpler topographic framework and the quality of geological evidence of past fluctuations against which to evaluate model behaviour. I later apply the climate driver of the Fennoscandian model to the British ice sheet, using the reasonable assumption that these forcing functions should be similar and that the model has had a degree of testing.

Geological evidence for the past Fennoscandian ice sheet has been studied in great detail (e.g. [Denton and Hughes, 1981](#); [Sejrup *et al.*, 1994](#); [Boulton *et al.*, 2001b](#); [Mangerud *et al.*, 2002](#)). Its past form and behaviour has also been considered by inverting relative sea-level data (e.g. [Lambeck *et al.*, 1998](#); [Tushingham and Peltier, 1991](#)) and using three-dimensional ice sheet models (e.g. [Arnold and Sharp, 2002](#); [Charbit *et al.*, 2002](#); [Boulton *et al.*, 1995](#)). The simulations reported here were undertaken in a similar way to those of [Boulton *et al.* \(1995\)](#). The model was forced using a global sea-level change record based on SPECMAP, a temperature record and a time series describing the vertical movement of the equilibrium line altitude (ELA). The global sea-level change record and the temperature record were taken as known inputs. The ELA forcing function was then adjusted in such a way that the model output agreed with a geological reconstruction of the ice margin along a profile through the south-western part of the ice sheet. This procedure is outlined in [Figure 3.1](#) and

described in greater detail below. The parameter set used to obtain this result thus constitutes a standard model run on which all subsequent experiments were based and relative to which they were assessed.

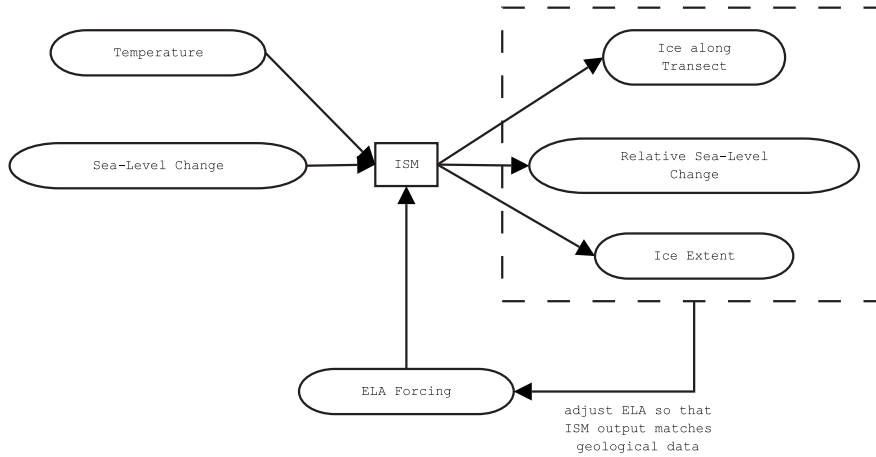


Figure 3.1: Schematic plan illustrating the setup of the past European ice sheet experiment. Rounded boxes indicate data sets, ISM is the ice sheet model and the data sets within the dashed box are model outputs.

Ultimately, ice sheet models can be used to integrate different forms of glaciological evidence to form a single, coherent picture of past glaciations. It should be possible to design an inversion procedure that automatically selects the parameter set leading to the best fit with different forms of geological evidence. Unfortunately, the full inversion problem cannot be addressed directly because current computing power is too limited to permit a comprehensive search of the complete parameter space. A first step toward systematically exploring the parameter space is to modify key model parameters and compare the results with an unmodified model run (the standard run). The effects of surface temperature, sliding parameterisation and ice flow parameters are explored in Section 3.3.

3.1 Model Setup

3.1.1 Topography

Initially, it was important to provide the ice sheet model with a suitable representation of the ice sheet bed throughout Fennoscandia. There are a number of global Digital Elevation Models (DEMs) available with an appropriate resolution. Two well-researched and widely used ones are ETOPO5¹ ([Data Announcement 88-MGG-02, 1988](#)) and GTOPO30², available for free download.

¹<http://www.ngdc.noaa.gov/mgg/global/setopo.html>

²<http://edcdaac.usgs.gov/gtopo30/gtopo30.html>

Both ETOPO5 and GTOPO30 use geographic (longitude, latitude) coordinates with a grid spacing of 5 arcminutes and 30 arcseconds, respectively. GTOPO30 does not contain bathymetry. The approach used was, therefore, to interpolate ETOPO5 onto a 30" grid and then merge it with GTOPO30 using GMT³, a suite of free programs that permits the manipulation and display of scientific data. The regular longitude/latitude grid was projected onto an Albers Equal Area Conic Projection. The irregular coordinates obtained are then resampled to a regular Cartesian grid with a resolution of 10km on the same projection. The Albers Equal Area projection is commonly used to map areas of large East–West extent in mid–Latitudes. The projection is defined by a central meridian, the latitudes of two standard parallels and the origin. The scale of the projection is true along the standard parallels, smaller between them and larger outside. The projection being equal area has the important property of preserving mass advection across the grid without correction. All European experiments were run with a resolution of 10km. Figure 3.2 shows a plot of the European bedrock topography used in the model.

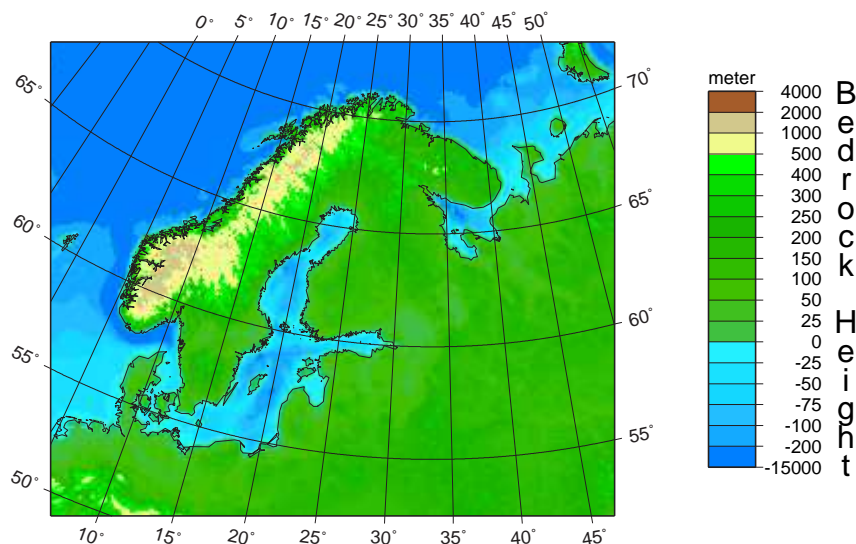


Figure 3.2: Bedrock topography model with a resolution of 10km used in the experiments reported herein.

3.1.2 Temperature Forcing

Surface temperatures play an important role in controlling the evolution of an ice sheet since ice flow is temperature–dependent. Climate is not directly modelled, and consequently a time dependent description of the three–dimensional temperature field is required. Temperatures are assumed to decrease with

³<http://gmt.soest.hawaii.edu/>

increasing elevation according to the atmospheric lapse rate, b , which is assumed to be constant in time and space. The resulting two-dimensional temperature field is further simplified by assuming no longitudinal dependence. Two time and latitude dependent temperature models were developed and used in the subsequent experiments.

Temperature Model for the Standard Experiment

Palaeoclimatic data in Europe during the last glacial cycle is discontinuous in time. It was therefore necessary to use temperature estimates during the last glacial cycle. The palaeotemperatures were estimated, on the basis of proxy data, at 21 locations along the transect indicated in Figure 3.3. Boulton *et al.* (2001c) based long-term palaeoclimatic variations on the Lac du Bouchet record. This information was then interpolated along the transect by estimating maximum and minimum temperatures during each marine isotope stage for each location along the transect. Each temperature estimation contains 651 points every 200

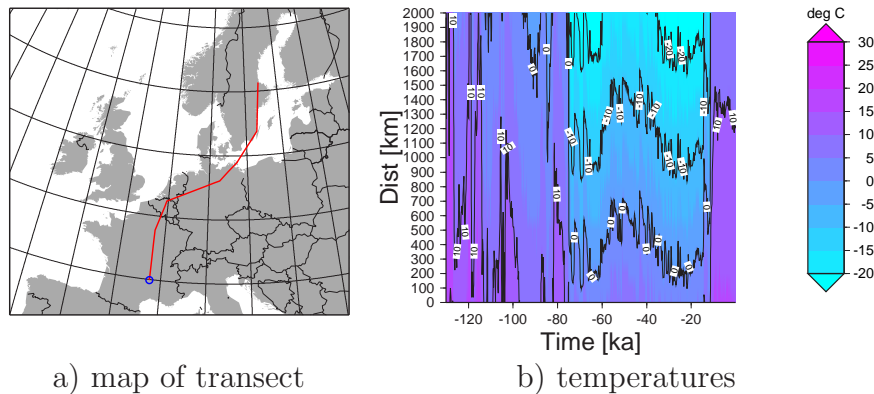


Figure 3.3: Map of Europe indicating the temperature transect (red line) and the location of the Lac du Bouchet (blue circle) (a) and the corresponding temperature data (b) derived from the interpretation of proxy data (Boulton *et al.*, 2001c).

years starting 100 years ago and going through to 130ka ago. In total there are 13671 temperature reconstructions. Distances along the transect are converted to geographic locations using a number of known locations along the transect and interpolation.

These temperature data points varying in time and with latitude were used as the basis of a model of sea-level temperature variations. Two models were formulated. In the first model, Equation (3.1a), the latitudinal variation of temperature remains fixed in time but the whole temperature field is raised and lowered as a function of time. In the second model, Equation (3.1b), the shape of the temperature variation with time is also allowed to vary. The two models

of sea-level temperature, T , varying with latitude, λ , are:

$$T_{\text{Model 1}}(\lambda, t) = a + b\lambda + c\lambda^2 + d\bar{T}(t), \quad (3.1a)$$

$$T_{\text{Model 2}}(\lambda, t) = a(t) + b(t)\lambda + c(t)\lambda^2, \quad (3.1b)$$

where a , b , c , and d are parameters and $\bar{T}(t) = (\sum_i^{N_\lambda} T_i)/N_\lambda$ the average temperature at time t and N_λ is the number of temperature reconstructions at time t . The first model was extended to give Model 2, which also allows the shape of the temperature field to vary with time. The constant coefficients of Model 1 become time dependent in Model 2. The time-dependent average temperature of Model 1 is integrated into the parameter $a(t)$ of Model 2. The input temperature data plotted as a function of latitude (Fig. 3.4) clearly shows two distinct climate modes. On this basis, the second model, Equation (3.1b), was expected to perform better.

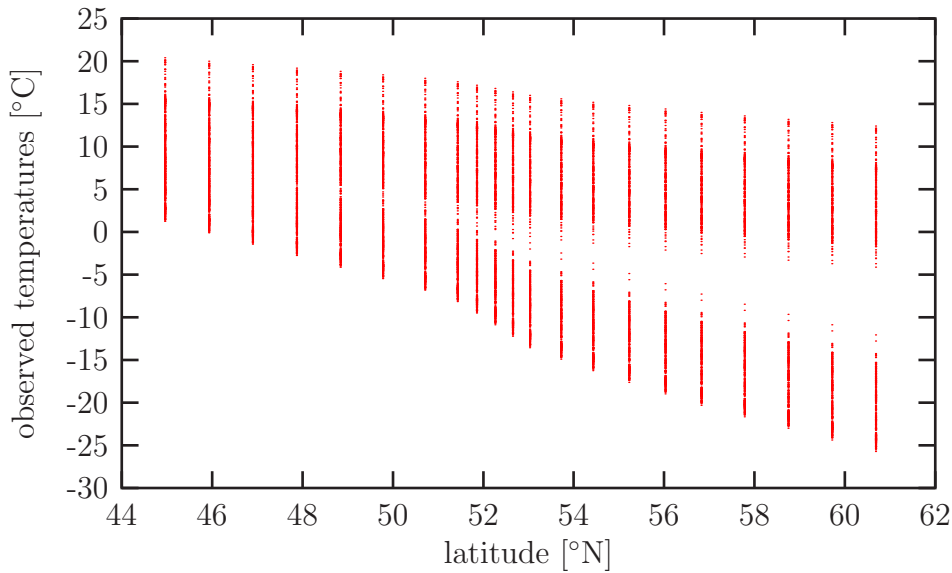


Figure 3.4: Input temperature data plotted as a function of latitude. This plot suggest two distinct temperature modes.

The model parameters were chosen so that the difference between the inferred temperature field and the modelled temperatures was minimised in a least squares sense. This was done using a design function

$$\chi^2 = \sum_i^N \frac{(T_i - T_{\text{Model}}(\lambda_i, t_i))^2}{\sigma_i}, \quad (3.2)$$

where the summation is over all N reconstructed values T_i each of which is associated with a latitude λ_i and time t_i . The quantity χ^2 was minimised using the Levenberg–Marquardt algorithm for non-linear least square fitting (Press *et al.*,

1992). The standard errors associated with the temperature reconstructions are unknown. The standard error is, therefore, assumed to be constant ($\sigma_i = \sigma$) and initially taken to be an arbitrary value ($\sigma = 1$). σ is then recalculated once a best-fitting model is found,

$$\sigma^2 = \sum_i^N \frac{(T_i - T_{\text{Model 1}}(\lambda_i, t_i))^2}{(N - M)}, \quad (3.3a)$$

where N is the total number of reconstructions and M the number of parameters. The standard error of the time-dependent model (3.1b) is also time-dependent, i.e. the standard error is calculated for each time, t_i :

$$\sigma(t_i)^2 = \sum_i^{N'} \frac{(T_i - T_{\text{Model 2}}(\lambda_i, t_i))^2}{(N' - M)}, \quad (3.3b)$$

where N' is the number of reconstructions at time t_i . Obviously, this approach does not allow an independent assessment of goodness-of-fit. However, it does give some indication of how well the model performs.

The best fit is obtained by the parameter set shown in Table 3.1; average temperatures as a function of time are shown in Figure 3.5. Figure 3.6 shows best fitting parameters of the second model. The second model performs better as expected. The first model gives a standard error, as calculated using (3.3a), $\sigma = \pm 2.65^\circ\text{C}$, whereas the maximum standard error of the second model is $\sigma_{\text{max}} = \max(\sigma(t_i)) = \pm 1.03^\circ\text{C}$.

$a = 70.81$	$c = 3.55 \cdot 10^{-3}$	$\chi^2 = 96227.335$
$b = -1.53$	$d = 1.0$	$\sigma = \pm 2.65^\circ\text{C}$

Table 3.1: Parameters for temperature Model 1 leading to the best fit with the observations.

It is interesting to note that the time-dependent parameters affecting the temperature gradient of Model 2, $b(t)$ and $c(t)$, appear to change on different time scales from that on which the offset, $a(t)$, changes (see Fig. 3.6). In fact, $a(t)$ contains both time scales. The most likely explanation for this behaviour is that the fitting process revealed the interpolation process adopted by Boulton *et al.* (2001c).

The second model, Equation (3.1b), is able to account for time-dependent temperature gradients. This capability is reflected in the better fit of the second model. Figures 3.7 and 3.8 show plots of transect versus modelled temperatures and the distribution of residuals (reconstructed - modelled temperatures) for both models. The residuals of the first model are not normally distributed (Fig. 3.7). This indicates that the model is not particularly well suited. We expected this, however, considering the two distinct climate modes shown in Figure 3.4.

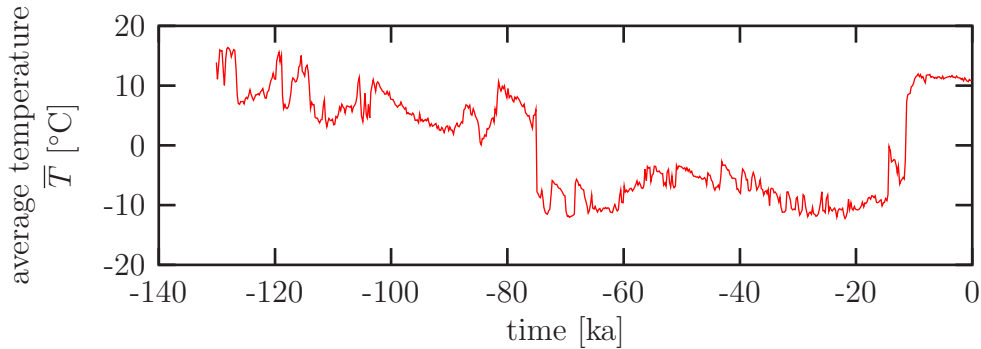


Figure 3.5: Spatially averaged input temperatures as a function of time.

New Temperature Forcing

Running the standard experiment it became clear that temperatures used were too low. Two new temperature reconstructions based on the GRIP core, S-10 and S-15 (Johnsen *et al.*, 1992) together with a time dependent gradient were therefore used:

$$T(\lambda, t) = a(t) + b(t)\lambda. \quad (3.4)$$

Figure 3.9 shows temperatures as a function of time at 60°N using the new data, S-10 and S-15, and the standard model.

In conclusion, a more complex temperature model is required to faithfully reconstruct the pattern of variation in time and space inferred on the base of proxy data. In turn, this is reflective of the changing latitudinal distribution of energy balance through the last glacial cycle.

3.2 ELA Forcing and Ice Sheet Evolution

The evolution of the ice sheet is found by solving the ice thickness continuity equation, Equation (2.1). This equation can be solved only when the mass balance is known. The mass balance is the sum of ice accumulation and ablation. The physical processes underlying ice accumulation and ablation are complicated and, whereas some aspects are relatively well understood, e.g. radiation balance in ablation, other processes, such as snowfall, are much harder to estimate. Moreover, taking a ‘physically based’ approach to reconstructing ablation and accumulation would require input data on timescales of less than a day. Reconstructing seasonally-averaged accumulation/ablation balances for long time periods over the whole area requires a simpler approach. The mass balance approximation used here follows a commonly used approach where the integrated surface mass balance is assumed to vary with altitude, relative to the ELA (see Section 2.1.2).

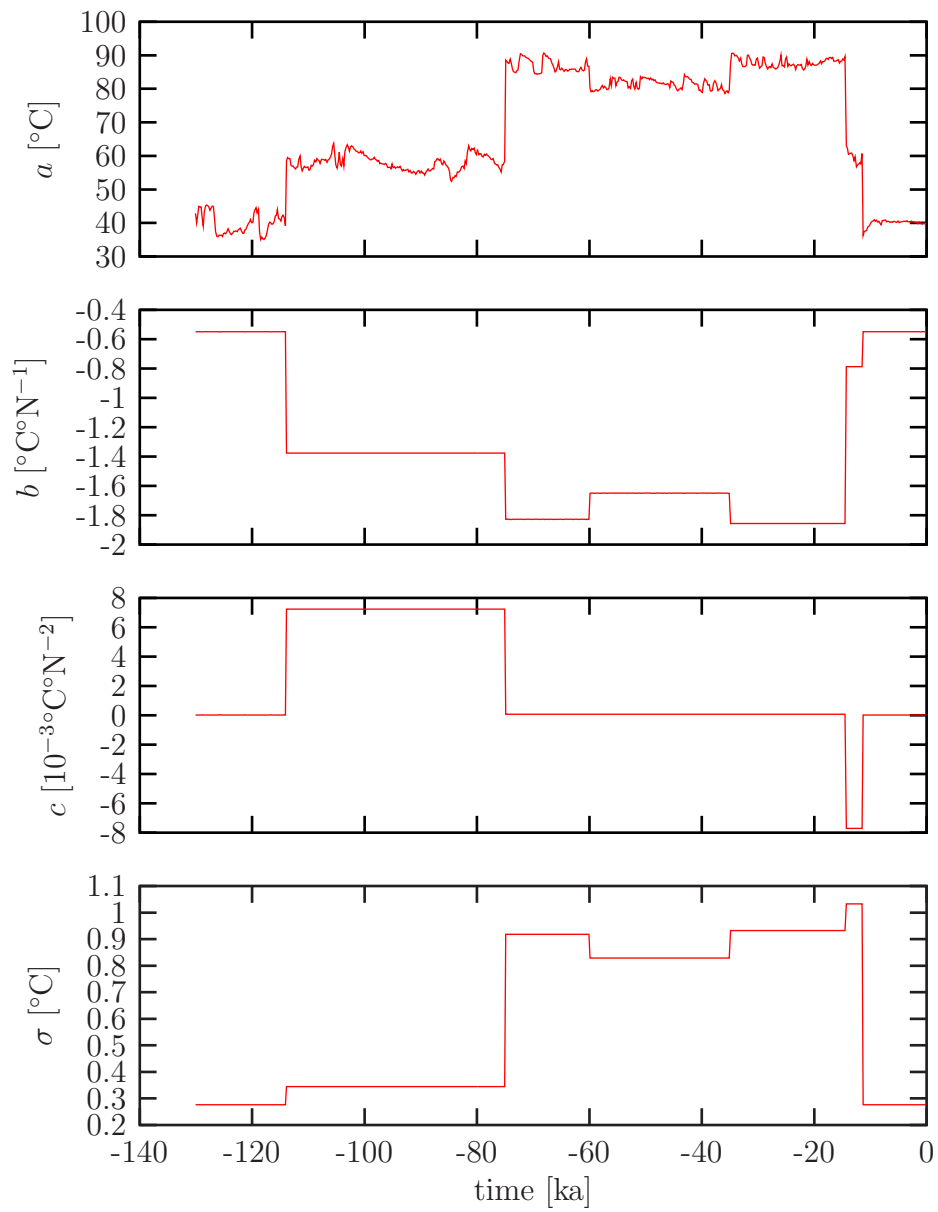


Figure 3.6: Parameters of Temperature Model 2 and calculated standard error, $\sigma(t_i)$, as a function of time.

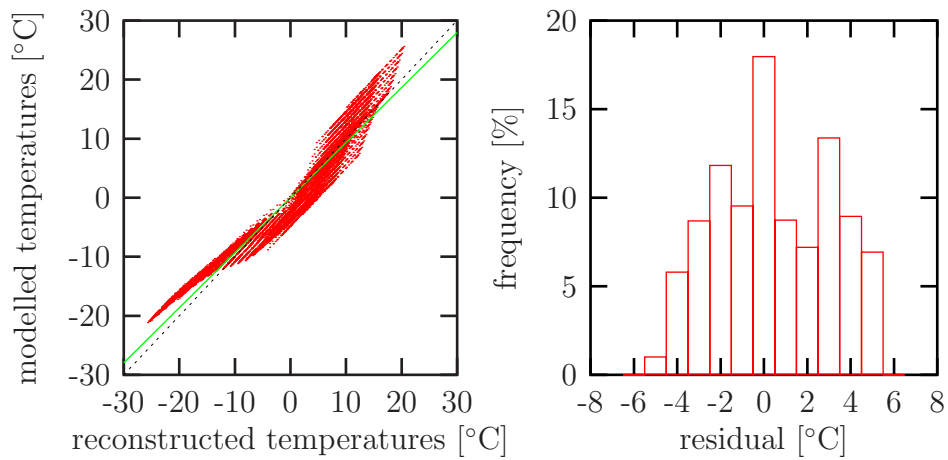


Figure 3.7: Modelled temperatures plotted against palaeoclimatic reconstructions and histogram of residuals for Temperature Model1. The line indicates the best fitting line with intercept 0.012 ± 0.022 and slope 0.932 ± 0.002 . The dashed line is $y = x$.

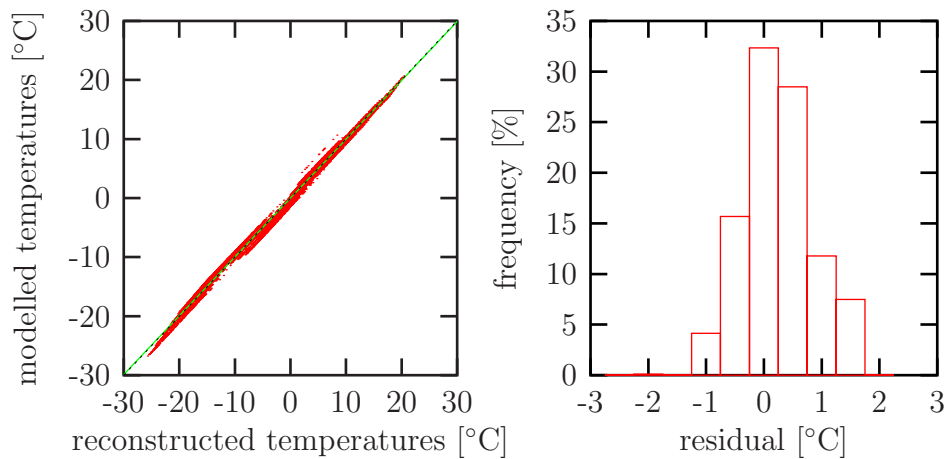


Figure 3.8: Modelled temperatures plotted against palaeoclimatic reconstructions and histogram of residuals for Temperature Model 2. The line indicates the best fitting line with intercept 0.0006 ± 0.0053 and slope 0.9964 ± 0.0005 . The dashed line is $y = x$.

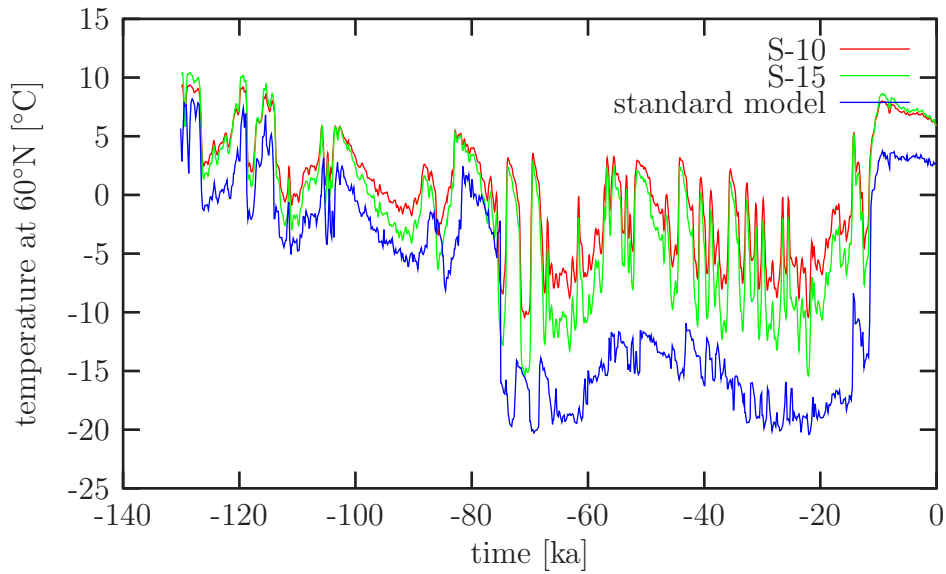


Figure 3.9: Temperatures at 60°N using the standard model and models S-10 and S-15 derived from the GRIP core.

This approximation is further simplified by assuming that the mass balance variation relative to the ELA and the ELA distribution in space are constant in time. The ice sheet model can then be driven by moving the entire ELA field upward or downward. The ELA forcing function was adjusted so that the modelled ice margin matched with its geological reconstructions along the transect shown in Figure 3.10. This particular transect was chosen for historical reasons: Boulton and Payne (1992a) used it for a 2D modelling study. Also, this transect was later used by Boulton *et al.* (1995, 2001b). The geological reconstructions are based on the reconstruction of the past European ice sheet by Mangerud (1991) and agree with the reconstruction of Lundqvist (1986a,b). The transect approximates a flow line except for the Southern part where ice flow was potentially deflected westward due to ice stream activity. The divergence of ice flow is important in 2D studies since it cannot be simulated using a 2D flowline model. However, the precise location of the transect and whether it is a flowline is not important here, since the ice sheet model is three-dimensional and can be used to reconstruct ice margins along any transect.

A simple, piecewise in time, fitting procedure was adopted (see Fig. 3.11). Ice sheet evolution along the transect was considered at 5ka intervals, starting at $t_0 = -120\text{ka}$ (assumed to be the beginning of the last glacial cycle). During each interval, the ELA forcing was adjusted until the model output compared well with the reconstruction. The quality of the fit was assessed by visual inspection. The next time interval was then processed until the entire glacial cycle had been simulated. Figure 3.12A shows the resulting ELA forcing function. There are a number of shortcomings with the fitting approach outlined above:

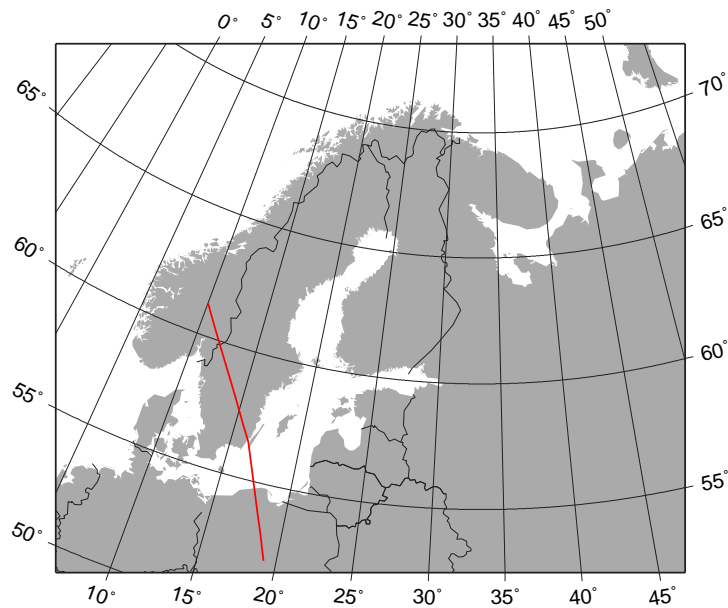


Figure 3.10: Flowline through Europe.

1. The fitting process is manual and takes a long time. Unfortunately, the way the model works at present, does not allow for an automated fitting process.
2. The fitting process is not objective. For example, the sum of residuals could be used as a measure for the goodness of fit. However, this measure would only be useful if different ELA models were to be compared with each other.
3. The fitting process only involves the reconstruction of one flowline in the southwestern part of the Fennoscandian ice sheet.
4. In addition, a number of different fitting metrics could be employed, if suitable data were available.

The ice sheet model was run using the standard (Equation (3.1b)), S-10 and S-15 temperature models. Resulting ice evolution is shown in Figure 3.12B,C. Figure 3.12D shows that all three temperature forcing functions produce ice sheets of similar extent along the chosen transect except for the period between about 50ka and 30ka BP during which the S-10 and S-15 ice sheets are smaller. Overall, the ice sheet with the standard temperature forcing covers an area that is larger than the S-10 ice sheet and smaller than the S-15 ice sheet (Fig. 3.12C). This is also reflected in the plots of ice volume (Fig. 3.12B). This behaviour is expected since the temperature affects ice flow and thus ice thickness (see Section 3.3). It is interesting to note that both the ice extent and the position of the ice margin along the transect for the standard, S-10 and S-15 models are very similar during the build-up towards and at the last glacial maximum. In itself, this indicates one

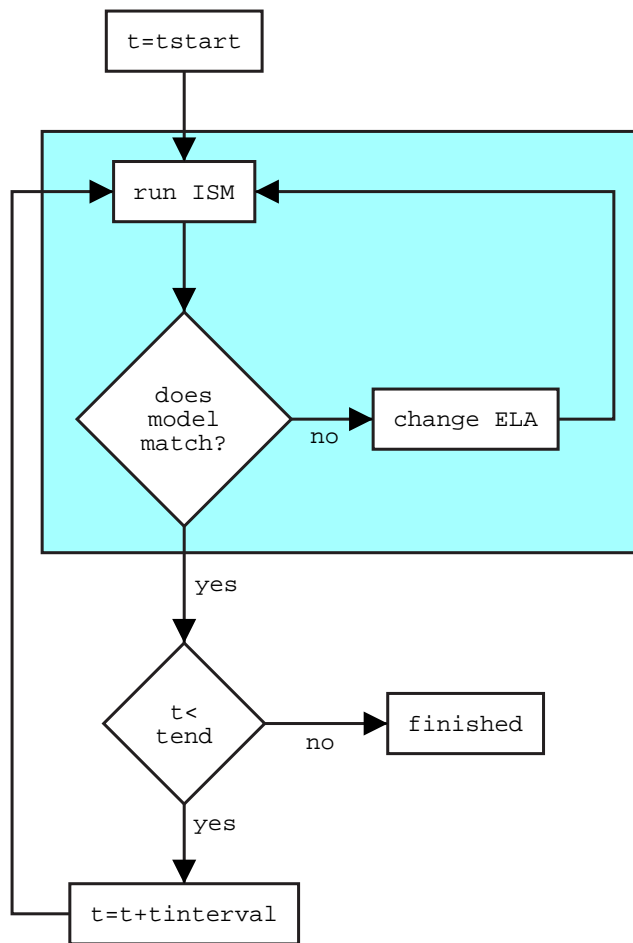


Figure 3.11: Flow diagram illustrating the fitting procedure adopted to determine the ELA forcing function. t_{start} and t_{end} are the determine the modelled period.

of the problems of using a single metric (ice extent) as the basis for an inversion procedure.

Snapshots of the S-10 model run are shown in Figures 3.13 and 3.14. In particular, Figure 3.14 also shows the ice extent of the ICE-4G model, which is based on an inversion of relative sea-level data (Peltier, 1993). The most notable difference between the ice sheet models developed here and ICE-4G is that our LGM occurs at -17ka, whereas the ICE-4G LGM occurs at -21ka. The extent of ice in the S-10 model at -17ka is comparable to the extent in the ICE-4G model at -21ka. The decay of both the standard and S-10 models after the LGM is very different from the decay of the ICE-4G model. In particular, the ice sheet model produces an ice sheet that is too large in its northeastern part as compared with the ICE-4G model. These differences are also very noticeable when comparing the calculated relative sea-level changes with the observations (Section 3.5).

These mismatches occur because only one metric (the transect shown in

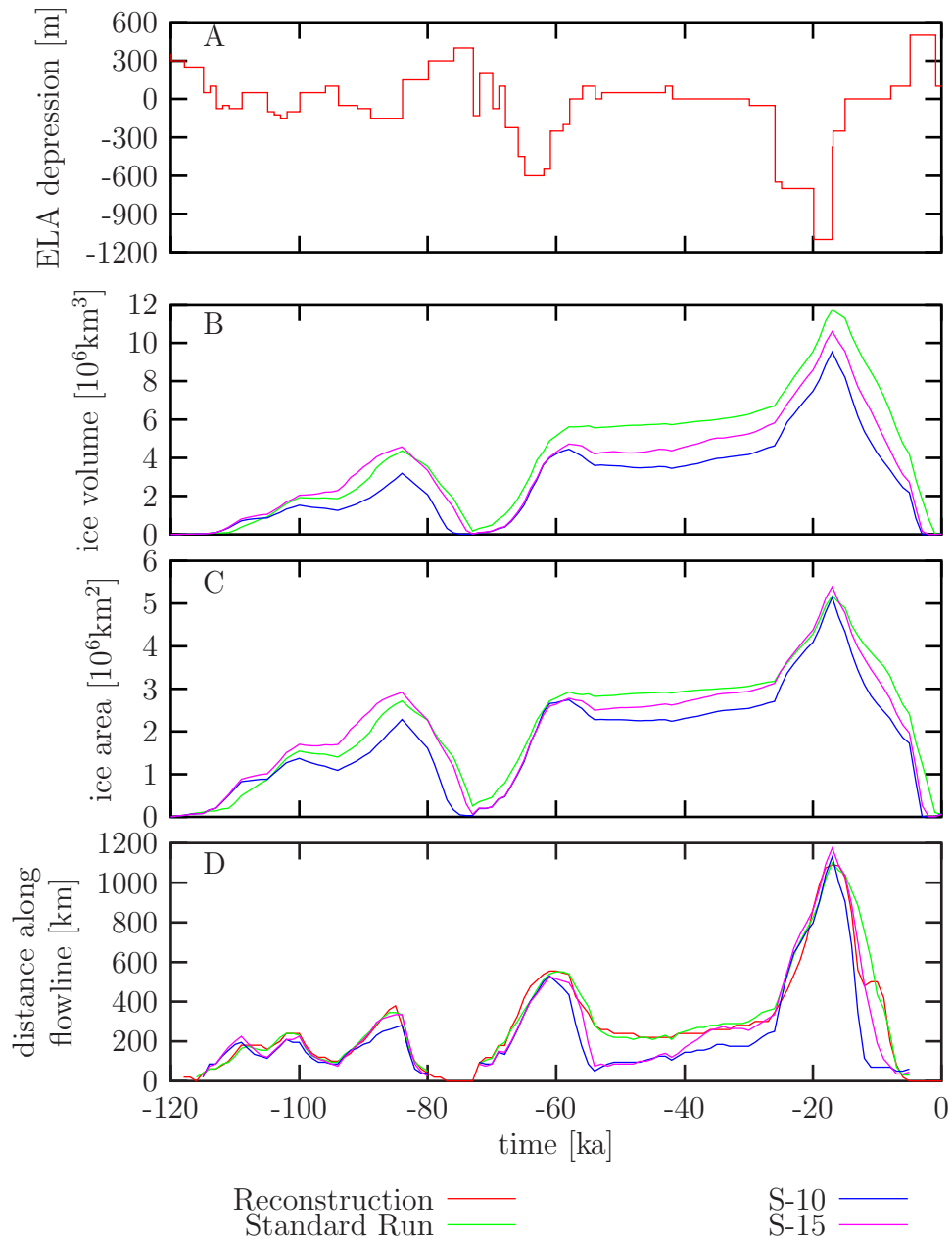


Figure 3.12: Mass balance forcing (A) and position of the ice margin along the transect shown in Figure 3.10 for the standard, S-10 and S-15 model runs (D). Panels (B) and (C) show ice volume and ice area as a function of time.

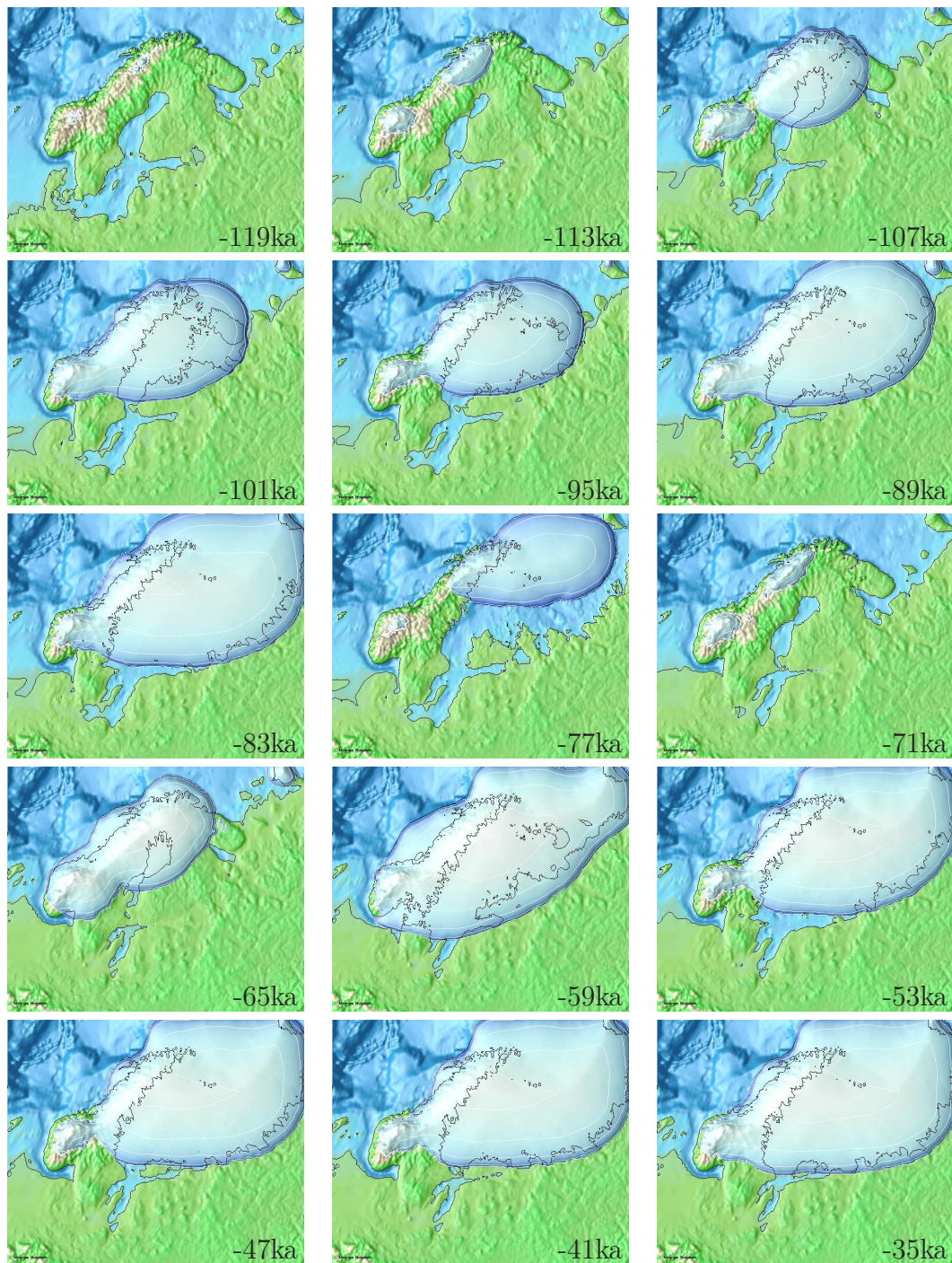


Figure 3.13: Evolution of the S-10 ice sheet model. Snapshots are every 6ka, from -119ka to -35ka.

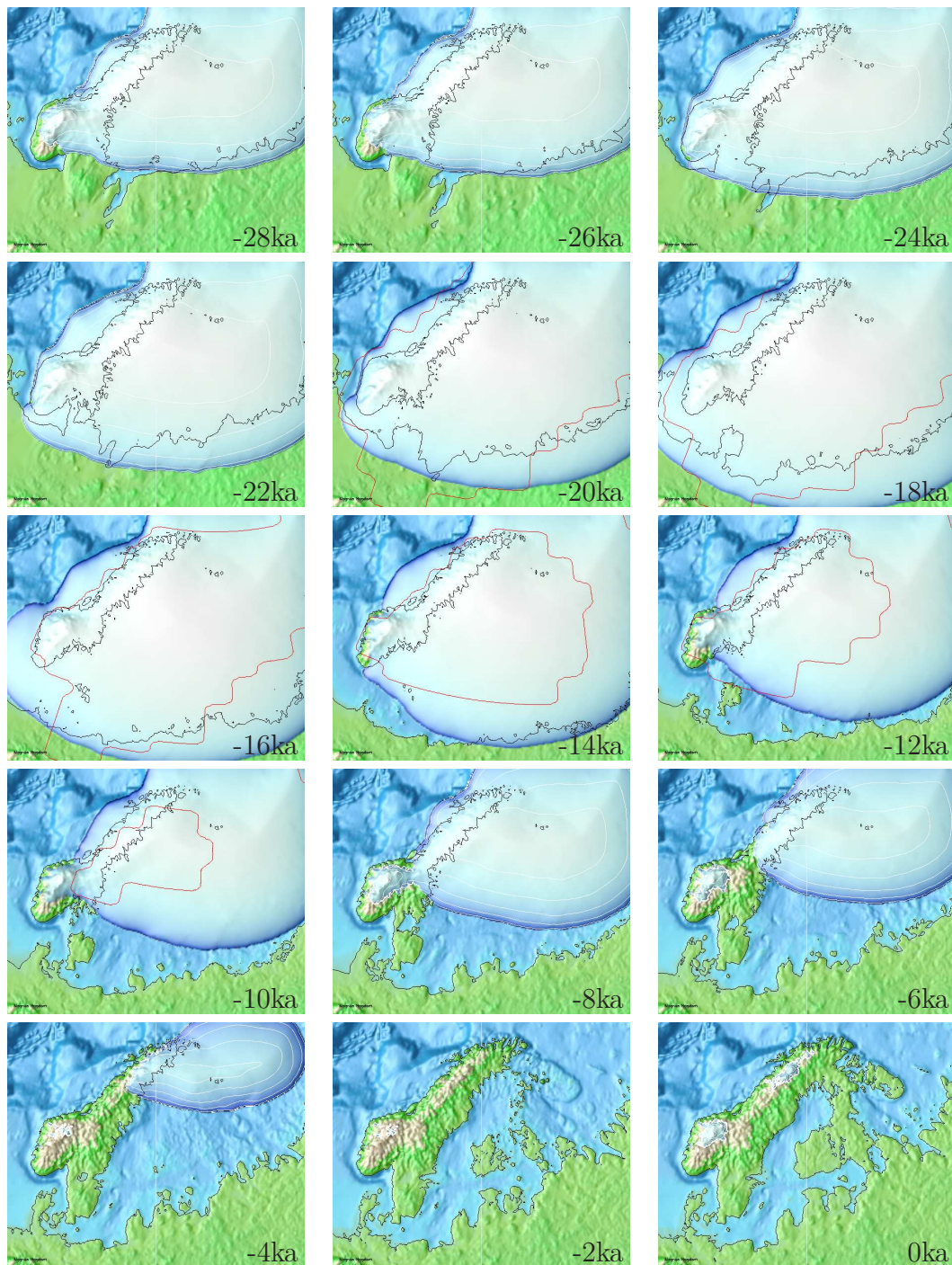


Figure 3.14: Evolution of the S-10 ice sheet model. Snapshots are every 2ka, from -28ka to 0ka. The red outlines indicate the extent of the ICE-4G model (Peltier, 1993). Note that the ICE-4G model has a resolution of $1^\circ \times 1^\circ$.

Fig. 3.10) was used, leaving the northeastern part of the modelled region unconstrained. Ideally more transects would be added. However, it was decided to move on and apply the forcing to the British Isles since climatic conditions in northeastern Europe are unlikely to influence climate in Western Europe.

3.3 Ice Sheet Parameters

The behaviour of the ice sheet model is determined by the values of a set of parameters. These parameters can be model forcing functions and boundary conditions varying in space and time, such as the temperature or mass balance fields or single values such as the sliding parameter which alter the global physical behaviour of the model. Palaeodata, such as temperature reconstructions, can be used as a guideline for suitable parameter values. The biggest problem is the potential for equifinality of model solutions with relatively limited data sets against which to evaluate its performance. For instance, increasing the ease of sliding might produce an extended margin which could also be achieved by increasing the mass balance. The ice sheets produced might be different in other respects such as temperature and surface elevation, but this is not discriminatory if only a single metric such as ice extent is used as a guide to model inversion. Temperature reconstructions are also, for instance, limited to a few sites and the uncertainties associated with the data can be very large. It is common to use modern analogues to augment palaeoclimatic data. In spite of issues of equifinality, it should be possible to choose at least one set of model parameters so that the results match geological data. Doing a full inversion is currently impossible because of the large computing resources needed and the paucity of data for comparison. Therefore, the parameter space cannot be sampled systematically. However, the relative importance of the model parameters can be assessed by running the model with different parameter values and then comparing the results with the available palaeodata.

The most important forcing function is the mass balance, since it determines the shape and size of the ice sheet directly. The simulation with the S-10 temperature curve was repeated with the ELA forcing moved by $\pm 50\text{m}$ and $\pm 100\text{m}$ to illustrate this dependence. Figure 3.15 shows the resulting variation in ice sheet size. Differences in ice sheet evolution are most pronounced during the first half of the simulated glacial cycle when ELA variations are relatively small. During the build-up to and at the simulated LGM, all five ELA forcing variations produce ice sheets of similar size suggesting that a) the ELA depression does not need to be very severe to produce an LGM sized ice sheet; and b) the simulated LGM ice sheet is far from equilibrium.

The temperature field also affects the shape of the ice sheet, since ice flow is temperature dependent. A cold ice sheet is relatively stiff and can support large ice thicknesses. On the other hand, a warm ice sheet is less stiff and ice flows faster, drawing down the ice surface. Internal ice deformation is also controlled by

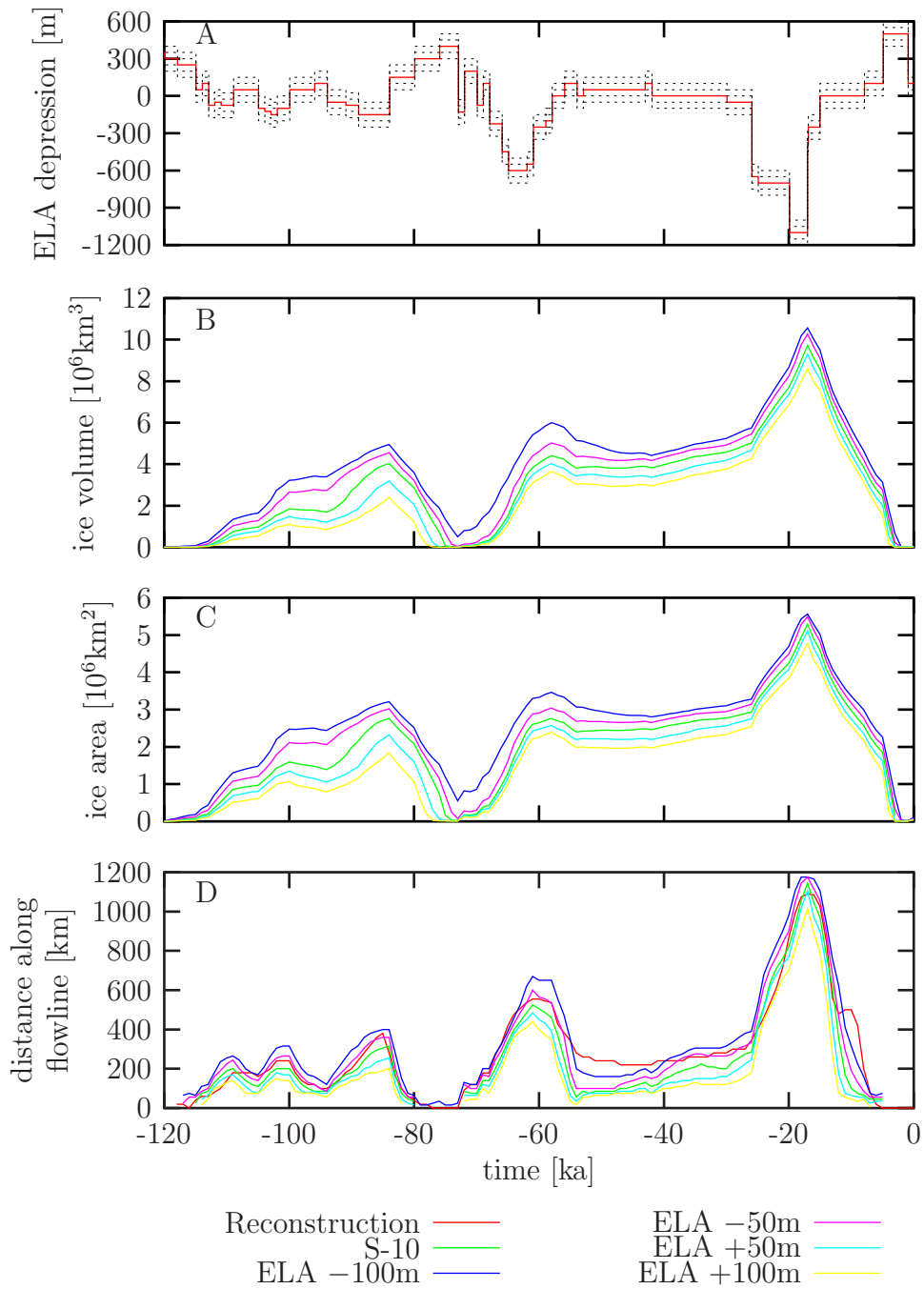


Figure 3.15: Mass balance forcing (A) and position of the ice margin along the transect shown in Figure 3.10 for the S-10 simulation and for simulations with the ELA moved by $\pm 50\text{m}$ and $\pm 100\text{m}$ (D). Panels (B) and (C) show ice volume and ice area as a function of time.

the ice flow enhancement parameter, f , in Equation (2.4). The parameterisation of basal décollement also affects the velocity distribution and thus the shape of the modelled ice sheet. Topography controls ice accumulation and location of ice streams since ice streams will preferentially follow bedrock troughs.

A set of experiments was designed to explore the effects of the values of key parameters on ice sheet evolution. The effects of using different isostasy models are discussed in Section 3.3.1. The effects of parameters affecting ice flow are explored in Section 3.3.2.

3.3.1 Isostatic Response

The ice sheet model was run with two different sets of parameter values for the elastic lithosphere/relaxed asthenosphere (ELRA) isostatic adjustment model. The first parameter set was based on the parameters used by Le Meur and Huybrechts (1996). The second parameter set (ELRA2) was found by fitting the ELRA response to the response of the full spherical model for disk loads of radius $r = 200\text{km}$, 300km , 400km , 500km (see Section 2.3.3). Table 3.2 summarises the ELRA parameters used. The ice sheet model was forced using the standard ELA forcing function, Figure 3.12, and the S-10 temperature curve, Figure 3.9. Isostatic adjustment due to the simulated ice sheet evolution was then calculated using the spherical Earth model.

ELRA	ELRA2
$D=10^{25}$	$D=0.24 \cdot 10^{25}$
$L_r=173\text{km}$	$L_r=92\text{km}$
$\rho_{\text{ast}}=3000\text{kgm}^{-3}$	$\rho_{\text{ast}}=3400\text{kgm}^{-3}$
$\tau=3000\text{a}$	$\tau=4000\text{a}$

Table 3.2: Earth model parameters used in Section 3.3.1.

Figure 3.16 shows the average isostatic adjustment, $\overline{\Delta\zeta^{\text{iso}}}(t) = \frac{1}{N} \sum_{i=0}^N \Delta\zeta_i^{\text{iso}}(t)$, where N is the number of grid nodes. The modelled isostatic response using the ELRA2 approximation matches the corresponding full spherical model much better than the ELRA model. The maximum average discrepancy occurs at the LGM and is about 25m for the ELRA2 and 60m for the ELRA model.

Figure 3.17 shows relative sea-level change and bedrock and ice surface elevation along transect E–F, shown in Figure 3.19 for times $t = -18\text{ka}$ and $t = -110\text{ka}$. The isostatic response of both ELRA models is too small underneath the centre of the ice sheet.

Both ELRA models produce similar ice sheet evolutions. In terms of ice dynamics, it does not seem to matter which particular Earth model is used. However, the ELRA models compute sea-levels which differ from the spherical Earth model by as much as 100m. This is not surprising, as the spherical Earth

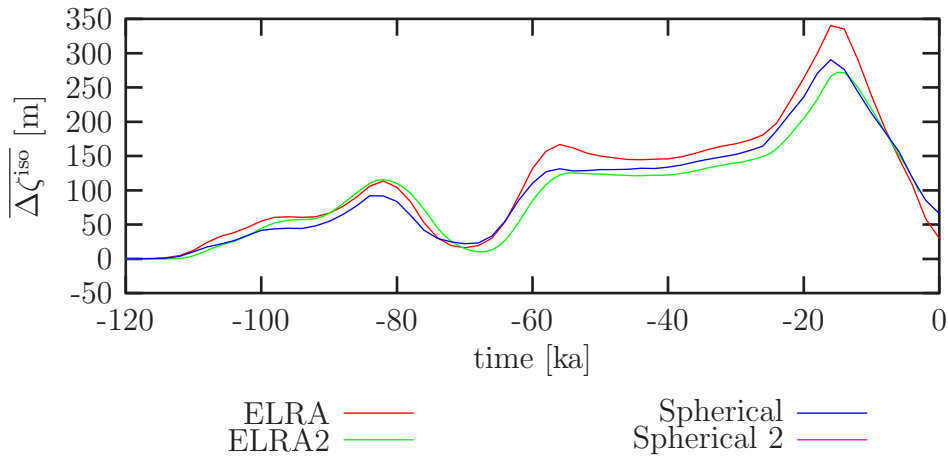


Figure 3.16: Average isostatic response of the Earth models as a function of time.

model includes processes that are not resolved by the ELRA approximation. However, isostatic adjustment, for the purpose of simulating the evolution of an ice sheet, can be simulated using a simple Earth model like the ELRA approximation, as the ice sheet evolution is relatively insensitive to the Earth model and its parameters used. On the other hand, the spherical Earth model should be used for calculating the final set of sea-level change (SLC) data, for the purpose of comparing the simulation with geological evidence, since it better captures physical processes of the real world.

Note that the simulation using the ELRA parameter set was affected by a software bug that resulted in the hydro-isostatic component being calculated with the wrong sign. Figure 3.17 shows this effect clearly where SLC over areas below sea-level, calculated by the ELRA model is positive when it should be negative. The model was not rerun since the ELRA2 parameter set was used subsequently.

3.3.2 Parameters Affecting Ice Flow

Surface temperatures, basal décollement and the flow law enhancement parameter affect ice flow and thus the shape and size of the ice sheet. Three variations of the S-10 model were run for 50ka to explore their effects on ice sheet evolution: i) the surface temperatures were reduced by 10°C for the *cold experiment*, ii) the model was run without basal décollement (*no sliding*) and iii) the ice flow parameter was reduced from 80 to 20 (*reduced speed-up*). Figure 3.18 shows the resulting ice volume and area covered by ice as a function of time. Figure 3.19 shows the ice sheet extent of the four models after 35ka when the modelled ice sheet reaches its maximum size for the modelled period.

Both Figure 3.18 and 3.19 clearly show that the fast flowing ice sheet (the

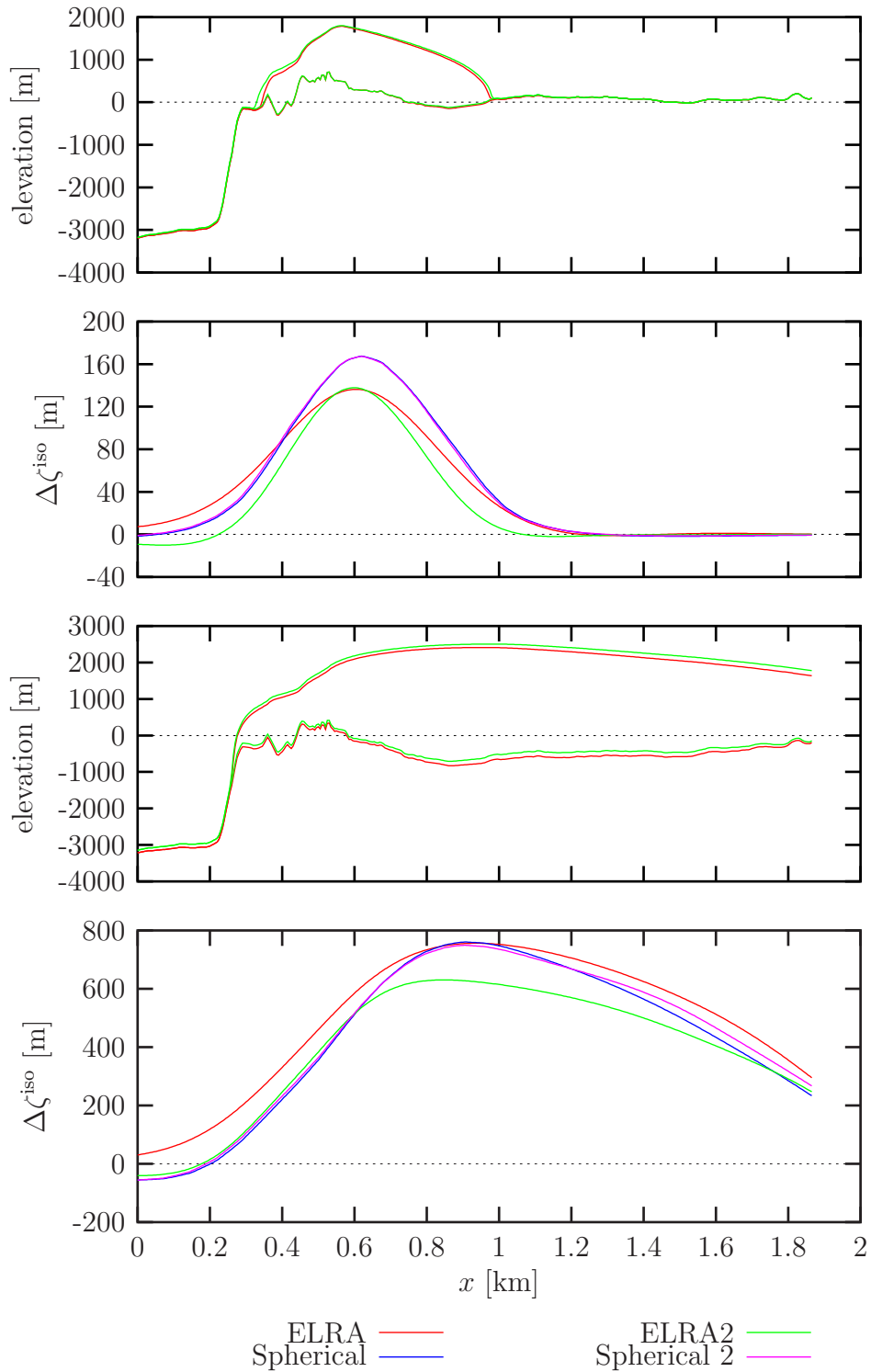


Figure 3.17: Plots of ice surface and bedrock elevation and isostatic adjustment along along transect E—F, shown in Figure 3.19 for times $t = -18\text{ka}$ and $t = -110\text{ka}$.

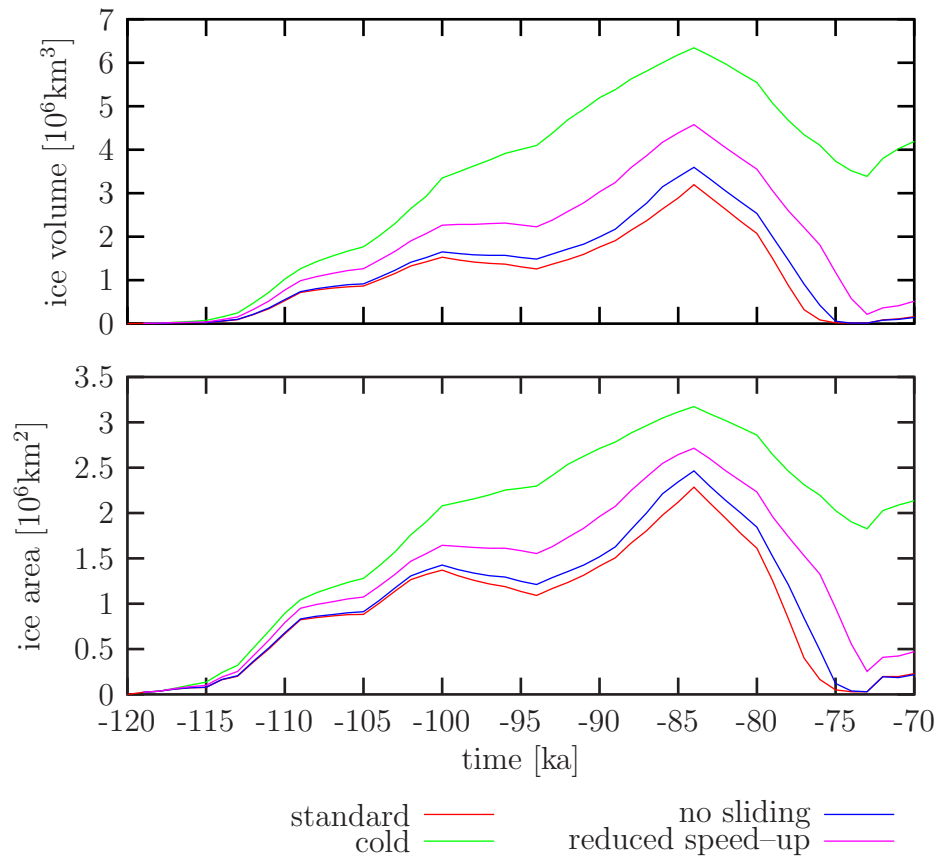


Figure 3.18: Area covered by ice and the corresponding ice volume as a function of time for the standard, cold, no sliding and reduced speed-up experiments.

S-10 model) is smallest. The ice sheets become larger with increasing stiffness. This might seem to be counter-intuitive, but this behaviour can be explained by the interaction between the ice sheet shape and mass balance. Ice sheets are conveyor belts transporting ice from high elevations where it accumulates, to low elevations, where it ablates. A fast-flowing ice sheet is very effective at transporting ice to areas where it is lost to the ice sheet thus lowering the surface profile. Slow flowing ice sheets, in particular the cold model, are less effective and therefore grow thicker. More ice accumulates at high altitudes allowing the stiff ice sheet to grow faster by accumulating more ice. Figure 3.20 shows ice bed and ice surface elevations along the three transects indicated in Figure 3.19. Finally, Figures 3.21 and 3.22 show snapshots at -85ka of the ice surface velocity and basal temperature fields of the four experiments. All four models show regions of relatively fast ice flow. These ice streams are discussed in more detail in the next section.

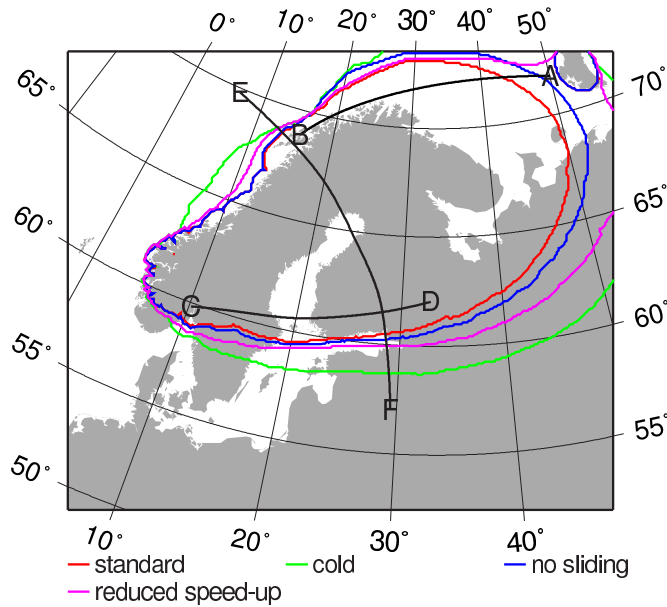


Figure 3.19: Ice sheet extent at -85ka for the standard, cold, no sliding and reduced speed-up models.

3.4 Ice Streams

Ice flow within ice sheets can be divided into: i) relatively stagnant sheet flow and ii) fast-flowing stream flow. Ice streams are important dynamic features of ice sheets because the majority of inland ice is discharged through ice streams and outlet glaciers in spite of their limited areal coverage. It has been estimated, for example, that 90% of the accumulated ice of the Antarctic ice sheet is drained through ice streams that cover only 13% of the coastline (McIntyre, 1985). Flow within ice streams (up to 800ma^{-1}) is typically two orders of magnitude faster than sheet flow ($\sim 10\text{ma}^{-1}$). The large ice flux of streams affects ice sheet configuration, drainage basins and ice divide location (Stokes and Clark, 2001). Ice streams discharge large amounts of fresh water into the oceans, thus affecting the thermal and saline circulation (Bennett, 2003). They also have the potential to affect atmospheric circulation patterns through their control of the overall thickness of an ice sheet.

In order to be able to model ice streams, it is important to understand why they form and how they operate. Ice streams are thought to fall into two groups: i) ice streams with strong topographical control and ii) ice streams with weak topographical control, also known as pure ice streams (Payne, 1999).

The reason for the existence of the first group can be easily seen. Thicker ice occupying troughs in the bedrock topography experiences larger gravitational driving stresses. Furthermore, thicker ice is warmer due to the increased insulation effect and, therefore, flows faster. This effect is further enhanced by a positive

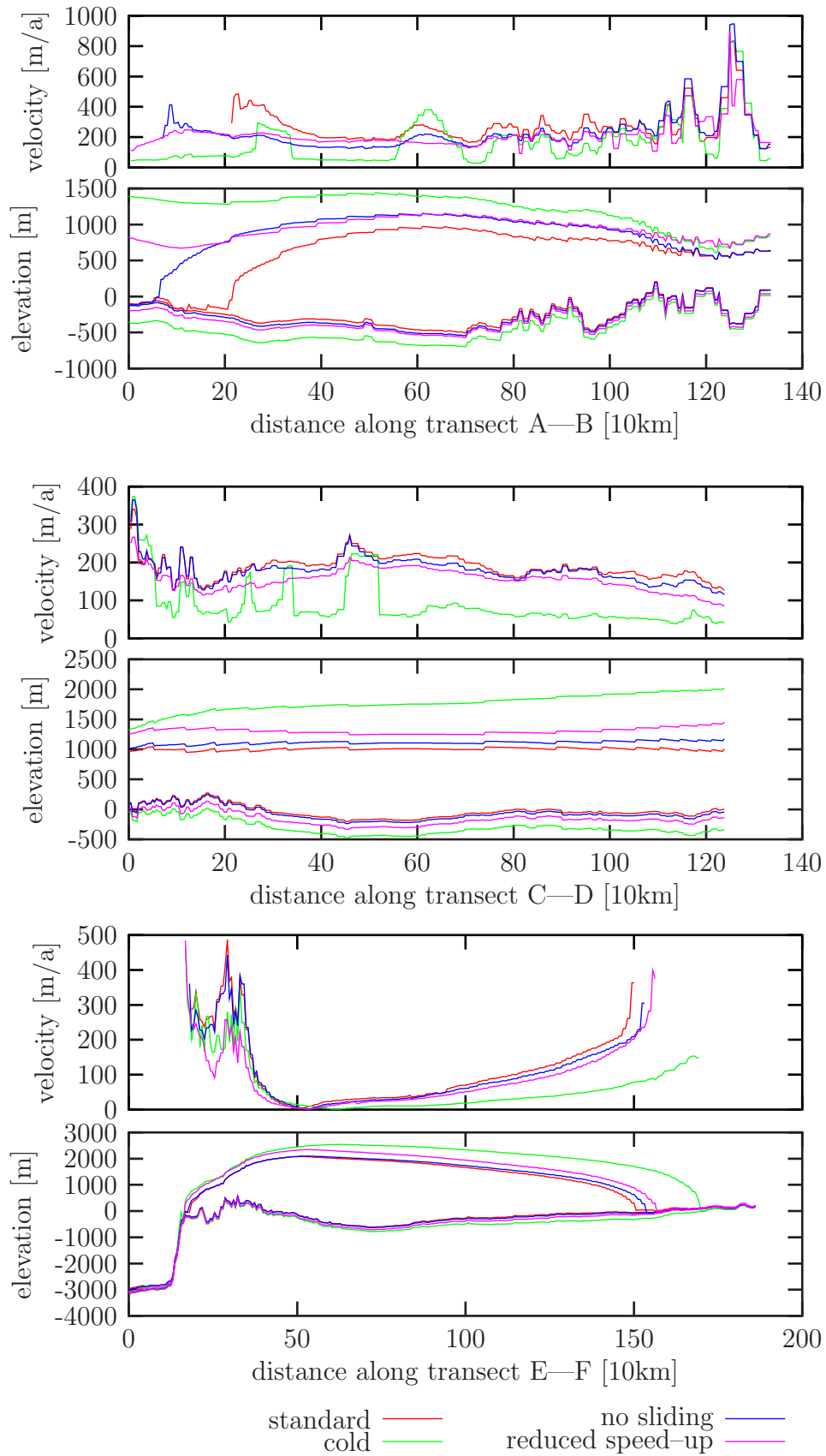


Figure 3.20: Ice bed and surface elevation and surface velocities along transects A—B, C—D, E—F at -85ka. The location of these transects is shown in Figure 3.19.

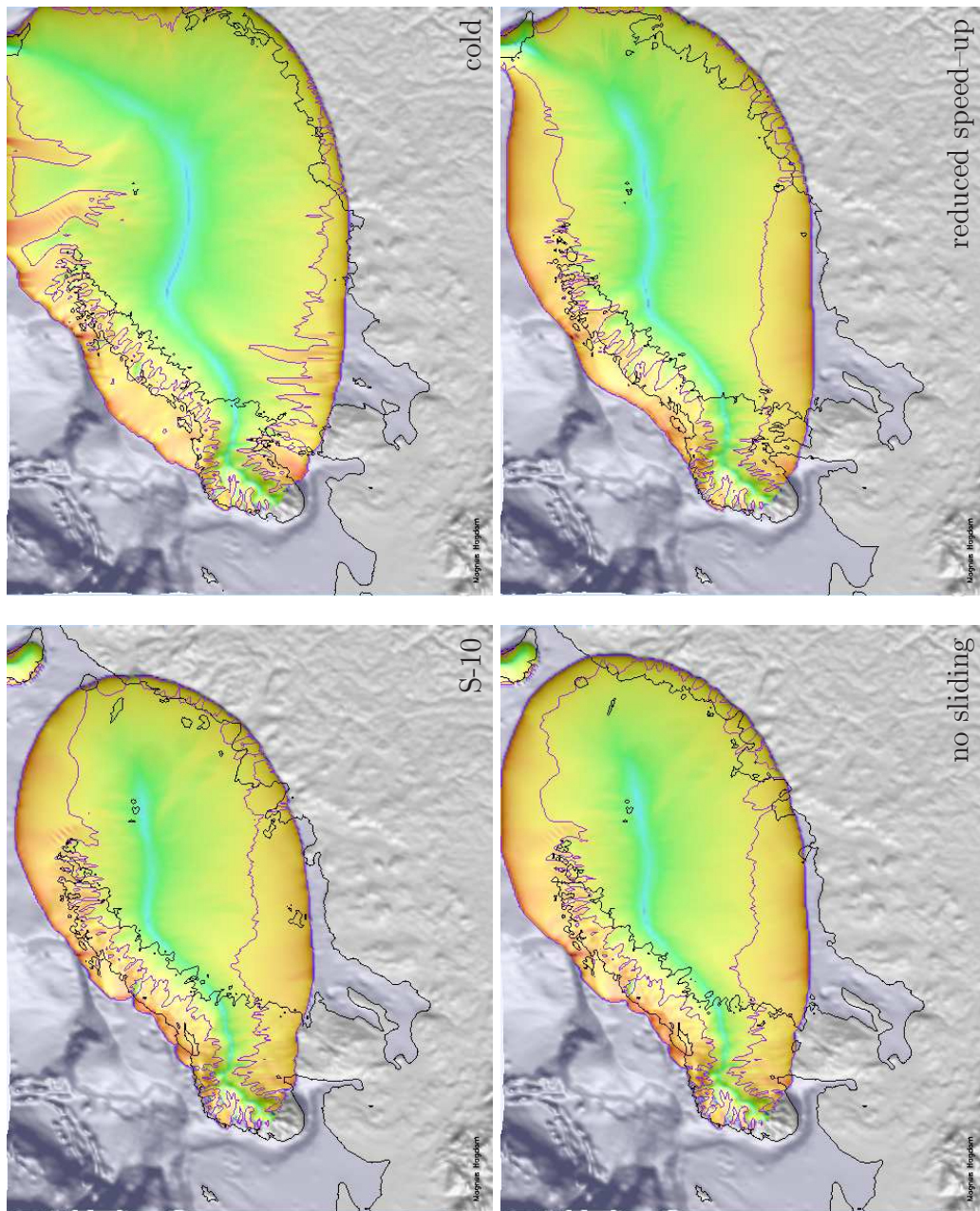


Figure 3.21: Surface velocities on a log scale for the S-10, cold, no sliding and reduced speed-up experiments at -85 ka . The 100 m/yr velocity contour is shown in purple.

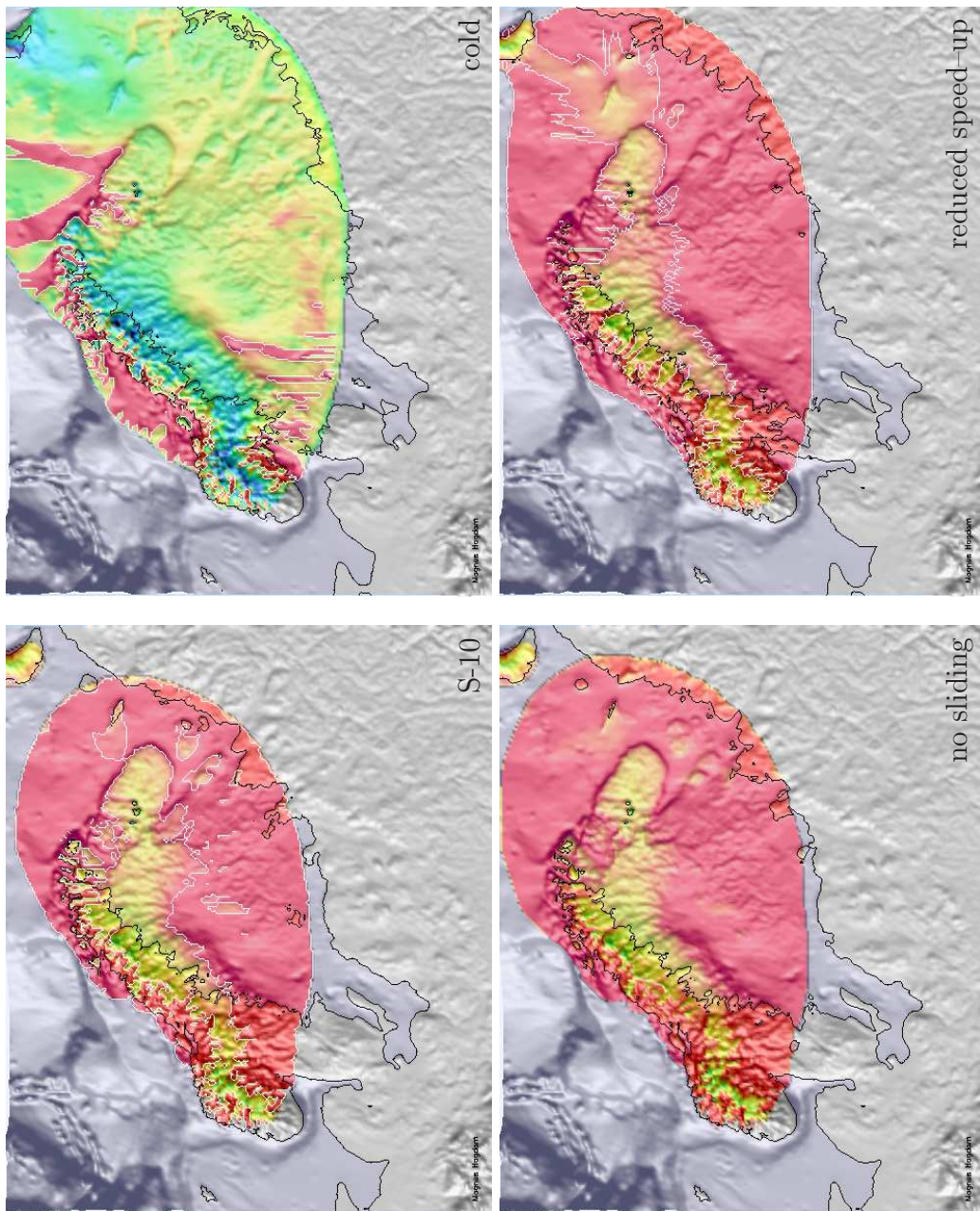


Figure 3.22: Basal temperatures corrected for the pressure melting point of ice for the S-10, cold, no sliding and reduced speed-up experiments at 85ka. The white contours indicate where sliding occurs.

feedback mechanism operating between the velocity and temperature field of an ice sheet. The ice velocity is linked to the temperature field via the non-linear flow law, Equation (2.3). Warmer ice is less viscous and can therefore flow faster. Fast flowing ice generates more frictional heat (third term of RHS of Eq. (2.7)) and thus increases the temperature. This feedback is known as *creep instability* (Clarke *et al.*, 1977).

The second group of ice streams with no or only little topographical control is much harder to explain. Contemporary examples of pure ice streams are the Siple Ice Streams of the West Antarctic Ice Sheet which drain into the Ross Ice Shelf. These streams are defined by lateral shear zones, marking the transition between sheet and stream flow. The base of the ice streams is at the pressure melting point, whereas ice is frozen to the bed at intervening ridges (Bennett, 2003). Furthermore, recent borehole investigation at Ice Stream B (Siple Coast, West Antarctica) revealed a water-saturated till layer at the ice base with a thickness of 10m. This till layer seems to be actively deforming as suggested by its high porosity and mixture of ages determined from fossils (Engelhardt *et al.*, 1990). The till mechanics of such layers is an area of active research. It is not clear if deforming layers of till exist as a consequence of the presence of an overlying ice stream (formed due to creep instability); or if the ice stream is caused by the presence of a deformable till layer. However, the subglacial hydraulic regime seems to play an important role in controlling ice streams (e.g. Boulton *et al.*, 2001a; Iverson *et al.*, 2003) since it controls the effective pressure at the ice bed and thus the coupling between basal ice and bed.

The ice sheet model used in this project includes a temperature-dependent flow law and should, therefore, be capable of simulating ice streams of the first type (e.g. Payne and Dongelmans, 1997). Payne (1998, 1999) used a similar ice sheet model to simulate the ice streams of West Antarctica. It should be noted that the assumptions of the shallow ice approximation are violated in the transition zone between sheet and stream flow where horizontal gradients are large. However, this should not affect the calculated location of ice streams (Payne, 1999).

The second type of ice stream is much harder to model. The ice sheet model uses a very simple approximation for basal décollement based on whether basal temperatures have reached the pressure melting point of ice or not (see Section 2.1.2). The model does not include a description of a deforming soft bed (e.g. Hindmarsh, 1997; Tulaczyk *et al.*, 2000) or basal hydrology (e.g. Boulton *et al.*, 2001a) which are necessary to formulate a more complete description of the boundary conditions at the ice base, since they are involved in feedback mechanisms with both the thermal and mechanical regimes at the ice base. The second type of ice stream cannot, therefore, be generated by the model.

The streaming behaviour of ice sheet models is further complicated by numerical problems arising from the non-linearity of ice flow. Both grid spacing and time steps influence computed ice sheet evolution, as they affect truncation

errors (Hindmarsh and Payne, 1996). However, Hulton and Mineter (2000) found that streams formed during simulations using different grid spacings showed similar sizes and occurred at similar frequencies.

3.4.1 Bedrock Topography Control

Topographic troughs play an important role in controlling the location of ice streams (e.g. Payne, 1998, 1999). One potential way of testing the significance of this effect is to conduct an experiment in which topographic variations are removed. This was done as part of this project. The standard Fennoscandian experiment was repeated with a stepped and then smoothed topography. The stepping adopted was

$$h^*(x, y) = \begin{cases} 1500\text{m} & \text{if } h(x, y) \geq 1500\text{m} \\ 1000\text{m} & \text{if } 1500\text{m} > h(x, y) \geq 1000\text{m} \\ 0\text{m} & \text{if } 1000\text{m} > h(x, y) \geq -300\text{m} \\ h(x, y) & \text{if } h(x, y) < -300\text{m} \end{cases} \quad (3.5)$$

The topography was stepped to remove all bedrock variations except for a high-elevation region over the Scandinavian Mountains, where ice sheet inception can occur. The surface $h^*(x, y)$ was then smoothed by applying a moving average filter to remove large horizontal gradients introduced by the step function. This experiment is similar to the EISMINT investigations (Payne *et al.*, 2000; Payne and Baldwin, 2000). However, the geometry of this problem is more complex than the simple EISMINT test case, because the model domain includes a marine margin and a more complex set of forcing functions. Figure 3.23 shows the resulting bedrock topography. In addition, the flow law enhancement parameter, f in Equation (2.4) had to be set to unity, because the model proved to be very unstable. The smoothed topography suppresses preferred directions of flow and flow lines are susceptible to wander causing the instabilities.

Figure 3.24 shows the resulting ice sheet at 40ka BP. The precise time is irrelevant since the smoothed topography is less elevated than the standard topography and, therefore, ice sheet inception occurs later. The ELA has to drop to a lower altitude before it intersects with the surface and ice can accumulate. The 40ka time slice was selected because ice sheet size and configuration of the smoothed topography experiment are similar to the S-10 ice sheet shown in Figures 3.21 and 3.22. The main ice divide is parallel to the Scandinavian Mountains and displaced to the South-East. Large parts of the ice sheet are at the pressure melting point of ice where basal décollement occurs and velocities are correspondingly high. Temperatures beneath the ice divide are well below the melting point of ice. The figure clearly illustrates the relationship between temperature and velocity. Regions of fast-flowing ice are warm, whereas regions of slow-flowing ice are cold. The smooth topography ice sheet shows no ice streams, but a dendritic pattern of cold regions perpendicular to the ice divide. These ‘cold fingers’ occur at regular spatial intervals and are constant in time.

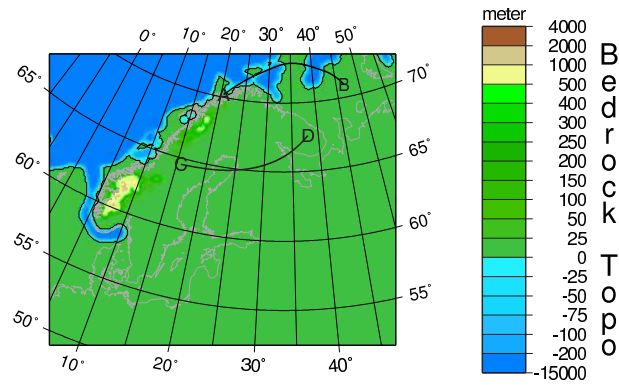


Figure 3.23: Topography used for the smoothed topography experiment. Most of the topography of the modelled region is set at 0m, except for two high–elevation areas over the Scandinavian Mountains where the ice sheet initiates. This Figure also shows two transects AB and CD along which velocities were extracted.

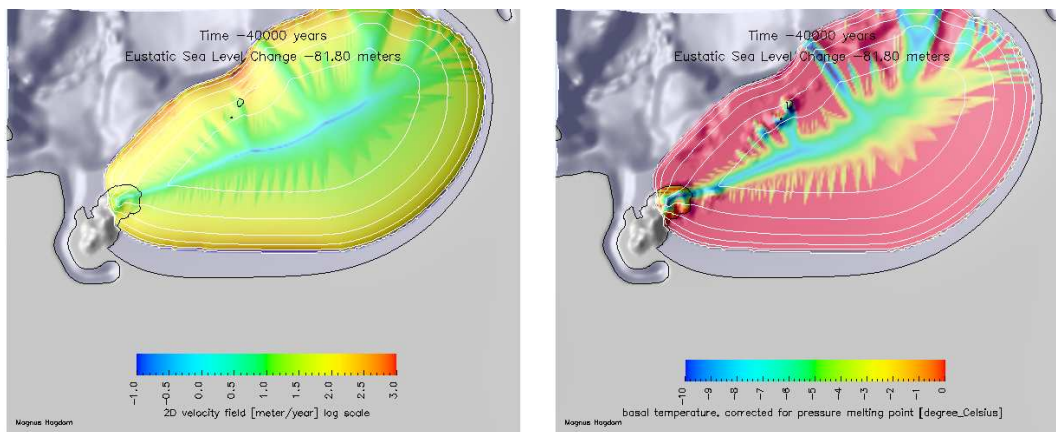


Figure 3.24: Magnitude of the surface velocity field on a log scale (left panel) and basal temperature corrected for pressure melting point of ice (right panel). The white contours indicate the ice surface; the contour interval is 500m. The black contour is the coast line.

The main exceptions to the regular pattern occur north of the ice divide. Two large ‘cold fingers’ extend from the divide to the edge of the ice sheet (see Figure 3.25). These large regions of stagnant ice occur next to shallow bedrock troughs. These troughs ‘escaped’ the smoothing process because of their depths. The upper panel of Figure 3.26 shows a temperature profile and basal and surface velocities along a transect cutting the northern streams. Ice is drawn into the troughs from the adjacent regions. The relatively fast flow heats the ice base to the pressure melting point due to internal friction. Once at the pressure melting point, sliding is triggered, enhancing the draw-down. Ridges form because of the channelling effect of the bedrock troughs. Ice flow diverges over the ridges and converges to form the fast flowing ice streams. The ice surface gradients enhance this process further.

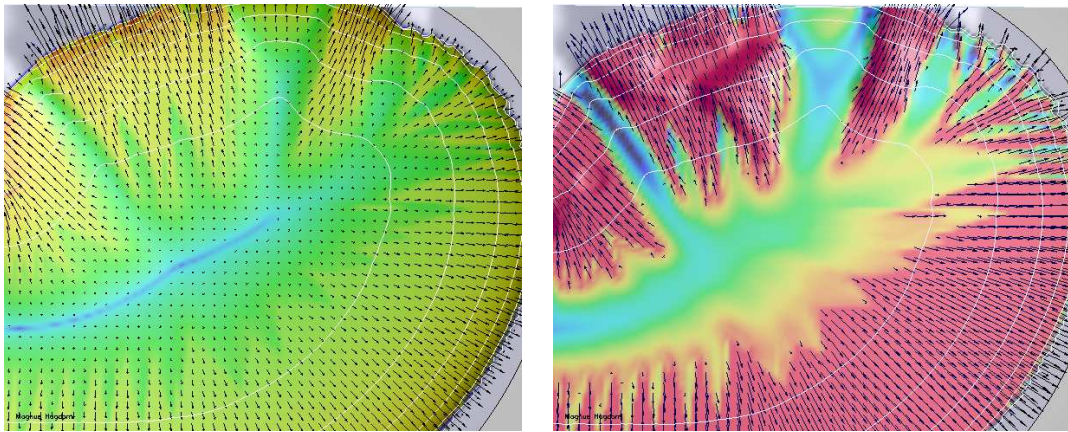


Figure 3.25: Enlargement of the northern part of the smoothed topography ice sheet. Surface velocities on a log scale and vectors indicating direction of flow (left panel). Basal temperatures corrected for the pressure melting point of ice and basal velocities (right panel).

In contrast to the northern ice streams, the streams south of the divide are clearly not controlled by topography. The lower panel of Figure 3.26 shows the temperature profile and basal and surface velocities along the southern transect indicated in Figure 3.26. These patterns are similar to the patterns discussed by [Hulton and Mineter \(2000\)](#) and occur as a consequence of creep instability and the sliding mechanism used.

3.4.2 Streams of the S-10 Experiment

The ice sheet experiments with the realistic bedrock topography also exhibit streaming. Two distinct regions can be identified: i) well-defined streams exist north of the Scandinavian Mountains which are channelled by the bedrock

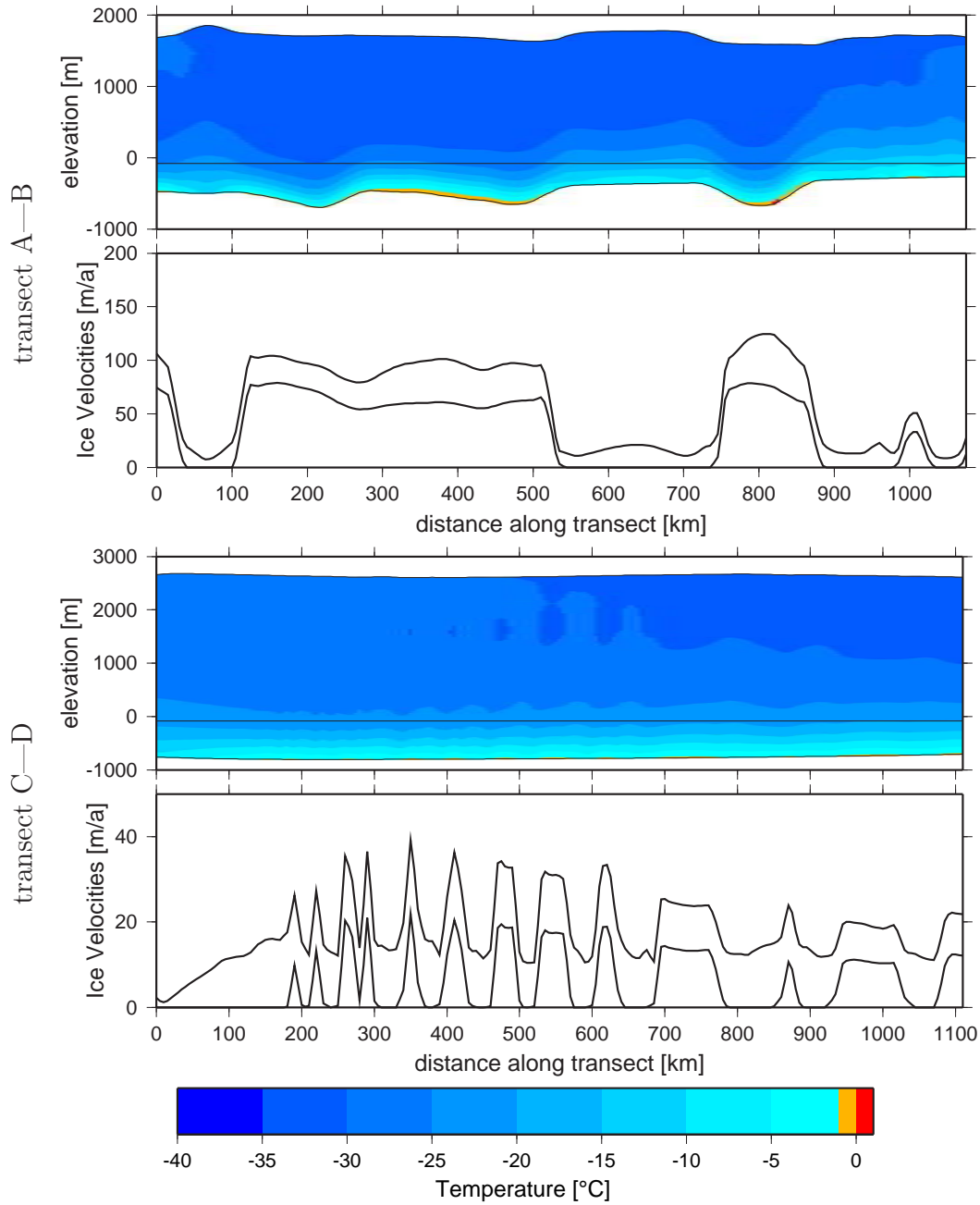


Figure 3.26: Temperature profile and surface and basal ice velocities along the transects indicated in Figure 3.25. The horizontal line in the temperature plot indicates sea level.

topography; ii) south of the ice divide variations of ice flow are less distinct, except for a stream forming in the Baltic Sea.

Figure 3.27 shows ice streams on the Norwegian coast of the S-10 experiment at -85ka. In addition to a map view, this figure also shows the temperature profile and basal and surface velocities along a transect cutting these streams. The figure clearly shows that stream location is directly related to bedrock topography: regions of fast flow occur over bedrock troughs, whereas velocities drop to relatively low values above intervening ridges.

Figure 3.28 shows the flow regime south of the ice divide. Ice velocity variations are relatively uniform except for a stream covering the Baltic Sea. In particular most of the ice bed is sliding with a uniform velocity except for two topographic highs where ice is frozen to the bed.

The flow regime of the smoothed topography simulation south of the ice divide clearly shows that topographic variations are not required to form regions of fast and slow ice flow as described by Hulton and Mineter (2000). However, regions of fast flow preferentially form over bedrock troughs (see Figs. 3.25 and 3.27). The fingers of cold ice observed in the smoothed topography experiment do not occur in the experiments using the realistic bedrock topography. Instead, streams form over relatively shallow bedrock depressions. In all cases, regions of fast flow tend to contain cold ice advected into the stream by the relatively large velocities.

Only one mechanism (creep instability) leading to the formation of ice streams is represented in the model. Although a sliding law, triggered when the ice base reaches the pressure melting point, is included, other relevant processes at the ice base, such as a deforming bed and a description of the basal hydrology, are not characterised. These omissions might explain why the velocities of the simulated ice streams are relatively small. The simulated stream velocities are typically between 100 and 200 ma^{-1} , whereas present Antarctic ice streams have velocities of up to 800 ma^{-1} (Bennett, 2003). There are also numerical problems arising from the discretisation of the non-linear thermomechanical equations governing ice sheet flow. These problems lead to instabilities, particularly in transition regions between slow and fast flow. The presence of these instabilities may affect the characteristics of these ice streams, but not their locations.

Ice streams are revisited in Chapter 4.2.1, where the Norwegian Channel Ice Stream is discussed in detail.

3.5 Relative Sea–Level Change

Relative sea–level (RSL) observations provide an excellent data set that can be used to constrain the size of past ice sheets. In particular, RSL data allows us to constrain past ice thickness for which otherwise there is little direct evidence. Assuming we can model sea–level change adequately (see Chapter 2.2), discrepancies between RSL observations and simulated time series can be due to i) wrong timing of events and/or ii) wrong size of ice load. The two sources

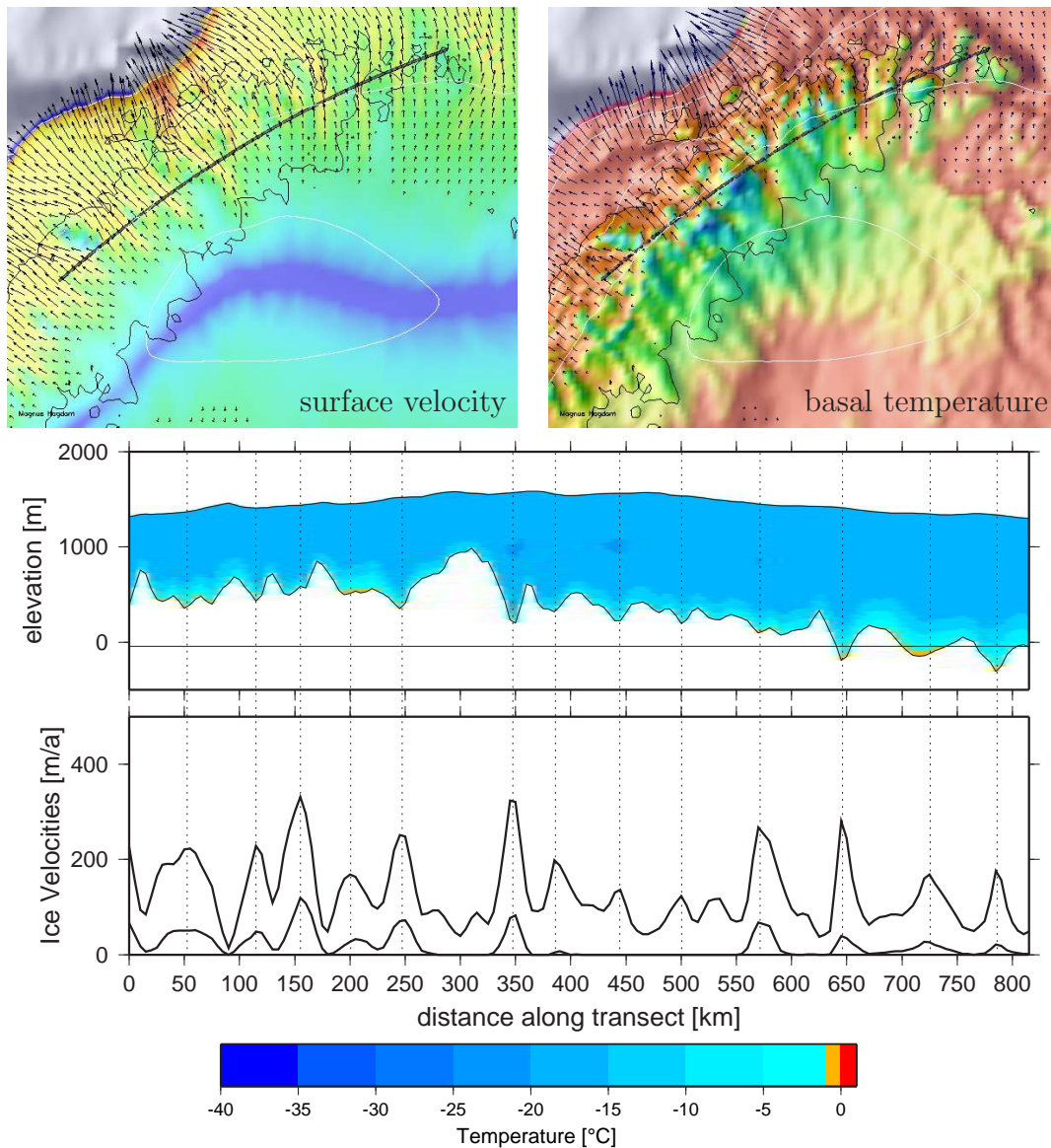


Figure 3.27: The top two panels show enlargement of the S-10 model run at -85ka . Surface velocities are on a log scale with vectors indicating flow direction (left panel) and basal temperatures corrected for pressure melting point of ice and vectors indicating direction of basal flow (right panel). The lower two panels show temperatures and surface and basal velocities along the transect indicated in the panels above.

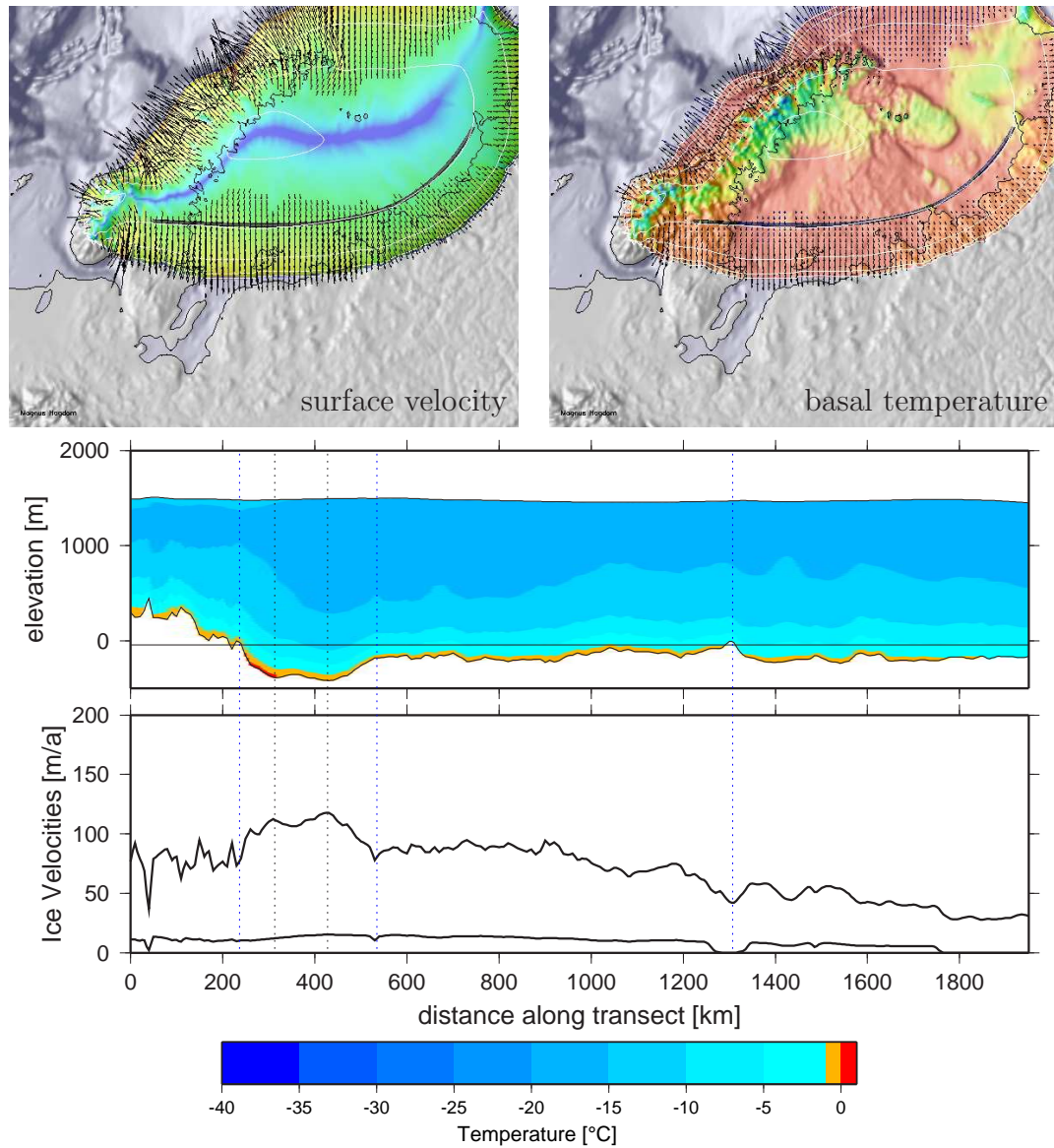


Figure 3.28: Plots of surface velocities on a log scale (top left panel) and basal temperatures corrected for pressure melting point of ice (top right panel) and vectors indicating surface and basal flow directions. The lower two panels show temperatures and surface and basal velocities along the transect indicated in the panels above.

of error can be distinguished by incorporating other lines of evidence such as reconstructions of past ice extent, i.e. RSL data is one component of a set of palaeoclimatic proxies. Causes for sea-level change are discussed in Chapter 1.4.1 and the relative sea-level data sets used for this project are summarised in Chapter 1.4.3.

The differences between simulated and observed relative sea-level change can be displayed in different ways. Figure 3.29 shows histograms of the RSL residuals ($\Delta\zeta_{\text{model}} - \Delta\zeta_{\text{obs}}$) of the standard and S-10 experiments using both the ELRA approximation and the full spherical Earth model. The histograms are produced by binning the RSL residuals using a bin size of $500\text{a} \times 10\text{m}$. Figure 3.29 also shows 1-dimensional histograms where the temporal dependence of the residuals is integrated.

The spatial distribution of residuals is investigated by calculating the average RSL residual at each site. Figure 3.30 shows the number of sites with a given residual (with a bin size of 10m) and the distribution of average residuals; each site is coloured according to the size of the average residual.

Figures 3.29 and 3.30 summarise the available data by integrating either the spatial or the temporal component. Figure 3.31 shows individual RSL curves for selected sites in Northern Europe (the data sources are described in Chapter 1.4.3). These sites are selected for geographic spread and number of observations.

The histograms and comparison of RSL curves suggests that, overall, both the standard and S-10 experiments produce ice sheets that are either too thick or decay too late. The standard experiment clearly performs worse. The S-10 experiment compares better with the relative sea-level observations, although there is still a large spread of residuals. The large residuals arise mainly in the northeastern part of the simulated ice sheet (see Figure 3.30). This mismatch should be expected considering that the ice sheet is matched with a single transect in the southwestern part of the modelled region. The match between simulated and observed RSL change at sites close to the transect (see Fig. 3.10) is surprisingly good, especially as the model was not tuned to fit the data.

Finally, present-day uplift rates can also be calculated from the model output. Figure 3.32 shows a map of uplift rates of the S-10 experiment. These data can be directly compared with GPS observations (e.g. Milne *et al.*, 2001).

Comparing the simulated ice sheet with the ICE-4G model (Fig. 3.14) clearly shows that the North-Eastern part of the ice sheet decays too late. Both the RSL curves in Figure 3.31 and the present-day uplift rates, Figure 3.32, confirm this shortcoming of the model. However, the calculated uplift rates of $2\text{-}8\text{mm}\text{a}^{-1}$ in region of the modelled transect are comparable with satellite observations of uplift rates reported by Milne *et al.* (2001).

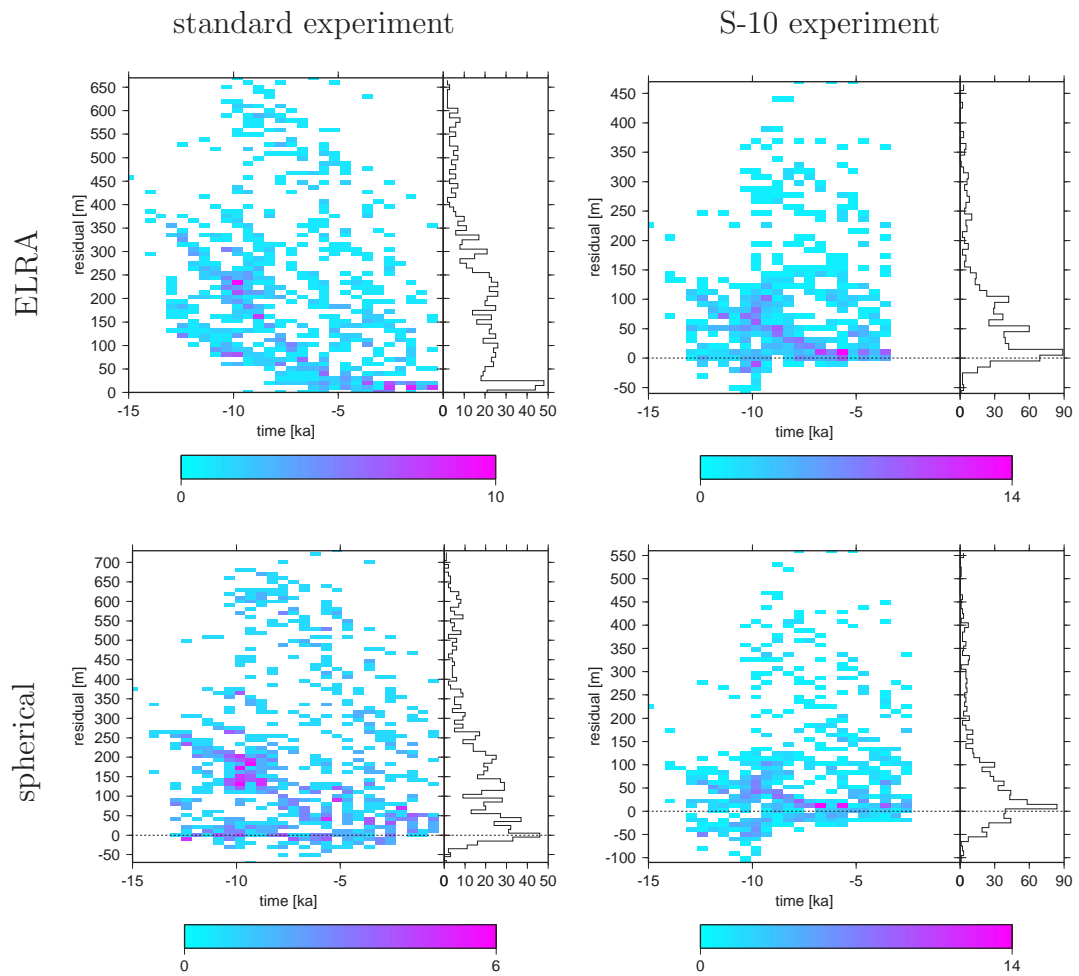


Figure 3.29: RSL residual histogram ($\Delta\zeta_{\text{model}} - \Delta\zeta_{\text{obs}}$) of the standard and S-10 experiments. The bin size is $500\text{a} \times 10\text{m}$. Relative sea-level change was calculated using the ELRA approximation (top row) and the spherical Earth model (bottom row). The colourmap indicates the number of data in each bin. Colours also indicate size of residuals.

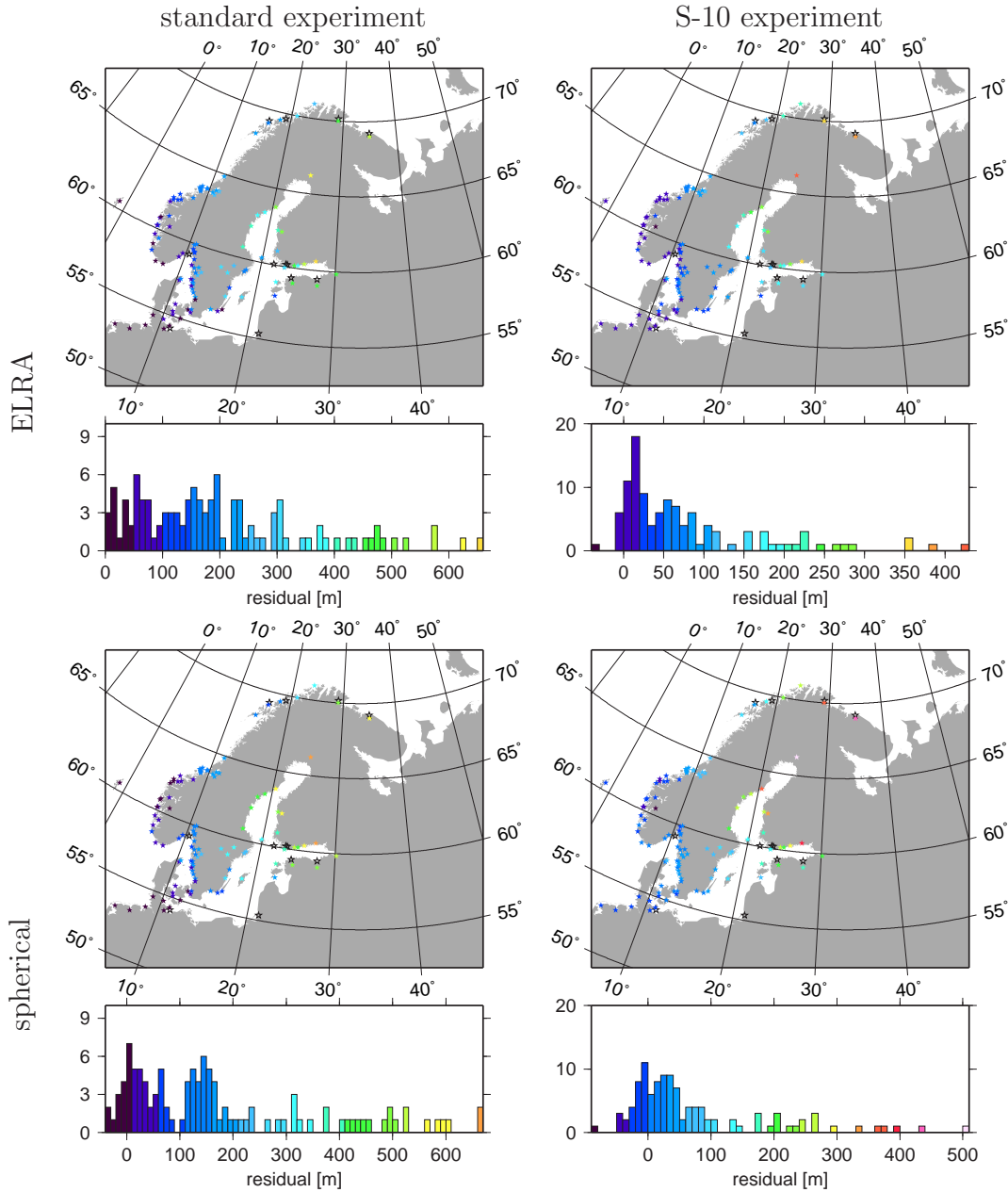


Figure 3.30: Distribution of RSL residuals ($\Delta\zeta_{\text{model}} - \Delta\zeta_{\text{obs}}$) for the standard and S-10 experiment using the ELRA approximation and full spherical Earth model. The temporal component of the residuals is integrated by taking the average residual at each site. The lower panels show the number of sites with a given residual, the upper panels show the locations of the RSL sites.

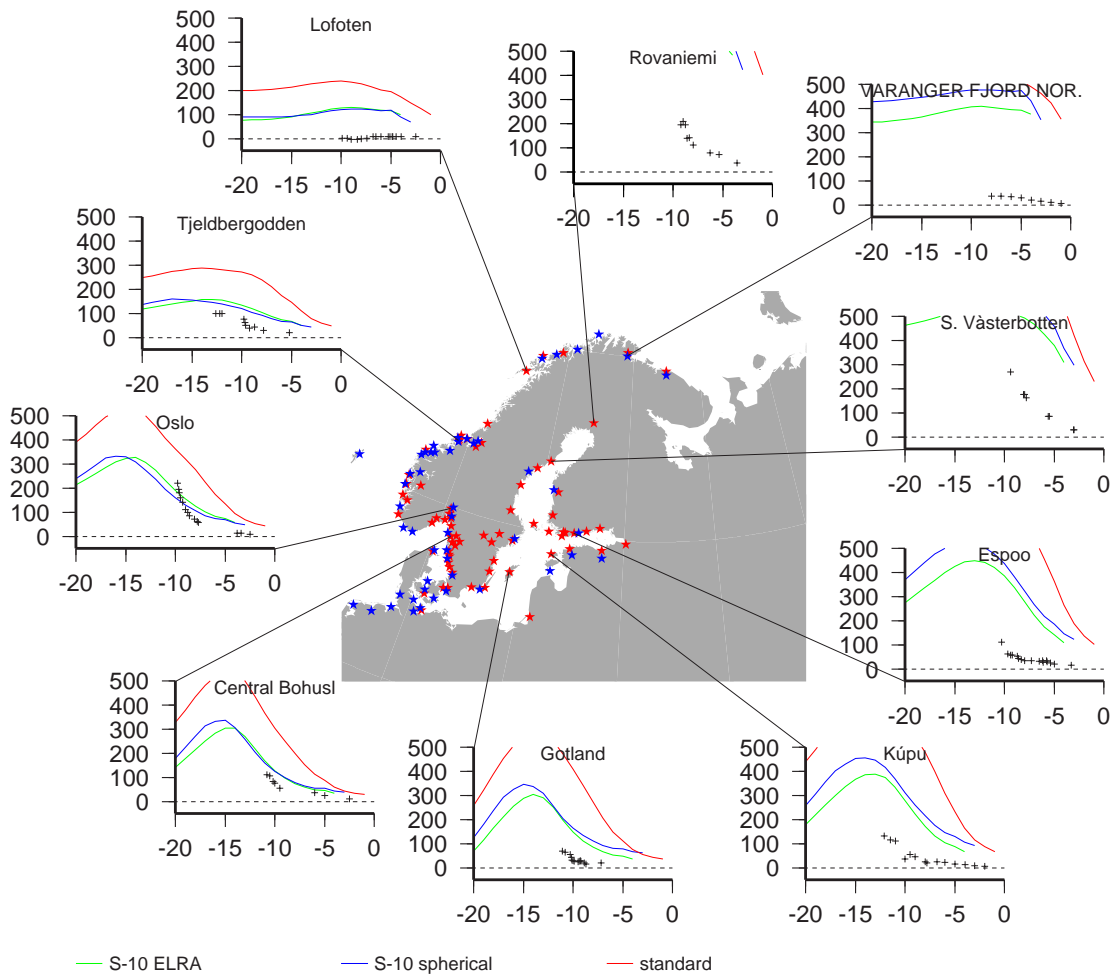


Figure 3.31: Sea-level change at selected sites for the standard European (red lines) and the S-10 experiment using the ELRA approximation (green lines) and the spherical Earth model (blue lines).

3.6 Conclusion

The evolution of the ice sheet model has been matched to the location of the ice margin along a transect in the southwestern part of the ice sheet by moving the entire ELA field up, to shrink the ice sheet, or down, to enlarge the ice sheet. Ice sheets are conveyor belts transporting mass from high elevations where ice accumulates to low elevations where it ablates. The efficiency of the ice transport depends on the stiffness of the ice and basal boundary conditions. Surface temperatures and the flow law enhancement factor affect internal ice deformation and, therefore, the size and shape of the ice sheet. A cold and, therefore, slow-flowing ice sheet can support steeper surface slopes. Also cold ice

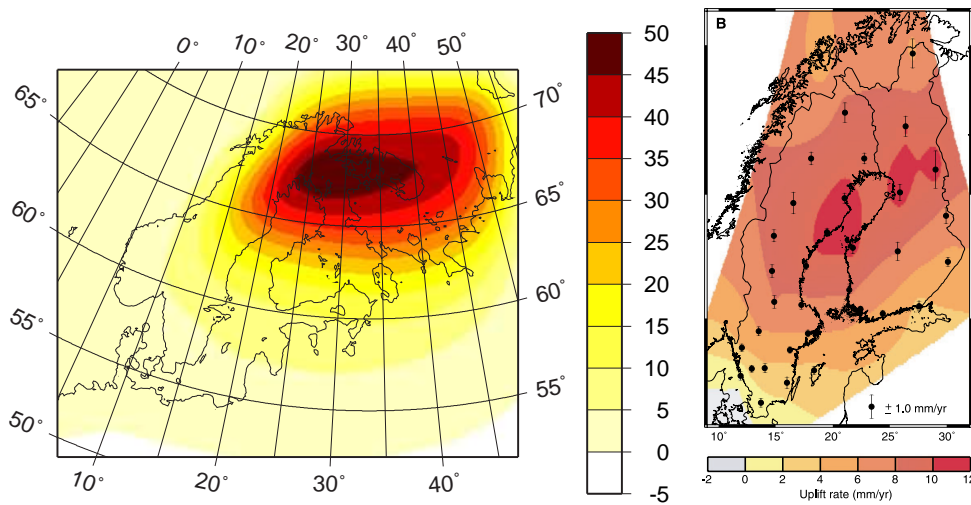


Figure 3.32: Simulated present-day crustal uplift rates from the S-10 experiment (scale in mma^{-1}). The right panel shows a map of present-day radial velocities constructed from GPS measurements (taken from [Milne et al., 2001](#)).

sheets are larger because a larger area is exposed above the ELA and thus more ice can accumulate.

The simulated relative sea-level change does not fit observations in the northeastern part of the ice sheet. This part of the ice sheet is unconstrained since the control transect is located with an origin in southwestern Norway and directed southeast. Comparisons of the simulated ice sheet evolution with the ICE-4G model ([Peltier, 1993](#)) clearly show that the Finnish part of the ice sheet decays too late, which causes the poor fit with the relative sea-level observations. These shortcomings of the simulation are also evident in the present-day uplift rates which are a factor of five too large over Finland. These mismatches occur because only one metric (ice margin position on the transect shown in [Figure 3.10](#)) is used, leaving the northeastern part of the modelled region unconstrained. Furthermore, some key parameters such as the latitudinal ELA gradient and continentality were not adjusted.

The current model is not capable of adequately representing ice streams. Simulations with an improved numerical description of the physics of ice flow would require larger computing resources. Also, software development of representations of the physics, notably bed processes, would take time. Aside from these practical issues there are also unresolved problems concerning the mechanisms causing and defining the characteristics of ice streams. In particular, processes at the basal boundary are not well understood, so representations of the physics of these processes, would have to proceed iteratively with other research investigations into their nature.

In spite of these problems, the simulated RSL curves match surprisingly well with observations in the southwestern part of the modelled region close to the

transect used for adjusting the model parameters. The procedure described in Chapter 3.2 is working well. Obviously the inversion procedure could be improved by fitting more transects and adding other metrics such as dispersal of erratics or sediment production. Increasing the number of metrics would also help to establish values for the latitudinal ELA gradient and continentality. Tools for data analysis and visualisation that have been developed in this project could be used for further experiments.

Clearly, the match between the model and observations could be improved. However, climatic conditions in Northeastern Europe are unlikely to influence climate in Western Europe. The next step in the procedure was, therefore, to transfer the forcing functions to the British Isles to simulate the past British Ice Sheet.

Chapter 4

Reconstruction of the Past British Ice Sheet

In this chapter, simulations of the past British ice sheet during the last glacial cycle are discussed. Geological reconstructions of the past British ice sheet suggest a relatively complicated ice sheet with multiple glaciation centres. The ice sheet model was, therefore, initially tested by simulating the comparatively simple past Fennoscandian ice sheet, as described in Chapter 3. These simulations demonstrated that the model is capable of simulating a realistic ice sheet at high resolutions, including topographically controlled ice streams and relative sea-level change.

There are a number of published models of the past British ice sheet based on geological reconstructions (e.g. Boulton *et al.*, 1977; Denton and Hughes, 1981; Boulton *et al.*, 1985): At the last glacial maximum, the British ice sheet reached Southern Ireland, the Bristol Channel and the Wash. There is some uncertainty about whether the British ice sheet was connected to the Fennoscandian ice sheet. For instance, inverting relative sea-level data, Lambeck (1993b,c) concluded that the North Sea was not covered by grounded ice. Sejrup *et al.* (1994), on the other hand, suggested that the North Sea was glaciated during the LGM. The models employed here aim to add further to this debate.

The climatic forcing function used to drive the Scandinavian model had to be modified in order to be able to grow a British ice sheet within the present forcing framework. The same temperature and equivalent sea-level change time series, described in Chapters 3.1 and 1.4.2, were applied to the British Isles. The basic pattern of a falling and rising ELA, as described in Chapter 3.2, was also retained. It was eventually necessary to introduce an additional longitudinal dependency of the ELA forcing function. This longitudinal dependency is necessary to initiate ice sheet growth in Britain and reflects the consideration that the British climate is more maritime than the relatively continental climate of Fennoscandia. Figure 4.1 outlines the approach taken.

Model setup and forcing of the simulation of the past British ice sheet are

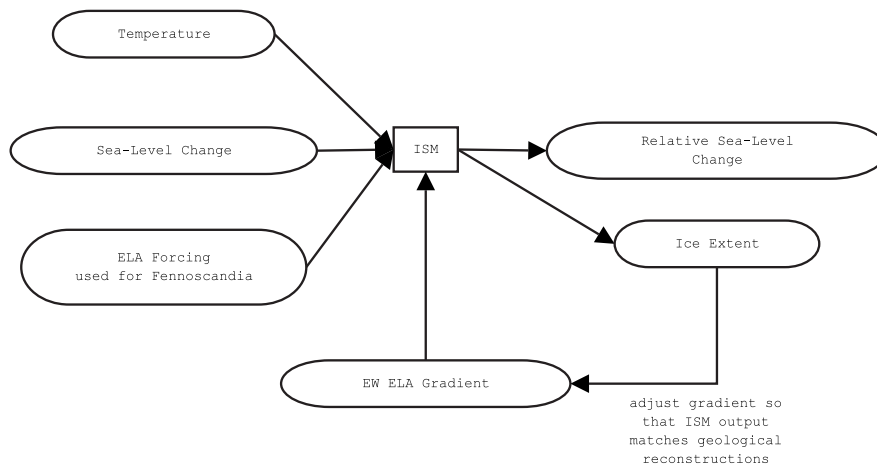


Figure 4.1: Schematic plan illustrating the setup of the past British ice sheet experiment. Rounded boxes indicate data sets, ISM is the ice sheet model.

described in detail in Section 4.1. Evolution of the simulated British ice sheet and associated relative sea-level change are discussed in Section 4.2.

4.1 British Ice Sheet Model Setup

The model setup for the simulation of the British ice sheet is the same as the standard setup of the Fennoscandian ice sheet simulations, described in Chapter 3.1. In particular, the temperature driver described in Chapter 3.1.2 is also applied to the simulation of the British ice sheet. Using the same climate driver for the British Isles simplifies the model setup for a combined British—European simulation. Bedrock topography and additional modifications to the ELA forcing function are described in this section.

4.1.1 Topography

The model requires an initial bedrock topography on which an ice sheet can advance and retreat. The digital terrain model, based on ETOPO5 and GTOPO30 and described in Chapter 3.1, was extended to include the British Isles. Again, a $10\text{km} \times 10\text{km}$ grid was used. The original data were provided on a longitude–latitude grid and were subsequently projected onto a Cartesian grid using the Albers Equal Area Conic Projection. Figure 4.2 shows the extended model domain. For simplicity, Iceland was removed from the dataset, but this should not affect the results discussed here. Figure 4.2 also shows two transects, A–B and C–D, which are used later on in Section 4.2.

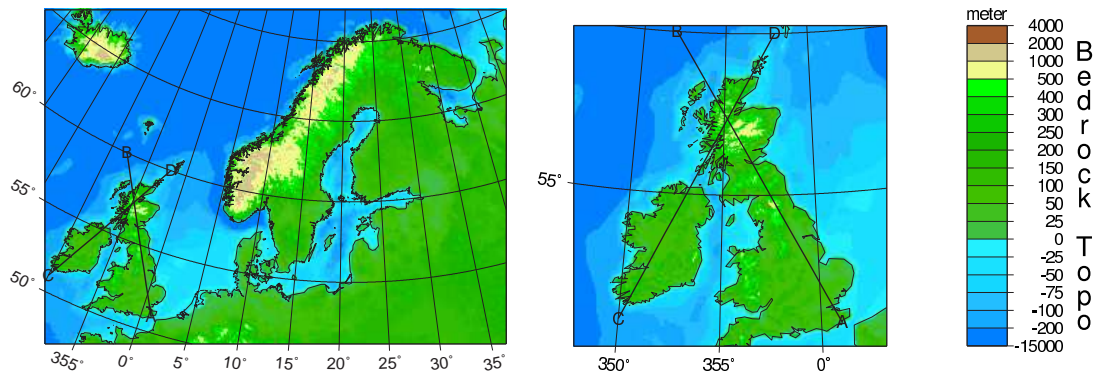


Figure 4.2: Topography based on ETOPO5 and GTOPO30 on a $10\text{km}\times 10\text{km}$ grid used for the British/Fennoscandian ice sheet model runs. The profile lines A—B and C—D are used later on in this Chapter.

4.1.2 ELA forcing

Simulations of the past British ice sheet proved to be particularly challenging. Not only did the topography give rise to multiple glaciation centres, it is also more subdued and lies further to the south than the mountainous regions where growth of the European ice sheet was initiated. Initially, the ice sheet model was forced with the European ELA function, as described in Chapter 3.2. However, running the ice sheet model with this standard set of parameters and climatic forcing functions did not produce any ice sheet growth in Britain.

Clearly, the ELA forcing function had to be modified in order to be able to grow a realistic British ice sheet. The ELA driver was modified to fulfill the following key requirements:

1. The simulated ice sheet should be compatible with geological reconstructions. At the LGM, the simulated British ice sheet should, therefore, extend no further than Southern Ireland, the Bristol Channel and the Wash.
2. It should be possible to run a combined British and European simulation without changing the mass balance and thus ice sheet evolution over Fennoscandia.

Both requirements could be fulfilled by introducing a longitudinal gradient to the ELA forcing function which is added to the standard latitudinal gradient. This gradient was set to zero at longitudes greater than 0°E in order to fulfil requirement 2. The maximum extent, described by requirement 1, is reached by lowering the ELA by 850m. This ELA depression results in large amounts of ice accumulating close to the continental shelf. This accumulation caused the simulation to become unstable. This instability was avoided by raising the ELA toward the West and introducing a minimum ELA which was set to 250m. Figure 4.3 shows the longitudinal ELA gradient used in the following experiments.

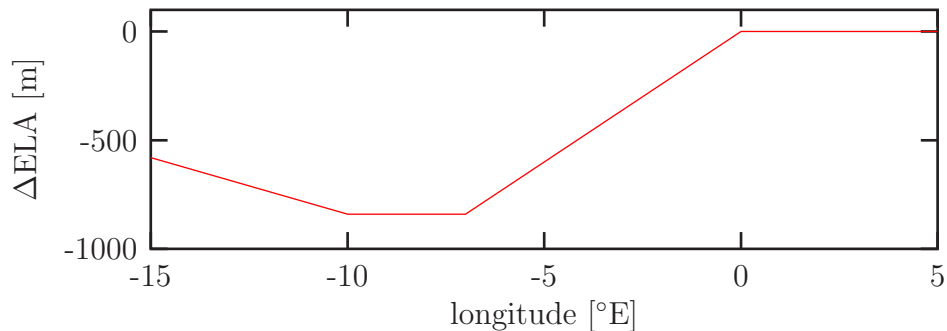


Figure 4.3: Additional equilibrium line altitude dependence on longitude introduced for the simulations of the past British ice sheet.

The additional longitudinal ELA gradient, introduced here, reflects differences in continentality between the British Isles (maritime climate) and Fennoscandia (maritime to continental climate). These variations of continentality are supported by simulations of the climate during the Last Glacial Maximum within the Palaeoclimate Modelling Intercomparison Project (PMIP¹) framework which suggest a strong longitudinal precipitation gradient (Pollard and PMIP Participating Groups, 2000). On the other hand, the ELA depression of 850m required to push the simulated British ice sheet to its reconstructed limit at the LGM, is very large. This suggests that the original latitudinal ELA distribution, described in Chapter 2.1.2, may not be well suited for simulating the past British ice sheet.

The results, shown here, are limited to the B5 and EB experiments which are defined by the same ELA setup. They differ in their modelled region: the B5 experiment covers only the British Isles, whereas the EB experiment covers both Fennoscandia and Britain. Results of the other experiments with slightly different longitudinal ELA gradients are omitted since they are very similar to the results of the B5 experiment.

4.2 Ice Sheet Evolution

The simulation, using the climate forcing and boundary conditions described in the previous section, leads to two glaciations. The first glaciation starts 65ka BP and finishes by 57ka BP and is less extensive than the second glaciation which is initiated 25.9ka ago. Both ice sheets are initiated in the Scottish Highlands. In the second glaciation, the individual mountain glaciers quickly coalesce to form a single ice dome by 24ka BP. The ice sheet reaches the continental shelf break by about 22ka BP, which inhibits further expansion to the West. Figure 4.4 shows the movement of the ice margins along transects A–B and C–D, indicated in

¹<http://www-pcmdi.llnl.gov/pmip/home.html>

Figure 4.2. The maximum ice sheet extent is reached by 17ka BP (see Fig. 4.5). Finally, the British ice sheet completely disintegrates by 14ka BP. Both figures also include results of the B5 experiment, with the same model setup, except that the modelled region is limited to the British Isles only.

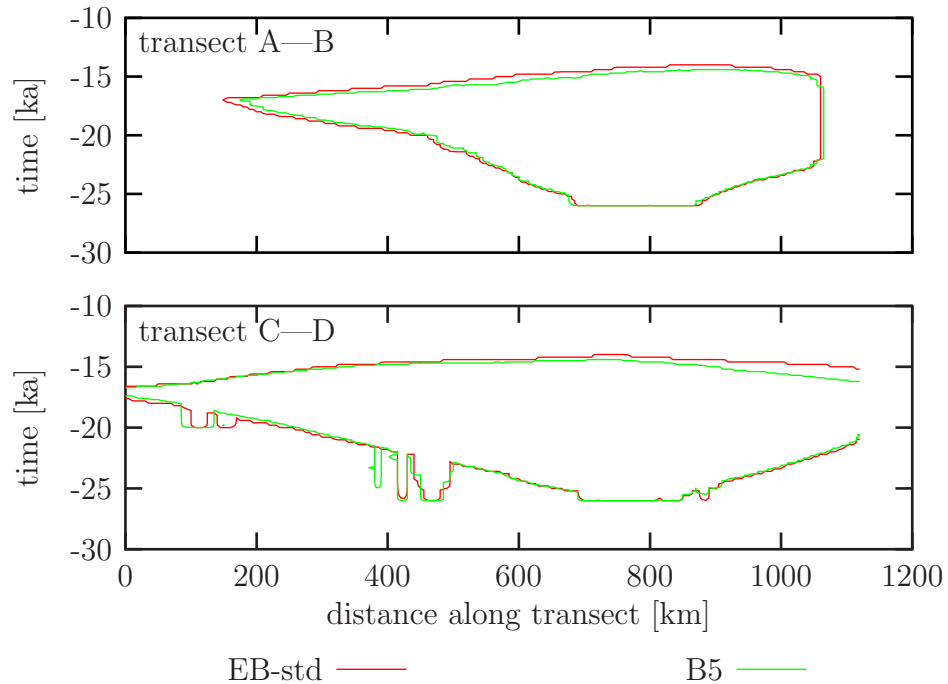


Figure 4.4: Time–distance diagrams showing the ice margins of the combined European/British and the B5 ice sheet experiments along transects A–B and C–D indicated in Figure 4.2.

Eighteen snapshots of the combined European and British ice sheet simulation, EB-std, between 21ka BP and 4ka BP are shown in Figure 4.6. In addition to ice surfaces the plots also show the extent of the ICE-4G model (Peltier, 1993).

These snapshots clearly show two major features of the simulated ice sheet relative to the ICE-4G model:

1. The simulated Last Glacial Maximum occurs 3 to 4ka later than the ICE-4G LGM.
2. The final stages of the European ice sheet produce an ice mass which is much larger and lies further north than the ICE-4G ice sheet.
3. The readvance of the British ice sheet during the Younger Dryas (\sim 11-10ka BP) is not simulated.

These differences arise because the ELA forcing was here tuned to fit the geological reconstruction shown in Figure 3.12D. The ICE-4G model is based on the

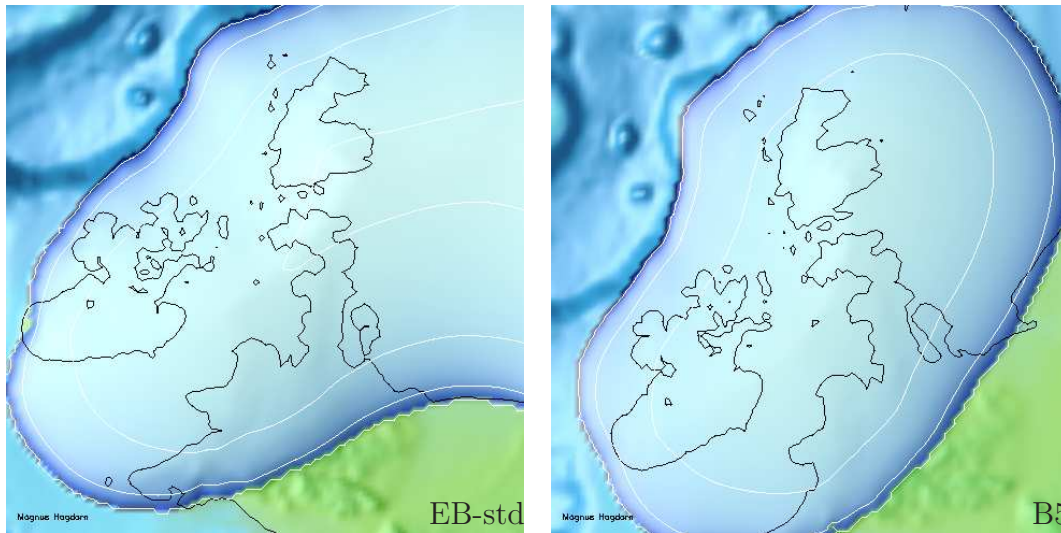


Figure 4.5: The simulated British ice sheet at the glacial maximum (European/British and B5 experiments), 17ka BP.

inversion of a single set of observations, relative sea-level change, and does not include other metrics. Furthermore, ICE-4G is a global model and its resolution of $1 \times 1^\circ$ is, therefore, low compared with the ice sheet model. However, the differences between the simulated ice sheet evolution, presented here, and the ICE-4G model indicate that modifications to the climate driver are necessary to improve model fit with RSL observations. In particular, model fit could be substantially improved by modifying the latitudinal ELA gradient and shifting the simulated LGM back in time.

During the Younger Dryas (~ 11 - 10 ka BP), the British ice sheet rapidly readvanced from ice-free conditions to limited ice-coverage mainly in the Western Highlands (Sissons, 1979b,a). This simulation of the British ice sheet does not show the Younger Dryas event because the ELA driver used to force the ice sheet model (see Fig. 3.12A) does not contain the Younger Dryas climate signal.

4.2.1 The Norwegian Channel Ice Stream

Figure 4.7 shows detailed snapshots of a simulation of when the British and Fennoscandian ice sheets coalesced. The simulated flow pattern of the British ice sheet is essentially radial and shows no indication of individual glaciation centres. The southwestern margin of the Fennoscandian ice sheet is dominated by a large ice stream through the Norwegian channel and smaller streams flowing through the valleys of the Scandinavian Mountains. These streams are controlled by the underlying bedrock topography through creep instability. Between 18ka and 16ka BP, when the British and Fennoscandian ice sheets are joined, the Norwegian Channel stream is split by an ice divide into a southern ice stream flowing through

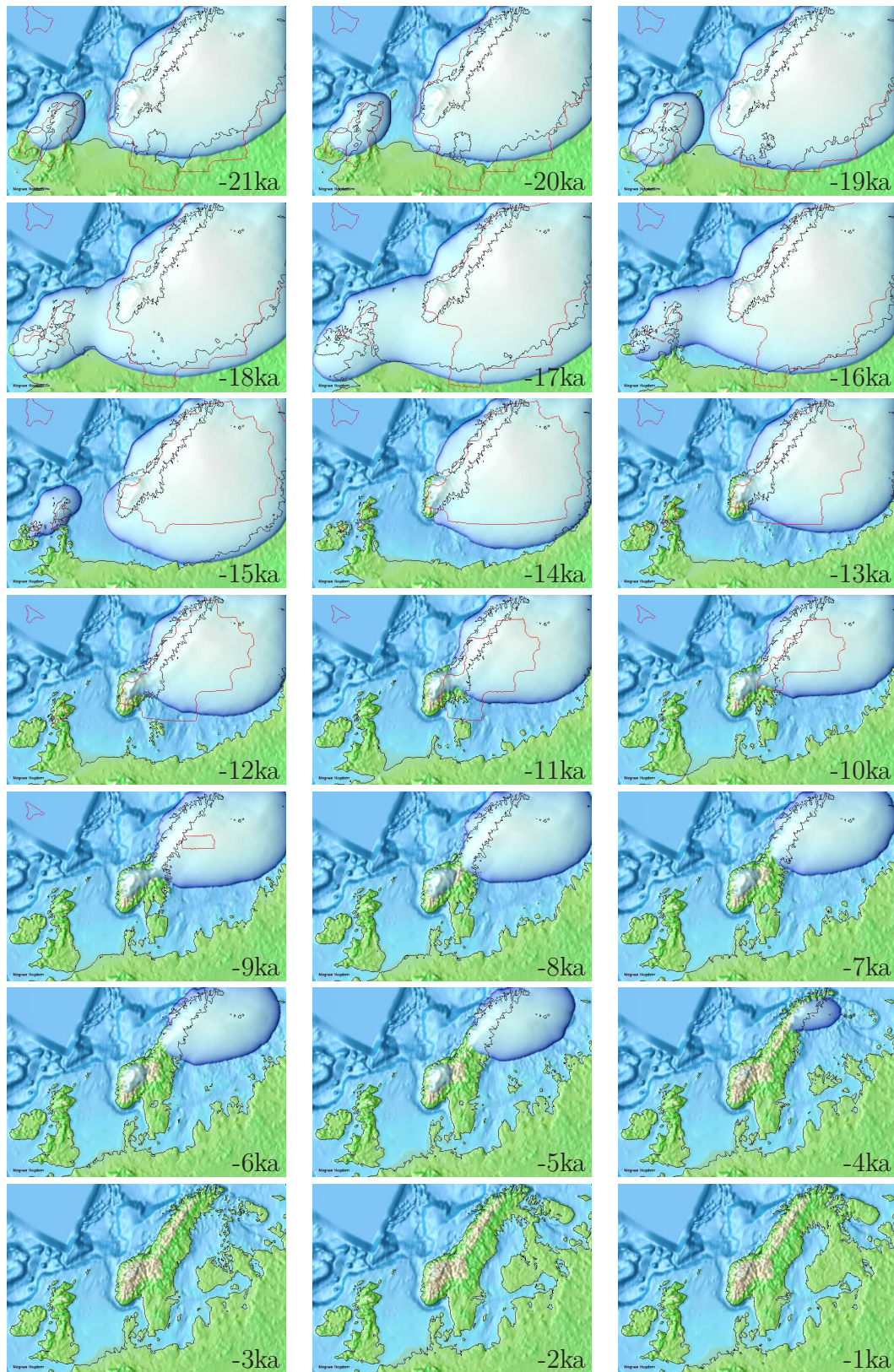


Figure 4.6: Plots of the combined Fennoscandian and British ice sheet model runs. The red lines indicate the ICE-4G ice extent (Peltier, 1993).

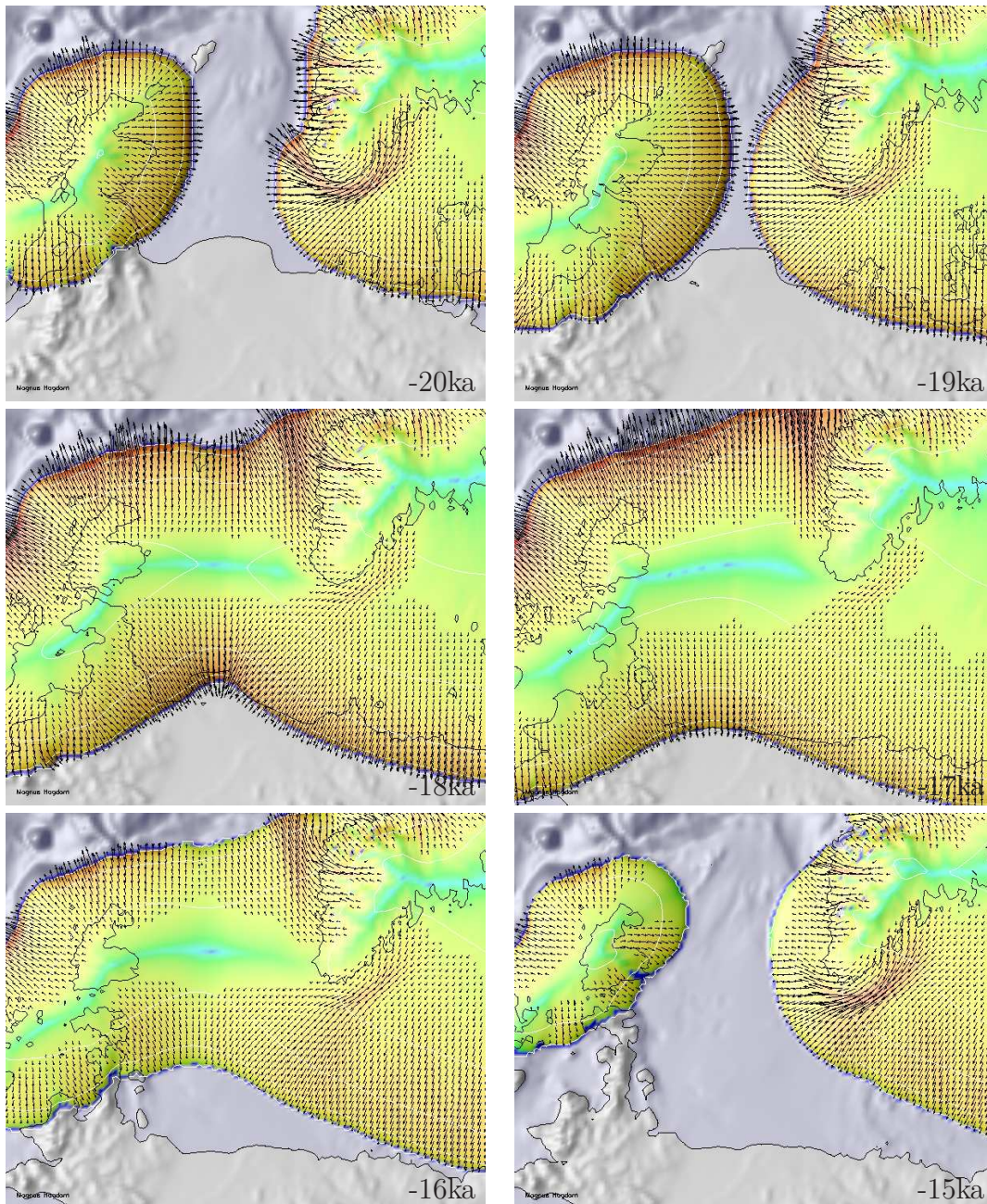


Figure 4.7: Snapshots of the combined European and British simulation showing the magnitude of the surface velocity field and ice flow directions.

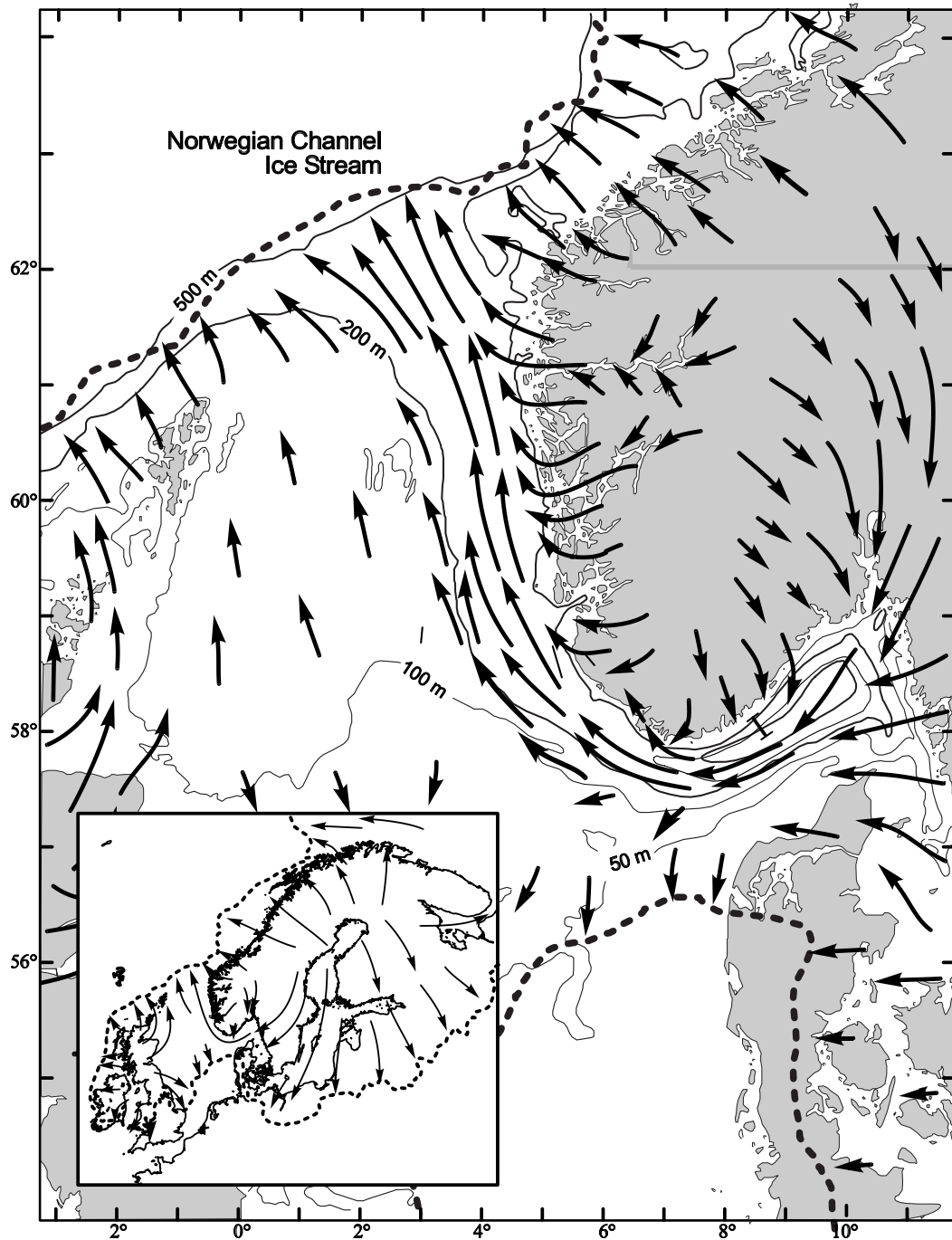


Figure 4.8: Reconstruction of the Norwegian Channel ice stream showing directions of ice flow (taken from [Sejrup et al., 1998](#)).

the Skagerrak and a northern ice stream. Ice is diverted out of the channel and spills over its edge to drain southward. By about 15ka BP, once the two ice sheets are separated again, the ice stream again follows the topography of the Norwegian Channel. The behaviour of the simulated Norwegian Channel ice stream compares well with the reconstruction proposed by [Sejrup *et al.* \(1998\)](#) shown in [Figure 4.8](#). It should be noted that the reconstruction by [Sejrup *et al.* \(1998\)](#) does not present evidence to support the transition in flow pattern. However, it would be expected that geological evidence of an interruption of the Norwegian Channel ice stream, as seen in [Figure 4.7](#), was destroyed by the activity of the ice stream once it had resumed flow along the channel.

4.2.2 Relative Sea-Level Change

The past British ice sheet was relatively small in comparison to the Fennoscandian ice sheet. The global equivalent sea-level signal is, therefore, relatively more important than the isostatic component due to the British ice sheet. This is particularly noticeable during the last 10ka at sites outside the former ice sheet. [Figure 4.9](#) shows relative sea-level curves for selected sites around the British Isles (the data is described in [Chapter 1.4.3](#)).

Overall, relative sea-level change residuals, $\Delta\zeta_{\text{model}} - \Delta\zeta_{\text{obs}}$ shown in [Figure 4.10](#), are smaller than the residuals of the European simulation. The distribution of residuals, also shown in [Figure 4.10](#), clearly shows that sites with small residuals are outside the former ice sheet, whereas sites within the former ice sheet have relatively large residuals. These differences arise because of the timing of the simulated LGM.

The main difference between the combined European/British experiment (EB-std) and the Britain-only simulation (B5) is that, in the EB-std experiment, the British and Fennoscandian ice sheets are joined. Simulated sea-level changes of the EB-std experiment are, therefore, larger than simulated sea-level changes in the B5 experiment.

4.3 Conclusion

The past British ice sheet was simulated by applying the European climate driver to the British Isles. In order to be able to initiate ice sheet growth over Britain, it was necessary to depress the ELA by 850m and introduce a strong gradient of continentality. The climate forcing then leads to two episodes of glaciation in Britain. The first glaciation started 65ka BP and finished by 57ka BP and was less extensive than the second glaciation which was initiated 25.9ka ago. The simulated British ice sheet completely collapses by 14ka BP.

As a first approximation, the simulated ice extent fits the geological evidence well. However, key features such as independent glaciation centres and the readvance of the British ice sheet during the Younger Dryas were not simulated.

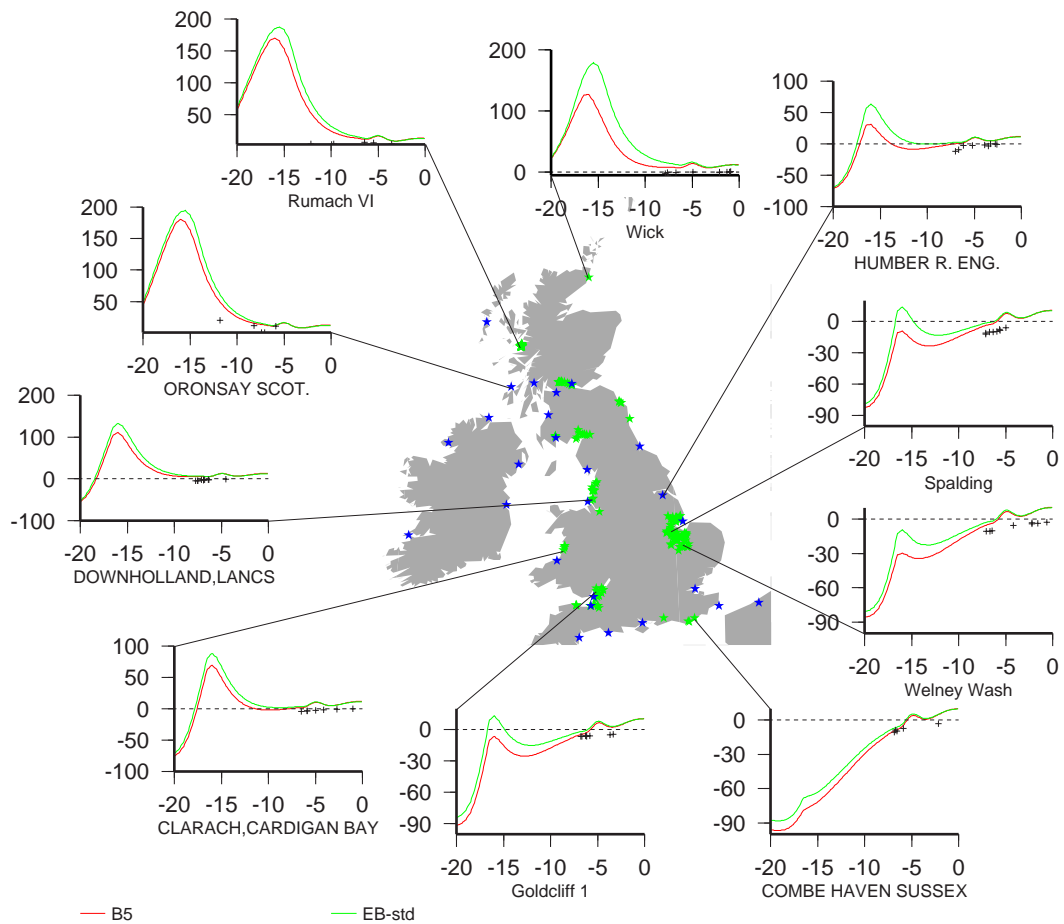


Figure 4.9: Relative Sea-Level Change at selected sites for the British ice sheet simulations.

These discrepancies arise from the choice of climate driver, in particular the ELA driver.

Overall, differences between relative sea-level observations and simulated RSL change are smaller than the differences for the European ice sheet. However, this is due to the relatively small size of the British ice sheet. Again, sea-level change was overpredicted, which suggests that the timing of events is incorrect, since the size of the simulated ice sheet is in broad agreement with geological evidence.

The ice simulation here differs from that provided by ICE-4G (Peltier, 1993). This highlights the results obtained by markedly different modelling approaches and the use of different data strands as modelling constraints. Each simulation is problematic in that it lacks realism with respect to one or more aspects of the input data or the physical realism of the model system dynamics.

It is reassuring, however, to find that the simulation of the Norwegian Channel ice stream and the glaciation over the North Sea matches the geological reconstruction by Sejrup *et al.* (1998) very well.

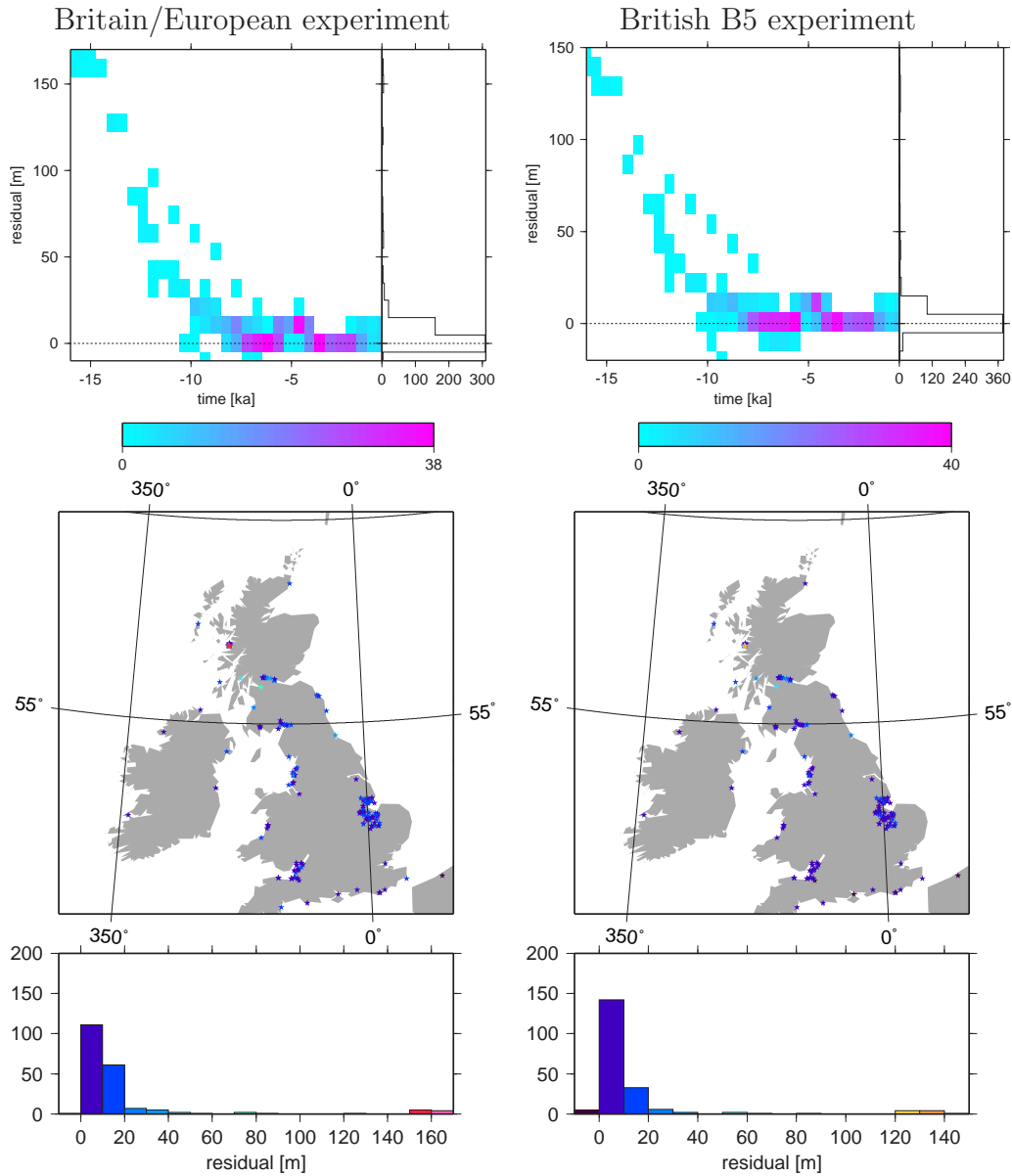


Figure 4.10: The upper panels show a histogram of RSL residuals, $\Delta\zeta_{\text{model}} - \Delta\zeta_{\text{obs}}$, as a function of time for the simulations EB-std and B5. The lower panels show the geographic location and number of occurrences of average RSL residuals. Colours indicate size of residual; averages are taken at each site. Residuals of the combined European/British simulation shown in this Figure are limited to the British Isles.

Improving the fit within the current framework would be difficult. In particular, the simulation of the British ice sheet suggests that the mass balance field was more varied than what can be achieved with a static ELA distribution which is raised to shrink the ice sheet or lowered to increase the ice sheet size. Nevertheless, it was considered useful to continue the process and construct climate drivers to simulate a potential future British ice sheet whilst recognising the limitations of the current model. However, given the limitations of the approach discussed above, the simulation should be considered illustrative of broad characteristics and little weight should be placed on details of the projection.

Chapter 5

Projecting the Evolution of a Future British Ice Sheet

The two previous chapters describe the application of the coupled ice sheet— isostatic adjustment model to the past Fennoscandian and British ice sheets, respectively. This chapter is concerned with the projection of potential future ice sheet growth and decay and associated sea-level change around the British Isles. Assuming the global climate system will not change substantially, we would expect another glacial period to occur during the next 100ka, with large parts of the Northern Hemisphere are covered by ice sheets. In order to be able to make a more quantitative projection of the next glacial period, the coupled ice sheet— isostatic adjustment model was run for the next 150ka assuming different climate scenarios including anthropogenic CO₂ forcing.

As stated before, this project is part of a larger programme to investigate the effects of potential future climate change in Britain, in particular with respect to future sea-level change which may impact the safety of disposal of intermediate and low-level radioactive waste at some possible locations for deep geological facilities. As part of the same programme, [Burgess \(1998\)](#) used the LLN-2D sectorial averaged, Northern Hemisphere atmosphere—ocean—cryosphere model, developed at the Université Catholique de Louvain ([Gallée *et al.*, 1991, 1992](#)), to simulate potential future climate change. Output from the LLN-2D simulations was used to drive the ice sheet model, since the ice sheet model does not incorporate an appropriate model for providing projections of future climate. The LLN-2D model was chosen for its capability to simulate climate change over long periods of time. More detailed climate models exist and could, in principle, be used for generating alternative scenarios of future climate change. However, the greater degree of complexity of general circulation models (GCMs) requires large computing resources and very detailed boundary conditions. They are, therefore, not suited to simulate climate change during an entire glacial cycle. An alternative approach, using a hierarchy of models, including Earth Models of Intermediate

Complexity (EMICs), is under development in the EU-funded BIOCLIM¹ project. However, this work was not sufficiently advanced to be used in the work reported herein.

The overall approach to driving the model in simulations of the future was to use a statistical approach (the Additivity and Variance Stabilising procedure, or AVAS) to link output from the LLN-2D climate model to the inputs required by the ice sheet model. The parameters used in this statistical linkage were found by modelling the past ice sheet driver using results from LLN-2D simulations as input. Future ice sheet climate drivers were then constructed from LLN-2D simulations of future climate scenarios and the previously obtained transfer functions. Figure 5.1 illustrates this approach.

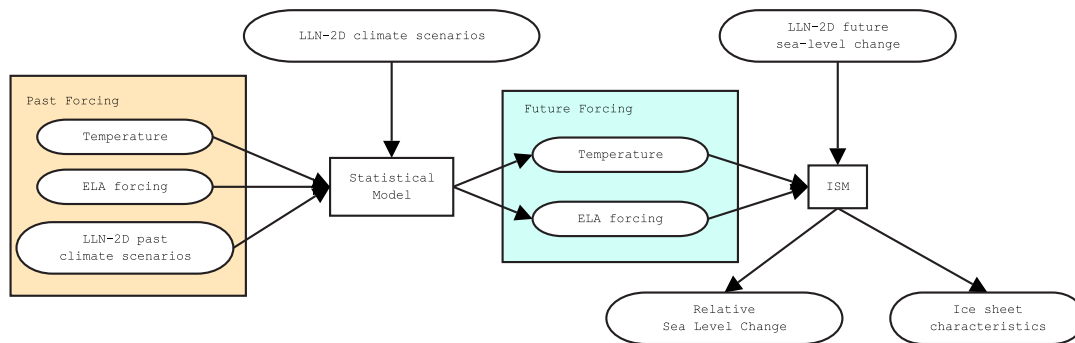


Figure 5.1: Schematic plan illustrating the setup of the future British ice sheet experiment. Rounded boxes indicate data sets, ISM is the ice sheet model. A statistical model, AVAS, was used to construct future forcing functions for various scenarios.

The AVAS procedure and its application to constructing forcing functions is described in detail in the next section. The transfer functions are then applied to reconstruct past climate drivers. Simulations of the past European and British ice sheets, using the AVAS climate drivers, are employed to benchmark the new set of climate drivers. The LLN-2D model and the simulations performed by Burgess (1998) are summarised in Section 5.3.1. Finally, the ice sheet model is run into the future, simulating the evolution of the British ice sheet under different CO₂ forcing scenarios.

5.1 Climate Drivers for Simulating Future Ice Sheet Scenarios

Each simulation using the coupled ice sheet—*isostatic* adjustment model requires a set of boundary and initial conditions describing how the simulated ice sheet system is embedded into the overall Earth system, in particular the climate system,

¹<http://www.andra.fr/bioclim/>

which is not directly simulated by the ice sheet model. The boundary conditions described in the previous two chapters are based on geological inferences. Attempting to simulate a future glacial cycle poses the obvious problem that most of the boundary conditions are unknown. It is, therefore, necessary to construct climate drivers from other modelling studies.

The ice sheet model was run on the same 10km grid-based digital elevation model, as described in Chapter 4.1.1. The same latitudinal ELA and temperature gradients, as described in Chapters 2.1.2 and 3.1.2, were retained. Furthermore, the longitudinal ELA gradient introduced in Chapter 4.1.2 for linking the British with the European climate was also used.

Future ELA and temperature time series were constructed from equivalent sea-level curves using the Additivity and Variance Stabilising (AVAS) method described in Section 5.1.1. More complicated AVAS models using time series of temperature, ice volume and its derivative are explored in Section 5.1.2. However, these more complex models were subsequently rejected because the quality of fit does not justify their additional complexity.

5.1.1 Additivity and Variance Stabilising Transformations (AVAS)

Many statistical studies use linear regression techniques to model data. These techniques are well understood and easy to apply. However, they impose restrictions on the transformations. Alternative techniques are more suited to model data if the transformations linking observations are expected to be non-linear. The Alternating Conditional Expectations procedure (ACE, [Breiman and Friedman, 1985](#)) and the Additivity and Variance Stabilising method (AVAS, [Tibshirani, 1988](#)) are non-linear regression techniques.

Non-linear regression methods differ from standard, linear regression models in that the coefficients of the linear models are replaced by real-valued functions. Both the AVAS and ACE methods are similar, in that they seek optimal transformations so that the correlation between the calculated response based on the regression variables and the observed response is maximised. They differ in their definition of ‘optimal’.

[Dagleish \(1996\)](#) used both AVAS and ACE to model palaeoclimatic data using orbital forcing time series as regression variables. [Dagleish \(1996\)](#) concluded that AVAS is more suited to palaeoclimatic modelling. In particular, the AVAS procedure ensures that the transformations of the dependent variable, $\Theta(Y)$, is monotonic and, therefore, an inverse transform, $\Theta^{-1}(Y)$, exists. The AVAS procedure can, therefore, be used for statistically modelling unknown processes. What follows is a brief summary of the AVAS procedure (see [Tibshirani, 1988](#); [Hastie and Tibshirani, 1990](#), for an in-depth discussion of ACE, AVAS and additive models in general). Notation in this section follows standard practise

where uppercase variables denote a random process and lower case variables denote observations.

For a dependent variable Y and regression variables X_0, X_1, \dots, X_n the AVAS procedure tries to find transformations $\Theta(Y), \phi_0(X_0), \phi_1(X_1), \dots, \phi_n(X_n)$ such that the additive model

$$\Theta(Y) = \phi_0(X_0) + \phi_1(X_1) + \dots + \phi_n(X_n) + \varepsilon = \sum_{i=0}^n \phi_i(X_i) + \varepsilon \quad (5.1)$$

approximates the data Y, X_0, X_1, \dots, X_n well. The error, ε , has a mean of 0 and is independent of the regression variables X_i . The transformations are determined such that

$$E \{ \Theta(Y) | X_0, X_1, \dots, X_n \} = \sum_{i=0}^n \phi_i(X_i), \quad (5.2a)$$

where $E \{ Z | w \}$ is the conditional expectation of Z given w , and the variance

$$\text{var} \left\{ \Theta(Y) \left| \sum_{i=0}^n \phi_i(X_i) \right. \right\} = \text{constant}. \quad (5.2b)$$

The statistical analysis described in Section 5.1.2 was performed using R², the GNU³ implementation of the object-oriented statistical programming language S/SPLUS.

5.1.2 Modelling the Past ELA Driver using AVAS

The main climate driver controlling the behaviour of the ice sheet model is the mass balance. As a first step, the ELA driver, determined in Chapter 3.2, was modelled using the AVAS procedure: $\Delta\text{ELA}(t)$ was assumed to be the dependent variable and was modelled using a combination of equivalent sea-level change $\Delta\zeta^{\text{esl}}(t)$, temperature at 60°N, $T_{60^\circ\text{N}}$, Northern Hemisphere ice volume, V_{ice} , and rate of change of Northern Hemispheric ice volume, \dot{V}_{ice} and $\dot{V}_{\text{ice}}/V_{\text{ice}}$ as independent regression variables. This particular set of variables was selected because a link between these variables and the ELA driver can be expected. Furthermore, these variables are available as output from the LLN-2D model.

The RSL record is described in Chapter 1.4.2. Temperatures at 60°N were calculated using the S-10 temperature record described in Chapter 3.1.2. The temperature record was only consider as an independent variable for completeness. Temperature is one component of the climate driver. A model of future temperature change, also based on the AVAS procedure, is described in Section 5.1.3. The ice volume and its derivatives were based on output of the LLN-2D LQ2 run (Burgess, 1998). Figure 5.2 shows plots of the time series used. A

²<http://www.R-project.org>

³GNU's Not Unix: collection of free software <http://www.gnu.org/>

smoothed temperature record was also used in addition to the highly variable original temperature record. The smoothed temperature record is denoted by adding a tilde, i.e. $\tilde{T}_{60^\circ\text{N}}$. Smoothing was done using a running lines scatterplot smoother called `supsmu` which is part of the R package. `supsmu` was chosen because it is also used by the AVAS procedure.

The time series with a resolution of 500a was processed using R. Five models, summarised in Table 5.1, with different combinations of regression variables were considered. The resulting transforms are shown in Appendix A.2. Figure 5.3 shows the resulting ELA forcing functions.

Out of the five models, Model 2 performed worst. Although Models 1 and 3 reproduce the ELA forcing function reasonably well, both models were excluded from further consideration because the transforms do not make physical sense, i.e. the response is linked to the regression variable by a transform with the wrong slope. Models 4 and 5 both produce physically meaningful transforms and reproduce the ELA forcing function relatively well, although not as well as Model 1. Model 5 is the preferred model, as it is less complex than Model 4.

5.1.3 Modelling the Past Temperature Driver using AVAS

A time series describing future temperature change is also required for simulating ice sheet evolution during the next glacial cycle. A model for future temperature change was obtained in a similar manner to the future ELA driver. However, instead of the original temperature time series $T_{60^\circ\text{N}}$, showing large millenia scale oscillations, the smoothed time series, $\tilde{T}_{60^\circ\text{N}}$, was used. Only two AVAS models are formulated since the temperature time series cannot be used as an independent variable. The two models are summarised in Table 5.2. Figure 5.4 shows comparisons of the resulting temperature time series and the original smoothed temperature time series.

Although the first model reproduces the temperature data faithfully between 80ka and 10ka BP, it shows large deviations around 110ka BP and present. The second model is simpler (it only uses $\Delta\zeta^{\text{esl}}$) and does not show these excursions. It is, therefore, the preferred model.

5.2 Simulating the Past Ice Sheets using the AVAS Drivers

5.2.1 The Past European Ice Sheet

The modelled ELA and temperature time series are necessarily different from the original ones used to simulate the Fennoscandian and British ice sheets in Chapters 3 and 4. In order to be able to assess the impact of these differences, the S-10 European experiment described in Chapter 3.2 was repeated with a) the AVAS ELA model together with the standard temperature time series, S-10; and

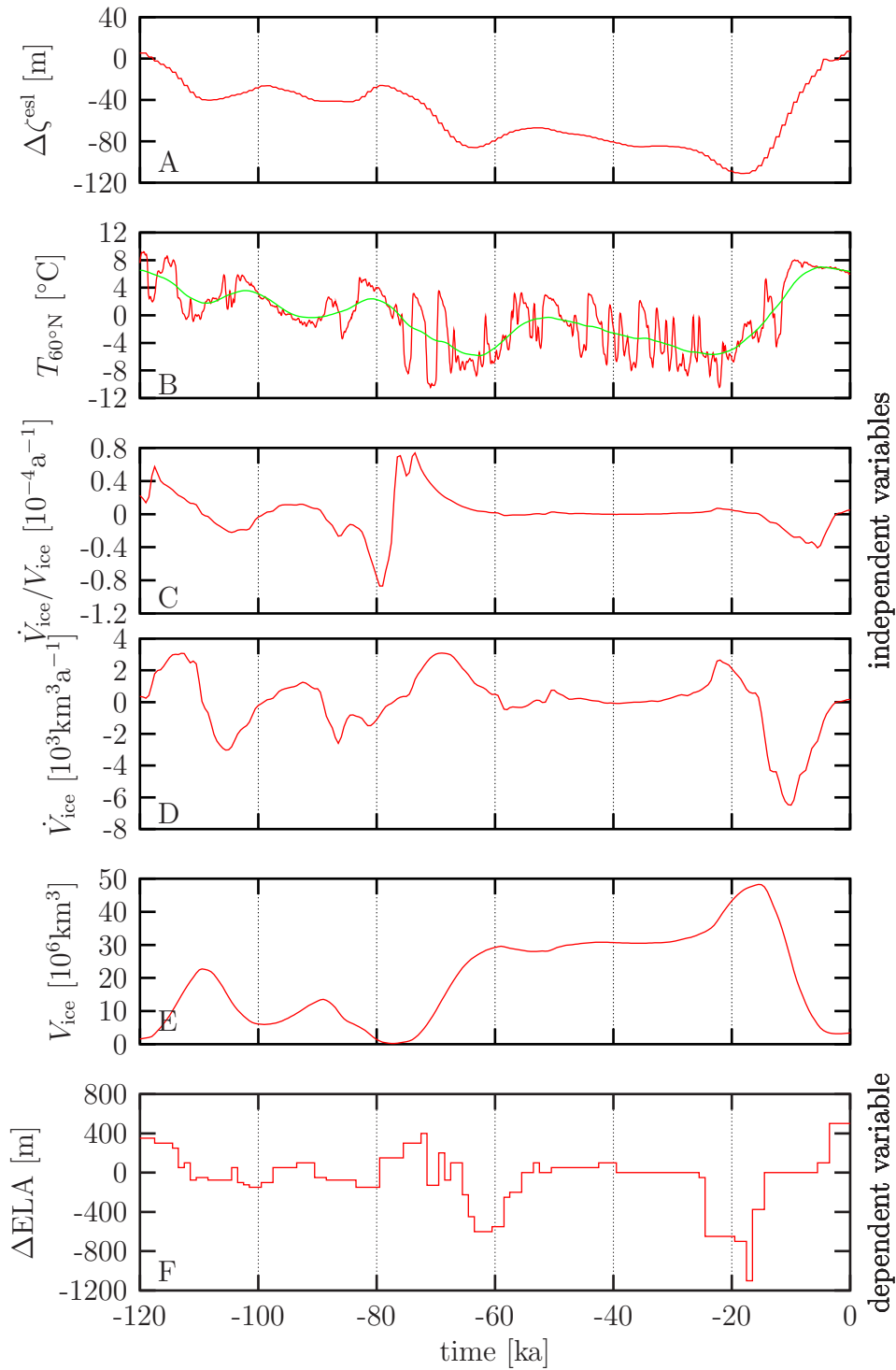


Figure 5.2: Plots of regression variables used for the AVAS procedure: A) equivalent sea-level change $\Delta\zeta^{\text{esl}}(t)$ (see Chapter 1.4.2); B) temperature at 60°N , $T_{60^\circ\text{N}}$ (temperature model S-10, Chapter 3.1.2) and smoothed temperatures, $\tilde{T}_{60^\circ\text{N}}$, using the R scatterplot smoother `supsmu`; C) fractional rate of ice volume change $\dot{V}_{\text{ice}}/V_{\text{ice}}$; D) rate of ice volume change \dot{V}_{ice} ; E) Northern Hemispheric ice volume, V_{ice} ; F) ELA forcing function, $\Delta\text{ELA}(t)$, as determined in Chapter 3.2.

	Regression Variables	Description
Model 1	$T_{60^\circ\text{N}}, V_{\text{ice}}, \Delta\zeta^{\text{esl}}$	The statistical model produces a reasonable fit, however the transforms ϕ_{temp} and $\phi_{\text{ice vol}}$ make no physical sense: the transforms imply that large ELA depressions depend on high temperatures and small ice volumes (see A.2.1).
Model 2	$\tilde{T}_{60^\circ\text{N}}, V_{\text{ice}}, \Delta\zeta^{\text{esl}}$	The transforms are similar to the transforms of Model 1, where ϕ_{temp} and $\phi_{\text{ice vol}}$ make no physical sense. Furthermore, the resulting forcing function does not match the original as well as Model 1 (see A.2.2).
Model 3	$\tilde{T}_{60^\circ\text{N}}, \dot{V}_{\text{ice}}/V_{\text{ice}}, \Delta\zeta^{\text{esl}}$	The temperature and sea-level transforms make physical sense, i.e. low temperatures and reduced sea-level produce large ELA depressions and vice versa. These contributions are small in comparison with the contribution of the ice volume change transform, $\phi_{\text{ice vol change}}$. The slope of $\phi_{\text{ice vol change}}$ is positive, i.e. a decaying ice sheet produces a large ELA depression, which is not what we expect, ruling out this model. Using \dot{V}_{ice} instead of $\dot{V}_{\text{ice}}/V_{\text{ice}}$ as regression variable produces similar results (see A.2.3).
Model 4	$\tilde{T}_{60^\circ\text{N}}, \Delta\zeta^{\text{esl}}$	Both transforms make physical sense, i.e. low temperatures and low sea-levels are correlated with large ELA depressions and vice versa. The temperature transform contributes very little to the ELA transform. The resulting ELA model matches the original relatively well, except for the ELA depression 60ka BP (see A.2.4).
Model 5	$\Delta\zeta^{\text{esl}}$	Result is very similar to Model 4 (see A.2.5).

Table 5.1: Statistical models using different combinations of regression variables for modelling the ELA forcing function.

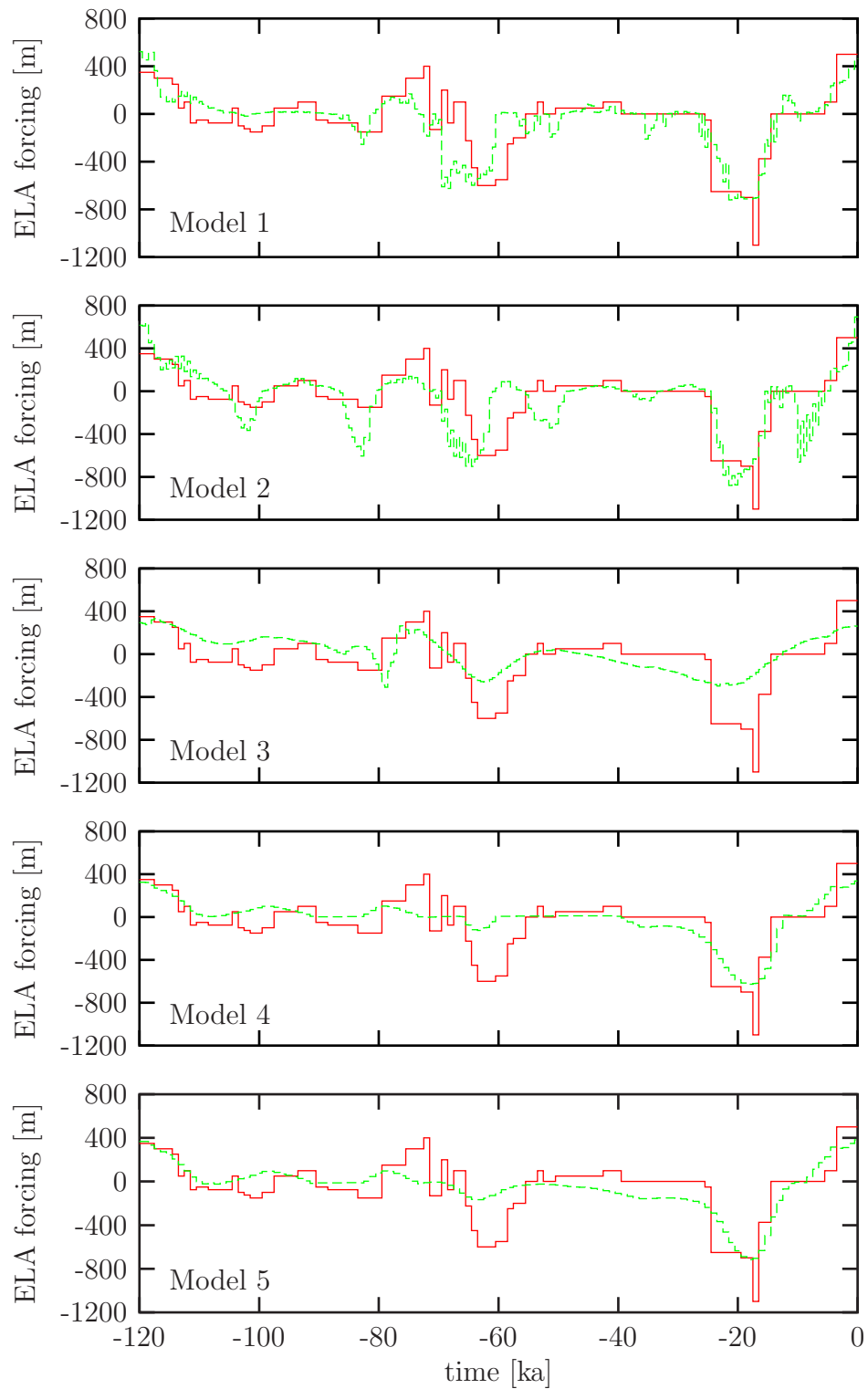


Figure 5.3: Comparisons of the original ELA forcing function (solid lines) and the modelled ELA forcing functions (dashed lines).

	Regression Variables	Description
Model 1	$V_{\text{ice}}, \Delta\zeta^{\text{esl}}$	The model produces a reasonable fit. The SLC transform behaves as would be expected: low sea-levels correspond to low temperatures. However, the relationship between ice volume and temperatures implies high temperatures when the ice volume is large (A.2.6).
Model 2	$\Delta\zeta^{\text{esl}}$	This simple model fits the smoothed temperature timeseries relatively well and the SLC transform make physical sense: low sea-levels correspond with low temperatures (A.2.7).

Table 5.2: Summary of the statistical models used for modelling the smoothed temperature forcing function.

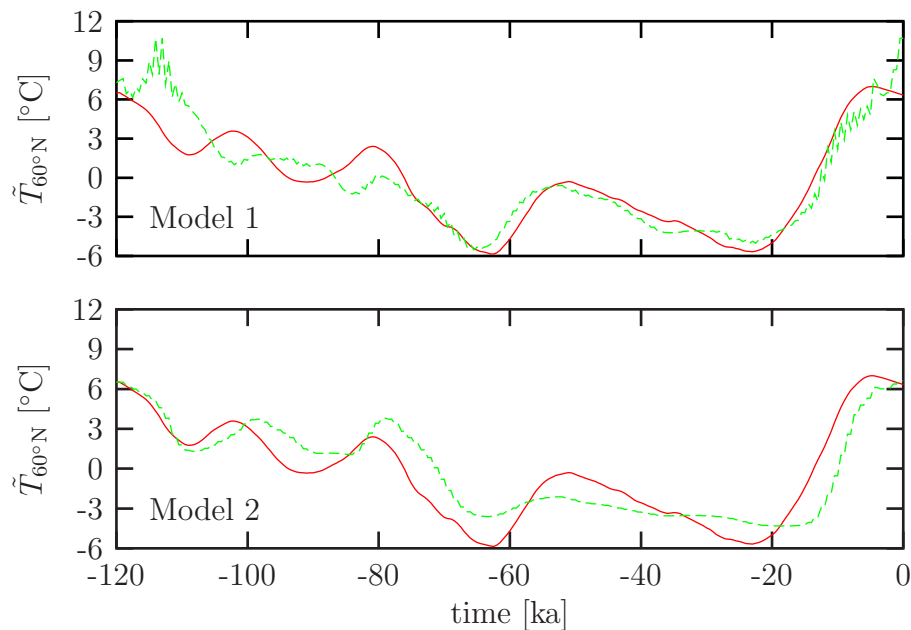


Figure 5.4: Modelled temperature (dashed lines) and the smoothed temperature time series (solid lines) for the two temperature AVAS models.

b) the AVAS ELA and temperature models. Figure 5.5 shows the resulting ice sheet evolutions together with the forcing functions.

Ice sheet evolution along the European flow line (see Fig. 3.10) is very similar for both simulations using the AVAS forcing functions and follows the S-10 European experiment. The main differences along the transect occur during the period between 80ka and 75ka BP when the S-10 ice sheet completely collapses. Both AVAS ice sheets do not advance as far as the S-10 ice sheet during the two maxima at about 60ka and 17ka BP because the simulated ELA depression is not as severe as the original ELA forcing function at those times. The AVAS procedure smooths both dependent and independent variables to estimate the transform functions. Therefore the resulting ELA model shows less variation than the original ELA driver (Fig. 5.3). For the same reason, the ice extent of both AVAS models during the intervening period is larger than that of the S-10 simulation, because the modelled ELA driver does not rise as much as the original ELA function.

Differences between the two AVAS models and the S-10 simulation become apparent when examining the area covered by the ice sheet and its volume (Fig. 5.5). In particular, during the period between 80ka and 75ka BP, the ice volume of the simulation using the AVAS temperature model diverges significantly from the other models. The difference between the two AVAS models arises because of the lower temperatures before that period which result in a colder and thicker ice sheet. The thicker ice sheet can grow larger due to the altitude–mass balance feedback mechanism. The AVAS ELA does not show the marked increase in altitude required to decay the ice sheet during the period between 80ka and 75ka BP. This effect is further enhanced for the simulation with the AVAS temperature forcing because the ice sheet is already thicker and covers a larger area.

During the run–up to the simulated LGM, ice extent and volume of both AVAS models are similar to the S-10 simulation. The simulation using the AVAS temperatures again results in a thicker and slightly larger ice sheet than the simulation using only the AVAS ELA forcing function. Figure 5.6 shows images of both AVAS ice sheets and the S-10 ice sheet at the simulated LGM. The S-10 ice sheet is able to extend further to the West because the ELA is lower. Both AVAS simulations of the European ice sheet do not extend over the North Sea and are thus not confluent with the British ice sheet.

The isostatic response of both simulations using the AVAS climate drivers is similar to the isostatic response of the simulation using the S-10/standard ELA forcing (see Figure 5.7). In detail, the isostatic responses differ in the same way that ice area and ice volume do: the simulation using both the AVAS ELA and temperature driver which produces the largest volumes and areas covered by ice also produces the largest isostatic response; the simulation using the AVAS ELA driver together with the S-10 temperature produces an intermediate isostatic response; and the simulation using the original forcing functions produces the smallest isostatic response. The timing of the maximum isostatic response of

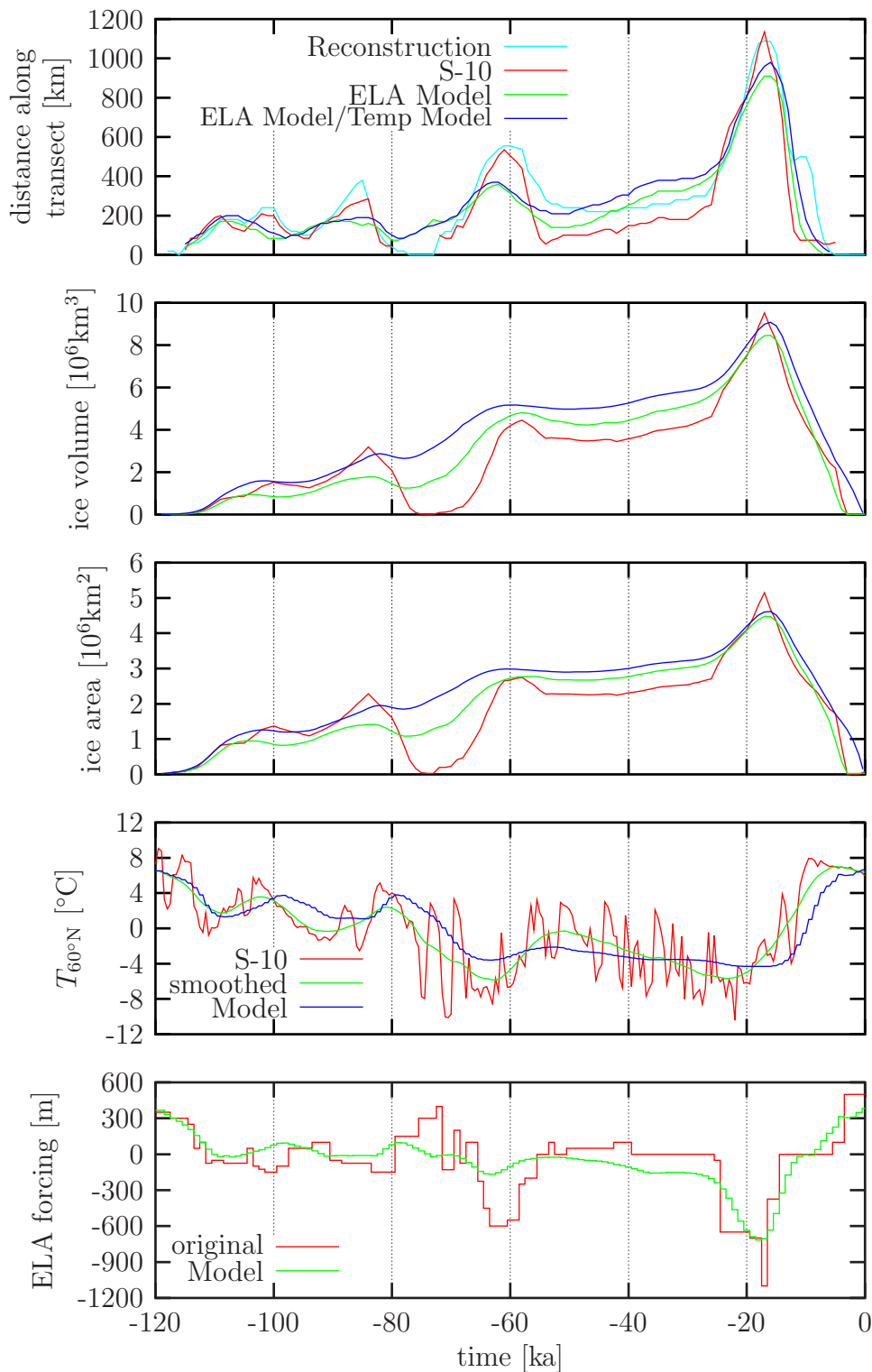


Figure 5.5: Plots of the ice sheet evolution of the two simulations forced with the AVAS ELA driver together with the S-10 temperatures (green) and the AVAS ELA driver together with the AVAS temperature driver (blue). Ice sheet evolution of the S-10 (red) experiment is also shown for comparison. The top three panels show, ice margin position along the European flow line (Fig. 3.10), ice volume and area covered by the simulated ice sheets. The lower two panels show the temperature and ELA forcing functions.

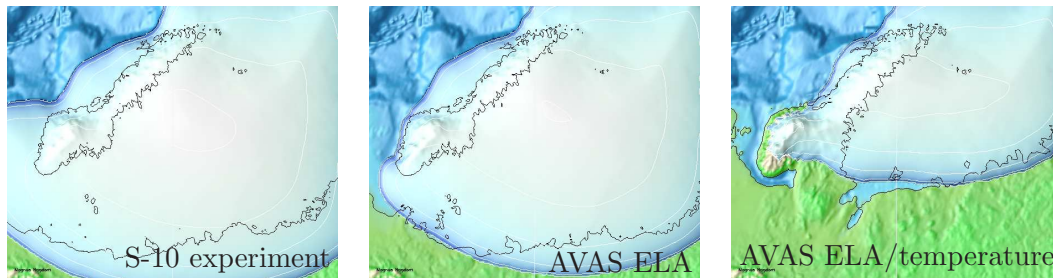


Figure 5.6: Snapshots of the S-10, AVAS ELA and AVAS ELA/temperature ice sheet experiments at the simulated LGM (17ka BP). The maximum ice thickness of all three simulations is about 3200m and occurs over the Baltic Sea.

both AVAS simulations is different from the timing of the original simulation. This offset is discussed further in the next section.

5.2.2 The Past British Ice Sheet

Simulations of the past British ice sheet provide another testbed for the AVAS climate drivers. The British ice sheet is smaller and, therefore, more sensitive to changes in the ELA driver than the European ice sheet. The increased sensitivity is due to the altitude–mass balance feedback mechanism. The standard ELA forcing used to simulate the British ice sheet only produces significant ice coverage during the period between about 25ka and 15ka BP.

Figure 5.8 shows the evolution of the British ice sheet forced with the B5 and AVAS drivers together with the forcing functions. The maximum size of the AVAS ice sheet is comparable to the size that the B5 ice sheet reached during the first growth phase before 20ka BP. This behaviour is not surprising, since the maximum AVAS ELA depression reaches a similar value to that of the standard ELA driver during the period between 25ka and 20ka BP. The standard ELA driver is further depressed during the simulated build–up to the LGM, but this further depression is not reproduced by the AVAS driver. The AVAS simulation ice sheet, therefore, does not grow as big as the B5 ice sheet. During the deglaciation phase, the standard ELA is raised by about 800m. This sharp rise is not reflected by the AVAS driver. The AVAS ice sheet, therefore, keeps growing until the ELA is sufficiently raised for deglaciation to occur. The steps of the original ELA forcing function are a consequence of the inversion process, detailed in Chapter 3.2. The steps of the AVAS ELA driver reflect the size of the time step of the independent variable, i.e. the equivalent sea–level record.

Figure 5.9 shows the location of the ice margin along transects A–B and C–D indicated in Figure 4.2 as a function of time. The time–distance diagrams clearly illustrate the behaviour described above: the AVAS ice sheet does not extend as far to the South as the B5 ice sheet; and it decays later than the B5 ice sheet (see also Figure 5.10).

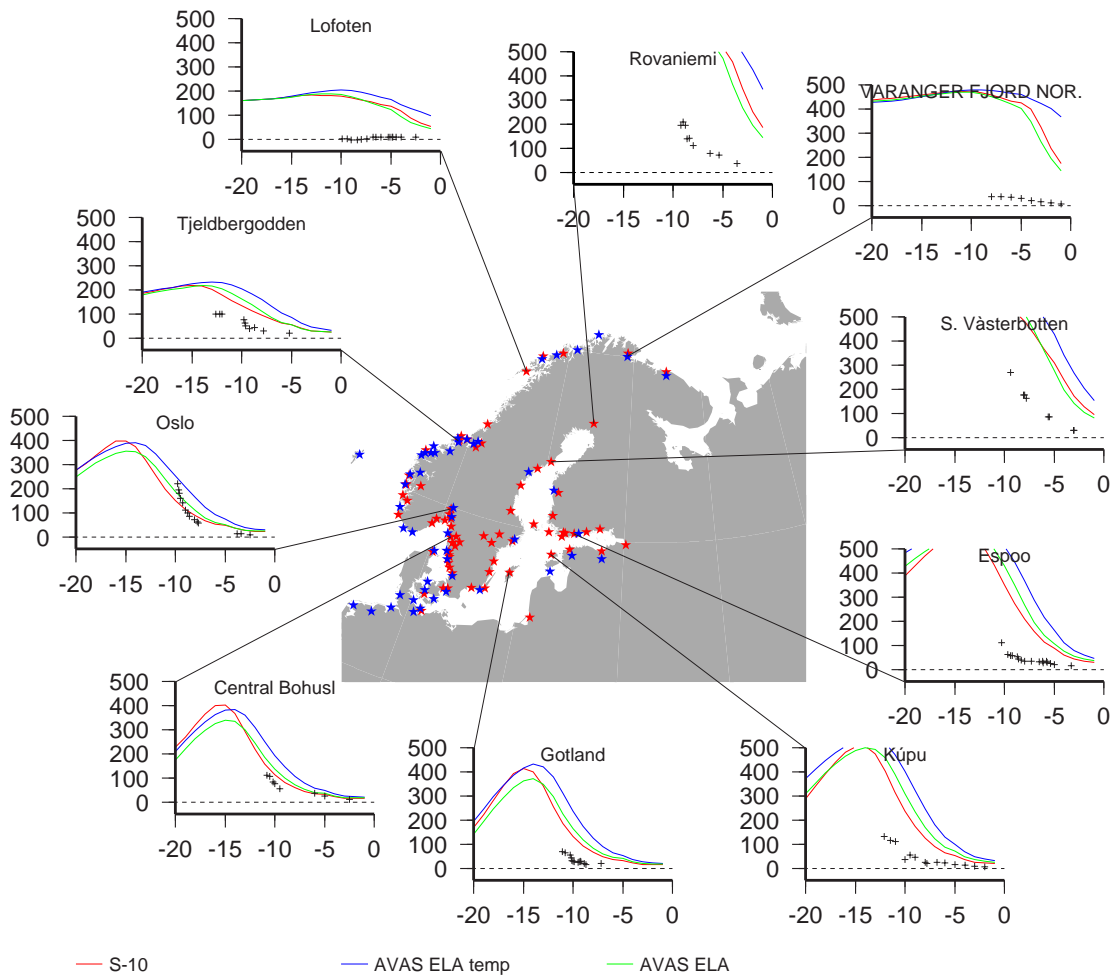


Figure 5.7: Relative sea-level change as computed by the experiment with the S-10 temperature function (red), the AVAS ELA forcing function (green) and the AVAS ELA and temperature functions (blue).

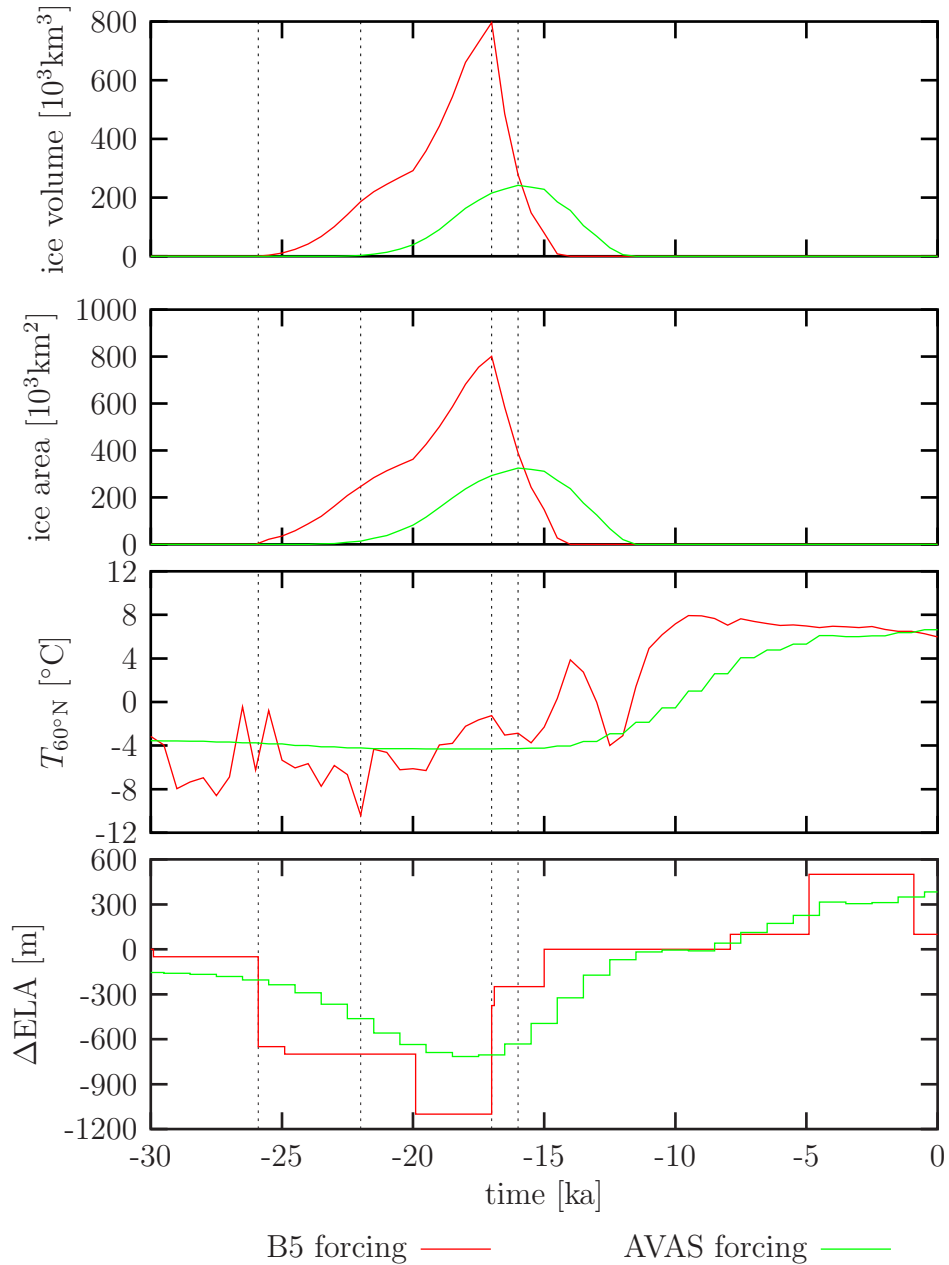


Figure 5.8: British ice sheet evolution using the B5 and AVAS climate drivers. The top two panels show ice volume and area covered by the simulated ice sheets. The lower two panels show the temperature and ELA forcing functions. The vertical lines indicate when ice growth is initiated and when the ice sheets reach their maximum size.

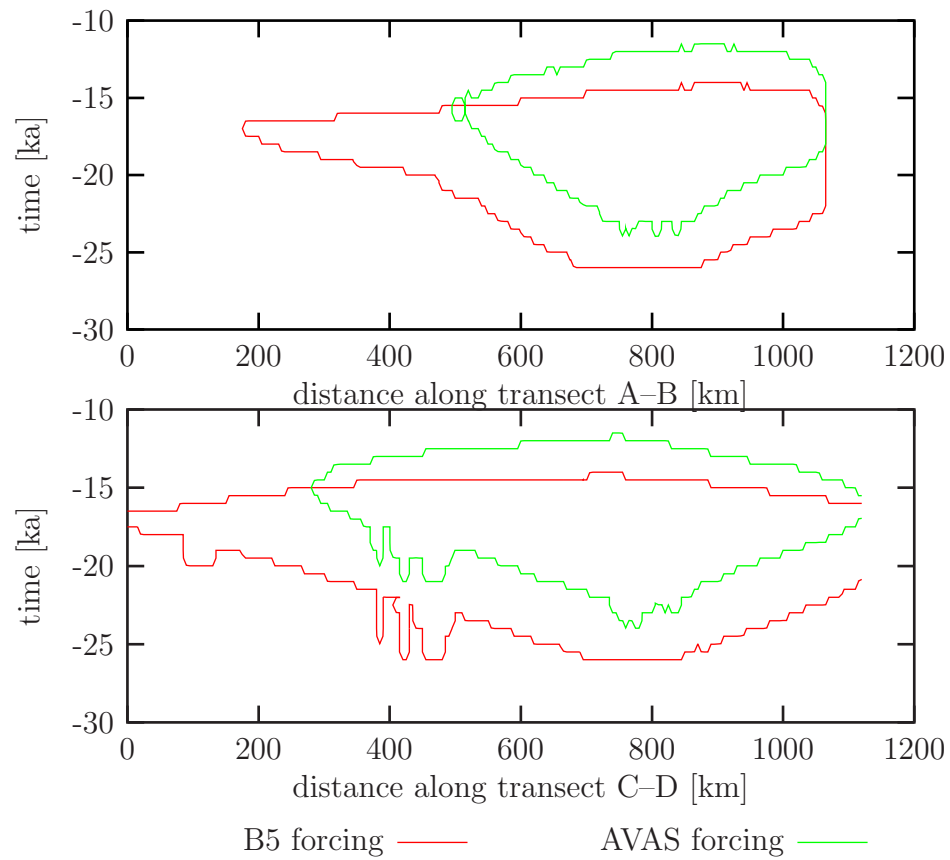


Figure 5.9: Time–distance diagrams showing the movement of the ice margin of the simulated ice sheets using the B5 and AVAS climate drivers along transects A–B and C–D indicated in Figure 4.2.

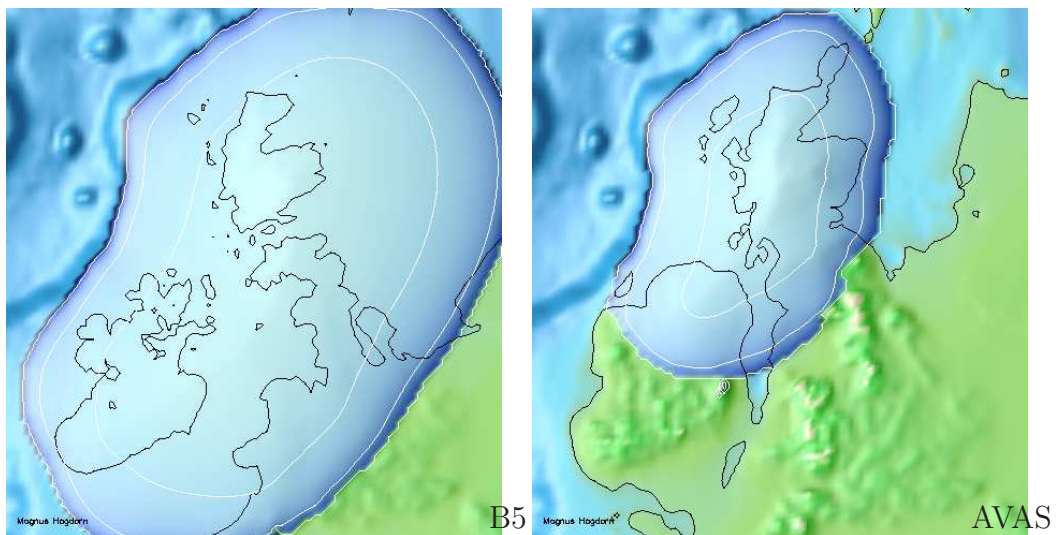


Figure 5.10: Snapshots of the maximum British ice sheet using the B5 forcing (at 17ka BP) and the AVAS forcing (at -15ka).

Simulations of the past Fennoscandian and British ice sheets using the AVAS drivers differ from the simulations using the original drivers as expected: the AVAS drivers produce smaller ice sheets because the ELA driver varies less than the original ELA forcing function. However, overall ice sheet evolution is similar. In particular, RSL simulations using the AVAS driver match the observations as well as RSL simulations using the original, S-10 driver. It seems, therefore, reasonable to use the AVAS transforms to find future climate forcing functions for simulating the evolution of the British ice sheet during the next glacial cycle. These simulations and the climate scenarios they are based on are discussed in the next section.

5.3 Simulating the Future British Ice Sheet

All experiments described so far investigated the behaviour of ice sheets in the past: the model was forced with time series derived from geological observations or by matching model behaviour with geological observations. In order to be able to simulate future ice sheet behaviour, it is necessary to obtain these boundary conditions from other modelling studies. The AVAS procedure was used to establish a relationship between equivalent sea-level change and ELA and temperature forcing. These relationships were applied to obtain future ELA and temperature forcing functions from future sea-level scenarios constructed by Goodess *et al.* (2000b) based on simulations of future climate change performed by Burgess (1998). These studies were also funded by United Kingdom Nirex Limited.

5.3.1 LLN-2D Climate Model and Future Global Sea-Level Scenarios

The LLN-2D model is a coupled, sectorially averaged atmosphere-ocean-cryosphere model developed for simulating the long-term response of the climate system to astronomical forcing (Gallée *et al.*, 1991, 1992). The model covers only the Northern Hemisphere and consists of seven sectors (sea ice, open ocean, snow field, snow-free land and the Fennoscandian, Laurentide and Greenland ice sheets). Each sector is averaged over zones of 5° of latitudinal extent. The atmospheric component is forced with changes in the seasonal and latitudinal distribution of top-of-the-atmosphere insolation and atmospheric CO_2 concentrations.

The LLN-2D model only resolves latitudinal variations and, therefore, does not include topography. The ice sheet model also depends only on latitude and has a resolution of 0.5° . It is coupled asynchronously to the climate model via the mass balance. The mathematical formulation of the LLN-2D ice sheet model also stems from the continuity equation, Equation (2.1). Lateral ice discharge is parameterised separately and assumes perfect plasticity. Longitudinal ice surface

profiles are, therefore, parabolic; their extent depends on the ice thickness at the ice divide. The Earth's response to changing surface loads is calculated using a local lithosphere and diffusive asthenosphere approximation (see Chapter 2.2.1).

Burgess (1998) used the LLN-2D model to simulate Quaternary climate (125-0ka BP) and possible future (0-150ka AP) climate scenarios (see Table 5.3). All simulations were forced by variations of the Earth's orbital parameters (see Chapter 1.3.2). The experiments for the Late Quaternary period were also forced by variations of atmospheric CO₂ concentrations derived from the Vostok ice core record (Barnola *et al.*, 1987; Jouzel *et al.*, 1993) and CO₂ concentrations estimated using a regression relationship between changes in insolation and the Vostok ice core record (Burgess, 1998). The regression relation developed on the basis of the LQ3 experiment was also applied to the period of 0-150ka AP to give the non-anthropogenically forced simulation, NAT. Anthropogenic CO₂ variations were based on emission scenarios derived from Sundquist (1990). Two basic low and high emission scenarios, termed 'Sundquist low' and 'Sundquist high' were further distinguished by assuming that the anthropogenic effects tail off after 30ka, 50ka, 100ka and 150ka. The anthropogenic CO₂ concentrations were added to the natural atmospheric CO₂ variations derived using the regression relationship.

Simulation	CO ₂ forcing	Period
LQ1	Barnola <i>et al.</i> (1987)	125-0ka BP
LQ2	Jouzel <i>et al.</i> (1993)	125-0ka BP
LQ3	Regression predicted	125-0ka BP
AN1	Sundquist low, decay 30ka AP	0-150ka AP
AN2	Sundquist high, decay 30ka AP	0-150ka AP
AN3	Sundquist low, decay 50ka AP	0-150ka AP
AN4	Sundquist high, decay 50ka AP	0-150ka AP
AN5	Sundquist low, decay 100ka AP	0-150ka AP
AN6	Sundquist high, decay 100ka AP	0-150ka AP
AN7	Sundquist low, decay 150ka AP	0-150ka AP
AN8	Sundquist high, decay 150ka AP	0-150ka AP
NAT	Regression predicted, using Jouzel <i>et al.</i> (1993)	0-150ka AP

Table 5.3: Summary of climate simulations performed by Burgess (1998) using the LLN-2D model (adapted from Goodess *et al.*, 2000b).

Northern Hemispheric ice volume simulated by the LLN-2D model using the LQ2 boundary conditions was used by Goodess *et al.* (2000b) to estimate relative sea-level data from the Huon Peninsula (Chappell and Shackleton, 1986; Chappell *et al.*, 1996) and the Barbados coral reef record (Bard *et al.*, 1990) using a linear regression model. This regression model provides the link between LLN-2D simulations and equivalent sea-level change data required by the AVAS model.

Future temperature and ELA forcing functions were then constructed using

the AVAS models described in the previous section together with the future global eustatic sea-level change scenarios of Goodess *et al.* (2000b). Figure 5.11 shows the resulting sets of future forcing functions for the CO₂ emission scenarios AN1-8 and NAT provided in Table 5.3. Simulations using the AN1-6 boundary conditions result in very similar future climate scenarios. In particular these simulations are nearly identical during the period between 100 and 110ka After Present (AP). Climate scenarios NAT and AN7,8 result in a smaller Northern Hemispheric ice volume at that time and, therefore, sea-levels do not drop as far as for scenarios AN1-6.

Behaviour of the ice sheet model is mainly determined by the mass balance forcing. Simulations of the past British ice sheet, using the AVAS driver (Figure 5.8) show that a British ice sheet can only grow when the ELA is depressed by more than 400m. Scenarios AN1-6 build-up enough ice for corresponding sea-levels to drop sufficiently far. The ELA depression reaches a maximum value of about 600m at 108ka AP. Since the scenarios where the ELA drops to sufficiently low altitudes to initiate ice sheet growth are very similar only one of the 6 scenarios was run into the future. The climate driver generated from the AN5 scenario was used to drive the ice sheet model into the future. The AN5 scenario was selected because it contains the largest sea-level change. As expected, a British ice sheet is initiated at 104ka AP and completely collapses by 112ka AP (see Figure 5.11, panels A and B).

The model was also run with the NAT and AN8 climate scenarios, in addition to the AN5 scenario, in order to be able to also calculate the hydro-isostatic component of sea-level change. Figure 5.12 shows relative sea-level change at selected sites around the British Isles for the period 0 to 150ka AP. The RSL curves are clearly dominated by the global signal.

Finally, Figure 5.13 shows snapshots of the AN5 simulation of the future British ice sheet during the period between 105ka and 119ka AP. Figure 5.13 also indicates the hydro- and glacio-isostatic adjustment of the lithosphere due to the changing water and ice masses.

5.4 Conclusion

The ice sheet model employed here does not contain a climate model that can generate a climate driver for the ice sheet model. In order to be able to simulate a future British ice sheet, it was necessary to find a way of relating output from a climate model to input to the ice sheet model. A statistical method, AVAS, was selected to find a non-linear regression relationship between climate model output and ice sheet model input. The AVAS algorithm smooths both dependent and independent variables as part of the fitting process. It is, therefore, not surprising that the resulting models produce smoothly varying climate drivers when compared with the original climate drivers. In other words, the modelled climate exhibits less severe changes.

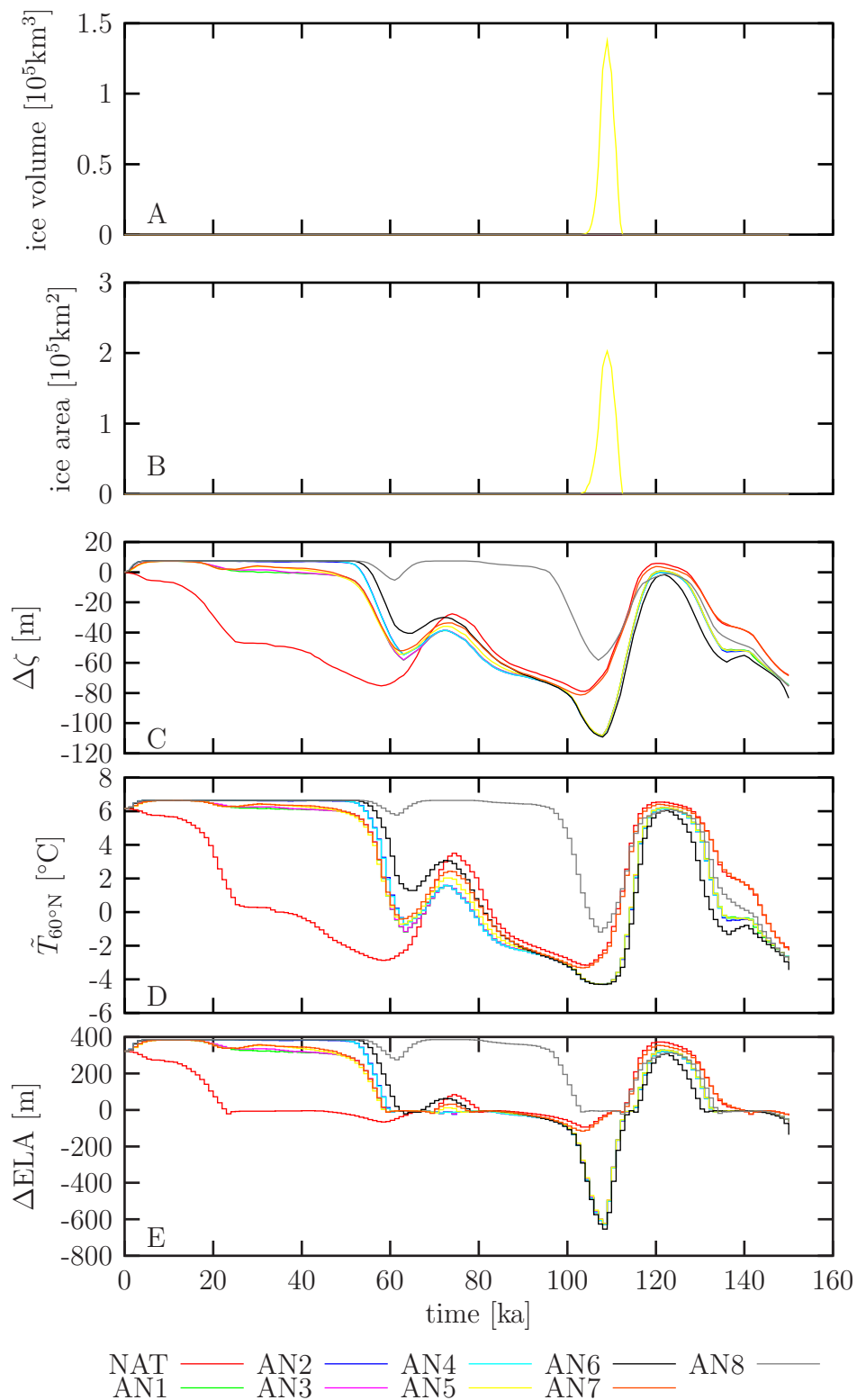


Figure 5.11: Plots of the simulated ice volume (A) and area covered by the ice sheet (B) and the corresponding forcing functions: global eustatic sea-level change (data from Goodess *et al.*, 2000b) (C), future temperature (D) and ELA forcing functions using the AVAS model together with the sea-level curves for different anthropogenic CO_2 emission scenarios (D) (see Table 5.3).

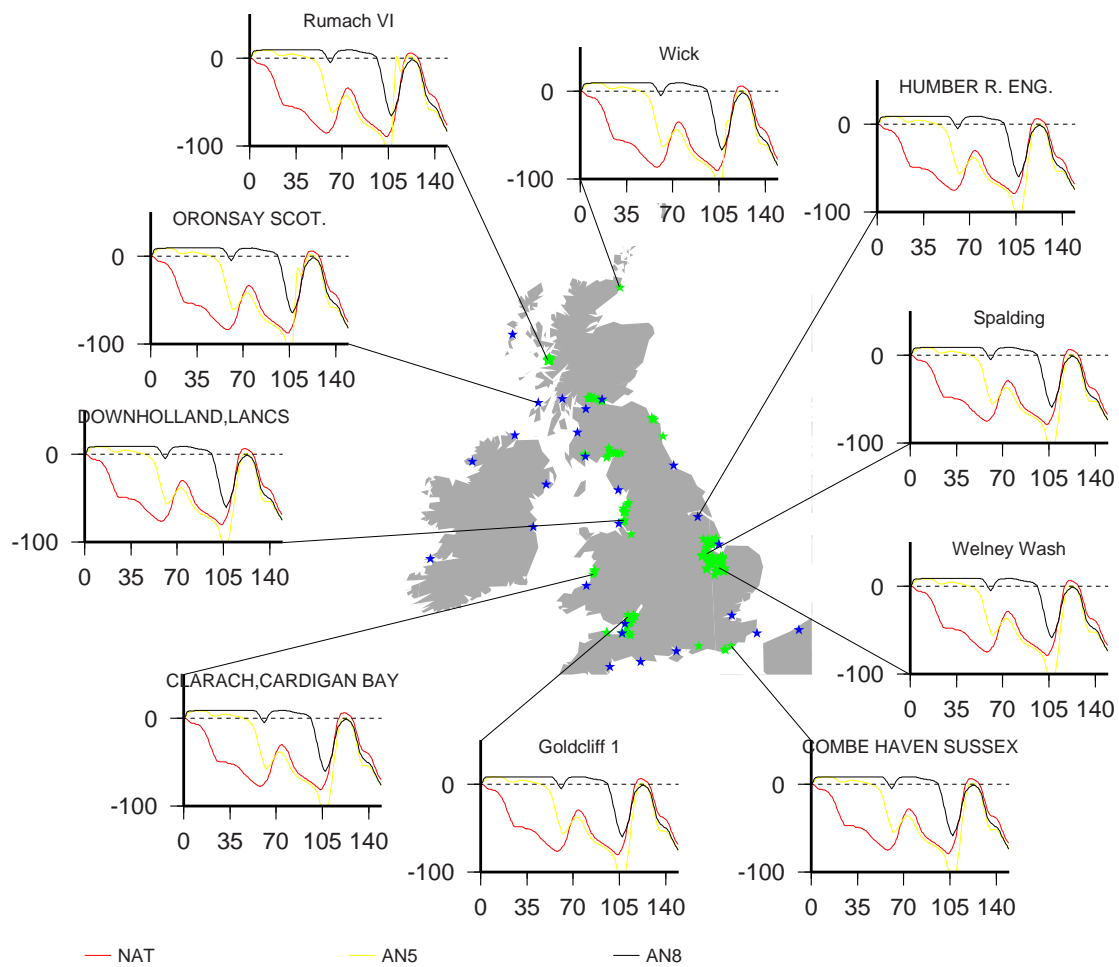


Figure 5.12: Sea-level change at selected sites for future British ice sheet simulations forced by the NAT (red), AN5 (yellow) and AN8 (black) scenarios.

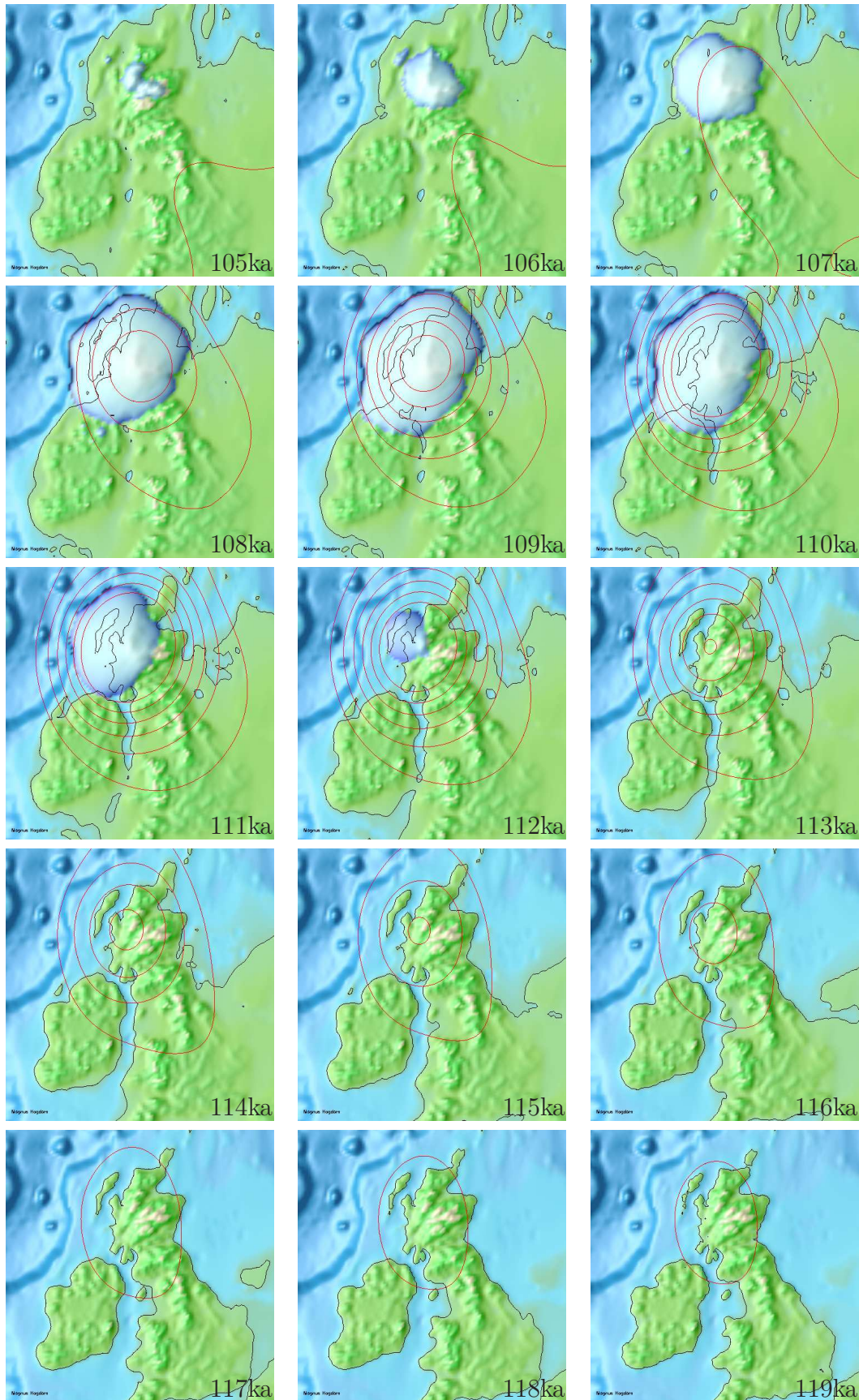


Figure 5.13: Snapshots of the future British ice sheet model forced by the AN5 climate scenario. Red contours indicate the hydro- and glacio-isostatic adjustment of the lithosphere (contoured every 10m, starting at 0m).

Simulations of the past European ice sheet using the AVAS climate drivers are similar to simulations using the original climate drivers. In particular, differences between RSL observations and simulated RSL change using the AVAS climate and differences between RSL observations and simulated RSL using the original climate drivers are of the same order of magnitude. The ice sheet model, when applied to the past European glaciation, is relatively insensitive to changes of the climate driver because of the size and location of the former European ice sheet. On the other hand, simulations of the past British ice sheet are more sensitive to changes in mass balance forcing because the British Isles are situated further South and their topography is more subdued. The simulation of the past British ice sheet using the AVAS climate driver produced a smaller ice sheet because ELA variations were less severe.

Future climate simulations were based on different CO₂ scenarios. All simulations based on increased anthropogenic CO₂ concentrations produce similar maximum Northern Hemisphere ice volumes (and thus sea-level changes) except for the two scenarios where the anthropogenic effects are assumed to tail after 150ka. The simulations that produce maximum Northern Hemisphere ice volumes only support a small British ice sheet during the period between 105ka and 119ka AP. The simulated sea-level curves are, therefore, dominated by the global, eustatic sea-level change signal.

It is interesting to note that only the post-anthropogenic scenarios produce climatic conditions supporting a British ice sheet. [Burgess \(1998\)](#) suggested that the counter-intuitive distinction in Northern Hemisphere ice volume between the natural and anthropogenically modified scenarios was due to the interplay between isostatic adjustment and net accumulation rates simulated by the LLN-2D model. Additionally, ice volumes predicted by the ice sheet model using the AVAS climate driver are considered likely to underpredict the size and duration of a future British glaciation for a given anthropogenically enhanced CO₂ concentration due to the smoothness of the climate driver used.

Chapter 6

Conclusions

6.1 Summary

This research has tried to contribute to knowledge about ice sheet behaviour within the climate system in a number of ways.

- The code of an existing three-dimensional, thermomechanical ice sheet model was improved and extended to also include a fully coupled Earth model capable of simulating sea-level change. The coupled model extended the range of model outputs that could be used to constrain the behaviour within the Earth system. The model has been developed so that it is capable of simulating ice sheets of varying complexity and configuration.
- The evolution of the past Fennoscandian ice sheet during the last glacial cycle was simulated. The simulation is consistent with geological reconstructions of the position of the ice margin along a transect and relative sea-level data in this area. It reveals significant information both about the climates compatible with the ice sheet history and the topographic constraints on ice behaviour.
- A new model was developed to include the British Isles by extending the model boundary and altering the climatic drivers. A plausible scenario for the behaviour of the combined ice sheet was simulated. Interesting aspects of behaviour were revealed by discrepancies between simulated ice sheet and geological observations. These differences highlight the spatial variability of climate during the past which is not fully resolved by the climatic drivers used here.
- The climate drivers were applied to future simulations of the next glacial cycle using a newly implemented statistical method. For the construction of future climate drivers different anthropogenic CO₂ emission scenarios were considered.

- The overall approach discussed in this thesis can be seen as a first step toward new ways of integrating detailed models that describe both ice and Earth physics in such a way that they can be simultaneously constrained by many different strands of proxy data.
- Numerous tools for data visualisation and analysis were developed. Such tools are essential for turning raw data into usefully, interpretable information with which model behaviour can be assessed and evaluated against evidence from the real world.

This brief summary is expanded in the following sections.

6.2 The Ice Sheet Model and Real Processes

A fundamental question is whether or not the ice sheet model can adequately represent the large-scale behaviour of large ice masses. In this project, a three-dimensional, thermomechanical ice sheet model was coupled to models that simulate the Earth's response to changing surface loads. The ice sheet model was run at relatively high resolutions, taking the shallow ice approximation, on which the model is based, to its limits. Run times of the ice sheet model were improved by updating the software to FORTRAN95 and reimplementing the parallelisation using MPI.

The ice sheet model used here is capable of simulating any ice sheet and has been employed to simulate a wide range of scenarios ranging from simple scenarios such as the EISMINT test cases to complex setups such as the Patagonian ice cap during the last glacial cycle. The ice sheet model can simulate 'ice streams' due to the creep instability and lithospheric adjustment at high resolutions. The general behaviour of the ice sheet model is further specified by finding solutions for particular configurations. For instance, the size and shape of the Fennoscandian ice sheet at the LGM is determined to a large extent by the position of the Scandinavian Mountains, the close proximity of the continental shelf to the West and relatively low topography to the South and East.

The simulated ice streams are regions of relatively fast flowing ice. However, they do not reach typical velocities of real ice streams. Some key processes, primarily at the ice base, are not resolved. On the other hand, the locations of the simulated ice streams, in particular the streams of the Norwegian coast and the Norwegian Channel, are realistic in spite of the unresolved processes at the basal boundary. Within the model, these 'streams' act as a mechanism to transport ice more readily via spatially constrained conducts, the net affect being to lower overall ice surface gradients.

Some of the experiments with the ice sheet model proved to be numerically unstable. These instabilities arose from the numerical treatment of the equations governing thermal evolution and the violation of the shallow ice approximation. The model could be improved by implementing a different discretisation scheme

for the thermal component. Replacing the ADI solver with an iterative solver, such as the conjugate gradient method, could further improve stability. Furthermore, this would allow larger time steps, thus reducing overall run time. Restrictions of the shallow ice approximation could be relaxed by also considering average longitudinal deviatoric stresses.

6.3 Coupling the Ice Sheet and the Lithosphere

The physics of ice sheets and the Earth operate on different characteristic spatial and temporal scales, yet they are coupled in the actual world. Simulating the nature of the feedback mechanisms operating between ice sheets and the lithosphere were an important challenge in this research.

Two approaches to simulating the Earth's response to changing ice sheets were investigated. First, the Earth's flexure due to changes of the mass distribution of ice and water was simulated by assuming that the lithosphere behaves like a thin, elastic plate on top of a viscous mantle. The second approach considers sea-level change over the entire Earth and includes sea-level change due to changing water and ice loads, changing ocean basin geometry and changes of the geoid. The approach taken was to simulate feedback mechanisms occurring between ice sheet evolution and sea-level change using initially the flat Earth approximation because its computational requirements are lower. Once the ice sheet evolution had been established, detailed sea-level curves were calculated using the spherical Earth model. These improved sea-level curves were then compared to sea-level change observations.

This approach to simulating past sea-level change differs from that taken by [Peltier \(1993\)](#) and [Lambeck \(1993b\)](#) in that the determined ice distribution is consistent with both sea-level observations *and* ice physics. The main point has been to develop a model of the coupled Earth — ice *system* rather than simply fixing one part and allowing the other part to be optimised. The simultaneous physical requirements across separate systems introduces a particular rigour when evaluating the model against sets of real data.

Run times of the spherical Earth model could be substantially reduced by reimplementing data I/O. The spherical Earth model is a global model taking the evolution of every ice sheet as input and producing sea-level change, including equivalent sea-level change, as output. Far-field ice sheets are currently not accounted for by the spherical Earth model. They could be included as boundary conditions. On the other hand, far-field effects are small except for equivalent sea-level change. Regional, planar Earth models might well be more suited to use with an ice sheet model, given the current misfit between sea-level observations and sea-level change due to the simulated ice sheet.

6.4 Model Simulations

A principle scientific focus for this research was to be able to explain via model simulations aspects of the functioning of past ice behaviour in specific localities, namely Fennoscandia and the British Isles and to use these insights to simulate the behaviour of a potential future British ice sheet.

6.4.1 Simulations of Past Ice Sheet Activity

The Past Fennoscandian Ice Sheet

The past Fennoscandian ice sheet was reconstructed by applying three forcing functions describing equivalent sea-level change, surface temperatures and mass balance. Of the three drivers, mass balance is the most important in determining the evolution of the ice sheet. The mass balance is assumed to vary parabolically around the ELA. The ELA, in turn, is found by fitting the ice sheet evolution to a reconstruction of the Fennoscandian ice sheet along a transect in southwestern Scandinavia. The simulation of the Fennoscandian ice sheet fits geological reconstructions and sea-level observations in the area covered by the transect reasonably well. Outside this area, in particular at the northeastern margin of the simulated region, the simulation was unconstrained and the fit with observations is poor.

The Past British Ice Sheet

In order to be able to simulate a British ice sheet compatible with geological reconstructions of its extent, it was necessary to introduce a strong longitudinal ELA gradient. This gradient can be partly justified by assuming that the past British climate was very maritime. However, the required ELA depression is very large, which suggests that the mass balance parameterisation may not be well suited for a simulation of the past British ice sheet. This view is further supported by the fact that the simulation leads to a single ice dome, which is incompatible with geological evidence. Furthermore, the ELA driver used does not resolve the readvance of the British ice sheet during the Younger Dryas.

On the other hand, the overall configuration of the combined Fennoscandian and British ice sheet is plausible. In particular, the simulated ice cover of the North Sea and the Norwegian Channel Ice Stream are in good agreement with geological reconstructions.

These results suggest a number of obvious possible improvements. There are two major misfits arising from the particular mass balance driver chosen: i) the simulated LGM occurs about 4ka later than usually assumed and ii) the northeastern part of the Fennoscandian ice sheet is too large and decays too late. The first misfit can be fixed relatively easily by adjusting the overall timing of events. The second problem, together with the results from the British simulations, suggest that the mass balance distribution is more varied than

assumed and highlight the spatial variability of climate during the past. Clearly, more reconstructions of past ice extent, in particular from different regions, would have to be employed to improve the mass balance driver. In particular the latitudinal dependence of the ELA driver needs to be reassessed and improved. Furthermore, the new climate driver should also account for key events such as the readvance of the British ice sheet during the Younger Dryas.

6.4.2 The Future British Ice Sheet

The fit of the model with geological reconstructions of both the Fennoscandian and British ice sheet could be improved substantially. However, I chose to complete the entire process, described in Chapter 1.5, in order to demonstrate the methodology. The model setup and forcing used are an initial attempt to fitting modelled ice sheet evolution to the geological record.

The climate drivers of simulations of both the past Fennoscandian and the past British ice sheet depend on geological observations. Climate drivers for simulation of a future British ice sheet had to be based on simulations of future climate change. A non-linear regression method was used to relate future temperature and ELA variations to future sea-level change simulated elsewhere. As a consequence of the regression method used, the climate drivers, in particular the ELA driver, are very smoothed. Model runs with these climate drivers, therefore, exhibit very limited glaciations in Britain.

The problems described above are difficult to solve within the employed mass balance forcing framework. Recognising this limitation, simulations of the future glaciation of the British Isles were undertaken without improving the simulation of the past British ice sheet. This simplification does not affect the logic of the approach taken. However, it does mean that the results obtained should not be considered realistic at detailed spatial and temporal scales.

6.4.3 Linking Ice Sheets to Climate

The experience of developing and manipulating a variety of climate drivers for different model settings is illustrative of some of the underlying difficulties associated with coupling ice sheet models and climate.

Generating boundary conditions for future ice sheet model runs is difficult, as the various models involved operate on different scales. The climate model used here is driven by time series of the Earth's orbital parameters. Orbital parameters could also be used as independent variables, in addition to equivalent sea-level change, to model the climate drivers for the ice sheet using the statistical method employed here. However, this approach would have the obvious drawback that anthropogenic effects could not be included.

In terms of being able to assess the safety of nuclear waste repositories, it might be sufficient to consider snapshots of specific scenarios. Detailed climate simulations using general circulation models could be performed. The GCM

output could then be used to construct climate drivers for the ice sheet model. This approach corresponds to simulations of the LGM ice sheet using a GCM climate as input. Integrated techniques using results from EMICs, GCMS and regional climate models are under development in the, EU-funded, BIOCLIM¹ project.

The problem of deriving climate models at suitable temporal and spatial scales remains only partly resolved and represents a major challenge for future research. Ideally, the requirements to specify climatic boundary conditions would be relaxed and the ice sheet model would be coupled to a climate model that is free to evolve and adjust to changing conditions set by the evolving ice sheet.

6.5 Using and Developing Models

The improvements to the modelling software environment mean that it is now easier to understand, maintain and expand the model. Additionally, these improvements also allow the model to be run on a range of computer systems; new target platforms can be easily added because only standard programming features and freely available libraries were used.

Numerical models produce large amounts of data. In particular, this ice sheet mode can easily produce many hundreds of Megabytes of data. This large amount of numbers is meaningless if it cannot be analysed and visualised. Numerous programs were, thus, developed to do this. Again, these technical improvements mean that it is now easier to use the model and greater sense can be made of the simulations with greater speed. Models are used to gain understanding of how natural systems work. Having models which are easier to operate, therefore, means that it is easier to experiment more widely in our understanding of these systems.

Data analysis and visualisation tools, together with the model itself, are a huge intellectual investment and cannot really be managed by a single person or group of persons. Scientific progress is made by sharing ideas and knowledge. The Open Source Software Movement² has demonstrated how shared software development can produce very good software at the cost of a little effort from the individual. The climate modelling community is in the process of defining standard model infrastructure and interfaces which are used to couple individual model components to form Earth System Models³. I think that the ice sheet modelling community could also greatly benefit from developing a commonly used ice sheet model. This model could then also be integrated into the wider Earth System Modelling effort.

¹<http://www.andra.fr/bioclim/>

²<http://www.opensource.org/>

³ PROgram for Integrated Earth System Modeling: <http://prism.enes.org/>
The Earth System Grid: <http://www.earthsystemgrid.org/>

6.6 Multi–Proxy Data and Inverse Approaches

The principle of seeking model solutions that cohere well with evidence across a number of elements of the climate system has been a major underlying principle of this research. It has been illustrated to operate specifically in coupling the ice sheet with the Earth and using simultaneously glacial extent and sea–levels as potential constraints on past ice behaviour. The approach could easily be extended to include other aspects of the Earth — ice sheet — climate system, refining different parts of the model with other strands of evidence.

The idea of using different data sets to constrain the past ice sheet behaviour was introduced in Chapter 1.3. The manual inversion procedure adopted for finding the past climate driver utilises only a small fraction of the available geological information of past ice sheet activity. In addition to using more data relating to past ice extent and relative sea–level records, other forms of geological evidence could be used. There is a great wealth of flow–directional features that could be used to constrain basal boundary conditions. The distribution of glaciogenic sediments and erratic dispersal patterns provides more constraints. These features can be modelled and, therefore, also used for inversion.

6.6.1 Data Management

This wealth of data is not very accessible. It would greatly help if the raw geological observations and their interpretations were collected in digital form. A geographic information system (GIS) could be setup to access the data. Furthermore, tools used for visualising ice sheet model results could be integrated with the GIS. Ice sheet model output could then be directly compared with the geological evidence available. The SLIP⁴ project attempts to integrate data collections and numerical ice sheet models using GIS.

6.6.2 An Automatic Inversion Procedure

Computers are becoming more and more powerful and a full inversion of the Earth — ice sheet — climate system might be possible. It is, therefore, worth considering how such an inversion might work. An idea is to automate the manual inversion procedure described here using a genetic algorithm: the model could be run forward in time for a short interval using various different boundary conditions. The branch that produces the best fit with observations would then be selected and the process repeated for the next time interval. One problem with this procedure might be that the overall solution could potentially diverge from the ‘best’ solution if, at some time step, the ‘wrong’ branch was selected. On the other hand this risk could be reduced by using multi–proxy data sets as suggested above. This scheme can only work with more flexible ice sheet models and good

⁴Southern Laurentide Ice–Sheet Project: <http://www.geology.wisc.edu/~slip/>

digital data collections. By the time these are in place, computers might well be powerful enough to tackle this problem.

Overall we want to better understand ice sheet behaviour during the Past, Present and Future. Models form an essential part of this undertaking. The large-scale behaviour of ice sheets is reasonably well understood and modelled. Problems occur when the ice sheet model is coupled to other parts of the Earth system. Models are best understood when there is evidence against which they can be evaluated. Confidence in the model to adequately represent the real operation of the system can be increased if a range of proxies can be simultaneously fitted. This research has tried to take some steps in this direction.

Appendix A

Mathematical Definitions

A.1 Kelvin Functions

$$\text{Ber}(x) = \sum_{j=0}^{\infty} \frac{(x/2)^{4j}}{((2j)!)^2} (-1)^j \quad (\text{A.1})$$

$$\text{Bei}(x) = \sum_{j=0}^{\infty} \frac{(x/2)^{4j+2}}{((2j+1)!)^2} (-1)^j \quad (\text{A.2})$$

$$\text{Ker}(x) = -[\ln(x/2) + \gamma] \text{Ber}(x) + \frac{\pi}{4} \text{Bei}(x) + \sum_{j=1}^{\infty} \frac{(x/2)^{4j}}{((2j)!)^2} \phi(2j) (-1)^j \quad (\text{A.3})$$

$$\text{Kei}(x) = -[\ln(x/2) + \gamma] \text{Bei}(x) - \frac{\pi}{4} \text{Ber}(x) + \sum_{j=0}^{\infty} \frac{(x/2)^{4j+2}}{((2j+1)!)^2} \phi(2j+1) (-1)^j \quad (\text{A.4})$$

where $\phi(n) = \sum_{j=1}^n \frac{1}{j}$ and the Euler constant $\gamma = 0.577215664901532860606512$ (Spiegel, 1968). The derivatives of the zeroth order Kelvin functions are:

$$\text{Ber}'(x) = \sum_{j=1}^{\infty} \frac{2j(x/2)^{4j-1}}{((2j)!)^2} (-1)^j \quad (\text{A.5})$$

$$\text{Bei}'(x) = \sum_{j=0}^{\infty} \frac{(2j+1)(x/2)^{4j+1}}{((2j+1)!)^2} (-1)^j \quad (\text{A.6})$$

$$\begin{aligned} \text{Ker}'(x) = & -[\ln(x/2) + \gamma] \text{Ber}'(x) - \frac{1}{x} \text{Ber}(x) + \frac{\pi}{4} \text{Bei}'(x) \\ & + \sum_{j=1}^{\infty} \frac{2j(x/2)^{4j-1}}{((2j)!)^2} \phi(2j) (-1)^j \end{aligned} \quad (\text{A.7})$$

$$\begin{aligned} \text{Kei}'(x) = & -[\ln(x/2) + \gamma] \text{Bei}'(x) - \frac{1}{x} \text{Bei}(x) - \frac{\pi}{4} \text{Ber}'(x) \\ & + \sum_{j=0}^{\infty} \frac{(2j+1)(x/2)^{4j+1}}{((2j+1)!)^2} \phi(2j+1) (-1)^j \end{aligned} \quad (\text{A.8})$$

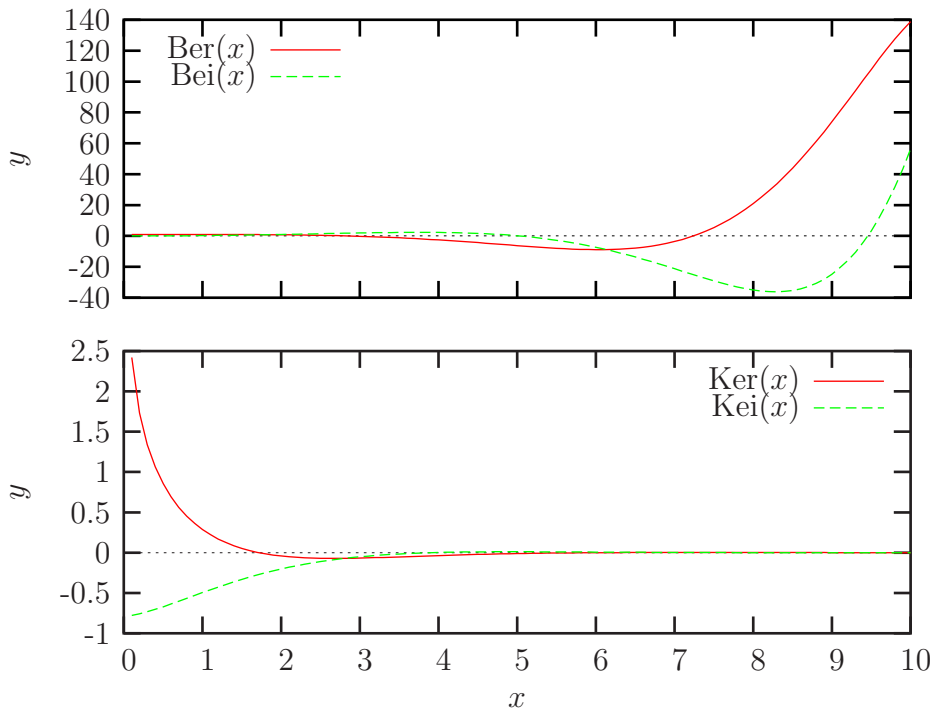
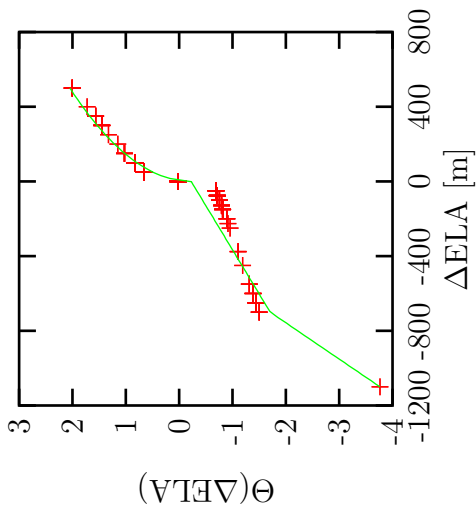


Figure A.1: Plots of the Kelvin functions on the interval $[0,10]$.

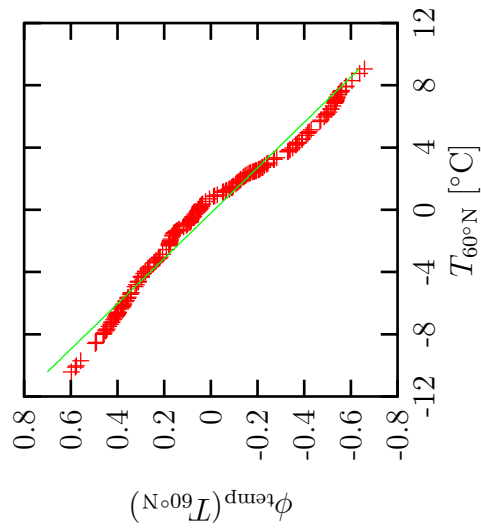
A.2 AVAS transforms

A.2.1 ELA Model 1



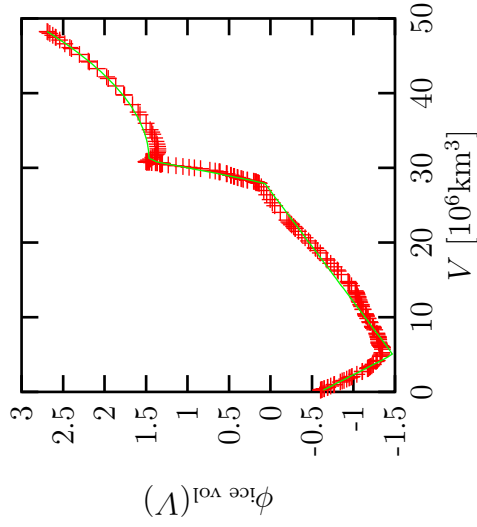
$$\Theta(\Delta\text{ELA}) = \begin{cases} -700c + b + d(\Delta\text{ELA} + 700) & : \Delta\text{ELA} \leq -700 \\ c\Delta\text{ELA} + b & : -700 < \Delta\text{ELA} < 0 \\ a\sqrt{\Delta\text{ELA}} + b & : \Delta\text{ELA} \geq 0 \end{cases}$$

$$\begin{aligned} a &= 0.101712 \pm 0.002217 & b &= -0.226164 \pm 0.02057 \\ c &= 0.00211412 \pm 7.709 \cdot 10^{-05} & d &= 0.00514556 \pm 0.000396 \end{aligned}$$



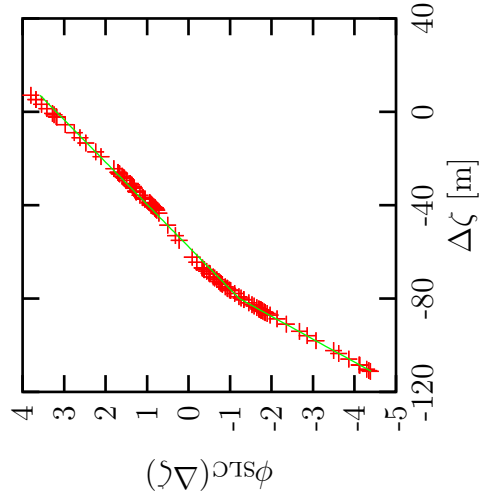
$$\phi_{\text{temp}}(T_{60^\circ\text{N}}) = aT_{60^\circ\text{N}} + b$$

$$a = -0.0686234 \pm 0.0006649 \quad b = -0.0147739 \pm 0.003083$$



$$\phi_{\text{ice vol}}(V/10^{15}) = \begin{cases} aV + b & : V < 5 \\ 5a + b + c(V - 5) & : 5 \leq V < 28 \\ 5a + b + 23c + d(V - 28) & : 28 \leq V < 31 \\ 5a + b + 23c + 3d + e(V - 31)^2 & : x \geq 31 \end{cases}$$

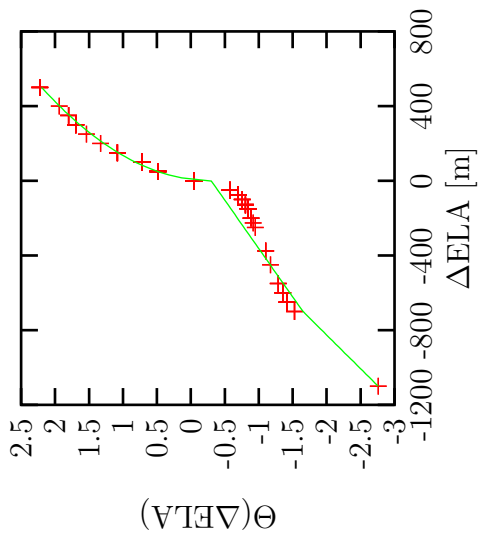
$$\begin{aligned} a &= -0.176288 \pm 0.004484 & b &= -0.593743 \pm 0.01822 \\ c &= 0.0673502 \pm 0.0007436 & d &= 0.463002 \pm 0.005522 \\ e &= 0.00412885 \pm 8.348 \cdot 10^{-05} \end{aligned}$$



$$\phi_{\text{SLC}}(\Delta\zeta) = \begin{cases} a(\Delta\zeta + 80) + b & : \Delta\zeta < -80 \\ c(\Delta\zeta + 80) + b & : \Delta\zeta \geq -80 \end{cases}$$

$$\begin{aligned} a &= 0.101943 \pm 0.0008441 & b &= -1.22348 \pm 0.009756 \\ c &= 0.0551435 \pm 0.0002315 \end{aligned}$$

A.2.2 ELA Model 2



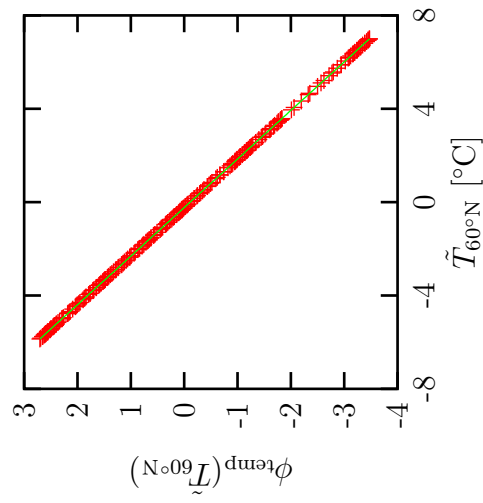
$$\Theta(\Delta\text{ELA}) = \begin{cases} -700c + b + d(\Delta\text{ELA} + 700) & : \Delta\text{ELA} \leq -700 \\ c\Delta\text{ELA} + b & : -700 < \Delta\text{ELA} < 0 \\ a\sqrt{\Delta\text{ELA}} + b & : \Delta\text{ELA} \geq 0 \end{cases}$$

$$a=0.111674 \pm 0.00186$$

$$b=-0.300073 \pm 0.01726$$

$$c=0.00192952 \pm 6.468 \cdot 10^{-05}$$

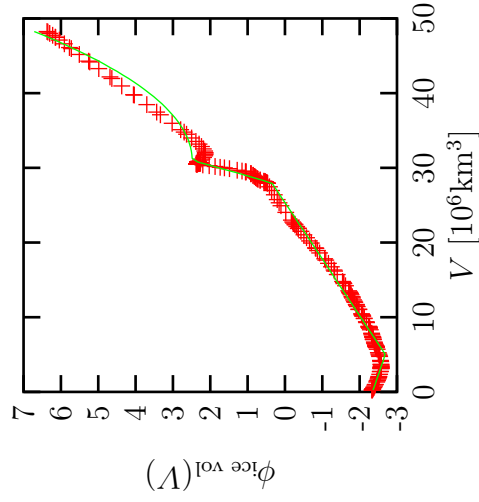
$$d=0.00277148 \pm 0.0003322$$



$$\phi_{\text{temp}}(\tilde{T}_{60^{\circ}\text{N}}) = a\tilde{T}_{60^{\circ}\text{N}} + b$$

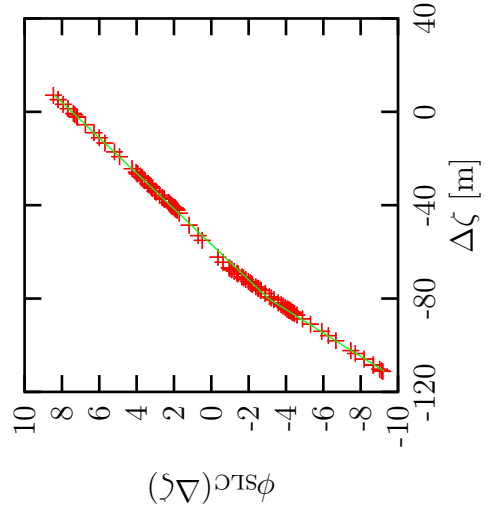
$$a=-0.480556$$

$$b=-0.111907$$



$$\phi_{\text{ice vol}}(V/10^{15}) = \begin{cases} aV + b & : V < 5 \\ 5a + b + c(V - 5) & : 5 \leq V < 28 \\ 5a + b + 23c + d(V - 28) & : 28 \leq V < 31 \\ 5a + b + 23c + 3d + e(V - 31)^2 & : x \geq 31 \end{cases}$$

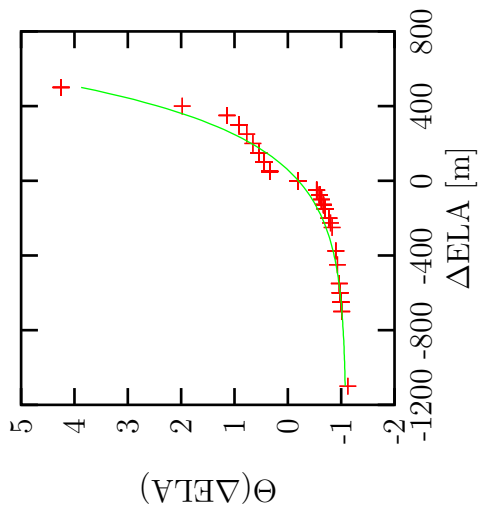
$$\begin{aligned} a &= -0.0690452 \pm 0.01082 & b &= -2.34279 \pm 0.04399 \\ c &= 0.131991 \pm 0.001795 & d &= 0.712066 \pm 0.01333 \\ e &= 0.0141885 \pm 0.0002015 \end{aligned}$$



$$\phi_{\text{SLIC}}(\Delta\zeta) = \begin{cases} a(\Delta\zeta + 80) + b & : \Delta\zeta < -80 \\ c(\Delta\zeta + 80) + b & : \Delta\zeta \geq -80 \end{cases}$$

$$\begin{aligned} a &= 0.199198 \pm 0.001253 & b &= -3.0612 \pm 0.01448 \\ c &= 0.131666 \pm 0.0003437 \end{aligned}$$

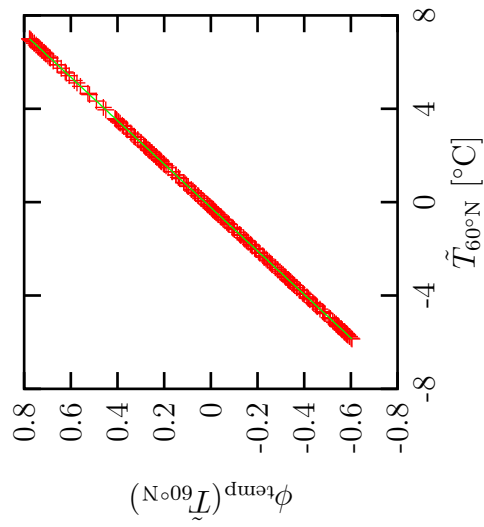
A.2.3 ELA Model 3



$$\Theta(\Delta\text{ELA}) = ae^{bx} + c$$

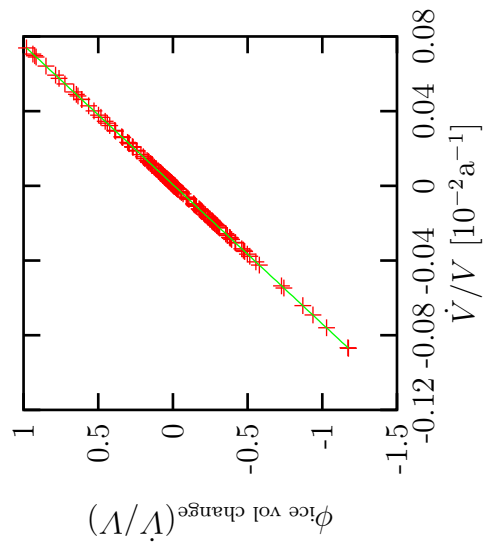
$$a = 0.896725 \pm 0.05475 \quad b = 0.00342465 \pm 0.000117$$

$$c = -1.09515 \pm 0.05166$$



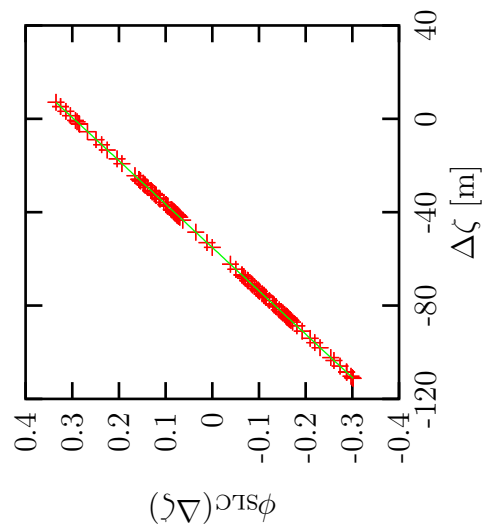
$$\phi_{\text{temp}}(\tilde{T}_{60^\circ\text{N}}) = a\tilde{T}_{60^\circ\text{N}} + b$$

$$a = 0.107469 \quad b = 0.0250262$$



$$\phi_{\text{ice vol change}}(\dot{V}/V) = a(\dot{V}/V) + b$$

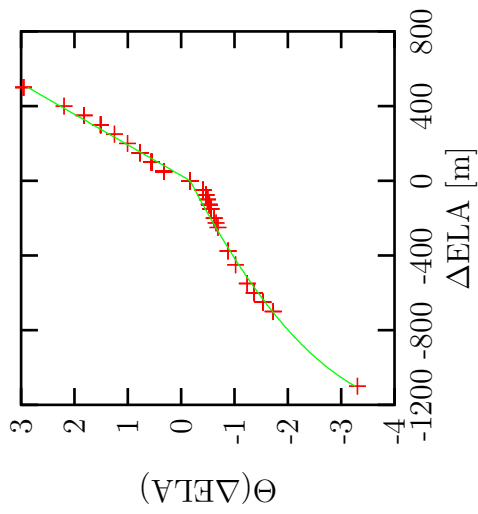
$$a=1340.35 \quad b=-0.0094071$$



$$\phi_{\text{SLIC}}(\Delta\zeta) = a\Delta\zeta + b$$

$$a=0.00538345 \quad b=0.296775$$

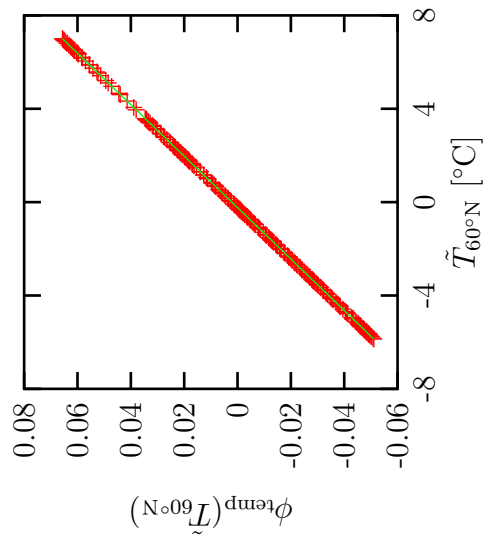
A.2.4 ELA Model 4



$$\Theta(\Delta\text{ELA}) = \begin{cases} a\sqrt{\Delta\text{ELA}} + b + c & : \Delta\text{ELA} \leq 0 \\ a\sqrt{b} + c + d\Delta\text{ELA} & : \Delta\text{ELA} > 0 \end{cases}$$

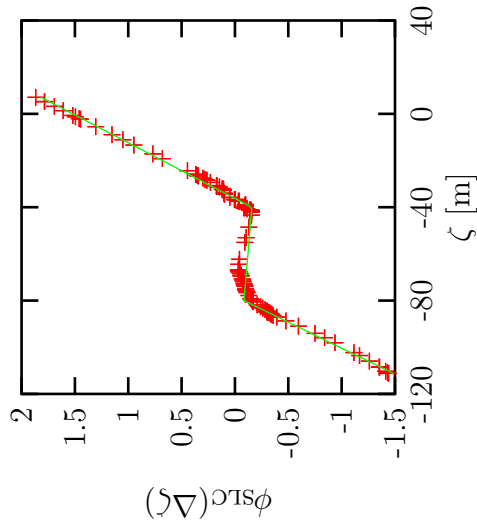
$$a = 0.125492 \pm 0.004421 \quad b = 1199.77 \pm 36.23$$

$$c = -4.51722 \pm 0.2106 \quad d = 0.006087 \pm 6.124 \cdot 10^{-5}$$



$$\phi_{\text{temp}}(\tilde{T}_{60^\circ\text{N}}) = a\tilde{T}_{60^\circ\text{N}} + b$$

$$a = 0.00907729 \quad b = 0.00210428$$

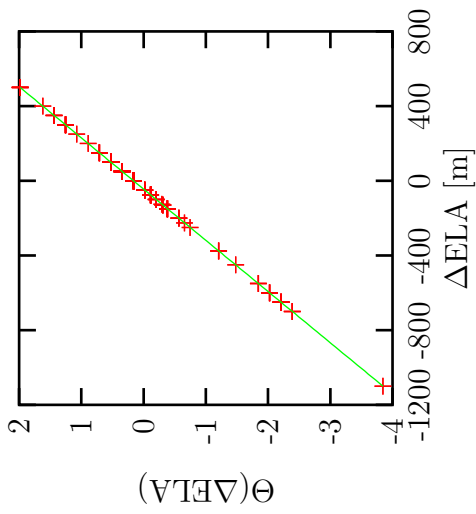


$$\phi_{\text{SLC}}(\Delta\zeta) = \begin{cases} a * \Delta\zeta + b & : \Delta\zeta < -80 \\ -80a + b + c(\Delta\zeta + 80) & : -80 \geq \Delta\zeta < -40 \\ -80a + b + 40c + d(\Delta\zeta + 40) & : \Delta\zeta \geq -40 \end{cases}$$

$$a=0.0448439 \pm 0.0004111 \quad b=3.50265 \pm 0.03626$$

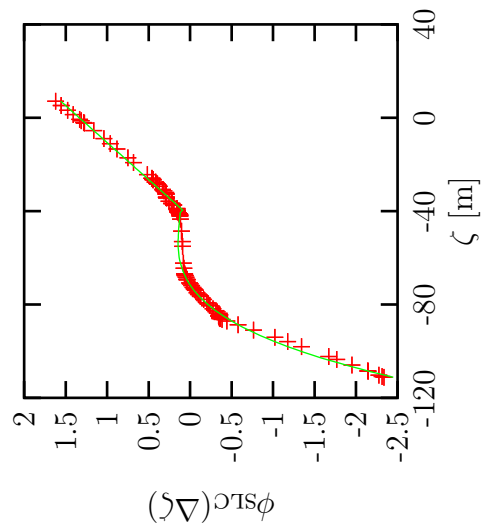
$$c=-0.00183332 \pm 0.0001889 \quad d=0.0419528 \pm 0.0002554$$

A.2.5 ELA Model 5



$$\Theta(\Delta\text{ELA}) = a\Delta\text{ELA} + b$$

$$a=0.00364524 \quad b=0.162145$$



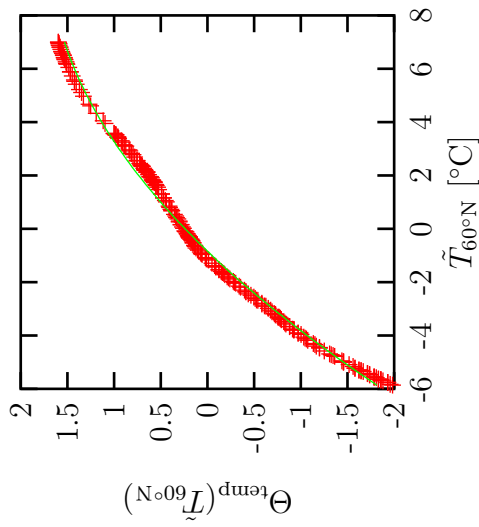
$$\phi_{\text{SIRC}}(\Delta\zeta) = \begin{cases} a(\Delta\zeta + b)^3 + c\Delta\zeta & : \Delta\zeta < -40 \\ d\Delta\zeta + e & : \Delta\zeta \geq -40 \end{cases}$$

$$a=8.6806 \cdot 10^{-6} \pm 2.974 \cdot 10^{-7} \quad b=42.8251 \pm 0.8673$$

$$c=-0.00289953 \pm 0.0001926 \quad d=0.0315223 \pm 0.0003621$$

$$e=1.33513 \pm 0.01007$$

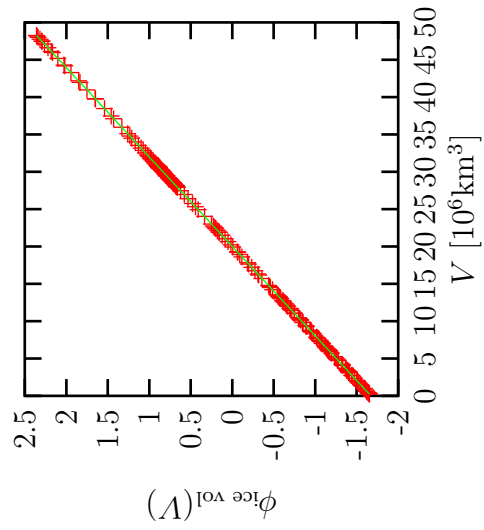
A.2.6 Temperature Model 1



$$\Theta(\tilde{T}_{60^{\circ}\text{N}}) = a\tilde{T}_{60^{\circ}\text{N}}^2 + b\tilde{T}_{60^{\circ}\text{N}} + c$$

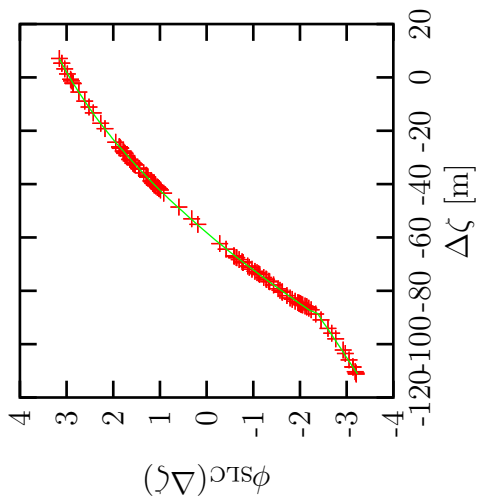
$$a = -0.0128553 \pm 0.0003581 \quad b = 0.274909 \pm 0.001343$$

$$c = 0.238335 \pm 0.006919$$



$$\phi_{\text{ice vol}}(V/10^{15}) = aV + b$$

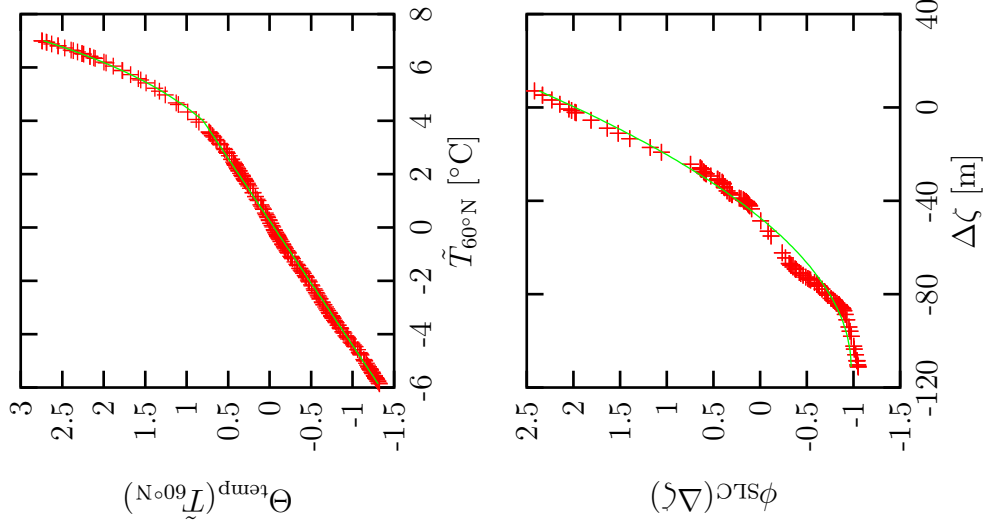
$$a = 0.0835304 \quad b = -1.67205$$



$$\phi_{\text{SLC}}(\Delta\zeta) = \begin{cases} a\Delta\zeta + b & : \Delta\zeta \leq -88 \\ -88a + b + c\Delta\zeta^2 + d\Delta\zeta + e & : \Delta\zeta > -88 \end{cases}$$

$$\begin{aligned} a &= 0.0378214 \pm 0.0004406 & b &= 0.970955 \pm 0.04516 \\ c &= -0.00029129 \pm 1.662 \cdot 10^{-06} & d &= 0.0334757 \pm 0.0001609 \\ e &= 5.29138 \pm 0.00786 \end{aligned}$$

A.2.7 Temperature Model 2



$$\Theta(\tilde{T}_{60^\circ\text{N}}) = \begin{cases} a\tilde{T}_{60^\circ\text{N}} + b & : \tilde{T}_{60^\circ\text{N}} < 4 \\ 4a + b + c(\exp(dx) - \exp(4d)) & : \tilde{T}_{60^\circ\text{N}} \geq 4 \end{cases}$$

$$\begin{aligned} a &= 0.213751 \pm 0.0005456 & b &= -0.0539003 \pm 0.001705 \\ c &= 0.288469 \pm 0.03011 & d &= 0.336189 \pm 0.01225 \end{aligned}$$

$$\begin{aligned} \phi_{\text{SLC}}(\Delta\zeta) &= a(x+b)^2 + c \\ a &= 0.00023964 \pm 6.257 \cdot 10^{-6} & b &= 111.019 \pm 1.554 \\ c &= -0.973846 \pm 0.01924 \end{aligned}$$

Appendix B

Software

B.1 CD-ROM

The CD-ROM included in a wallet at the back of the thesis contains electronic versions of this document, raw data files and additional images and animations of the simulations. The contents of the CD-ROM can be accessed via the `index.html` file located on the CD-ROM using a web browser. Alternatively, the data can be accessed directly. The data is split up into the following directories:

`thesis` There are three electronic copies of my thesis included on this CD-ROM. The pdf version is optimised for use on screen and contains clickable hyperreferences. The gzip'ed postscript version of the thesis is ideal for printing. Both versions are single space. Finally, there is also a gzip'ed postscript version of the official, double-space thesis.

`data` netCDF data files containing results from the combined European/British experiment of the last glacial cycle (120ka BP to present) and the future British ice sheet experiments AN5, AN8 and NAT (present to 150ka AP).

`animations` The animations included show i) a perspective view of the evolving Fennoscandian ice sheet using the S-10 boundary conditions; ii) ice surface and relative sea-level change of the combined European/British ice sheet experiment and iii) surface velocities of the ice sheet over the North Sea. The animations are encoded using two standard algorithms and should be viewable with any player software.

`images` The `images` directory contains snapshots of the the combined European/British experiment of the last glacial cycle (120ka BP to present) and the future British ice sheet experiments AN5, AN8 and NAT (present to 150ka AP). Furthermore, individual sea-level curves for all observation sites are also included.

The `index.html` file also contains links to the websites describing the Open Source software used throughout this project.

B.2 File Description

Dimensions		
Name	Size	Description
x	fixed length	first horizontal dimension
y	fixed length	second horizontal dimension
z	fixed length	vertical dimension
time	unlimited length	time
Global Attributes		
parameters specifying the grid and defining the Albers Equal Area Conic projection		
Name	Description	
long_ll	longitude of lower left corner	
lat_ll	latitude of lower left corner	
long_ur	longitude of upper right corner	
lat_ur	latitude of upper right corner	
xyscale	grid-node spacing	
semi_major_axis	of the Earth	
semi_minor_axis	of the Earth	
origin_latitude	latitude of projection centre	
central_meridian	longitude of projection centre	
std_parallel_1	1st standard parallel	
std_parallel_2	2nd standard parallel	
false_easting	false easting	
false_northing	false northing	
tolerance	of projection calculation	
Variables		
Name	Units	Description
x(x)	m	first horizontal axis
y(y)	m	second horizontal axis
z(z)	m	vertical axis
time(time)	a	model times
timestep(time)	a	timestep size
ih(time,y,x)	m	ice thickness
ihdt(time,y,x)	m	change in ice thickness
rh(time,y,x)	m	bedrock height
eus(time)	m	eustatic sea level change
rhdh(time,y,x)	ma ⁻¹	change of bedrock height
mbal(time,y,x)	ma ⁻¹	surface mass balance
ela(time,y,x)	m	equilibrium line altitude (ELA)
<i>continued on next page</i>		

<i>continued from previous page</i>		
<code>pmdt(time,y,x)</code>	$^{\circ}\text{C}$	basal temperature (corrected for pressure melting point)
<code>surft(time,y,x)</code>	$^{\circ}\text{C}$	surface temperature
<code>melt(time,y,x)</code>	ma^{-1}	melt rate
<code>cony(time,y,x)</code>	1	continentality
<code>lat(time,y,x)</code>	$^{\circ}\text{N}$	latitude
<code>long(time,y,x)</code>	$^{\circ}\text{E}$	longitude
<code>calv(time,y,x)</code>	ma^{-1}	calving rate
<code>land(time,y,x)</code>	1	land mask
<code>smask(time,y,x)</code>	1	slide mask
<code>meand(time,y,x)</code>	m^2a^{-1}	mean diffusivity
<code>slide(time,y,x)</code>	m^2a^{-1}	sliding diffusivity
<code>slc(time,y,x)</code>	m	sea level change
<code>vx(time,z,y,x)</code>	ma^{-1}	x-component of velocity
<code>vy(time,z,y,x)</code>	ma^{-1}	y-component of velocity
<code>vz(time,z,y,x)</code>	ma^{-1}	z-component of velocity
<code>hvx(time,y,x)</code>	ma^{-1}	vertically averaged velocity: x-component
<code>hvy(time,y,x)</code>	ma^{-1}	vertically averaged velocity: y-component
<code>svx(time,y,x)</code>	ma^{-1}	surface velocity: x-component
<code>svy(time,y,x)</code>	ma^{-1}	surface velocity: y-component
<code>svz(time,y,x)</code>	ma^{-1}	surface velocity: z-component
<code>bvx(time,y,x)</code>	ma^{-1}	basal velocity: x-component
<code>bvy(time,y,x)</code>	ma^{-1}	basal velocity: y-component
<code>bvz(time,y,x)</code>	ma^{-1}	basal velocity: z-component
<code>shearx(time,y,x)</code>	Pa	basal horizontal shear: x-component
<code>sheary(time,y,x)</code>	Pa	basal horizontal shear: y-component
<code>t(time,z,y,x)</code>	$^{\circ}\text{C}$	temperature field
<code>cdif(time,z,y,x)</code>	m^2a^{-1}	full diffusivity field
<code>trans_vx(time,y,x)</code>	ma^{-1}	transport velocity: x-component
<code>trans_vy(time,y,x)</code>	ma^{-1}	transport velocity: y-component
<code>sedib(time,y,x)</code>	m	thickness of dirty basal ice layer
<code>sedsl(time,y,x)</code>	m	thickness of deformable soft bed
<code>sedsl_max(time,y,x)</code>	m	max thickness of deformable soft bed
<code>sedsl2(time,y,x)</code>	m	thickness of non-deformable soft bed
<code>erosion_rate(time,y,x)</code>	ma^{-1}	instantaneous erosion rate
<code>erosion(time,y,x)</code>	m	total rock erosion since equilibrium defined
<code>xtracer(time,y,x)</code>	m	sediment packet tracer: x-component

continued on next page

<i>continued from previous page</i>		
<code>ytracer(time,y,x)</code>	m	sediment packet tracer: y-component
<code>rher(time,y,x)</code>	m	equilibrium rock surface - erosion
<code>eus_ice(time)</code>	m	eustatic sea level change for this simulation
<code>slc_ice(time,y,x)</code>	m	sea level change - ice component
<code>slc_water(time,y,x)</code>	m	sea level change - water component

References

- Andrews, J. (1970). *A geomorphological study of post-glacial uplift with particular reference to Arctic Canada*. No. 2 in Special Publication, Institute of British Geographers, London.
- Arnold, N. and Sharp, M. (2002). Flow variability in the Scandinavian ice sheet: modelling the coupling between ice sheet flow and hydrology. *Quaternary Science Reviews*, **21**, 485–502.
- Bard, E., Hamelin, B. and Fairbanks, R.G. (1990). U–Th ages obtained by mass spectroscopy in corals from Barbados: sea level during the past 130,000 years. *Nature*, **346**, 456–458.
- Barnola, J., Raynaud, D., Korotkevich, Y. and Lorius, C. (1987). Vostok ice core provides 160,000–year record of atmospheric CO₂. *Nature*, **329**, 408–414.
- Barrett, R., Berry, M., Chan, T.F., Demmel, J., Donato, J., Dongarra, J., Eijkhout, V., Pozo, R., Romine, C. and van der Vorst, H. (1994). *Templates for the Solution of Linear Systems: Building Blocks for Iterative Methods*. SIAM, Philadelphia, PA, 2nd edn.
- Benn, D.I. and Evans, D.J. (1998). *Glaciers & Glaciation*. Arnold, London.
- Bennett, M.R. (2003). Ice streams as the arteries of an ice sheet: their mechanics, stability and significance. *Earth–Science Reviews*, **61**, 309–339.
- Bice, K., Arthur, M. and Marincovich, L. (1996). Late Paleocene Arctic Ocean shallow–marine temperatures from mollusc stable isotopes. *Paleoceanography*, **11**, 241–249.
- Blanchon, P. and Shaw, J. (1995). Reef drowning during the last deglaciation: evidence for catastrophic sea–level rise and ice–sheet collapse. *Geology*, **23**, 4–8.
- Boulton, G.S. and Payne, A. (1992a). Simulation of the European ice sheet through the last glacial cycle and prediction of future glaciation. Tech. Rep. SKB 93-14, Swedish Nuclear Fuel and Waste Management Co.

- Boulton, G.S. and Payne, A.J. (1992b). Mid-latitude ice sheets through the last glacial cycle: glaciological and geological reconstructions. In J.C. Duplessy and M.T. Spyridakis, eds., *Long-Term Climatic Variations*, vol. 22 of *NATO ASI Series I*, 177–212, Springer-Verlag, Berlin, Heidelberg, New York.
- Boulton, G.S., Jones, A.S., Clayton, K.M. and Kenning, M.J. (1977). A British ice sheet model and patterns of glacial erosion and deposition in Britain. In F.W. Shotton, ed., *British Quaternary Studies: recent advances*, chap. 17, 231–246, Oxford University Press, Oxford.
- Boulton, G.S., Smith, G.D., Jones, A.S. and Newsome, J. (1985). Glacial geology and glaciology of the last mid-latitude ice sheets. *Journal of the Geological Society of London*, **142**, 447–474.
- Boulton, G.S., Hulton, N.R.J. and Vautravers, M. (1995). Ice-sheet models as tools for palaeoclimatic analysis: the example of the European ice sheet through the last glacial cycle. *Annals of Glaciology*, **21**, 103–110.
- Boulton, G.S., Dobbie, K.E. and Zatsepin, S. (2001a). Sediment deformation beneath glaciers and its coupling to the subglacial hydraulic system. *Quaternary International*, **86**, 3–28.
- Boulton, G.S., Dongelmans, P., Punkari, M. and Broadgate, M. (2001b). Paleoglaciology of an ice sheet through a glacial cycle: the European ice sheet through the Weichselian. *Quaternary Science Reviews*, **20**, 591–625.
- Boulton, G.S., Gustafson, G., Schelkes, K., Casanova, J. and Morén, L. (2001c). Palaeohydrology and geoforecasting for performance assessment in geosphere repositories for radioactive waste disposal. Project Report EUR 19784, European Commission.
- Bradley, R.S. (1999). *Paleoclimatology, Reconstructing Climates of the Quaternary*, vol. 64 of *International Geophysics Series*. Harcourt/Academic Press, San Diego, 2nd edn.
- Braithwaite, R.J. (1984). Calculations of degree-days for glacier-climate research. *Zeitschrift für Gletscherkunde und Glazialgeologie*, **20**, 1–8.
- Braithwaite, R.J. (1995). Positive degree-day factors for ablation on the Greenland ice sheet studied by energy-balance modelling. *Journal of Glaciology*, **41**, 153–160.
- Braithwaite, R.J. and Olesen, O.B. (1989). Calculation of glacier ablation from air temperature, West Greenland. In J. Oerlemans, ed., *Glacier Fluctuations and Climate Change*, 219–233, Kluwer Academic Publishers, Dordrecht.

- Breiman, L. and Friedman, J.H. (1985). Estimating optimal transformations for multiple regression and correlation. *Journal of the American Statistical Association*, **80**, 580–598.
- Broadgate, M.L. (1997). *An integrated approach to palaeoenvironmental reconstruction using GIS*. Ph.D. thesis, University of Edinburgh, Edinburgh.
- Broecker, W.S. (1994). Massive iceberg discharges as triggers for global climate change. *Nature*, **372**, 421–424.
- Bronstein, I.N. and Semendjajew, K.A. (1991). *Taschenbuch der Mathematik*. B.G. Teubner Verlagsgesellschaft, Stuttgart, 25th edn.
- Burgess, P. (1998). *Future Climatic and Cryospheric Change on Millennial Timescales: An Assessment using Two-Dimensional Climate Modelling Studies*. Ph.D. thesis, University of East Anglia, Climatic Research Unit, School of Environmental Sciences, Norwich, NR4 7TJ.
- Chappell, J. and Shackleton, N.J. (1986). Oxygen isotopes and sea level. *Nature*, **324**, 137–140.
- Chappell, J., Omura, A., Esat, T., McCulloch, M., Pandolfi, J., Ota, Y. and Pillans, B. (1996). Reconciliation of late Quaternary sea levels derived from coral terraces at Huon Peninsula with deep sea oxygen isotope records. *Earth and Planetary Science Letters*, **141**, 227–236.
- Charbit, S., Ritz, C. and Ramstein, G. (2002). Simulations of Northern Hemisphere ice-sheet retreat: sensitivity to physical mechanisms involved during the Last Glaciation. *Quaternary Science Reviews*, **21**, 243–265.
- Chen, J., Wilson, C., Chambers, D., Nerem, R. and Tapley, B. (1998). Seasonal global water mass budget and mean sea level variations. *Geophysical Research Letters*, **25**, 3555–3558.
- Chen, J., Wilson, C., Tapley, B., Chambers, D. and Pekker, T. (2001). Hydrological impacts on seasonal sea level change. *Global and Planetary Change*, **32**, 25–32.
- Clarke, G.K.C., Nitsan, V. and Paterson, W.S.B. (1977). Strain heating and creep instability in glaciers and ice sheets. *Reviews of Geophysics and Space Physics*, **15**, 235–247.
- Cliffe, K.A. and Morland, L.W. (2000). Full and reduced model solutions of steady axi-symmetric ice sheet flow over small and large bed topography slopes. *Continuum Mech. Thermodyn.*, **12**, 195–216.
- Cliffe, K.A. and Morland, L.W. (2001). A thermo-mechanically coupled test case for axi-symmetric ice sheet flow. *Continuum Mech. Thermodyn.*, **13**, 135–148.

- Cliffe, K.A. and Morland, L.W. (2002). Full and reduced model solutions of steady axi-symmetric ice sheet flow over bed topography with moderate slopes. *Continuum Mech. Thermodyn.*, **14**, 149–164.
- CLIMAP Project Members (1976). The surface of the Ice–Age Earth. *Science*, **191**, 1131–1137.
- Croll, J. (1867). On the excentricity of the Earth’s orbit, and its physical relations to the glacial epoch. *Philosophical Magazine*, **33**, 119–131.
- Crowley, T.J. and North, G.R. (1991). *Paleoclimatology*. No. 18 in Oxford Monographs on Geology and Geophysics, Oxford University Press.
- Dalgleish, A.N. (1996). *Statistical Characterisation of Long Term Climate Change*. Ph.D. thesis, The University of Edinburgh.
- Data Announcement 88-MGG-02 (1988). Digital relief of the Surface of the Earth. Tech. rep., NOAA, National Geophysical Data Center, Boulder, Colorado, eTOPO5.
- Dawson, S., Dawson, A. and Edwards, K. (1998). Rapid Holocene relative sea-level changes in Gruinart, Isle of Islay, Scottish Inner Hebrides. *Holocene*, **8**, 183–195.
- Denton, G.H. and Hughes, T.J., eds. (1981). *The Last Great Ice Sheets*. John Wiley & Sons, New York.
- Duff, D. (1993). *Holmes’ Principles of Physical Geology*. Chapman & Hall, London, 4th edn.
- Dziewonski, A.M. and Anderson, D.L. (1981). Preliminary reference Earth model. *Phys. Earth Planet. Inter.*, **25**, 297–356.
- Ehlers, J. (1996). *Quaternary and Glacial Geology*. John Wiley & Sons, Chichester.
- Engelhardt, H., Humphrey, N., Kamb, B. and Fahnestock, M. (1990). Physical conditions at the base of a fast moving Antarctic ice stream. *Science*, **248**, 57–59.
- England, P. (1992). Deformation of the continental crust. In G.C.B.C.J. Hawkesworth and R.C.L. Wilson, eds., *Understanding the Earth*, chap. 14, 275–300, Cambridge University Press, Cambridge.
- Fairbanks, R.G. (1989). A 17000–year glacio–eustatic sea level record: influence of glacial melting rates on the Younger Dryas event and deep–ocean circulation. *Nature*, **342**, 637–642.

- Fairbridge, R.W. (1983). Isostasy and eustasy. In D.E. Smith and A.G. Dawson, eds., *Shorelines and Isostasy*, no. 16 in Institute of British Geographers, Special Publication, chap. 1, 3–25, Academic Press, London.
- Fastook, J.L. and Holmlund, P. (1994). A glaciological model of the Younger Dryas event in Scandinavia. *Journal of Glaciology*, **40**, 125–131.
- Fleming, K. (2000). *Glacial Rebound and Sea-level Change: Constraints on the Greenland Ice Sheet*. Ph.D. thesis, Australian National University.
- Fowler, A.C. and Schiavi, E. (1998). A theory of ice-sheet surges. *Journal of Glaciology*, **44**, 104–118.
- Fukumori, I., Raghunath, R. and Fu, L. (1998). Nature of global large-scale sea level variability in relation to atmospheric forcing: A modeling study. *Journal of Geophysical Research — Oceans*, **103**, 5493–5512.
- Gallée, H., van Ypersele, J.P., Fichefet, T., Tricot, C. and Berger, A. (1991). Simulation of the last glacial cycle by a coupled, sectorially averaged climate–ice sheet model 1. The climate model. *Journal of Geophysical Research*, **96**, 13139–13161.
- Gallée, H., van Ypersele, J.P., Fichefet, T., Marsiat, I., Tricot, C. and Berger, A. (1992). Simulation of the last glacial cycle by a coupled, sectorially averaged climate–ice sheet model 2. Response to insolation and CO₂ variations. *Journal of Geophysical Research*, **97**, 15713–15740.
- Gehrels, W., Belknap, D., Black, S. and Newnham, R. (2002). Rapid sea-level rise in the Gulf of Maine, USA, since AD 1800. *The Holocene*, **12**, 383–389.
- Goodess, C.M., Watkins, S. and Palutikof, J. (2000a). Eustatic sea-level scenarios for the next 150kyrs. Tech. rep., Climatic Research Unit, University of East Anglia.
- Goodess, C.M., Watkins, S.J. and Palutikof, J.P. (2000b). The construction of global eustatic sea-level scenarios for the next 150kyr. Tech. rep., Climatic Research Unit, University of East Anglia.
- Greve, R. and Calov, R. (2002). Comparison of numerical schemes for the solution of the ice-thickness equation in a dynamic/thermodynamic ice-sheet model. *Journal of Computational Physics*, **179**, 649–664.
- Gropp, W., Lusk, E. and Skjellum, A. (1994). *Using MPI*. Massachusetts Institute of Technology.
- Harvey, N., Belperio, A., Bourman, R. and Mitchell, W. (2001). Geologic, isostatic and anthropogenic signals affecting sea level records at tide gauge sites in southern Australia. *Global and Planetary Change*, **32**, 1–11.

- Hastie, T.J. and Tibshirani, R.J. (1990). *Generalized Additive Models*. No. 43 in Monographs on Statistics and Applied Probability, Chapman and Hall, London, New York, Tokyo, Melbourne, Madras.
- Hindmarsh, R.C.A. (1993). Modelling the dynamics of ice sheets. *Progress in Physical Geography*, **17**, 391–412.
- Hindmarsh, R.C.A. (1997). Deforming beds: viscous and plastic scales of deformation. *Quaternary Science Reviews*, **16**, 1039–1056.
- Hindmarsh, R.C.A. and Payne, A.J. (1996). Time-step limits for stable solutions of the ice-sheet equation. *Annals of Glaciology*, **23**, 74–85.
- Hinton, A. (2000). Tidal changes and coastal hazards: Past, present and future. *Natural Hazards*, **21**, 173–184.
- Holton, J.R. (1992). *An Introduction to Dynamic Meteorology*, vol. 48 of *International Geophysics Series*. Academic Press, New York, 3rd edn.
- Hubbard, A. (1999). High-resolution modeling of the advance of the Younger Dryas ice sheet and its climate in Scotland. *Quaternary Research*, **52**, 27–43.
- Hughes, T. (2002). Calving bays. *Quaternary Science Reviews*, **21**, 267–282.
- Hulton, N.R.J. and Mineter, M.J. (2000). Modelling self-organization in ice streams. *Annals of Glaciology*, **30**, 127–136.
- Hulton, N.R.J. and Purves, R.S. (2000). Experiments in linking regional climate, ice-sheet models and topography. *Journal of Quaternary Science*, **15**, 369–+.
- Hulton, N.R.J. and Sugden, D. (1997). Dynamics of mountain ice caps during glacial cycles: the case of Patagonia. *Annals of Glaciology*, **24**, 81–89.
- Hulton, N.R.J. and Sugden, D.E. (1995). Modelling mass balance on former maritime ice caps: a Patagonian example. *Annals of Glaciology*, **21**, 304–310.
- Hulton, N.R.J., Sugden, D., Payne, A. and Clapperton, C. (1994). Glacier modeling and the climate of Patagonia during the last glacial maximum. *Quaternary Research*, **42**, 1–19.
- Hulton, N.R.J., Purves, R.S., McCulloch, R.D., Sugden, D.E. and Bently, M.J. (2002). The Last Glacial Maximum and deglaciation in southern South America. *Quaternary Science Reviews*, **21**, 233–241.
- Hutter, K. (1983). *Theoretical Glaciology*. Mathematical Approaches to Geophysics, D. Reidel Publishing Company, Dordrecht, Boston, Lancaster.

- Huybrechts, P. (1986). A three-dimensional time-dependent numerical model for polar ice sheets; some basic testing with a stable and efficient finite difference scheme. Tech. rep., Geografisch Instituut, Vrije Universiteit Brussel, Belgium.
- Huybrechts, P. (2002). Sea-level changes at the LGM from ice-dynamic reconstructions of the Greenland and Antarctic ice sheets during the glacial cycles. *Quaternary Science Reviews*, **21**, 203–231.
- Huybrechts, P., Payne, A.J. and intercomparison group, E. (1996). The EISMINT benchmarks for testing ice-sheet models. *Annals of Glaciology*, **23**.
- Imbrie, J., Hays, J.D., Martinson, D.G., McIntyre, A., Mix, A.C., Morley, J.J., Pisias, N.G., Prell, W.L. and Shackleton, N.J. (1984). The orbital theory of Pleistocene climate: support from a revised chronology of the marine $\delta^{18}\text{O}$ record. In A. Berger, J. Imbrie, J. Hays, G. Kukla and B. Saltzman, eds., *Milankovitch and Climate Part I*, vol. 126 of *NATO ASI Series*, 269–306, D. Reidel Publishing Company, Dordrecht, Boston, Lancaster.
- Iverson, N., Cohen, D., Hooyer, T.S., Fischer, U.H., Jackson, M., Moore, P.L., Lappégard, G. and Kohler, J. (2003). Effects of basal debris on glacier flow. *Science*, **301**, 81–84.
- Johnsen, S.J., Clausen, H.B., Dansgaard, W., Fuhrer, K., Gundestrup, N., Hammer, C.U., Iversen, P., Jouzel, J., Stauffer, B. and Steffensen, J.P. (1992). Irregular glacial interstadials recorded in a new Greenland ice core. *Nature*, **359**, 311–313.
- Johnston, P.J. (1993a). *Deformation of the Earth by surface loads*. Ph.D. thesis, The Australian National University.
- Johnston, P.J. (1993b). The effect of spatially non-uniform water loads on prediction of sea-level change. *Geophys. J. Int.*, **114**, 615–634.
- Johnston, P.J. (1995). The role of hydro-isostasy for Holocene sea-level changes in the British Isles. *Marine Geology*, **124**, 61–70.
- Johnston, P.J. and Lambeck, K. (2000). Automatic inference of ice models from postglacial sea level observations: Theory and application to the British Isles. *Journal of Geophysical Research*, **105**, 13179–13194.
- Jouzel, J., Barkov, N., Barnola, J., Bender, M., Chappellaz, J., Genthon, C., Kotlyakov, V., Lipenkov, V., Lorius, C., Petit, J., Raynaud, D., Raisbeck, G., Ritz, C., Sowers, T., Stievenard, M., Yiou, F. and Yiou, P. (1993). Extending the Vostok ice-record of palaeoclimate to the penultimate glacial period. *Nature*, **364**, 407–411.
- Karato, S. and Wu, P. (1993). Rheology of the Upper Mantle: a synthesis. *Science*, **260**, 771–778.

- Kaufmann, G. and Wu, P. (2002). Glacial isostatic adjustment in Fennoscandia with a three-dimensional viscosity structure as an inverse problem. *Earth and Planetary Science Letters*, **197**, 1–10.
- Kennett, J. (1982). *Marine Geology*. Prentice–Hall, Englewood Cliffs, N.J.
- Kuhn, M. (1984). Mass budget imbalances as criterion for a climatic classification of glaciers. *Geografiska annaler*, **66A**, 229–238.
- Lambeck, K. (1993a). Glacial rebound and sea-level change: an example of a relationship between mantle and surface processes. *Tectonophysics*, **223**, 15–37.
- Lambeck, K. (1993b). Glacial rebound of the British Isles — I. Preliminary model results. *Geophys. J. Int.*, **115**, 941–959.
- Lambeck, K. (1993c). Glacial rebound of the British Isles — II. A high-resolution, high-precision model. *Geophys. J. Int.*, **115**, 960–990.
- Lambeck, K. and Chappell, J. (2001). Sea level change through the last glacial cycle. *Science*, **292**, 679–686.
- Lambeck, K. and Nakiboglu, S.M. (1980). Seamount loading and stress in the ocean lithosphere. *Journal of Geophysical Research*, **85**, 6403–6418.
- Lambeck, K., Smither, C. and Johnston, P.J. (1998). Sea-level change, glacial rebound and mantle viscosity for northern Europe. *Geophys. J. Int.*, **134**, 102–144.
- Le Meur, E. and Huybrechts, P. (1996). A comparison of different ways of dealing with isostasy: examples from modelling the Antarctic ice sheet during the last glacial cycle. *Annals of Glaciology*, **23**, 309–317.
- Le Meur, E. and Huybrechts, P. (1998). Present-day uplift patterns over Greenland from a coupled ice-sheet/visco-elastic bedrock model. *Geophysical Research Letters*, **25**, 3951–3954.
- Long, A., Innes, J., Kirby, J., Lloyd, J., Rutherford, M., Shennan, I. and Tooley, M. (1998). Holocene sea-level change and coastal evolution in the Humber estuary, eastern England: an assessment of rapid coastal change. *Holocene*, **8**, 229–247.
- Lundqvist, J. (1986a). Late Weichselian glaciation and deglaciation in Scandinavia. *Quaternary Science Reviews*, **5**, 269–292.
- Lundqvist, J. (1986b). Stratigraphy of the central area of the Scandinavian glaciation. *Quaternary Science Reviews*, **5**, 251–268.

- Mahaffy, M.W. (1976). A three-dimensional numerical model of ice sheets: tests on the Barnes Ice Cap, Northwest Territories. *Journal of Geophysical Research*, **81**, 1059–1066.
- Mangerud, J. (1991). The Scandinavian ice sheet through the last glacial/interglacial cycle. In B. Frenzel, ed., *Klimageschichtliche Probleme der letzten 130 000 Jahre*, 307–330, G. Fischer, Stuttgart.
- Mangerud, J., Astakhov, V. and Svendsen, J.I. (2002). The extent of the Barents–Kara ice sheet during the Last Glacial Maximum. *Quaternary Science Reviews*, **21**, 111–119.
- Mattor, N., Williams, T.J. and Hewett, D.W. (1995). Algorithm for solving tridiagonal matrix problems in parallel. *Parallel Computing*, **21**, 1769–1782.
- Mayer, C. (1996). *Numerische Modellierung der Übergangszone zwischen Eisschild und Schelfeis*, vol. 214 of *Berichte zur Polarforschung*. Alfred–Wegener–Institut für Polar– und Meeresforschung, Bremerhaven.
- McCrea, W.H. (1975). Ice ages and the galaxy. *Nature*, **255**, 607–609.
- McIntyre, N.F. (1985). The dynamics of ice-sheet outlets. *Journal of Glaciology*, **31**, 99–107.
- Milankovitch, M. (1941). *Kanon der Erdbestrahlung und seine Anwendung auf das Eiszeitproblem*, vol. 133 of *Spec. Publ.*. Königliche Serbische Akademie Belgrad.
- Milne, G.A., Davis, J.L., Mitrovica, J.X., Scherneck, H.G., Johansson, J.M., Vermeer, M. and Koivula, H. (2001). Space-geodetic constraints on glacial isostatic adjustment in Fennoscandia. *Science*, **291**, 2381–2385.
- Mineter, M. and Hulton, N.R.J. (2001). Parallel processing for finite-difference modelling of ice sheets. *Computers & Geosciences*, **27**, 829–838.
- Moore, G.E. (1965). Cramming more components onto integrated circuits. *Electronics*, **38**.
- Mörner, N.A. (1987). Models of global sea-level changes. In M.J. Tooley and I. Shennan, eds., *Sea-Level Changes*, vol. 20 of *Institute of British Geographers special publication*, chap. 11, 332–355, Basil Blackwell, Oxford.
- Mound, J. and Mitrovica, J. (1998). True polar wander as a mechanism for second-order sea-level variations. *Science*, **279**, 534–537.
- Nakada, M. and Lambeck, K. (1987). Glacial rebound and relative sea-level variations: a new appraisal. *Geophys. J. R. astr. Soc.*, **90**, 171–224.
- Oerlemans, J. (2002). On glacial inception and orography. *Quaternary International*, **95-6**, 5–10.

- Oerlemans, J. and Reichert, B. (2000). Relating glacier mass balance to meteorological data by using a seasonal sensitivity characteristic. *Journal of Glaciology*, **46**, 1–6.
- Oerlemans, J. and van der Veen, C.J. (1984). *Ice Sheets and Climate*. D. Reidel Publishing Company, Dordrecht, Boston, Lancaster.
- O’Nions, K. (1992). The continents. In G.C.B.C.J. Hawkesworth and R.C.L. Wilson, eds., *Understanding the Earth*, 145–163, Cambridge University Press, Cambridge.
- Oreskes, N., Shrader–Frechette, K. and Belitz, K. (1994). Verification, validation and confirmation of numerical models in the Earth Sciences. *Science*, **263**, 641–646.
- Paterson, W.S.B. (1994). *The Physics of Glaciers*. Butterworth–Heinemann, Oxford, 3rd edn.
- Pattyn, F. (1996). Numerical modelling of a fast–flowing outlet glacier: experiments with different basal conditions. *Annals of Glaciology*, **23**, 237–246.
- Payne, A.J. (1998). Dynamics of the Siple Coast ice streams, West Antarctica: results from a thermomechanical ice sheet model. *Geophysical Research Letters*, **25**, 3173–3176.
- Payne, A.J. (1999). A thermomechanical model of ice flow in West Antarctica. *Climate Dynamics*, **15**, 115–125.
- Payne, A.J. and Baldwin, D.J. (2000). Analysis of ice–flow instabilities identified in the EISMINT intercomparison exercise. *Annals of Glaciology*, **30**, 204–210.
- Payne, A.J. and Dongelmans, P.W. (1997). Self–organisation in the thermomechanical flow of ice sheets. *Journal of Geophysical Research*, **102**, 12219–12233.
- Payne, A.J., Huybrechts, P., Abe–Ouchi, A., Calov, R., Fastook, J.L., Greve, R., Marshall, S.J., Marsiat, I., Ritz, C., Tarasov, L. and Thomassen, M.P.A. (2000). Results from the EISMINT model intercomparison: the effects of thermomechanical coupling. *Journal of Glaciology*, **46**, 227–238.
- Peltier, W.R. (1993). Time dependent topography through glacial cycle. IGBP PAGES/Center–A for Paleoclimatology Data Contribution. Tech. Rep. 93-015, NOAA/NGDC Paleoclimatology Program, Boulder CO, USA.
- Peltier, W.R. (1994). Ice age paleotopography. *Science*, **265**, 195–201.
- Peltier, W.R., Goldsby, D.L., Kohlstedt, D.L. and Tarasov, L. (2000). Ice–age ice–sheet rheology: constraints from the Last Glacial Maximum form of the Laurentide ice sheet. *Annals of Glaciology*, **30**, 163–176.

- Pirazzoli, P.A. (1991). *World Atlas of Holocene Sea-Level Changes*, vol. 58 of *Elsevier Oceanography*. Elsevier, Amsterdam.
- Plag, H.P. and Tsimplis, M. (1999). Temporal variability of the seasonal sea-level cycle in the North Sea and Baltic Sea in relation to climate variability. *Global and Planetary Change*, **20**, 173–203.
- Pollard, D. and PMIP Participating Groups (2000). Comparisons of ice-sheet surface mass budgets from Paleoclimate Modeling Intercomparison Project (PMIP) simulations. *Global and Planetary Change*, **24**, 79–106.
- Press, W., Teukolsky, S., Vetterling, W. and Flannery, B. (1992). *Numerical Recipes in FORTRAN*. Cambridge University Press, 2nd edn.
- Purves, R.S. and Hulton, N.R.J. (2000). A climatic-scale precipitation model compared with the UKCIP baseline climate. *International Journal of Climatology*, **20**, 1809–1821.
- Ritz, C. (1987). Time dependent boundary conditions for calculation of temperature fields in ice sheets. In *The Physical Basis of Ice Sheet Modelling*, no. 170 in IAHS Publications, 207–216.
- Sejrup, H.P., Hafliðason, H., Aarseth, I., King, E., Forsberg, C.F., Long, D. and Rokoengen, K. (1994). Late Weichselian glaciation history of the northern North Sea. *Boreas*, **23**, 1–13.
- Sejrup, H.P., Landvik, J.Y., Border, A., Janocko, J., Eiriksson, J. and King, E. (1998). The Jæren area, a border zone of the Norwegian Channel Ice Stream. *Quaternary Science Reviews*, **17**, 801–812.
- Shennan, I., Lambeck, K., Horton, B., Innes, J., Lloyd, J., McArthur, J., Purcell, T. and Rutherford, M. (2000). Late Devensian and Holocene records of relative sea-level changes in northwest Scotland and their implication for glacio-hydro-isostatic modelling. *Quaternary Science Reviews*, **19**, 1103–1135.
- Siegert, M.J. (2001). *Ice Sheets and Late Quaternary Environmental Change*. John Wiley & Sons, Chichester.
- Sissons, J.B. (1979a). The Loch Lomond Stadial in the British Isles. *Nature*, **280**, 199–203.
- Sissons, J.B. (1979b). Palaeoclimatic inferences from former glaciers in Scotland and the Lake District. *Nature*, **278**, 518–520.
- Spiegel, M.R. (1968). *Mathematical Handbook of Formulas and Tables*. Schaum's Outline Series, McGraw-Hill Book Company, New York.
- Stacey, F.D. (1992). *Physics of the Earth*. Brookfield Press, Brisbane, 3rd edn.

- Stokes, C.R. and Clark, C.D. (2001). Palaeo-ice streams. *Quaternary Science Reviews*, **20**, 1437–1457.
- Sundquist, E.T. (1990). Long-term aspects of future atmospheric CO₂ and sea level changes. In R. Revelle, ed., *Sea-level Change*, National Research Council Studies in Geophysics, 193–207, National Academy Press, Washington D.C.
- Takeda, A., Cox, S. and Payne, A.J. (2002). Parallel numerical modelling of the Antarctic Ice Sheet. *Computers & Geosciences*, **28**, 723–734.
- Tarasov, L. and Peltier, W.R. (1999). Impact of thermomechanical ice sheet coupling on a model of the 100kyr ice age cycle. *Journal of Geophysical Research*, **104**, 9517–9545.
- Tarasov, L. and Peltier, W.R. (2000). Laurentide ice sheet aspect ratio in models based on Glen’s flow law. *Annals of Glaciology*, **30**, 177–186.
- Tibshirani, R. (1988). Estimating transformations for regression via additivity and variance stabilization. *Journal of the American Statistical Association*, **83**, 394–405.
- Tooley, M.J. (1993). Long term changes in eustatic sea level. In R.A. Warrick, E.M. Barrow and T.M.L. Wigley, eds., *Climate and Sea Level Change: observations, projections and implications*, chap. 6, 81–107, Cambridge University Press, Cambridge.
- Tulaczyk, S., Kamb, W.B. and Engelhardt, H.F. (2000). Basal mechanics of Ice Stream B, West Antarctica, 2, Undrained plastic bed model. *Journal of Geophysical Research*, **105**, 483–494.
- Tushingham, A.M. and Peltier, W.R. (1991). ICE-3G: A new global model of Late Pleistocene deglaciation based upon geophysical predictions of post-glacial relative sea level change. *Journal of Geophysical Research*, **96**, 4497–4523.
- Tushingham, A.M. and Peltier, W.R. (1992). Validation of the ICE-3G model of Würm–Wisconsin deglaciation using a global data base of relative sea level histories. *Journal of Geophysical Research*, **97**, 3285–3304.
- Tushingham, A.M. and Peltier, W.R. (1993). Relative sea level database. IGBP PAGES/World Data Center-A for paleoclimatology data contribution. Tech. Rep. 93-016, NOAA/NGDC Paleoclimatology Program, Boulder CO, USA.
- van der Veen, C.J. (1987). The West Antarctic Ice Sheet: the need to understand its dynamics. In C.J. van der Veen and J. Oerlemans, eds., *Dynamics of the West Antarctic Ice Sheet*, 1–16, D. Reidel Publishing Company, Dordrecht, Boston, Lancaster.

-
- van der Veen, C.J. (2002). Polar ice sheets and global sea level: how well can we predict the future? *Global and Planetary Change*, **32**, 165–194.
- van der Veen, C.J. and Whillans, I.M. (1989). Force budget I: theory and numerical methods. *Journal of Glaciology*, **35**, 53–60.